UNIVERSITAT POLITÈCNICA DE CATALUNYA

DEPARTAMENT D'ENGINYERIA ELÈCTRICA

Doctoral Thesis

Induction heating converter's design, control and modeling applied to continuous wire heating

Autor: **Guillermo Martín Segura**

Director: **Daniel Montesinos i Miracle**

Barcelona, June 2012

Acta de qualificació de tesi doctoral

Curs acadèmic:

Nom i cognoms

DNI / NIE / Passaport

Programa de doctorat

Unitat estructural responsable del programa

Resolució del Tribunal

Reunit el Tribunal designat a l'efecte, el doctorand / la doctoranda exposa el tema de la seva tesi doctoral titulada
_____
_____.

Acabada la lectura i després de donar resposta a les qüestions formulades pels membres titulars del tribunal, aquest atorga la qualificació:

☐ APTA/E ☐ NO APTA/E

(Nom, cognoms i signatura) President/a	(Nom, cognoms i signatura) Secretari/ària
(Nom, cognoms i signatura) Vocal	(Nom, cognoms i signatura) Vocal	(Nom, cognoms i signatura) Vocal

_____, _____ d'/de _____ de _____

El resultat de l'escrutini dels vots emesos pels membres titulars del tribunal, efectuat per l'Oficina de Doctorat, a instància de la Comissió de Doctorat de la UPC, atorga la MENCIÓ CUM LAUDE:

☐ SI ☐ NO

(Nom, cognoms i signatura) Vicerectora de Recerca Presidenta de la Comissió de Doctorat	(Nom, cognoms i signatura) Cap de l'Oficina de Doctorat Secretària de la Comissió de Doctorat	(Nom, cognoms i signatura) Secretari/ària del tribunal (o membre del tribunal de la UPC)

Barcelona, _____ d'/de _____ de _____

Diligència "Internacional del títol de doctor o doctora"

Com a secretari/ària del tribunal faig constar que la tesi s'ha defensat en part, i com a mínim pel que fa al resum i les conclusions, en una de les llengües habituals per a la comunicació científica en el seu camp de coneixement i diferent de les que són oficials a Espanya. Aquesta norma no s'aplica si l'estada, els informes i els experts externs provenen d'un país de parla hispana.

(Nom, cognoms i signatura)   Secretari/ària del tribunal

Esta tesis no se podría haber realizado sin la colaboración desinteresada de muchas personas que me han brindado su ayuda, sus conocimientos y su apoyo a lo largo de estos años. Aunque me sea imposible nombrarles a todos, quisiera agradecerles todo cuanto han hecho por mí.

En primer lugar quisiera agradecerle el apoyo prestado a mi director Daniel Montesinos y a Toni Sudrià. Por supuesto también a todos mis compañeros de trabajo, más bien amigos, de los que he aprendido muchas de las cosas que hay aquí plasmadas y con los que aun sigo aprendiendo y divirtiéndome cada día.

También querría agradecer muy especialmente a aquellos ex compañeros de trabajo con los que pasé interminables horas delante de estos armarios de calentamiento por inducción, intentando que aquello funcionara. Al final parece ser que funcionó. Es imposible nombrarlos a todos, pero en especial quiero agradecer a Coia por su grata compañía durante estos años, aunque siempre me tocase cargar con las cosas y destornillar en los sitios más inaccesibles. A Quim, que no deja de sorprenderme y del que aún no dejo de aprender cosas. Y a Miquel, por su humor y por todas las cosas que me ha enseñado durante estos años.

Agradecer a mis amigos de toda la vida por ayudarme a airearme y a reír cuando lo necesitaba, sin eso, difícilmente hubiese continuado.

No puedo dejarme a mi familia. A mi abuelo, del que aprendí la importancia de educar a los hijos y lo poco que sé de arreglar bicicletas, quizás de sus inventillos venga mi vena ingenieril. A mi abuela, de la que aprendí la bondad y la generosidad de aquellos que menos tienen, además de algunos guisos memorables. A mi abuelito, del que aprendí la importancia de leer todo cuanto pueda, y sin el que probablemente no hubiese llegado aquí. Aún recuerdo aquel maldito examen de castellano con el que me martirizó durante un semestre a base de dictados y a partir del cual empecé a sacar buenas notas. Aunque no haya podido demostrarlo a lo largo de esta tesis, aprendí que albahaca efectivamente se escribía con H. A mi abuelita, de la que supongo he heredado la cabezonería y perseverancia que tanto me han ayudado estos últimos años, y de la que aún no dejo de aprender las artes culinarias más selectas. A mi madre, de la que heredé la inquietud por la ciencia y el saber, y sin la que probablemente jamás hubiese llegado hasta aquí. A mi padre, por enseñarme muchísimas cosas, entre ellas a tener curiosidad por las cosas, no sólo por los convertidores. También por enseñarme

lo que es la ética y los principios a los que uno no debe nunca renunciar. A mi hermano, por enseñarme que existen muchas cosas más allá de la ingeniería y que muchas veces son menospreciadas. En definitiva a todos, por educarme, enseñarme y apoyarme en todos los sentidos desde que empecé con esto.

Y ya por último, a la persona sin la que indiscutiblemente esto no hubiese podido ser y que merecería el título honorífico de coautora. A mi novia Olatz, no sólo por su apoyo incondicional y por aguantarme, por lo que ya merecería un premio, sino también por los millones de folios que se ha tenido que leer a medida que iba haciendo y por todo lo que me ha ayudado en la redacción de la memoria. Realmente esto no hubiese quedado así de no ser por ella.

En fin, a todos ellos: muchas gracias! Esta tesis es para vosotros.

Acknowledgements

I would like to thank all the people from the scientific community who shared with me their expertise and research insight generously and unselfishly. It is surprisingly gratifying to find that, still, one can find people who share their knowledge and spend their time with beginners. I have to admit that they helped to revive my faith in human beings.

I would like to thank specially Dr. Andras Kelemen and Dr. Valentin Nemkov for their interest and for their thoughtful advises and experience that served me during this thesis. To Dr. Mircea Chindris, Dr. Ioan Vadan and the Department of Electrical Machines from the Technical University of Cluj-Napoca for their interest and support of this work. I would like to thank all the researchers that helped me during my PhD, spending their time answering simple questions from an unknown PhD student from another part of the world. It is impossible to write all the names, but some of them were Szelitzky Tibor, Dr. Nimrod Kutasi, Dr. Virgiliu Fireteanu, Dr. Valery Rudnev or Dr. Xavier Bohigas.

The author would also like to thank AUTOMAT Industrial S.L for their support to this work during all this years.

This work has been supported by the University and Research Commissioner of the Innovation, Universities and Enterprises Department of the Catalan Government and the European Social Fund.

iv

Resumen

El calentamiento por inducción es un método de calentamiento para materiales conductores que aprovecha el calor generado por las corrientes de Foucault, generadas a su vez a partir de un campo magnético variable. Desde que en 1831 Michael Faraday descubrió la inducción electromagnética, este fenómeno ha sido ampliamente estudiado en diversas aplicaciones como por ejemplo transformadores, motores o generadores. A principios del siglo XX la inducción empezó a investigarse como un método de calentamiento, hecho que condujo en 1927 a la construcción por parte de la Electric Furnace Company del primer equipo industrial de fusión por inducción. Así mismo, Midvale Steel y Ohio Crankshaft Company crearon el primer equipo de endurecimiento de acero con calentamiento por inducción en la misma época [1,2]. Aún y así, no fue hasta la II Guerra Mundial, cuando el calentamiento por inducción experimentó un gran aumento, debido a su utilización en la producción de proyectiles y piezas para vehículos.

Al principio, los campos magnéticos necesarios para generar el calor se obtenían con generadores de chispas, generadores de válvulas o grupos motor-generador. Con la aparición de semiconductores comerciales en los años sesenta, estos sistemas fueron poco a poco remplazados por generadores que empleaban este tipo de dispositivos. Actualmente, la mayoría de convertidores de calentamiento por inducción emplean dispositivos semiconductores, utilizando la mayoría IGBTs y MOSFETs en aplicaciones de alta frecuencia y media-alta potencia.

En lo que se refiere a la caracterización del sistema pieza-inductor, los primeros modelos utilizados para entender su comportamiento se basaban en métodos analíticos. Estos modelos resultaban útiles para analizar la tendencia general del sistema, pero no eran suficientemente precisos para análisis más rigurosos y además se limitaban a geometrías simples. Con la aparición de los ordenadores, los métodos numéricos experimentaron un gran crecimiento en los años noventa y se empezaron a utilizar en el campo del calentamiento por inducción. Actualmente, el desarrollo de softwares comerciales que permiten este tipo de análisis ha propiciado su uso por parte de centros de investigación y empresas. Este tipo de softwares permiten una gran variedad de análisis de gran complejidad con gran precisión, reduciendo de esta manera la necesidad de largos procesos de prueba y error.

Los adelantos realizados en las últimas décadas, la utilización de métodos numéricos y la aparición y mejora de los dispositivos semiconductores, con su correspondiente reducción de costes, han producido un aumento notable del uso del calentamiento por inducción en numerosos campos. Así, el calentamiento por inducción puede encontrarse en multitud de aplicaciones como por ejemplo en cocinas domésticas, hornos de fundición o equipos de sellado empleados en el sector de la automoción. Esta proliferación se debe en gran parte a las ventajas que presenta frente a otros métodos convencionales de calentamiento, como son su facilidad de control, su rapidez y el ahorro de energía que se deriva de su uso.

La presente tesis se centra en la aplicación del calentamiento por inducción en el calentamiento de alambre. El calentamiento de alambre por inducción es un proceso industrial en el que el alambre circula de forma continua por el inductor, consiguiendo elevadas tasas de producción con sistemas de reducidas dimensiones. Suelen ser procesos industriales de mediana-gran potencia que trabajan 24 horas al día.

Los primeros capítulos de esta tesis introducen las bases del calentamiento por inducción, su modelización y los convertidores y tanques empleados. Posteriormente, se realiza el diseño y la implementación de un convertidor multicanal para aplicaciones de gran potencia y elevada frecuencia. El objetivo de este tipo de estructura es aprovechar su modularidad para la reducción del tiempo de diseño, del coste de producción y del coste de mantenimiento. Además, este convertidor aumenta la fiabilidad del sistema dado que su modularidad permite tiempos de reparación reducidos, hecho de especial interés en procesos de trabajo continuos.

Adicionalmente, se ha diseñado e implementado un lazo de seguimiento de fase programado. Este sistema es de gran versatilidad, puesto que permite el control de diferentes aplicaciones con el mismo hardware, característica que resulta de gran interés para aplicaciones industriales. Posteriormente, este sistema se ha utilizado para diseñar e implementar un sistema de control que varía sus consignas en función de la carga, de manera que permite la conmutación suave en un rango mayor, mejorando así las prestaciones del convertidor.

Finalmente, se ha realizado la modelización de un sistema de endurecimiento continuo con calentamiento por inducción. En estos sistemas, la interdependencia entre parámetros magnéticos, térmicos y eléctricos dificulta el análisis de los mismos. En esta tesis, se ha realizado un análisis mediante métodos numéricos incorporando el comportamiento del convertidor y su

influencia en el proceso térmico y electromagnético. Este sistema se ha simulado y también se han realizado pruebas experimentales para verificar los resultados obtenidos.

Abstract

Induction heating is a heating method for electrically conductive materials that takes advantage of the heat generated by the eddy currents originated by means of a varying magnetic field. Since Michael Faraday discovered electromagnetic induction in 1831, this phenomenon has been widely studied in many applications like transformers, motors or generators' design. It was not until the turn of the 20th century that induction started to be deeply studied as a heating method. The investigations on this field led to the construction of the first industrial induction melting equipment by the Electric Furnace Company in 1927 and the first induction hardening equipment by Midvale Steel and Ohio Crankshaft Company some years later [1,2]. In the II World War the use of induction heating experienced a great increase due to its utilization in the manufacturing of projectiles and vehicle parts.

At first, the varying magnetic fields were obtained with spark-gap generators, vacuum-tube generators and low frequency motor-generator sets. With the emergence of reliable semiconductors in the late 1960's, motor-generators were replaced by solid-state converters for low frequency applications. Nowadays, most of the converters for induction heating applications are based on semiconductors technology, most of them using IGBT and MOSFET devices in medium-power and high-frequency applications.

With regard to the characterization of the inductor-workpiece system, the first models used to understand the load's behavior were based on analytical methods. These methods were useful to analyze the overall behavior of the load, but they were not accurate enough for a precise analysis and were limited to simple geometries. With the emergence of computers, numerical methods experienced a tremendous growth in the 1990's and started to be applied in the induction heating field. Nowadays, the development of commercial softwares that allow this type of analysis have started to make the use of numerical methods popular among research centers and enterprises. This type of softwares allow a great variety of complex analysis with high precision, consequently diminishing the trial and error process.

The research realized in last decades, the increase in the utilization of numerical modeling and the appearance and improvement of semiconductor devices, with their corresponding cost reduction, have caused the spread of induction heating in many fields. Induction heating equipments can be

found in many applications, since domestic cookers to high-power aluminum melting furnaces or automotive sealing equipments, and are becoming more and more popular thanks to their easy control, quick heating and the energy savings obtained.

The present thesis focuses on the application of induction heating to wire heating. The wire heating is a continuous heating method in which the wire is continuously feeding the heating inductor. This heating method allows high production rates with reduced space requirements and is usually found in medium to high power industrial processes working 24 hours per day.

The first chapters of this study introduce the induction heating phenomenon, its modeling and the converters and tanks used. Afterwards, a multichannel converter for high-power and high-frequency applications is designed and implemented with the aim of providing modularity to the converter and reduce the designing time, the production cost and its maintenance. Moreover, this type of structure provides reliability to the system and enables low repairing times, which is an extremely interesting feature for 24 hours processes.

Additionally, a software phase-locked loop for induction heating applications is designed and implemented to prove its flexibility and reliability. This type of control allows the use of the same hardware for different applications, which is attractive for the case of industrial applications. This phase-locked loop is afterwards used to design and implement a load-adaptive control that varies the references to have soft-switching according to load's variation, improving converter's performance.

Finally, the modeling of a continuous induction wire hardening system is realized, solving the difficulty of considering the mutual influence between the thermal, electromagnetic and electric parameters. In this thesis, a continuous process is modeled and tested using numerical methods and considering converter's operation and influence in the process.

Thesis outline

The present thesis focuses on the application of induction heating to continuous round wire heating . It has been structured as follows: Chapters 1, 2 and 3 are the introduction to induction heating phenomenon, its modeling and the converters used for this heating method; and Chapters 4, 5, 6 and 7 study the definition of a multichannel structure, the control systems used in IH applications and the modeling considering converter's operation. Although this thesis focuses in round wire heating, most of the concepts and conclusions presented can be extrapolated to other application areas.

In Chapter 1, the basic mechanisms of heat generation and the basic concepts with regards to induction heating are explained. A first and simple analytical model of the inductor-workpiece system is presented, introducing the concepts of penetration depth, critical frequency and efficiency used in induction heating applications.

In Chapter 2, a more extensive introduction on the inductor-workpiece system modeling is realized. The inductor-workpiece modeling is performed using analytical and numerical methods. In this chapter, a brief introduction on analytical methods is exposed, explaining its limitations and benefits. Afterwards, a short overview on numerical methods is done, providing a first bibliography and explaining the main characteristics of these methods in induction heating.

In Chapter 3, an extensive explanation of the different converter topologies used in induction heating field are shown. Firstly, the series and parallel resonant tanks and their associated topologies are broadly presented and, afterwards, other topologies like three element tanks, the converters without intermediate power control stage, converters using matching transformers and those based on parallel and series connection of inverters are introduced.

In Chapter 4, a multichannel converter structure is studied for high-power and high-frequency applications. The aim of this chapter is to study the different converter structures and connections that can be used to realize a converter based on basic structures. The underlying concept with regards to this design procedure is to profit this modularity to reduce the designing

time, the production cost and the maintenance. In Chapter 5, the concepts presented in the previous chapters are used for designing a software phase-locked loop for induction heating applications. This software PLL allows a control with less analog components, avoiding variations due to part spread or temperature drift, and benefiting from the flexibility of a software programmed control.

In Chapter 6, the software phase-locked loop designed in Chapter 5 is used to implement a load-adaptive phase-locked loop. The aim of this control system is to provide an optimum commutation sequence that allows soft-switching even when the load varies.

In Chapter 7, based on the introduction of Chapter 2 for modeling induction heating systems and the concepts regarding converters' operation explained in Chapter 3, the modeling of a continuous induction wire hardening system is realized. The system is modeled using numerical methods and considering the frequency variation and the power control loop typical from converters' operation.

Finally, in Chapter 8, the conclusions are summarized, presenting the contributions and explaining the challenging research fields that this thesis has not dealt with.

Contents

Contents

Contents

List of Figures

List of Figures

List of Figures

List of Tables

Nomenclature

Roman Items

$\hat{i}_{tank}$ Amplitude of i_{tank}.

$\hat{u}_{tank}$ Amplitude of u_{tank}.

A Magnetic vector potential.

A_a Cross-section of the gap.

A_w Cross-section of the workpiece.

B Magnetic field density.

C Capacitance.

c Average value of the specific heat of a material.

C_p Parasitic capacitance.

C_{CE} Collector-emitter capacitance.

C_{oes} Output capacitance.

C_{res} Miller capacitance.

D Electric displacement field.

d_c Inner coil diameter.

d_w Workpiece diameter.

E Electric field intensity.

f Frequency.

f_c Critical frequency.

f_n Undamped natural frequency.

Nomenclature

f_r	Resonant frequency.
$f_r p$	Parallel resonant frequency of the LCL tank.
$f_r s$	Series resonant frequency of the LCL tank.
$f_s w$	Commutation frequency.
f_{phase0}	Frequency at which the phase-shift is zero.
H	Magnetic field intensity.
H_s	Common magnetic field intensity.
HC	Heat content.
I	Current.
i	transformer's turns ratio.
I_e	Current of the DC source.
i_C	Current at the resonant capacitor.
i_L	Current at the resonant inductor.
$i_{R_{eq}}$	Current at the equivalent resistor.
i_{tank}	Current at the output of the inverter.
J	Current density.
J_s	Source current density.
K	Constant used for the calculation of the inductor-workpiece equivalent circuit.
k	Thermal conductivity.
k_r	Correction factor considering the space between turns.
$k_\varphi *$	Constant used for the calculation of $t_\varphi *$.
$k_d *$	Constant used for the calculation of $t_d *$.
K_r	Workpiece resistance factor.
L	Inductance.

Nomenclature

l_c Coil length.

L_p Parasitic inductance.

l_w Workpiece length.

L_a Gap inductance.

L_c Coil inductance.

L_w Workpiece inductance.

m Mass.

N_c Turns of the inductor.

P Power in the workpiece.

p Adimensional factor used for the calculation of the inductor-workpiece equivalent circuit.

p_r Production.

p_v Induced power density.

P_{act} Active power.

P_{rect} Reactive power.

$P_{Thermallosses}$ Thermal losses through the surface of the workpiece.

P_w Power to heat the workpiece.

Q Quality factor.

q Adimensional factor used for the calculation of the inductor-workpiece equivalent circuit.

$Q_{parallel}$ Quality factor of the workpiece-coil parallel model.

Q_{serie} Quality factor of the workpiece-coil series model.

R_b Resistance used in the MOSFET's model.

r_c Inner coil radius.

r_w Workpiece radius.

Nomenclature

R_c Coil resistance.

$R_{eqparallel}$ Resistance of the workpiece-coil parallel model.

$R_{eqserie}$ Resistance of the workpiece-coil series model.

R_{eq} Equivalent resistance of a workpiece-coil.

R_s Superficial resistance.

R_w Workpiece resistance.

S Apparent power.

S_{heated} Surface heated.

t Required heating time.

t_φ Time delay between u_{tank} and i_{tank}, in seconds.

$t_\varphi*$ Time delay reference between u_{tank} and i_{tank}, in seconds.

t_{clock} Period of the clock.

t_d Dead-time.

t_d* Dead-time reference.

T_{final} Average value of the final temperature.

$T_{initial}$ Average value of the initial temperature.

U Voltage.

U_e Voltage of the DC source.

u_C Voltage at the resonant capacitor.

u_L Voltage at the resonant inductor.

$u_{R_{eq}}$ Voltage at the equivalent resistor.

u_{tank} Voltage at the output of the inverter.

$Z_{eqparallel}$ Impedance of the workpiece-coil parallel model.

$Z_{eqserie}$ Impedance of the workpiece-coil series model.

Z_{tank} Impedance of the resonant tank.

Z'_{tank} Impedance of the resonant tank referred to the primary.

Greek Items

β Phase-shift between the instant at which the gate signal of the switch becomes low and the moment at which i_{tank} changes polarity.

β' Phase-shift between the instant at which the gate signal of the switch becomes high and the moment at which u_{tank} changes polarity.

δ Penetration depth.

δ_c Penetration depth of the coil.

δ_w Penetration depth of the workpiece.

η_T Total efficiency.

$\eta_{electrical}$ Electrical efficiency.

$\eta_{Thermal}$ Thermal efficiency.

μ Magnetic permeability.

μ_0 Magnetic permeability of the vacuum.

μ_r Relative magnetic permeability.

ω Angular frequency.

ω_n Resonant frequency (angular).

ω_n Undamped natural frequency (angular).

ω_{phase0} Frequency at which the phase-shift is zero(angular).

ω_{ri} Frequency at which the current in the inductor is maximum (angular).

ρ Electrical resistivity.

ρ_m Mass density.

ρ_c Electrical resistivity of the coil.

ρ_w Electrical resistivity of the workpiece.

Nomenclature

φ Phase-shift between u_{tank} and i_{tank}.

φ' Phase-shift between i_{tank} and u_{tank}.

$\varphi*$ Phase-shift reference between u_{tank} and i_{tank}.

ζ Damping ratio.

Acronyms

AC   Alternating Current.

ADC   Analog to Digital Converter.

BEM   Boundary Element Method.

BJT   Bipolar Junction Transistor.

CFPRI   Current-Fed Parallel-Resonant Inverter.

CITCEA-UPC Centre d'Innovació Tecnològica en Convertidors Estàtics i Accionaments.

DC   Direct Current.

DSP   Digital Signal Processors.

FDM   Finite Differential Method.

FEM   Finite Element Method.

FPGA   Field-Programmable Gate Arrays.

FREDFET Fast Recovery Epitaxial Diode Field-Effect Transistors.

IGBT   Insulated Gate Bipolar Transistor.

IH   Induction Heating.

MOSFET Metal Oxide Semiconductor Field Effect Transistor.

PDM   Pulse Density Modulation.

PLC   Programmable Logic Controller.

PLL   Phase-Locked Loop.

PWM   Pulse Width Modulation.

RMS   Root Mean Square.

UPC   Universitat Politècnica de Catalunya.

VCO   Voltage-Controlled Oscillator.

VFSRI Voltage-Fed Series-Resonant Inverter.

ZCS   Zero Current Switching.

ZVS   Zero Voltage Switching.

Chapter 1

Induction heating basics

1.1 Introduction

Induction heating (IH) is a method of heating electrically conductive materials taking advantage of the heat produced by the eddy currents generated in the material. It has many advantages compared to other heating systems (e.g. gas- and oil-fired furnaces), such as quicker heating, faster start-up, more energy saving and higher production rates [1, p. 7]. The research done these last years in specific power supplies for this application, the numerical and computational methods developed, as well as the decrease of the cost of these systems, has lead to a widespread of IH in many processes and applications, such as cooking, automotive sealing, motor heating, paper making, tube and bar heating or aluminum melting.

Since Michael Faraday discovered electromagnetic induction in 1831 [3], this phenomenon has been widely studied in many applications, as for example transformers and other magnetic designs. The basic electromagnetic phenomena in which IH relies has been described and discussed extensively in many texts, including several college textbooks and some handbooks like [1, 2, 4–7].

This chapter pretends to introduce the basis of IH and enhance the comprehensibility to the reader for next chapters. A short overview of IH principles needed for this study is provided, avoiding long and extensive demonstrations and formulas, that can be found in the bibliography provided along this chapter. It has to be noted that most of the general concepts explained during this thesis can be applied to any IH application. However, the study is particularized for continuous wire heating and, thus, the formulas exposed are simplified for this specific case.

First, in Section 1.2, the mechanisms of energy dissipation on which IH is based are explained. Afterwards, in Section 1.3, the inductor-workpiece

electrical model is presented, where simplified formulas for estimating equivalent resistor and inductor values are given for wire heating. Then, in Section 1.4, the efficiency of a IH process is shown and the concept of penetration depth and critical frequency is introduced. The importance of the inductor-workpiece geometry in the efficiency is also briefly commented. Next, in Section 1.5, a practical but simple procedure to calculate the inductor and power requirements in an IH process is explained. The aim of this section is to help the reader have a wider view of the process and explain general considerations used by the engineers when designing an IH system. Finally, in Section 1.6, the main points of this chapter are summarized.

It has to be noted that the aim of this chapter is to give a first introduction to IH, especially for those researchers involved in power electronics that are not used to deal with this phenomenon and its principles. Therefore, the formulas presented in here are oversimplifications based on old classic books that serve the reader to understand the tendency and the overall system's behavior, but not to realize an accurate design of the IH system.

1.2 Induction heating: Joule and hysteresis losses

The most basic elements composing an IH system are the piece to be heated, also known as a workpiece, and the inductor or coil that produces the magnetic field needed to generate the heat. The inductor and the workpiece can have any shape and the piece is usually placed inside the coil to have a better coupling. Considering that this study focuses on the heating of round wires, the inductor used is a solenoid and the workpiece a round wire.

IH phenomenon is based on two mechanisms of energy dissipation:

1. *Energy losses due to Joule effect*: When applying an alternating voltage to an induction coil, an alternating current is generated in the coil. This current produces an alternating magnetic field (Ampere's law) that induces voltage in the workpiece, which opposes to the variation of this magnetic field (Lenz's law). These voltage creates currents in the workpiece, called eddy or Foucault currents, which have the same frequency but opposite direction than the original current. These eddy currents produce heat in the piece by Joule effect.

2. *Energy losses due to hysteresis*: These losses are caused by friction between dipoles when ferromagnetic materials are magnetized in one direction and another. They appear in ferromagnetic materials below

their Curie temperature (temperature at which the material becomes non-magnetic).

In most of IH applications, hysteresis losses represent less than the 7 % of the eddy current losses [2, p. 153] . Therefore, eddy currents are the main mechanism of energy dissipation and, so, the most important in IH.

1.3 Inductor-workpiece electrical model

In most of engineering fields studying a physical phenomenon is necessary to create a model with a similar behavior to the real case. The purpose of this model is to simplify the real problem to a formulation that allows the authors to study the behavior of the phenomenon without the need of a trial and error process. In case of IH, this need has lead to many different models based on different simplifications and assumptions. In case of the models designed for electrical engineers, the inductor-workpiece system is usually modeled by inductors and resistors.

In Section 1.3.1 an equivalent electrical model is presented. This model is based on the simplification of the inductor-workpiece system to an equivalent resistor and inductor, which are more extensively explained and formulated in Section 1.3.2. It has to be noted that the model presented is one of the most basic simplifications, but it helps to understand the overall behavior of an IH system in a very simple manner.

1.3.1 Series and parallel model

Generally, the induction-coil and the workpiece are electrically modeled by an inductor, L, and an equivalent resistor, R_{eq}. The equivalent resistor represents the resistor of the workpiece as reflected in the coil and the resistance of the inductor itself. Its value depends on the coil and workpiece geometries and materials, the frequency of the process and other parameters.

There are two main models representing the induction-coil and the workpiece: the series model and the parallel model (see Figure 1.1).

Series model

In any IH application, one of the parameters that characterizes the inductor-workpiece system is the quality factor (Q). This factor is defined as the ratio between the reactive and the active power of the system
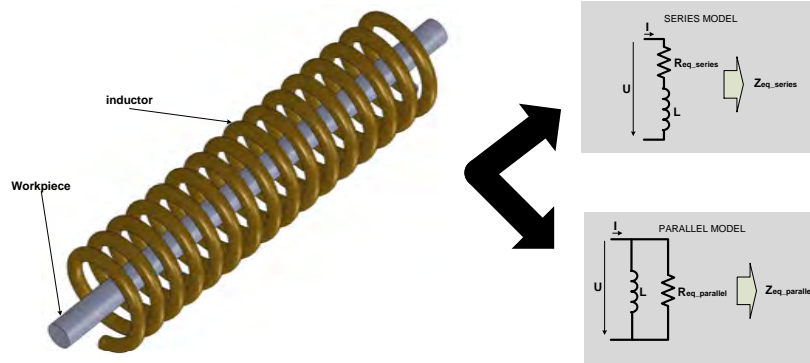
Figure 1.1: Electrical model of the inductor-workpiece.

$$Q = \frac{|P_{rect}|}{P_{act}} \tag{1.1}$$

In case of the series model, the inductor and the equivalent resistor are in series. Thus, the power is equal to

$$S = I^2 \bar{Z}_{eqserie} = I^2 \left(R_{eqserie} + j\omega L \right) \tag{1.2}$$

Then, the quality factor can be expressed as

$$Q_{serie} = \frac{|P_{rect}|}{P_{act}} = \frac{\omega L}{R_{eqserie}} \tag{1.3}$$

Parallel model

In the parallel model, the inductor and the equivalent resistor are in parallel, see Figure 1.1. In this case, the power is equal to

$$S = \frac{U^2}{\bar{Z}_{eqparallel}} = U^2 \left(\frac{1}{R_{eqparallel}} + \frac{1}{j\omega L} \right) \tag{1.4}$$

and the quality factor becomes

$$Q_{parallel} = \frac{1/\omega L}{1/R_{eqparallel}} = \frac{R_{eqparallel}}{\omega L} \tag{1.5}$$

Even if this model differs from the series model, it is demonstrated that for high quality factors the behavior at resonant frequency is analogous [8, p. 28–38]. Considering this, the energetic behavior is the same in both cases and the following equation is accomplished

$$Q = Q_{parallel} = Q_{serie} \qquad (1.6)$$

then, it is possible to pass from one model to another by using the following condition

$$R_{eqparallel} = R_{eqserie}Q^2 \qquad (1.7)$$

Most authors tend to use the series model (e.g. [1, 2, 8]) as it is more intuitive and sometimes the calculations are easier, due to use of the same current in L and R_{eq}. In the present study, the model used is the series model.

1.3.2 Equivalent resistance and inductance

Equivalent resistance

The equivalent resistor is the resistor that dissipates as much heat as all the eddy currents in the workpiece [1, p. 16]. Thus, it represents the power dissipated in the workpiece. Taking this into consideration and following Maxwell laws, it can be demonstrated that in case of using a long solenoid and a conductive workpiece, the equivalent resistor is [9, pp. 2–16]

$$R_{eq} = R_s K_R S_{heated} \frac{N_c^2}{l_w^2} \qquad (1.8)$$

where

- R_S is the superficial resistor of the piece, obtained from

$$R_s = \frac{\rho_w}{\delta_w} \qquad (1.9)$$

  being ρ_w the electrical resistivity of the workpiece and δ_w its penetration depth, explained afterwards in Section 1.4.1.

- K_R is an adimensional factor that takes into account the variation of the electrical path between the equivalent diameter of the piece and the penetration depth. This factor is equal to

$$K_R = 1 - e^{\frac{-2r_w}{\delta_w}} \tag{1.10}$$

with r_w being the radius of the workpiece.

- S_{heated}, represents the surface heated. It is usually simplified by the perimeter of the piece multiplied by its own length.

- l_w is the workpiece length.

- N_c are the turns of the induction-coil.

Therefore, for a solid round bar of radius r_w, the equivalent resistor is equal to

$$R_{eq} = K_R N_c^2 \rho_w \frac{2\pi r_w}{\delta_w l_w} \tag{1.11}$$

It has to be noted that this equation is an approximation and that there are formulas with additional factors to be considered when having short solenoids, short loads or solenoids made with high diameters tubes, found in [1, pp. 22–23] and [4].

Inductance

There are not many references in IH literature concerning a simple analytical method for calculating the inductor of the inductance-workpiece model. In case of a solenoid, a rough but useful approximation is to suppose the solenoid long and without core.

In case of air-core inductors, there are many equations, approximation techniques and methods to calculate them depending on the geometry, some of them are shown in [10]. In IH applications, Wheeler's formulas ([11, p. 421]) can be used to calculate the inductance value for a thin-wall finite-length solenoid, an example is found in [12]. In this approach, the inductance value becomes

$$L \approx \frac{10\pi\mu_0 N_c^2 r_c^2}{9r_c + 10l_c} = 3,9410^{-5} \frac{d_c^2 N_c^2}{18d_c + 40l_c} \tag{1.12}$$

where

- L is the inductance value.

- l_c is the coil length.

- r_c is the radius and d_c the diameter.

- μ_0 is the magnetic permeability of the vacuum, which is equal to $4\pi \cdot 10^{-7} H/m$.

This is a simple method to have a first approximation for a particular case. However, it has to be noted that the inductance value varies depending on the inductor-workpiece geometry and depending on the material of the workpiece, which in turn depends on the temperature. For example, when introducing a workpiece in the coil, the inductor has a value. But when the workpiece reaches its Curie temperature, the magnetic permeability μ ($\mu = \mu_r\mu_0$, being μ_r the relative magnetic permeability of the material) decreases until it reaches the vacuum permeability and the inductor comes back to its initial value without workpiece [9, p. 10]. Thus, the inductor value, as well as the equivalent resistor, depend on many parameters and its determination is extremely complex.

It has to be noted that there are more sophisticated analytical methods to obtain the inductance value. However, the use of numerical modeling and computing is becoming an efficient tool to have more precise models. In Chapter 2 some more explanations are done regarding more complex models and numerical simulation. However, the approximations done in this section provide an easy and practical approximation of the reality.

1.4 Efficiency

The efficiency of the energy transfer from the coil to the workpiece is an important matter during the design of an IH system. The efficiency of this transmission can be extremely low if the design is not well accomplished. In case of IH, the frequency of the process and the inductor-workpiece geometries are two of the main parameters affecting the efficiency. The election of the proper frequency and coil geometry can determine the success of the design.

In Section 1.4.1, a parameter called penetration depth and critical frequency are introduced. These parameters help the designers decide which is the optimum frequency of the process. Afterwards, in Section 1.4.2, some considerations regarding the inductor-workpiece geometries are briefly commented.

1.4.1 Penetration depth and critical frequency

When an alternating current flows through a conductor, the current distribution within its cross-sectional area is not uniform. In IH, the currents that create heat in the workpiece are not continuous and its distribution is not uniform. The frequency of these currents, which is the same as the magnetic fields and the currents in the coil, define the area where these currents flow and where the heat is generated.

In case of a solenoid heating a wire, the currents induced in the workpiece create a magnetic field that opposes to the original magnetic field. These magnetic fields cancel each other and the resultant magnetic field in the center is weak. Therefore, the induced currents in the center are smaller and tend to flow near the surface of the workpiece. This phenomenon is known as skin effect and causes the concentration of eddy currents in the surface layer of the workpiece, see Figure 1.2.
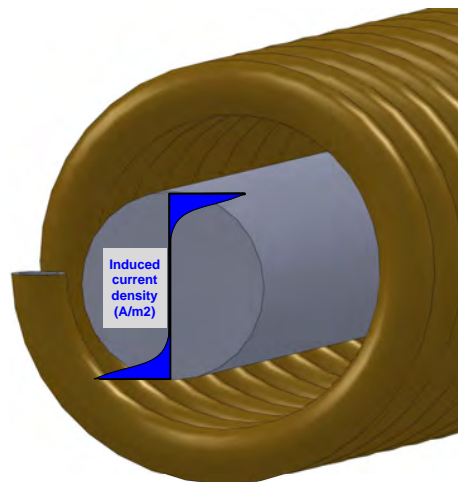
Figure 1.2: Qualitative representation of the induced currents through the cross-sectional area of the workpiece.

In case of flat thick bodies with constant electromagnetic properties, this current decrease is exponential and only the 63 % of current and the 86 % of power are located in the surface layer of depth δ, as explained in [7, p. 436]. The parameter δ is called penetration depth and is defined as

$$\delta = \sqrt{\frac{2\rho}{\mu\omega}} = 503\sqrt{\frac{\rho}{\mu_r f}} \tag{1.13}$$

where

- δ is the penetration depth.

- f is the frequency of the current, that is the same as the original one, and ω is the angular frequency with $\omega = 2\pi f$.

- ρ is the resistivity of the material.

- μ_r is the relative magnetic permeability of the material, which is adimensional ($\mu = \mu_r \mu_0$, where $\mu_0 = 4\pi \cdot 10^{-7} H/m$ for vacuum).

Observing Figure 1.2, in an extreme case, when having a high penetration depth (i.e at low frequencies), eddy currents of opposite sign can cancel each other. In this case, the heat in the workpiece decreases and so does the efficiency of the heating process. In this context, it becomes necessary to define a minimum frequency that guarantees that there is no cancelation of eddy currents and, thus, the efficiency is high enough.

With regards to the definition of R_{eq} in Section 1.3.2, this loss of efficiency is represented in Equation 1.11 by the K_R factor. In case of increasing the frequency, the penetration depth decreases and the K_R factor increases, increasing R_{eq} and the power generated in the workpiece for a given current. In the limit case, the frequency is infinite and the penetration depth tends to 0, thus, the factor K_R becomes 1. The contrary happens if the frequency of the process is lower.

Considering this, the critical frequency f_c is defined as the frequency below which the efficiency starts to decrease rapidly due to eddy current cancellation [1, p. 19]. Above this critical frequency, the efficiency gained is very slight and transmission losses grow, resulting in a decrease of the global efficiency.

Observing the representation of K_R as a function of workpiece's diameter and penetration depth in [1, p. 18] and [9, p. 13], for penetration depths smaller than $\frac{1}{4}$ of the diameter, the gain in efficiency is not substantial. Therefore, as a rule of thumb for round workpieces, in [1, p. 86] and [2, p. 467] f_c is chosen so that the piece's diameter is 4 times the penetration depth. The use of higher frequencies tend to decrease the total efficiency due to higher transmission losses and, in case of much higher frequencies, can cause a non-uniform heating of the piece.

It has to be noted that penetration depth varies during a heating treatment due to the changes of the material's properties with temperature. In

case of magnetic steels, it rises with temperature because there is an increase in resistivity and a decrease in magnetic permeability. This is very noticeable when these materials pass their Curie Temperature and become non-magnetic. Due to these changes in magnetic permeability during the heating, the penetration depth of a non-magnetic material can vary to 2 or 3 times its initial value, whereas in magnetic steels could suffer variations up to 20 times its initial value [1, p. 16].

Considering this, for magnetic workpieces the power supply frequency must be calculated for the maximum temperature of the workpiece. In non-magnetic materials, the difference is not so noticeable for different temperatures. And, in case of having different wire diameters to be heated with the same resonant tank, the frequency must be chosen in order to accomplish that the lower wire diameter is 4 times the reference depth.

1.4.2 Inductor-workpiece coupling

Concerning the efficiency of transmission due to the coupling between the inductor and the workpiece, the tighter are the diameters the better. The lower the distance between the internal diameter of the coil and the workpiece, the more magnetic field lines crossing the workpiece and the more efficient is the energy transfer. However, a space between both diameters is needed to avoid a short-circuit in the inductor. In some cases, a refractory material between coil and workpiece is introduced. This material avoids short-circuits, but also diminishes thermal losses by radiation or convection. The diameter of the inductor and the thickness of this refractory material is a compromise between the losses due to a worst coupling and those due to surface heat losses [2, p. 145].

1.5 Estimation of the inductor and power supply requirements

Once the workpiece (shape and material) and the heat treatment (temperature and productivity) are defined, it is necessary to define the frequency of the process, the length of the coil and the power requirements of the converter feeding the resonant tank. Bearing in mind the considerations done in the previous sections, the aim of this section is to provide a short overview of the procedure followed by designers to determine the inductor and power converter requirements.

1.5 Estimation of the inductor and power supply requirements

First, the procedure of choosing the frequency of the process is explained in Section 1.5.1. Then, a simple method of estimating the power needed is presented in Section 1.5.2. And finally, some considerations regarding the coil length are specified in Section 1.5.3.

1.5.1 Frequency selection

Regarding the explanations done in Section 1.4.1, the power converter has to be able to commutate at a frequency that generates a penetration depth (Equation 1.13) lower than $\frac{1}{4}$ of wire's diameter.

1.5.2 Power requirements

The power needed to heat a workpiece to a given temperature is [2, p. 141]

$$P_w = \frac{mc(T_{final} - T_{initial})}{t} \tag{1.14}$$

where

- P_w is the workpiece power.

- m is mass of the workpiece.

- T_{final} and $T_{initial}$ are the average values of initial and final temperatures.

- c is the average value of the specific heat of the material.

- t is the required heating time.

There are some manufacturers dealing with continuous processes that prefer using the heat content concept to determine the required power because it includes the amount of energy corresponding to the phase transformation. The heat content, HC in kWh/kg, is defined by the following equation

$$P_w = p_r HC \tag{1.15}$$

being p_r the production in kg/h. Some values of heat content are provided in [2, p. 142] and [1, pp. 99–101].

Considering that P_w represents the power needed to heat the piece, the power the converter has to provide is bigger due to the losses. Thus, the effective power of the converter is [2, p. 143]

$$P_c = \frac{P_w}{\eta_T} \tag{1.16}$$

where

$$\eta_T = \eta_{Thermal}\eta_{electrical} \tag{1.17}$$

which considers the thermal and electrical efficiency.

Thermal efficiency

Thermal efficiency includes surface losses due to radiation and convection, as well as those due to conduction at the end of the coil. These losses can be diminished thanks to the insulation provided by a refractory, but it has to be carefully designed to avoid the deterioration of electromagnetic coupling that may cause the increase of electrical losses.

For cylindrical coils with concrete as a refractory, the following formulas can be used [2, p. 144]

$$\eta_{Thermal} = \frac{P_w}{P_w + P_{Thermallosses}} \tag{1.18}$$

and

$$P_{Thermallosses} = 3,74 \cdot 10^{-4} \frac{l_c}{log_{10}(\frac{d_c}{d_w})} \tag{1.19}$$

where

- $P_{Thermallosses}$ are thermal losses through the surface.

- d_c and d_w are the inside coil diameter and workpiece diameter, respectively.

- l_c is the coil length.

Regarding thermal efficiency and heat exchange, more detailed explanations can be found in [2, p. 136–141]. Although these formulas are a first approximation, using numerical computation methods is highly recommended for having better results.

1.5 Estimation of the inductor and power supply requirements

Electrical efficiency

Electrical efficiency represents the losses in coil turns and surroundings. As a first approximation, when heating a solid cylinder in a long solenoid coil, the following formula can be used [2, p. 143]

$$\eta_{electrical} = \frac{1}{1 + \frac{d_c + \delta_c}{d_w - \delta_w} \sqrt{\frac{\rho_c}{\mu_r \rho_w}}} \tag{1.20}$$

where,

- δ_c and δ_w are coil and workpiece's penetration depth, respectively.

- ρ_c and ρ_w are coil and workpiece's electrical resistivity, respectively.

- μ_r is the relative magnetic permeability of the workpiece.

It can be observed that the highest coil efficiency is reached when heating magnetic materials with a high resistivity and with small air gap between inductor and workpiece.

Similarly to the thermal efficiency, it is difficult to calculate this value in a precise manner with approximate formulas and numerical computing has become an essential tool for doing these analysis.

1.5.3 Coil length

In case of continuous wire heating, it is necessary to know which is the coil length needed for the heating treatment. Considering a wire at a given velocity, the length of the inductor determines the time that the wire spends inside. The shorter the inductor, the less number of turns and, thus, the lower R_{eq}, as shown in Equation 1.11. Consequently, for giving an amount of power, more current is needed and more losses occur in the inductor. Therefore, the power needed and the length of the inductor establish the current and voltage across its terminals, determining the specifications of the converter and vice versa. In this case, the coil length is selected taking into account the converter's limits and the maximum current allowed in the coil.

Usually, in industrial applications the heating inductor tend to be refrigerated with water. Thus, if the current is very high, the cooling system needs to be oversized. In case of thick pieces, other aspects have to be considered because the length of the coil (in continuous processes) or the time that the

piece is heated (in static processes) are determined by the heat propagation time to the center of the piece. If the power is high and the time that the piece is inside the coil is low, the surface increases its temperature, but the center does not heat as fast. Under these circumstances, the heating is non-homogeneous and mechanical stress can appear in the workpiece.

To avoid these situations, during the calculations a maximum power per surface area and a maximum temperature difference between surface and center of the workpiece are imposed. For simple workpiece shapes, the analytical method can be found in [6]. And some tables are provided in [13] regarding the power density (kW per surface area of the material) needed to avoid this heterogeneity. In any case, having an accurate result is not simple and, again, numerical computation is necessary for a precise analysis.

1.6 Summary

IH is a heating method for electrically conductive materials that takes profit of the heat losses due to eddy currents. Although there are also hysteresis losses that generate heat during the process, for the case presented they do not represent a major contribution.

In case of IH systems, the inductor-workpiece system is electrically modeled by an inductor and a resistor that can be connected in series or in parallel. The concept of quality factor Q, as the ratio between the reactive and active power, is used to compare the parallel and series models. Though both models are valid, the model used during this study is the series model.

Some formulas regarding the resistor and inductor values are presented. These formulas are simplified formulas for the case of wire heating. In case of the equivalent resistor, the value depends on many parameters like the resistivity, radius, frequency, magnetic permeability of the workpiece and the number of turns of the inductor. In case of the inductor, the value is simplified by using the equation for a long and empty solenoid based on Wheeler's formulas. Though both formulas are rough simplifications, they represent a practical approximation from an engineer's point of view and help to understand qualitatively the influence of the parameters on the load's behavior.

Regarding the efficiency of the power transmission from the inductor to the workpiece, the frequency and the inductor-workpiece geometry play an important role. In case of choosing a low frequency value, the eddy currents

in the workpiece cancel each other and the efficiency of the power transmission decreases remarkably.

To overcome this situation, two parameters are presented: the penetration depth and the critical frequency. The penetration depth is a parameter that helps the designer to chose the correct frequency of the process and have high efficiency. And the critical frequency, f_c, is the frequency below which the efficiency decreases rapidly due to eddy current cancellation. As a rule of thumb for round workpieces, f_c is chosen such that the piece's diameter is 4 times the reference depth. Using higher frequencies tends to decrease the total efficiency due to higher transmission losses and can additionally cause non-uniform heating.

The efficiency of the process is also affected by the coupling between inductor and workpiece. If the distance between the internal diameter of the coil and the workpiece is low, most of the magnetic field lines cross the workpiece and the efficiency increases.

Finally, a simple but rough procedure to calculate the inductor and power supply requirements in an IH process is presented. The power needed to heat the workpiece depends on the production rate and the temperature of the process. But, the total power needed, depends on the thermal and electrical efficiency, that depend on the frequency, diameters and materials used. Some simplified formulas are presented for wire heating, but the use of numerical computation is highly recommended to obtain accurate results. Finally, some considerations are given to decide the length of the coil. In this case, the coil length is selected taking into account the converter's limits and the maximum current allowed in the coil.

Chapter 2

Modeling of induction heating systems

2.1 Introduction

In order to study the electrical, electromagnetic or thermal behavior of the inductor-workpiece system in IH, a model and a method of solving the equations governing these systems are needed. There are different solving methods applied to IH, but they can be classified in two big groups: analytical and numerical methods.

In the previous chapter, an analytical method based on an equivalent circuit composed of an inductor and a f was presented. The value of R_{eq} was obtained from a simplified formula for round wires and the inductor value was calculated according to the formula for a long and empty solenoid. Though it is a good starting point, there are more rigorous analytical methods for solving this problem. In this chapter, in Section 2.2, a basic bibliography and a more complex analytical method are presented.

In order to study complex workpiece shapes heating or to analyze accurately a heating process, numerical methods are needed. In the second section of this chapter, Section 2.3, an overview of the numerical methods in IH and their basis is presented. Finally, in Section 2.4, the whole chapter is summarized.

Authors would like to note that the aim of this chapter, like in Chapter 1, is to give to the reader an introduction to IH phenomena and its simulation, specially focusing on readers involved in power electronics. However, to have a rigorous view on IH and simulate the correct behavior of their systems, it is necessary to utilize numerical simulation and consult specialized books dealing with this topic. Taking this into account, some of the basic bibliography can be found in this chapter.

2.2 Analytical methods

There are many simple analytical methods for calculating the equivalent circuit of the inductor-workpiece. The one presented in the previous chapter is one of them, but another excellent starting point can be found in [4]. This book makes a practical and simple introduction to IH and, regarding the calculation of R_{eq}, considers a correction factor due to the finite length of the coil. It also introduces other parameters in the model like R_c, which is the coil resistance, that affects to the efficiency of the process. However, most of values are obtained through tables, which is impractical when calculating.

A good review of analytical methods for IH can be found in [14], but, bearing in mind the need of an accurate but simple model of the load, the most useful approximation is the one made in [6, pp. 230–234] and [5, pp. 43–46]. This approximation considers the analogy between an induction heating system and a transformer, assuming Baker's series circuit [6, p. 233]. This model is represented in Figure 2.1, where the parameter R_w represents the workpiece resistance, R_c is the coil resistance, L_a is the gap inductance, L_w is the workpiece inductance and L_c the coil inductance. The mathematical development and the equations for a solenoid heating a solid cylinder are explained in [6] and compiled in Appendix A.
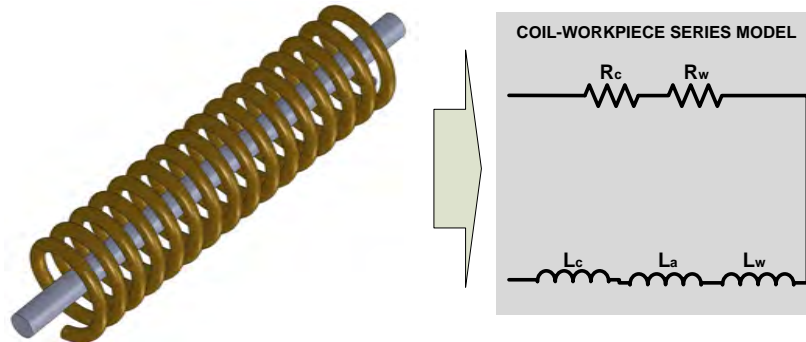
Figure 2.1: Series electrical model of the inductor-workpiece system.

The values of the parameters in Figure 2.1 for a long solenoid heating a solid cylinder are

$$R_w = K \left(\mu_w p A_w \right) \tag{2.1}$$

$$R_c = K \left(k_r \pi r_c \delta_c \right) \tag{2.2}$$

$$L_a = K \left(\frac{A_a}{2\pi f} \right) \tag{2.3}$$

$$L_w = K \left(\frac{\mu_w q A_w}{2\pi f} \right) \tag{2.4}$$

$$L_c = \frac{R_c}{2\pi f} \tag{2.5}$$

where

- K is a constant, which value is obtained from

$$K = \frac{2\pi f \mu_0 N_c^2}{l_c} \tag{2.6}$$

  being N_c the coil's number of turns and l_c its length.

- A_w is the cross-section of the workpiece, equal to

$$A_w = \pi r_w^2 \tag{2.7}$$

  being r_w the workpiece radius.

- A_a is the cross-section of the gap in m^2, equal to

$$A_a = \pi \left(r_c^2 - r_w^2 \right) \tag{2.8}$$

  with r_c being the coil inner radius.

- μ_w is the relative magnetic permeability of the workpiece, which is adimensional ($\mu = \mu_w \mu_0$, where $\mu_0 = 4\pi 10^{-7} H/m$ for vacuum).

- p and q are adimensional factors defined in Appendix A (Equations A.44 and A.45).

- δ_c is the penetration depth in the coil, following the Equation 1.13 for the material of the coil (copper).

- f is the frequency.

- k_r is a correction factor considering the space between turns, which value is between 1 and 1.5 (usually 1.15).

Considering this, the electrical efficiency (introduced in Section 1.5.2) is denoted by the following formula

$$\eta_{electrical} = \frac{R_w I_c^2}{(R_c + R_w)\, I_c^2} = \frac{R_w}{R_c + R_w} \tag{2.9}$$

The resistance of the workpiece, R_w, depends on the p factor, which is plotted together with q in Figure 2.2 as a function of d_w/δ_w, being δ_w the penetration depth and d_w the diameter of the workpiece. Assuming that the diameter of the workpiece and all the variables are constant except the frequency, the penetration depth decreases as the frequency increases (see Equation 1.13). Thus, increasing the frequency decreases the penetration depth and p varies, having a peak when the diameter is 3,5 times the penetration depth. After this, the value of p diminishes.

Figure 2.3 shows the values of R_w, R_c and efficiency in an example of a 1 cm diameter iron workpiece heated by a 2 cm inner diameter inductor. It is observed how the value of R_w increases with frequency. The reason is that the decrease of p after the peak is compensated by the increase in frequency in Equation 2.6. The same happens with R_c, due to the decrease of δ_c. However, the increase in R_w is higher than the increase in R_c, causing an increase of the electrical efficiency. As can be observed in Figure 2.3, there is a noticeable increase in the efficiency until the ratio d_w/δ_w equals 3.

This results coincide with the design criteria exposed in Section 1.4.1, which explained that IH designers usually choose a frequency that allows a penetration depth at least 4 times smaller than the diameter of the workpiece.

Regarding the thermal efficiency, presented in Section 1.5.2, it has to be noted that in case of continuous IH of wires, the wire is inside a refractory material that decreases thermal losses due to convection and radiation. Then, the thermal efficiency is high below 850 °C and the thermal losses can be neglected for this case, as explained in [6, p. 211].

The model presented in this section, based in an analytical method, is more complex than the one presented in the previous chapter. It includes more parameters like the effect of the air-gap, the resistance of the coil and the inductance due to the workpiece. Even though some of these parameters depend on Kelvin functions, nowadays, the solution of these equations do not present great difficulties.

These type of analytical solutions, as well as many others, represent a first approximation to the study of IH problems. From a power converter's point
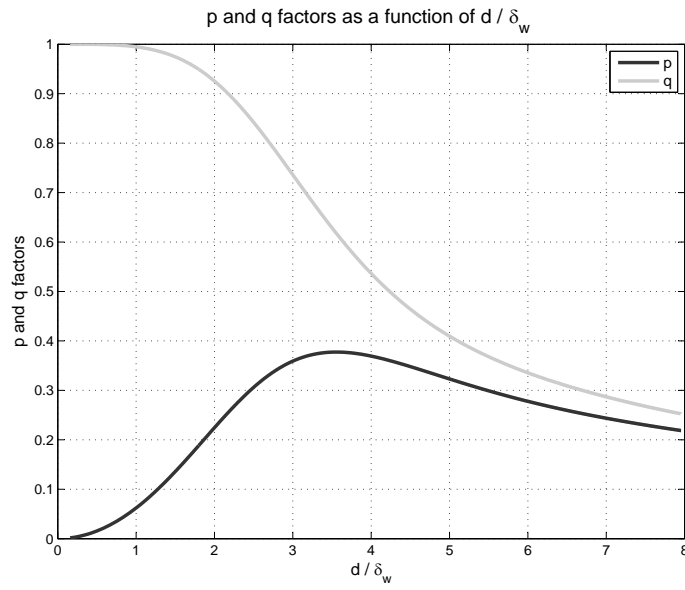
Figure 2.2: p and q factors as a function of d_w/δ_w.
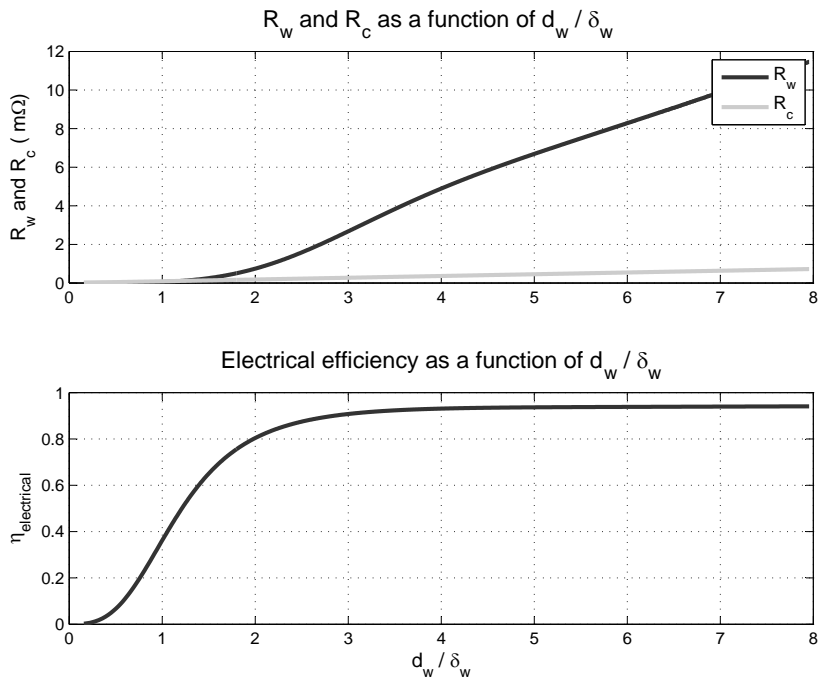
Figure 2.3: R_w, R_c and $\eta_{electrical}$ as a function of d_w/δ_w.

of view, this simplifications allow a flexible manner to understand load's behavior and set the limits that the converter has to withstand. Moreover, they allow modeling the converter's performance in specialized power converter design softwares like $Pspice^{©}$, $Matlab-Simulink^{©}$ or $Powersim^{©}$. Even though they cannot substitute the use of numerical simulation for a proper design, they can be a valuable tool that permit a first approach for rapid prototyping. These methods can be useful in case of studies whose main point is not the IH phenomena itself and in case of not having access to appropriate numerical simulation softwares.

However, these type of solutions have limitations depending on the analysis to be carried out. For example, in case of continuous steel wire heating, where the material properties (magnetic permeability, electrical resistivity, heat capacity, etcetera) depend on the temperature, one of the problems that arises is which value should be chosen during the analysis. It has to be considered that at the entrance of the coils the wire is at ambient temperature, but at the end it reaches 700 °C or even more. In case of resistivity, it varies more or less linearly with temperature and one option is using the integrated resistivity [6, p. 208]. But the case of magnetic permeability is more complex, since it is nonlinear and, additionally, it depends on the magnetic field intensity. The heat capacity has also a nonlinear behavior with a peak near the Curie temperature, increasing the complexity of the analysis.

Considering the complexity of the problem and the limitations of the analytical analysis, their use is very limited and old-fashioned, thus, numerical methods are preferred. In fact, in case of researchers involved in thermal or magnetic analysis, numerical simulations are nowadays an essential tool to face up their studies.

2.3 Numerical methods

Analytical methods have been applied since the beginnings of IH for simple geometries (e.g. planes, cylinders or tubes) and linear materials. But, as the complexity of the processes and geometries increased, the analytical methods became limited for these analysis. Although some attempts were done before, it was not until the 90's that the numerical computation started to be widely used, thanks to the expansion of computers. It has been during these last two decades that the importance of numerical methods in IH applications has been discovered [15].

The emergence of high performance computers and the decrease in their

cost have facilitated the application of numerical methods and the growth of commercial computer simulation programs. Though most of commercial softwares are thought for wider market applications (e.g. motor design or actuators), some of them have been developed considering IH needs and nowadays have improved their performance [16]. For example, some specialized softwares used in industry are $Elta^{©}$, which is a 1D program, and $Inducto^{©}$ from Integrated Engineering Software, which is a 2D program. Some general softwares also used in IH applications are $Flux2D/3D^{©}$, $ANSYSMaxwell^{©}$, $Opera^{©}$, $Comsol^{©}$ or $Jmag^{©}$.

Nowadays, numerical computing is becoming widely used in IH and its presence in industry is expected to increase even more. Proof of this are the recommendations done by the ASM Heat Treating Society's Research & Development Committee, which suggest more investment in next years in R & D for computer simulation models and its transfer to American industries of IH [17, 18]. However, at the moment, the complexity of these methods and softwares is still high and require highly skilled staff dedicated to the resolution of these problems. The investment in human capital and the cost of these softwares, become important barriers for their incorporation into small and medium research groups and industries.

An exhaustive explanation of the methods employed in numerical simulation is beyond the scope of this work and a more complete information, but a great bibliography can be found in [2, pp. 172–183], [7, pp. 427–498] and [19]. Nevertheless, a brief and just introductory explanation of numerical methods in IH is presented below.

In Section 2.3.1, the general electromagnetic formulation used in IH problems is briefly presented. In Section 2.3.2, the different resolution methods used in numerical analysis for IH problems are introduced. And finally, in Section 2.3.3, the different ways of coupling the electromagnetic and thermal problems are concisely explained.

2.3.1 Magnetoquasistatic and time-harmonic formulation

The electromagnetic behaviour is defined by Maxwell equations, whose formulation in differential form is

$$\nabla \times \mathbf{E} = -\frac{\partial \mathbf{B}}{\partial t} \tag{2.10}$$

$$\nabla \times \mathbf{H} = -\frac{\partial \mathbf{D}}{\partial t} + \mathbf{J} \tag{2.11}$$

$$\nabla \cdot \mathbf{D} = \rho \tag{2.12}$$

$$\nabla \cdot \mathbf{B} = 0 \tag{2.13}$$

with B being the magnetic field density, H the magnetic field intensity, E the electric field intensity, J the current density and D the electric displacement field.

Usually, authors define three general electromagnetic problems [20]:

- Static fields: the time dependency is neglected.

- Fields in the frequency domain: the time dependency is considered by means of sinusoidal functions of a single angular frequency. Maxwell equations are usually reduced to the electro and magnetoquasistatic formulation.

- Fields in the time domain: the time dependency is not specified. Maxwell equations are usually reduced to the electro and magneto-quasistatic formulation.

Considering this, in IH most of numerical simulations are done in the frequency domain and using the magnetoquasistatic approximation. Under these circumstances, it is assumed that the displacement currents, originated by $\mathbf{D}$, are small compared to the conduction currents ($\mathbf{J}$) and Equation 2.11 becomes

$$\nabla \times \mathbf{H} = \mathbf{J} \tag{2.14}$$

Moreover, the computed physical quantities are sinusoidal time-varying and are expressed using their complex images, obtaining a solution of the problem which is not time dependent. Therefore, Equation 2.10 becomes

$$\nabla \times \mathbf{E} = -j\omega \mathbf{B} \tag{2.15}$$

Therefore, most of numerical analysis in IH applications use the magnetoquasitatic approximation and Maxwell's equations in the time-harmonic form.

2.3.2 Numerical resolution methods

There are many numerical methods employed in the resolution of IH problems. The most commonly used are the Finite Differential Method (FDM), the Finite Element Method (FEM) and the Boundary Element Method (BEM). There are two main types of methods for solving electromagnetic numerical modeling: differential and integral methods.

Differential methods solve the problem using a differential approach of electromagnetic governing equations. Within them, the most commonly used are the FDM and the FEM. The FDM consists in an approximate method of solving differential equations by means of replacing derivatives by equivalent finite difference approximations. First of all, the object to be studied is discretized constructing a grid with points which we are interested in solving. Afterwards, the differential equations of the process are approximated by a finite difference equivalence that relates the solutions to grid points. And finally, the problem is solved considering the prescribed boundary conditions and/or initial conditions.

Similar to FDM, FEM is another group of numerical techniques based on the discretization of the solution region into elements and the resolution of a trial function in their nodes. Some of them are based on the Galerkin method, Ritz Method, pseudo-variant methods, etcetera. The benefits of FEM compared to FDM are that FEM can overcome analysis with complicated geometries and boundary conditions. However, FDM can be easier to implement.

Integral methods start the problem from an integral formulation in which electromagnetic parameters are connected with their sources. These sources can be primary, which means that they are originated by a known circuit or external source, or secondary, which are those describing variations originated by the components of the system. In Integral methods, we can find numerical methods like the BEM and the mutual impedance method. BEM is employed for long systems where FDM and FEM would need a great mesh and its combination with differential methods gives goods results.

There is not an unique method for the IH problem and, depending on the situation, one or another numerical method is used. A proof of this is that commercial softwares use different solving methods. For example, $Elta^{©}$ uses FDM in combination with analytical methods, $Inducto^{©}$ uses FEM or BEM and $Flux2D/3D^{©}$ and $ANSYSMaxwell^{©}$ use FEM. A brief review of the advantages and considerations for these resolution methods can be found in [7, p. 482] and [2, p. 180].

2.3.3 Coupling of electromagnetic and thermal problems

IH problems involve not only electromagnetic but also thermal phenomena, which are closely interrelated. The material properties used during the computation depend on the temperature and, therefore, the electromagnetic and thermal variables depend upon each other. There are two main solving procedures depending on the type of coupling between the electromagnetic and thermal problems: the indirect and the direct.

The indirect coupling, also known as weak or sequential coupling, solves the problem in successive steps, see Figure 2.4. The coupling is accomplished by applying the results from the first analysis (electromagnetic) as input parameters for the second analysis (thermal). In this case system equations are solved separately, providing more flexibility and less complexity to the solving procedure.
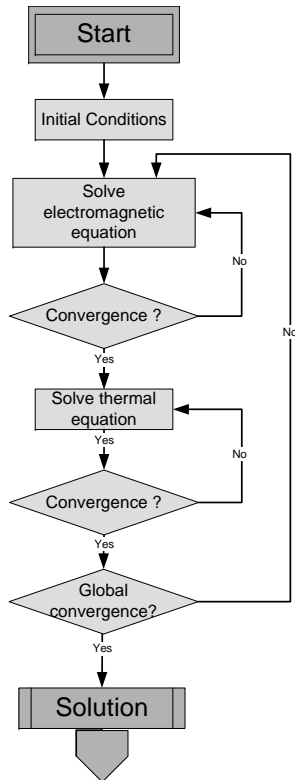
Figure 2.4: Indirect coupling solving procedure.
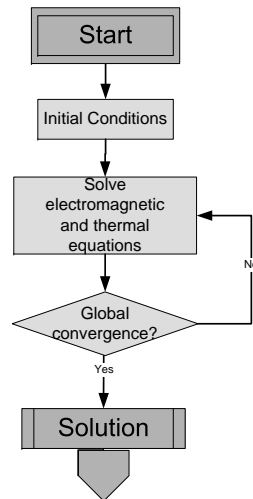
Figure 2.5: Direct coupling solving procedure.

The direct or strong coupling solves simultaneously both system equations considering all the variables, see Figure 2.5. In this case, the electromagnetic and thermal unknown parameters are part of the global matrix used to solve the problem. It is much more complex and is just used when there is a high interaction between both problems and the processes have similar time constants.

Considering that usually time constants of the electromagnetic and thermal processes are different, for most IH applications the indirect coupling is valid.

2.4 Summary

In this chapter, different methods of modeling IH systems are presented. First of all, the analytical methods are introduced, presenting a more complex analytical method with an equivalent circuit based on 5 parameters. These parameters are the workpiece resistance(R_w), the coil resistance (R_c), the gap inductance (L_a), the workpiece inductance (L_w) and the coil inductance (L_c). Regarding the electrical efficiency, this model presents a similar behavior to the model presented in Section 1.3.

Analytical methods are simple and rough methods of calculation used before, that allow dealing with simple geometries using materials with constant properties. Even they use and results are very limited, they can serve for a first approach for power converter designers in case of not having appropriate numerical simulation softwares. However, in case of needing an accurate and precise analysis it is mandatory to use numerical methods.

The emergence of high performance computers and the decrease of their cost have facilitated the incorporation of numerical methods in IH industry. Nowadays, the development of commercial softwares is favoring the adoption of numerical methods by IH designers.

In IH applications, numerical methods are usually based on the resolution of Maxwell equations assuming the magnetoquasistatic approximation and using their harmonic form. There are many methods of solving these equations classified in two main groups: differential and integral methods. In the differential methods are included the FDM and the FEM, and in the integral methods the BEM. There is not an unique resolution method for all the cases. Depending on the application, one method, another or their combination may be preferable. It has to be noted that in IH the combination of thermal and electromagnetic problems pose a difficulty. Concerning this,

the coupling of both problems can be direct or indirect, although in most applications the indirect coupling is suitable.

Although numerical methods are becoming more and more popular and play an important role in IH, there are still some barriers for their incorporation in small and medium research groups and enterprises. The usability of commercial softwares has improved clearly in last years, becoming much more intuitive and user friendly. However, their complexity still require of highly skilled staff completely devoted to the resolution of these problems. Anyway, it has to be stressed that 1D softwares for not so highly skilled staff exist, an example of that is $Elta^{©}$, with which is possible to realize an analysis in few minutes and starting from zero. Another barrier for the use of these softwares in small and medium laboratories and enterprises starting in this field is their cost.

Chapter 3

Induction heating converters

3.1 Introduction

In IH, the heat is generated by eddy currents which are originated by a varying magnetic field that is obtained by means of a varying current circulating in an inductor, as shown in Chapter 1. To have a high varying current in the inductor, most authors tend to use an oscillatory circuit formed by the inductor and a capacitor in series or in parallel. This oscillatory circuit, also known as resonant tank, is usually fed by a converter, whose characteristics depend on the frequency, the power and the type of resonant tank.

IH converters belong to the so-called load-resonant converters family, [21, p. 249]. Commutating at resonant frequency allows having more efficient equipments, which may be essential in some high frequency applications, although the main reason is that permits having higher currents in the inductor.

There are many criteria to make a classification of IH converters, for example the one presented in [2, p. 637]. One common criteria is classifying the converters according to the type of resonant tank, where the most basic topologies are those based on series and parallel tanks, as shown in Figure 3.1. The converters associated to these tanks are the voltage-fed series resonant inverters (VFSRI) and the current-fed parallel resonant inverters (CFPRI) respectively. In most IH applications, the converters used derive from them.

In this chapter, the basic concepts and main topologies regarding IH converters are introduced. Firstly, VFSRI and the CFPRI structures and their tanks are extensively presented in Sections 3.2 and 3.3, as they represent the base for understanding other structures and the main concepts used in IH field. First of all with the ideal circuit and afterwards some additional considerations are given. Next, an overview of other structures, as well as their basic bibliography, is provided in Section 3.4. Finally, the main ideas
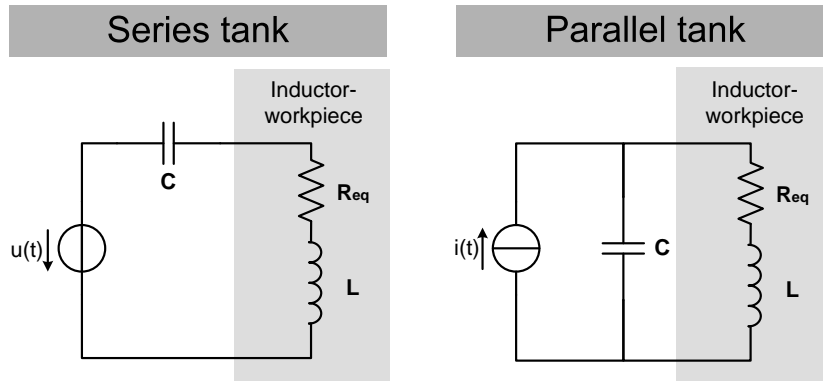
Figure 3.1: Series and parallel tank.

of this chapter are summarized in Section 3.5, summing up in a table the differences between VFSRI and CFPRI.

For the sake of simplicity, the inductor-workpiece system is modeled during the whole chapter by a constant resistance and inductance in series. This assumption is based on the model described in Chapter 1.

3.2 Voltage-fed series resonant inverters

In series resonant tanks, the inductor is connected in series with the capacitor. In this case, the tank behaves as a current source and the inverter used is a voltage-fed inverter, which means that the inverter is fed with a constant voltage source. This implies that the inverter is fed by a capacitor with a high capacitance value that maintains the voltage constant. In Figure 3.2, a series tank and an ideal VFSRI are shown.

In most applications above 5 kW, the inverter used is the H-bridge [22], as shown in Figure 3.2. This topology is used because allows transmitting the same power with less current for a given voltage U_e [21, p. 319]. Considering that the application of this study is the industrial heating of round wires, where the converters have a power of more than tens of kilowatts, the H-bridge structure is the most commonly found. This is the reason why the H-bridge is the inverter used during the whole study.

In voltage-fed inverters, two switches of the same inverter leg cannot be turned-on at the same time, otherwise short-circuit occurs. The time between the turning-off of one of these switches and the turning-on of the
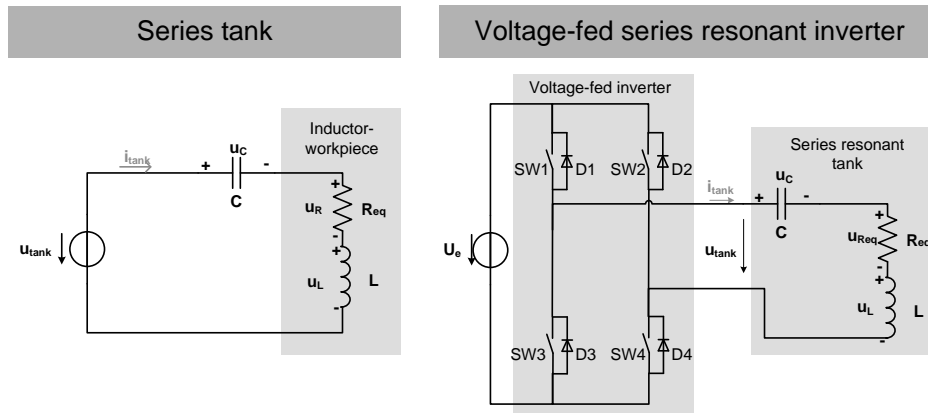
Figure 3.2: Series tank and a VFSRI.

other is called dead-time. In this topology, antiparallel diodes are necessary to allow inductor's current conduction when the opposite switches are turned-off.

The most representative methods of controlling the power in VFSRI are exposed in Section 3.4.3. However, during this section, it is assumed that switches $SW1$ & $SW4$ and $SW2$ & $SW3$ commutate alternatively with a duty-cycle of 50 % and the power is controlled by varying the voltage of the source U_e shown in Figure 3.2.

In the following sections, some concepts regarding the converter's operation and control are introduced. Firstly, in Sections 3.2.1 and 3.2.2, the definition of resonant frequency and the influence of the quality factor in VFSRI are presented. After this, in Section 3.2.3, the basic equations for calculating the power transmitted to the workpiece are shown. Afterwards, in Section 3.2.4, the sequence of events and implications when commutating at resonant frequency and out of resonance are explained. Finally, in Section 3.2.5, some additional considerations are given regarding the inductive switching, the semiconductors and the matching transformer needed in most of VFSRI.

3.2.1 Resonant frequency

The resonant frequency ω_r is defined as the frequency at which the maximum module of a transfer function occurs [23, p. 544].

Observing the RLC circuit of a VFSRI in Figure 3.2, the following equa-

tion is accomplished

$$u_{tank} = u_{R_{eq}} + u_L + u_C = R_{eq}i_{tank} + L\frac{di_{tank}}{dt} + \frac{1}{C}\int i_{tank}dt \qquad (3.1)$$

Using Laplace transformation with initial conditions equal to zero, Equation 3.1 becomes

$$U_{tank}(s) = R_{eq}I_{tank}(s) + sLI_{tank}(s) + \frac{1}{sC}I_{tank}(s) \qquad (3.2)$$

obtaining the following second order system with a zero

$$H_s(s) = \frac{I_{tank}(s)}{U_{tank}(s)} = \frac{sC}{s^2LC + sCR_{eq} + 1} = sC\frac{w_n^2}{s^2 + 2\zeta\omega_n s + \omega_n^2} \qquad (3.3)$$

The roots of this second order system are

$$s_1, s_2 = -\zeta\omega_n \pm j\omega_n\sqrt{1 - \zeta^2} \qquad (3.4)$$

where [23, p. 390]

- ω_n is the undamped natural frequency of the system, which is the radial distance of the roots to the origin of the s-plane and is equal to

$$\omega_n = \frac{1}{\sqrt{LC}} \qquad (3.5)$$

- ζ is the damping ratio, which is the cosine of the roots to the negative real axis of the s-plan and is equal to

$$\zeta = \frac{R_{eq}}{2}\sqrt{\frac{C}{L}} = \frac{R_{eq}}{2\omega_n L} \qquad (3.6)$$

Transferring Equation 3.3 to the frequency domain, the transfer function $H_s(s)$ becomes

$$H_s(s)|_{s=j\omega} = \frac{j\omega C}{1 - \omega^2 LC + j\omega CR_{eq}} \qquad (3.7)$$

that has the following module

$$|H_s(\omega)| = \frac{C}{\sqrt{(CR_{eq})^2 + (\omega LC - \frac{1}{\omega})^2}} \qquad (3.8)$$

Calculating the derivative of Equation 3.8, the next equation is obtained

$$\frac{d\,|H_s(\omega)|}{dw} = C\left[-\frac{1}{2}\left[(CR_{eq})^2 + (\omega LC - \frac{1}{\omega})^2\right]^{\frac{-3}{2}}\left[2\omega L^2 C^2 - 2\frac{1}{\omega^3}\right]\right] \quad (3.9)$$

that has a zero at

$$\omega_r = \frac{1}{\sqrt{LC}} \quad (3.10)$$

being this zero the maximum of Equation 3.3 and, thus, the resonant frequency of the circuit.

In this case, the resonant frequency ω_r is equal to the undamped natural frequency ω_n and the transfer function at this frequency is equal to

$$H_s(\omega_r) = \frac{I_{tank}(\omega_r)}{U_{tank}(\omega_r)} = \frac{1}{R_{eq}} \quad (3.11)$$

It has to be noted that the frequency in rad/s (denoted by ω) and in Hz (denoted by f) is used indistinctly. The relation between these frequencies is $\omega = 2\pi f$ and their subindex is used to distinguish the referred frequency (e.g ω_r and f_r correspond to the resonant frequency).

In Figure 3.3, the Bode analysis of the transfer function $H_s(\omega)$ is shown. In this case, the tank is composed of an R_{eq} of 1558 $m\Omega$, an L of 9.78 μH and a C of 0.26 μF. Observing this figure, there is an unique maximum at approximately 100 kHz, corresponding to the resonant frequency. Bearing in mind that $H_s(\omega)$ is the inverse of the impedance (see Equation 3.3), the impedance at resonant frequency is minimum. Therefore, if a voltage with a frequency equal to the resonant frequency feeds the RLC circuit, the current is maximum and so it is the heat generated in the workpiece. One of the reasons of using these oscillatory circuits in IH applications is that they allow high currents using relatively low voltages.

Another thing observed in Figure 3.3 is that, at resonance frequency, the impedance equals R_{eq}. Under these circumstances, the inductive and the capacitive part cancel each other and the voltage and current are in phase. Thus, the switching losses are theoretically zero because the current is close to zero during the commutation. This is the reason why IH converters can commutate at higher frequencies.

This commutation process without losses is generically known as soft-switching, contrarily to the conventional hard-switching, where losses do
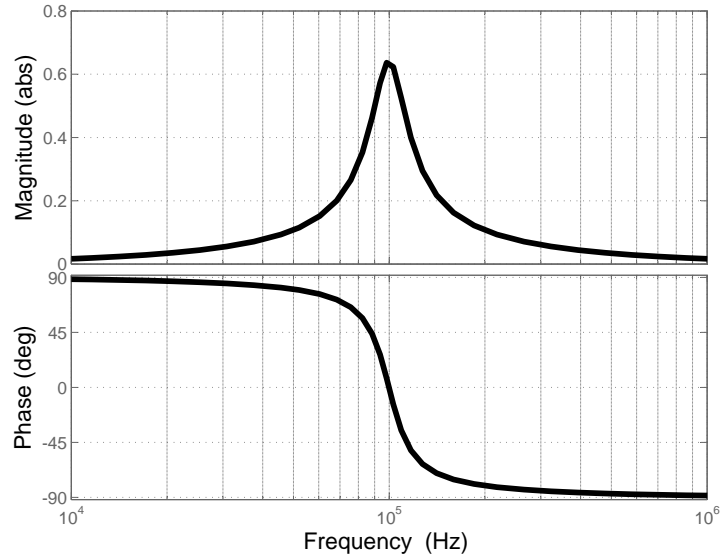
Figure 3.3: Bode analysis of the transfer function $H_s(\omega)$ with $R_{eq} = 1558$ $m\Omega$, $L = 9.78\ \mu H$, $C = 0.26\ \mu F$ and $f_r = 99.8\ kHz$.

occur. There are two basic switching mechanisms with regards to soft-switching: zero voltage switching (ZVS) and zero current switching (ZCS). ZVS is associated to the turn-on of the switch, that is realized with zero voltage, while ZCS is associated to the turn-off of the semiconductor, that occurs without current. These concepts are frequently used during this section and the following ones to explain the commutation mechanisms occurring in IH converters.

3.2.2 Quality factor

The quality factor is presented in Section 1.3.1 as the ratio between the reactive and the active power of the inductor-workpiece system. In this section the relation between this Q factor and the electrical parameters is discussed. Firstly, explaining the relation between the quality factor and the current waveform and, secondly, explaining the relation between this factor and the voltage on the tank components.

Quality factor and current

Considering that the converter is commutating at resonant frequency, the quality factor, as defined in Section 1.3.1, is equal to

$$Q = \frac{|P_{rect}|}{P_{act}} = \frac{\omega_r L}{R_{eq}} = \frac{1}{\omega_r C R_{eq}} \tag{3.12}$$

Combining this equation with the definition of damping ratio in Equation 3.6 and knowing that the resonant and the natural frequency are equal for the series tanks, the following equation is accomplished

$$Q = \frac{1}{2\zeta} \tag{3.13}$$

As the RLC circuit of the tank is a second order system, it becomes more undamped and oscillatory as the imaginary part of the roots increases and the real part decreases [23, p. 393]. Therefore, bearing in mind Equation 3.4, ζ has to be smaller than one to have an oscillatory circuit, since in case of $\zeta < 1$ the system is an underdamped system and in case of $\zeta = 0$ the system is undamped. Taking this into consideration and observing Equation 3.13, the quality factor gives an idea of how damped is a system. The higher the Q value is, the closer to zero is ζ and the more undamped is the system.

In Figure 3.4, a Bode analysis of $H_s(\omega)$ (Equation 3.3) for three different resonant tanks is shown. These circuits have the same inductance (9.78 μH) and capacitance (0.26 μF), but vary in the R_{eq} value, that takes the following values: 15.58 Ω, 3.58 Ω and 1.58 Ω. The corresponding values of Q for these three cases are 0.39, 1.71 and 3.88. In Figures 3.5, 3.6 and 3.7 the time response of u_{tank} and i_{tank} are shown for these three different cases commutating at resonant frequency, where the commutation frequency f_{sw} is equal to resonant frequency f_r.

In Figure 3.4, it can also be observed how the peak value increases as the Q value increases. This is logical because the peak value is equal to the inverse of R_{eq} (see Equation 3.11), whose value decreases.

Observing the time response for these cases in Figures 3.5, 3.6 and 3.7, it can be seen how the current increases with Q and how, in case of Figure 3.5, the current is not sinusoidal. Examining these figures and thinking in the RLC circuit as a tuned filter, the quality factor can also be understood as a value of how good the filtering at resonant frequency is. Considering that the voltage is a square waveform at resonant frequency, if the system is overdamped ($\zeta > 1$ and $Q < 0.5$) like in Figure 3.5, the harmonic components of the current are significant and the current is not sinusoidal. On the
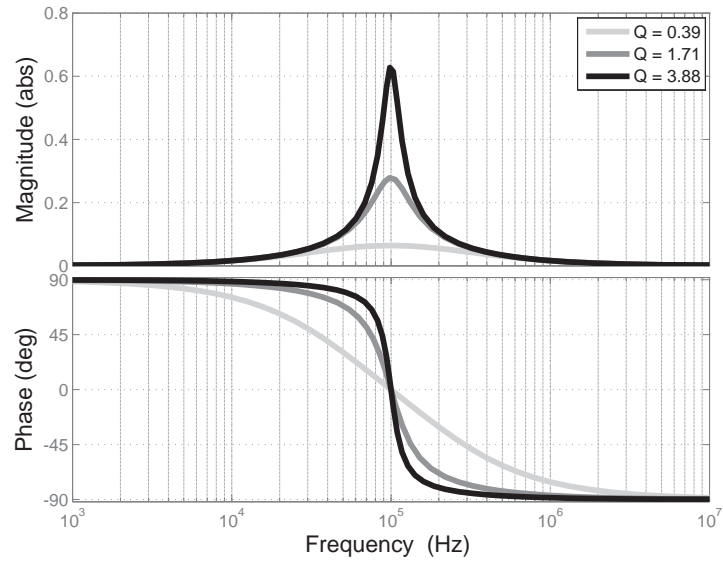
Figure 3.4: Bode analysis of the transfer function $H_s(\omega)$ for three systems with different Q values.
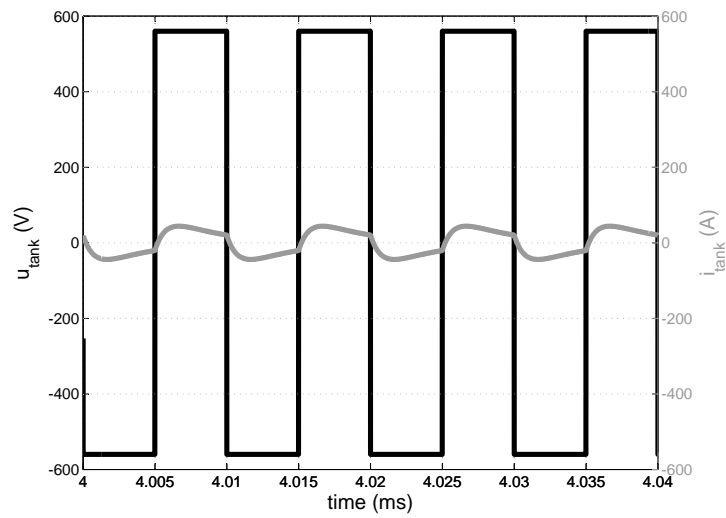
Figure 3.5: Voltage and current in the tank with a ζ of 1.25 and a Q of 0.39 ($U_e = 560$ V, $R_{eq} = 15.58$ Ω, $L = 9.78$ μH, $C = 0.26$ μF, $f_{sw} = f_r = 100$ kHz).
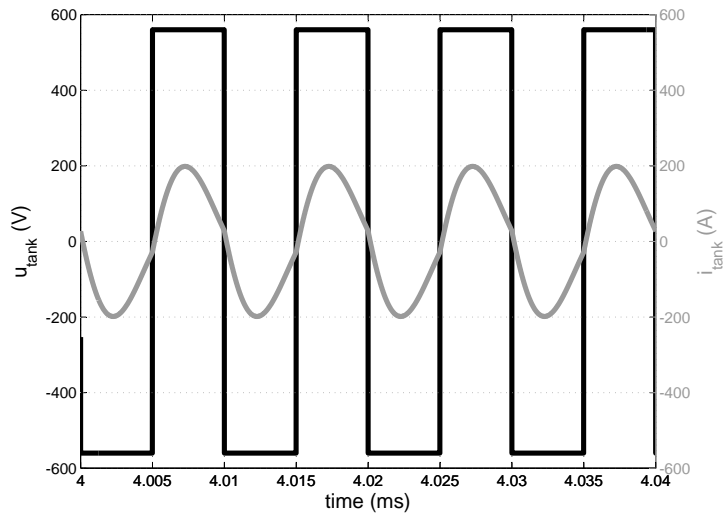
Figure 3.6: Voltage and current in the tank with a ζ of 0.29 and a Q of 1.71 ($U_e = 560$ V, $R_{eq} = 3.58$ Ω, $L = 9.78$ μH, $C = 0.26$ μF, $f_{sw} = f_r = 100$ kHz).
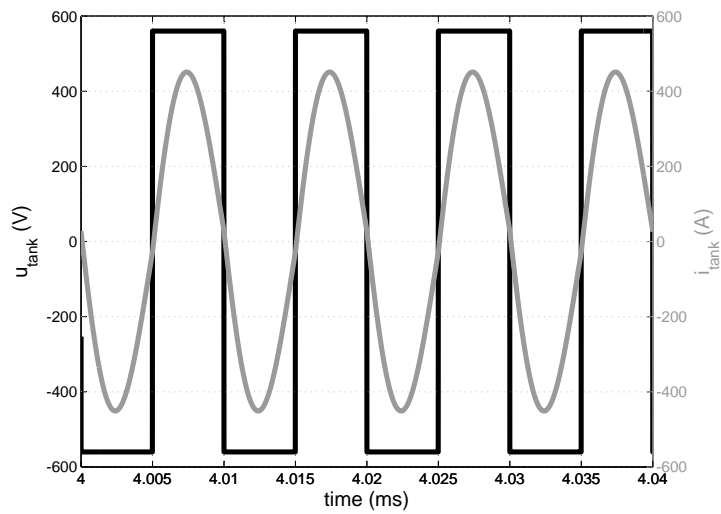
Figure 3.7: Voltage and current in the tank with a ζ of 0.13 and a Q of 3.88 ($U_e = 560$ V, $R_{eq} = 1.58$ Ω, $L = 9.78$ μH, $C = 0.26$ μF, $f_{sw} = f_r = 100$ kHz).

37

other hand, if the system is underdamped ($\zeta < 1$ and $Q > 0.5$) the harmonic components are lower and the current is quite sinusoidal, as in Figures 3.6 and 3.7.

Therefore, in IH systems is interesting to have a high Q value because the current is higher and so it is the heat in the workpiece. Additionally, allows soft-switching during the commutation. For example, in Figure 3.6 the system is underdamped (ζ is 0.29 and Q is 1.7), but the Q value is not high enough to permit soft-switching at the resonant frequency.

Taking this fact into consideration, it is always interesting to have a high Q value. However, depending on the application, this is not always possible because the value of Q depends on the equivalent circuit, which is at the same time determined by the geometries and materials of the inductor-workpiece, as shown in Chapters 1 and 2.

Quality factor and voltage gain

The voltage on the capacitor at resonant frequency accomplishes the next equation

$$U_c(\omega_r) = \frac{1}{j\omega_r C} I_{tank}(\omega_r) \tag{3.14}$$

As the load is equal to the equivalent resistance (Equation 3.11), combining Equation 3.14 with the definition of Q factor (Equation 3.12) and assuming that $U_{tank}(\omega_r)$ represents the fundamental component of the inverter output voltage, then

$$U_c(\omega_r) = \frac{1}{j\omega_r C} \frac{U_{tank}(\omega_r)}{R_{eq}} = -jQU_{tank}(\omega_r) \tag{3.15}$$

Thus, at resonant frequency, the voltage at the capacitor is Q times the voltage at the output of the inverter and 90 degrees delayed.

Similarly happens with the inductor voltage, which is equal to

$$U_L(w_r) = j\omega_r L I_{tank}(\omega_r) = j\omega_r L \frac{U_{tank}(\omega_r)}{R_{eq}} = jQU_{tank}(\omega_r) \tag{3.16}$$

In this case the voltage is Q times the voltage at the output of the inverter but 90 degrees advanced.

In case of the equivalent resistance, the voltage is equal to the voltage at the output of the converter

$$U_{R_{eq}}(\omega_r) = R_{eq} I_{tank}(\omega_r) = R_{eq} \frac{U_{tank}(\omega_r)}{R_{eq}} = U_{tank}(\omega_r) \qquad (3.17)$$

In the previous section, the need of having high Q values has been introduced. Nevertheless, considering that the voltage at the capacitor is Q times higher, this value has to be limited. For example, having Q values over 10, entails having more than 1000 V at the capacitors for 100 V in the output of the converter. This implies having more capacitors in series to withstand these voltages, but also paying attention to problems of isolation and security due to the high voltages and frequencies involved. It is very difficult to define a limit for the Q value because it depends on the application. However, IH designers tend to use Q values between 3 and 15.

In the previous section, it was explained that the RLC circuit acts as a filter tuned at the resonant frequency, thus, in most cases, just the first harmonic is considered. For example, in case of having a Q factor of 3 and a square wave at the output of the inverter, the first harmonic is 24 times higher than the next one [24]. Therefore, even though u_{tank} is a square wave, it can be simplified to its first harmonic with the following equation

$$U_{tank} \approx \frac{4U_e}{\sqrt{2}\pi} \qquad (3.18)$$

being U_{tank} the root mean square (RMS) value of the first harmonic. It has to be noted that this assumption can be used in Equations 3.15, 3.16 and 3.17.

This approximation can be observed in Figure 3.8, where the voltage and current waveforms are shown for a certain tank commutating at resonant frequency. In this case, the RMS voltage at the resistance $U_{R_{eq}}$ is equal to 504 V, which coincides with the first harmonic of u_{tank} using Equation 7.1 with U_e equal to 560 V. The same occurs with the voltage at the capacitor U_C, that is 1965 V in RMS and is practically equal to Q times U_{tank}. Additionally, the resistor voltage is in phase with tank voltage and the capacitor voltage is 90 degrees delayed.

Observing the inductor voltage, u_L advances 90 degrees the tank voltage (u_{tank}), but the waveform is not sinusoidal. In fact, u_L is the sum of a sinus (Q times the first harmonic of u_{tank}) plus the difference between $u_{R_{eq}}$ (sinusoidal) and u_{tank} (square wave). In any case, from a practical point of view, Equation 3.16 can be used as a good approximation.
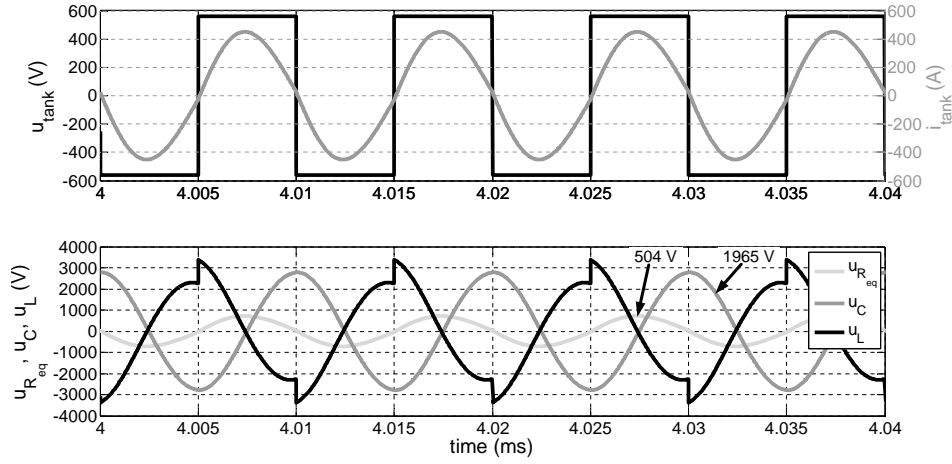
Figure 3.8: Voltage and current in the tank and in the RLC circuit ($U_e =$ 560 V, $R_{eq} = 1.58$ Ω, $L = 9.78$ μH, $C = 0.26$ μF, $f_{sw} = f_r =$ 100 kHz, $Q = 3.88$).

3.2.3 Power in the workpiece

With regard to the power transmitted to the workpiece, it can be easily calculated considering that R_{eq} represents the workpiece resistance (Section 1.3.2). Assuming this definition, the power is equal to

$$P = I_{tank}^2 R_{eq} = \frac{U_{R_{eq}}^2}{R_{eq}} \tag{3.19}$$

Bearing in mind that the power is maximum when the current is maximum, the power is maximum at resonant frequency (Section 3.2.1). Considering that the voltage across the resistance is equal to the first harmonic of u_{tank} (Equations 3.17 and 7.1), then

$$P(\omega_r) = \frac{\left(U_{R_{eq}}(\omega_r)\right)^2}{R_{eq}} = \frac{\left(\frac{4U_e}{\sqrt{2}\pi}\right)^2}{R_{eq}} = \frac{8U_e^2}{\pi^2 R_{eq}} \tag{3.20}$$

It is observed from Equation 3.20, that the power delivered to the workpiece can be controlled by the voltage of the voltage-source U_e. This is the most intuitive power control method, but in Section 3.4.3 other methods are briefly presented.

In this case, the model of inductor-workpiece explained in Section 1.3 has been used to introduce the manner of calculating the power. However, the

analytical model explained in Section 2.2 can also be applied. In that case, the inductance and resistances used for doing the calculations are the sum of them and the power delivered to the workpiece is calculated using R_w.

3.2.4 Commutation analysis

That resonant frequency is the point where the maximum power is given to the workpiece, was explained in previous sections. It was also explained that, at this frequency, the commutation occurs when the current is close to zero, diminishing the commutation losses. However, in real systems is almost impossible be at perfect resonance, due to small changes in the load or just because there are small inaccuracies in the control system. Therefore, during normal operation the converter is most of time slightly above or under resonance. These different commutation circumstances are studied in this section. The aim of this study is to understand the sequence of events occurring during the commutation process and disclose the preferable behavior of the converter.

In Figure 3.9, a simple scheme of a VFSRI that illustrates the variables used during the explanations is presented. In Figures 3.10, 3.11 and 3.12, the current and the voltage on the tank are shown. The current in $SW1$ and $D1$, as well as the gate signals of switches, are also plotted to make the sequence of events described below the graph more comprehensible. It has to be noted that, in case of VFSRI, to avoid short-circuit two switches of the same inverter leg cannot be conducting at the same time. In this section, the dead-time is neglected and the turn-on and off are supposed ideal, without any delay.

Authors would like also to note that the explanations realized in this section are based on unreal simplifications that serve to introduce the commutation states and principles to the reader. However, the explanation of ZVS and ZCS is only reasonable when considering the parasitic components, as it is done in Section 3.2.5.

Commutating at resonant frequency ($f_{sw} = f_r$)

Figure 3.10 shows the corresponding sequence for an inverter commutating at resonant frequency. In this case, the commutation, illustrated by the gate signals, occurs when the current is crossing zero. Observing $SW1$ and its antiparallel diode, the current is flowing through $SW1$ half of the cycle and the diode is never conducting.
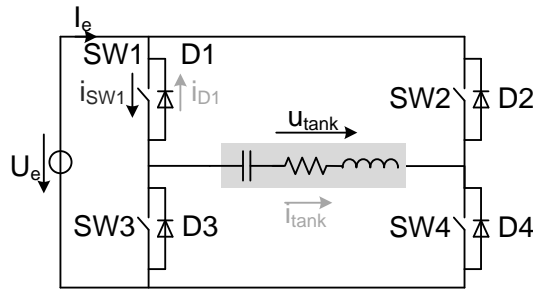
Figure 3.9: VFSRI circuit and variables studied.
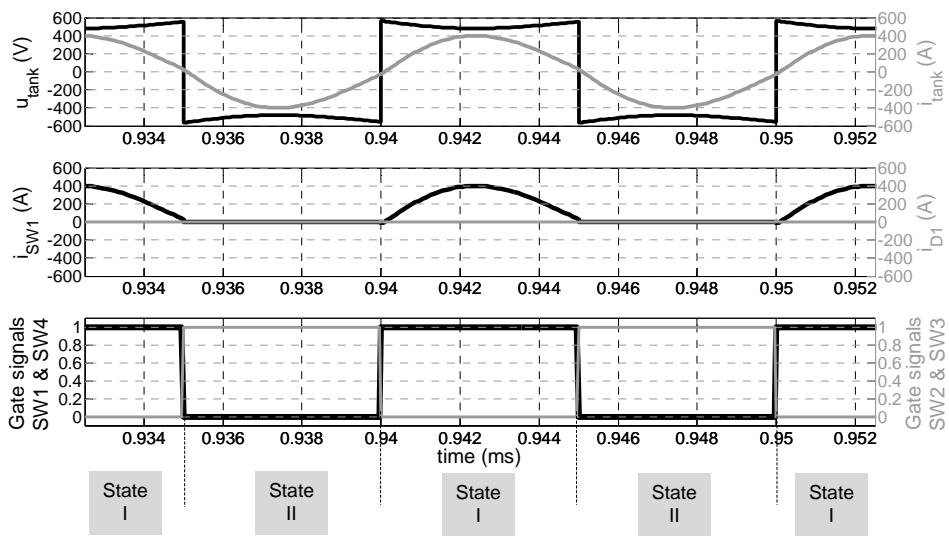
Sequence of events

Figure 3.10: Output waveforms and sequence of events commutating at resonant frequency ($U_e = 560$ V, $R_{eq} = 1.58$ Ω, $L = 9.78$ μH, $C = 0.26$ μF, $f_{sw} = f_r = 100$ kHz).

Under these circumstances there are just two possible states. The first one, when $SW1$ and $SW4$ are conducting and, the second one, when $SW2$ and $SW3$ conduct. Considering losses, there are no commutation losses because switches commutate when the current is zero.

This is the ideal situation with regards to switching losses, but the probability of being at perfect resonance is low. Thus, the other situations need to be studied.

Capacitive switching ($f_{sw} < f_r$)

In Figure 3.11, the waveforms and the corresponding sequence of events when switching below resonance are shown. Observing this figure, it is noticed that the commutation and the voltage's zero crossing, occur after the current's zero crossing. In this case, the current advances the voltage, so that this type of commutation is called capacitive switching. The relation between frequency and current and voltage phase-shift can be observed in the Bode diagram of Figure 3.3 in Section 3.2.1.

Compared to the previous case, $SW1$ does not conduct half of the period and its antiparallel diode is conducting for a short period of time. In fact, $D1$ is forward-biased after the current's zero crossing and before the turn-off of $SW1$. In this case, i_{tank} is slightly lower than in the previous case, but the difference is not noticeable. This difference can also be observed in the Bode diagram of Figure 3.3 where, depending on the Q factor and the frequency, there is a higher or lower decrease on the gain.

Observing the sequence of events in Figure 3.11, in State I the current is flowing through $SW1$ and $SW4$. Afterwards, i_{tank} changes polarity, while $SW1$ and $SW4$ are turned-on, and diodes $D1$ and $D4$ are forward-biased with ZVS (State II). Then, $SW1$ and $SW4$ are turned-off with ZCS because their antiparallel diodes are conducting (State III). Finally, $SW2$ and $SW3$ are turned-on hardly, causing the hard turn-off of diodes $D1$ and $D4$ (State IV). In regard to States V and VI, they are similar to States II and III, but with the opposite switches and diodes.

In this case, diodes' turn-off and switches' turn-on are hard, but the turn-on of diodes and the turn-off of switches is soft. One of the problems derived from diodes' hard turn-off is that large recovery currents can create voltage spikes. This causes an increase of electromagnetic interferences, losses and, in the worst case, the destruction of semiconductors. Thus, capacitive switching has to be avoided if possible.

43
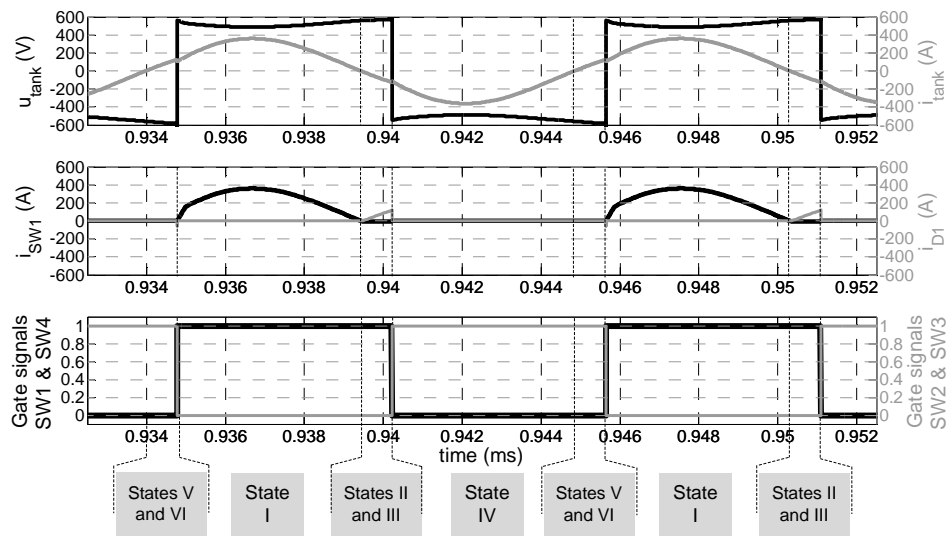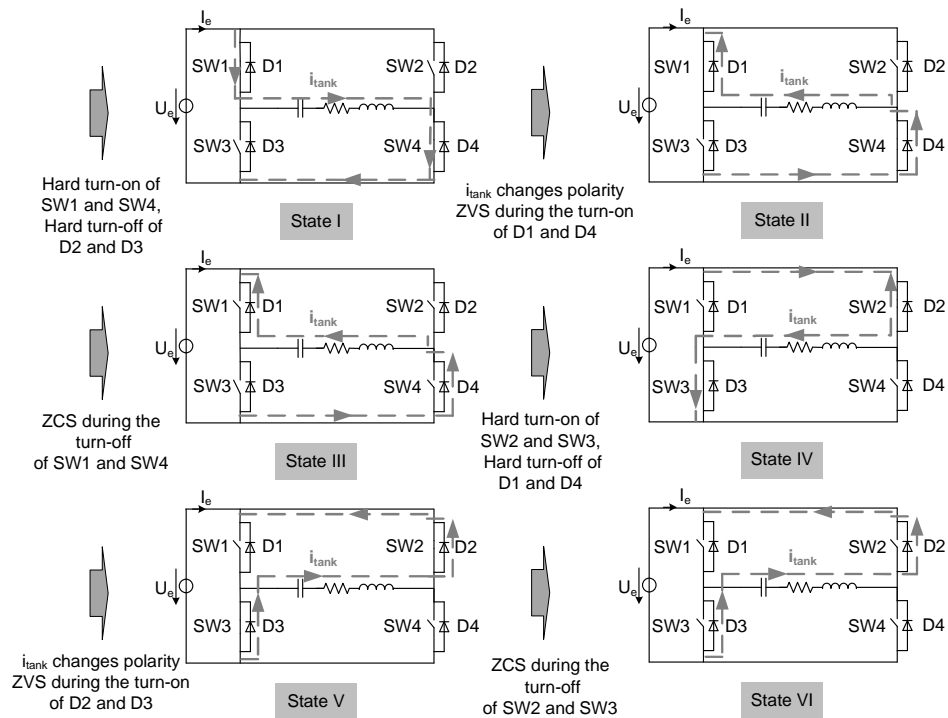
Figure 3.11: Output waveforms and sequence of events commutating below resonant frequency ($U_e = 560\ V$, $R_{eq} = 1.58\ \Omega$, $L = 9.78\ \mu H$, $C = 0.26\ \mu F$, $f_{sw} = 92\ kHz$, $f_r = 100\ kHz$).

Inductive switching ($f_{sw} > f_r$)

Figure 3.12 shows the corresponding waveforms and sequence of events when the inverter is commutating above resonant frequency. In this case, the commutation and the voltage's zero crossing occur before the current's zero crossing. Under these circumstances, the current delays the voltage and this type of commutation is known as inductive switching.

Similarly to capacitive switching, $D1$ is forward-biased. But, in this case, $D1$ conducts after the commutation and before the change of polarity of i_{tank}. The value of i_{tank} is also slightly lower than in case of switching at resonant frequency, but the difference is not noticeable.

Observing the sequence of events in Figure 3.12, the current is flowing through $SW1$ and $SW4$ in State I. Then, switches $SW1$ and $SW4$ are turned-off hardly, causing the hard turn-on of $D2$ and $D3$ (State II). Immediately afterwards, $SW2$ and $SW3$ are turned-on with ZVS because the current is flowing through their antiparallel diodes (State III). And finally, i_{tank} changes polarity and diodes $D2$ and $D3$ are blocked with ZCS because the current starts conducting through $SW2$ and $SW3$ (State IV). States V and VI are similar to States II and III, but with the opposite switches and diodes.

Contrarily to the previous case, diodes' turn-on and switches' turn-off is hard, but the turn-off of diodes and the turn-on of switches is soft. Considering the low probability of being at perfect resonance and the problems derived from the hard turn-off of antiparallel diodes, authors like [25] and [26] suggest working above resonant frequency. Under these circumstances, it has to be noted that it is mandatory to use switches with unidirectional voltage capability but bidirectional current capability, thus, using antiparallel diodes becomes necessary.

3.2.5 Additional considerations

Until the moment, an ideal circuit with ideal sources has been supposed. The dead-time has been neglected and the parasitic components have been omitted. The switches are supposed ideal and no references are given about the current in the converter. However, these parameters need to be considered during the design because they determine the converter's performance.

In this section, the effect of the parasitic capacitors and dead-time on the commutation and on the switching frequency are considered. Afterwards, some considerations concerning power semiconductors in VFSRI are given.
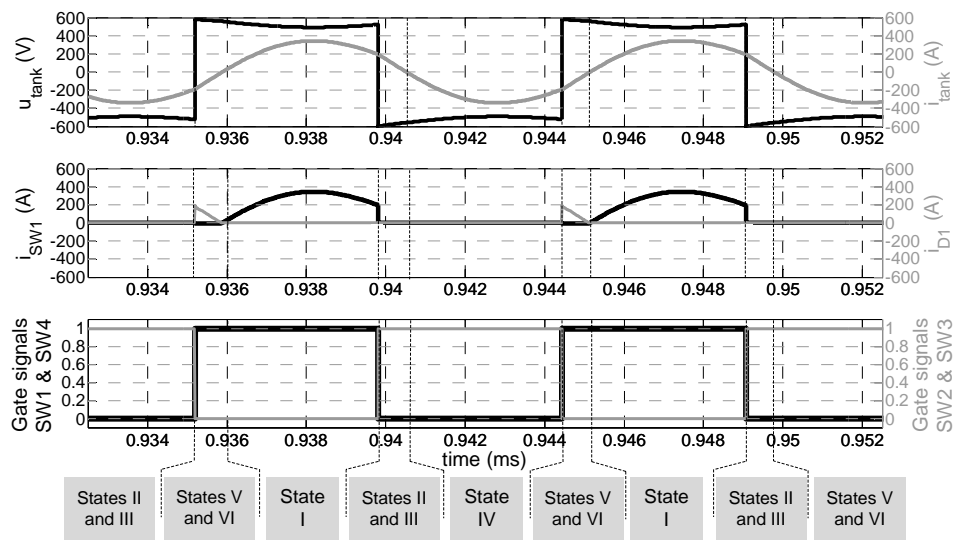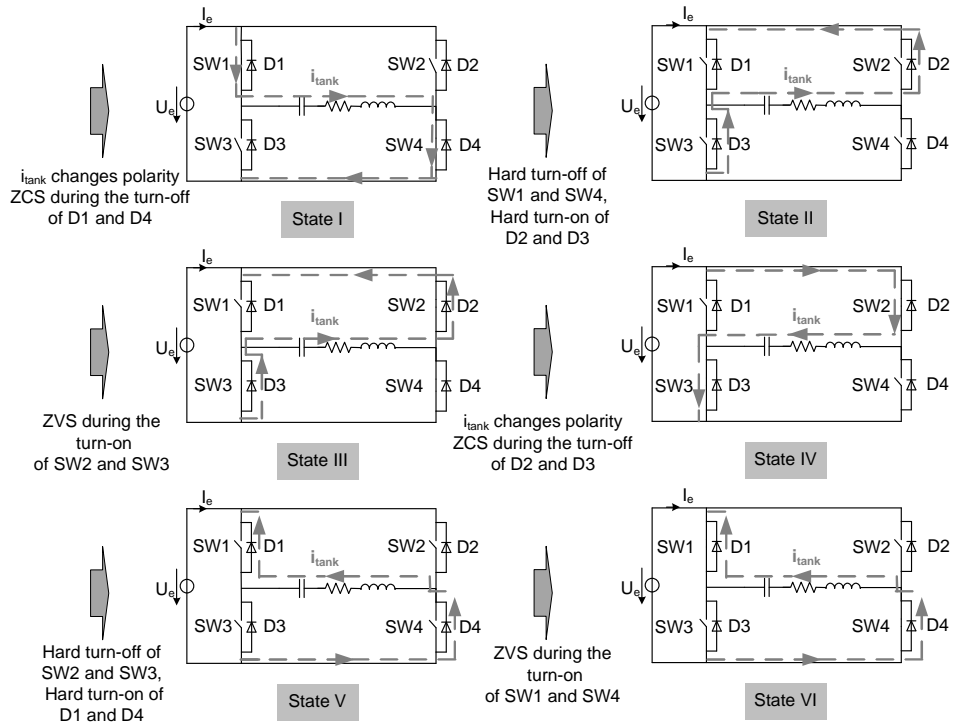
Sequence of events
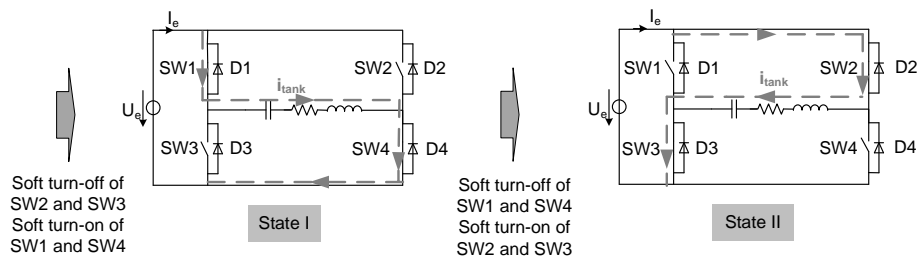

Figure 3.12: Output waveforms and sequence of events commutating above resonant frequency ($U_e = 560$ V, $R_{eq} = 1.58$ Ω, $L = 9.78$ μH, $C = 0.26$ μF, $f_{sw} = 108$ kHz, $f_r = 100$ kHz).

Finally, the need of a transformer between the load and the converter due to the high currents through semiconductors is exposed.

Commutation sequence considering parasitic capacitances and dead-time

In Section 3.2.4, the different sequences of events when switching at resonant frequency, below and above are explained. Due to the problems derived from the reverse recovery currents in diodes, most authors commutate above resonant frequency. Nevertheless, during these analyses, parasitic capacitances of semiconductors and dead-times between switches have not been considered. In this section, the influence of these parameters is explained.

In Figure 3.13, the electrical scheme for a VFSRI considering parasitic capacitances (C_p) is shown. It has to be noted that this capacitance includes the parasitic capacitance, but also the snubber in case of having it. Assuming the inverter is switching above resonance, Figure 3.14 shows the output waveform and the events considering these capacitances and the dead-time between switches. The states shown in this figure are related to those defined in Figure 3.12 .

Observing Figure 3.12, the sequence that accomplishes soft-switching in case of inductive switching is shown. The sequence of events occurring in this figure is the following:

1. Switches $SW2$ and $SW3$ turn-off hardly.

2. The parasitic capacitance C_p of $SW2$ and $SW3$ charge, while C_p of switches $SW1$ and $SW4$ discharge, increasing the voltage of u_{tank} up to U_e.

3. The antiparallel diodes $D1$ and $D4$ are forward-biased when u_{tank} exceeds U_e.

4. Switches $SW1$ and $SW4$ are turned-on with ZVS (their antiparallel diodes are conducting).

5. The current i_{tanc} changes polarity, conducting through $SW1$ and $SW4$ and turning-off with ZCS the antiparallel diodes $D1$ and $D4$.

So far, it was supposed that ZVS during switches' turn-on and ZCS during diodes' turn-off always occurred when switching above resonance. However, observing Figure 3.14, it is noticed that ZVS and ZCS do not always occur.
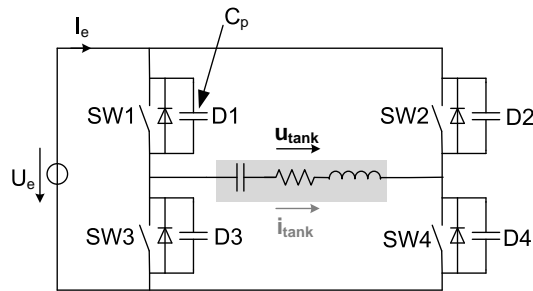
Figure 3.13: VFSRI considering parasitic capacitances C_p.
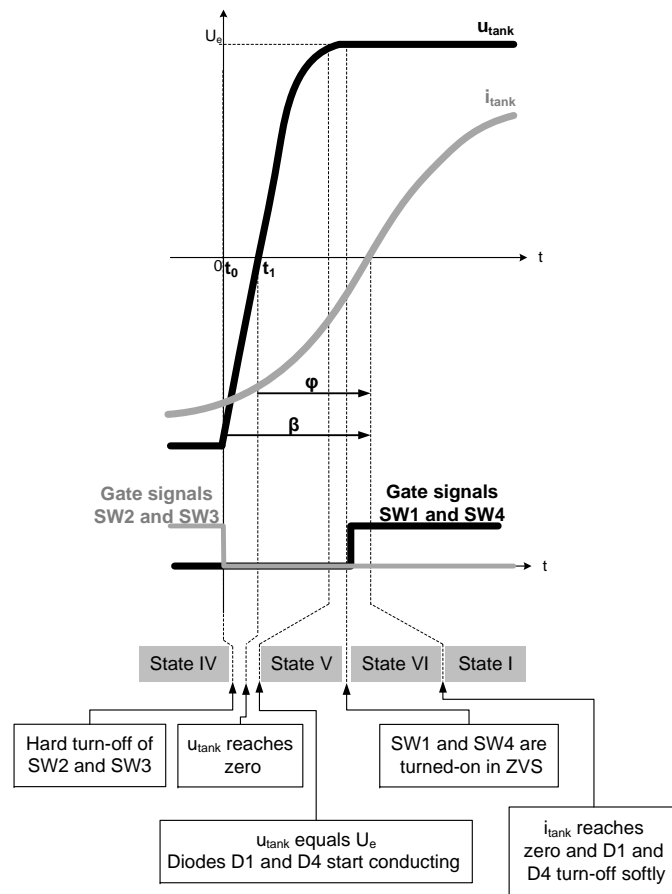
Figure 3.14: Output waveforms and sequence to have ZVS and ZCS commutating above resonance.

For example, in case of low dead-times, $SW1$ and $SW4$ turn-on before u_{tank} reaches U_e and there is not ZVS. This situation can occur if the capacitance C_p is high and lasts more than the dead-time to be charged. Another example is the case in which the phase-shift between voltage and current is low and the current changes polarity before $SW1$ and $SW4$ turn-on. In this case, there is neither ZVS nor ZCS.

Under real circumstances, the combination of C_p, current, phase-shift and dead-time determine the type of commutation. Different combinations of these parameters and the resulting output waveforms are shown in [27] and more in detail in [28]. A brief resume and the basic equations, including those shown in this section, are found in Appendix B. Considering this, the conditions to obtain the correct sequence described above are

$$\beta \geq arccos\left[1 - \frac{2U_e C_p \omega}{\hat{i}_{tank}}\right] \tag{3.21}$$

and

$$\varphi \geq arccos\left[1 - \frac{U_e C_p \omega}{\hat{i}_{tank}}\right] \tag{3.22}$$

where (see Figure 3.14)

- β, is the phase-shift between the instant at which the gate signal of the switch becomes low and the moment at which i_{tank} changes polarity.

- φ is the phase-shift between u_{tank} and i_{tank}.

- $\hat{i}_{tank}$ is the amplitude of i_{tank}.

- U_e is the voltage of the DC source, as shown in Figure 3.13.

- C_p is the sum of the parasitic capacitance and the snubbers of the switches.

Observing Equations 3.21 and 3.22, it is observed that the control needed to accomplish a correct commutation process is complex. Furthermore, in case of low currents or high capacitances, β and φ are high. Under these circumstances, the switching frequency and the reactive power supplied by the inverter increase and, for providing the same active power, the voltage U_e needs to be higher.

Power semiconductors

Due to the intrinsic operation of VFSRI, the switches of the inverter need to be unidirectional in voltage but bidirectional in current. Therefore, in most applications up to 1 MW and 600 kHz, MOSFETs and IGBTs are frequently used nowadays [27]. The use of MOSFETs is relegated to applications with frequencies above 150 kHz, where IGBTs usually cannot be employed due to their higher switching losses.

In section 3.2.4, the problem derived from commutating below resonance has been introduced. In that case, the turn-off of the antiparallel diodes is hardly done and the reverse recovery currents can cause undesired effects, like voltage spikes and electromagnetic interferences. Although authors tend to switch above resonance to avoid this situation, there are some cases in which the capacitive switching is practically unavoidable. For example, in case of a workpiece that touches the inductor and there is short-circuit. Under these circumstances, the inductance diminishes abruptly and the resonant frequency of the tank increases, causing a capacitive switching because the control is still imposing the previous resonant frequency.

Regarding capacitive switching, MOSFETs are more sensitive than IGBTs and can be more easily destroyed, as explained in [28] and [29]. However, during normal operation (switching above resonant frequency) some failures have been reported for ZVS converters with light loads in [30–33].

An equivalent circuit of a MOSFET is shown in Figure 3.15, extracted from [28, p. 180] and [30]. The origin of MOSFETs failure is related to the activation of the parasitic BJT that, in case of resonant converters, is generally originated by the MOSFET's intrinsic diode.
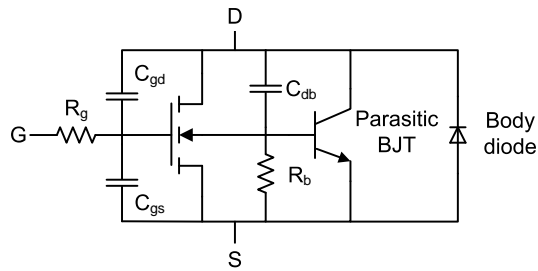
Figure 3.15: MOSFET model

In case of capacitive switching, the diode is turned-off hardly (Figure 3.11 in Section 3.2.4), generating a reverse recovery current and a high du/dt. The

sum of this du/dt and the leakage current, might cause a current trough the resistance R_b (seen in Figure 3.15) that can lead to the turn-on of the BJT.

In case of switching above resonance, the antiparallel diode is turned-off softly (Figure 3.12 in Section 3.2.4), thanks to the voltage drop of the MOS-FET that starts conducting. This low reverse voltage, that is proportional to the load's current, causes a slow reverse recovery of the antiparallel diode. Afterwards, when the MOSFET turns-off, a high reverse voltage is applied to the diode. Due to the stored charge, this high reverse voltage can generate a reverse recovery current that can result in the turning-on of the parasitic BJT. This phenomenon is accurately described in [31].

Therefore, special care has to be taken regarding the reverse recovery time and current of the antiparallel diode in case of using MOSFETs. Authors recommend using MOSFETs with fast diodes, most of them using fast-recovery epitaxial diode field-effect transistors (FREDFET), as in [30–34]. To have a more complex but more reliable system, some authors like [28,29] and [35, p. 27] suggest canceling the antiparallel diode and adding an external free-wheeling diode, as shown in Figure 3.16.
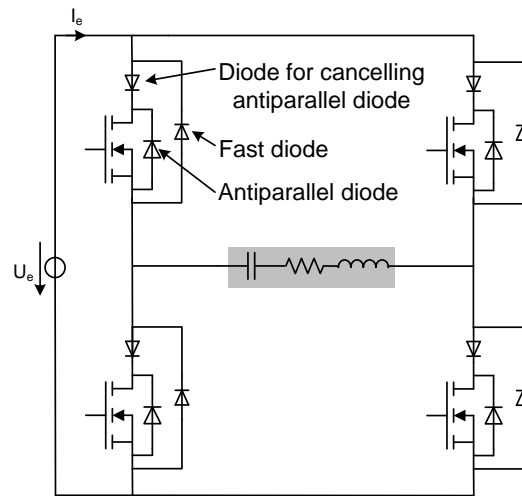
Figure 3.16: Annulling MOSFET's body diode

Although the previous considerations regarding antiparallel diodes have to be taken into account, nowadays there have been great improvements in MOSFET's antiparallel diodes. Manufacturers like IXYS© and MICROSE-MI© produce power MOSFETs incorporating fast diodes and, at the mo-

ment, silicon carbide technologies are starting to emerge with the promise of diodes without reverse recovery currents. In fact, this new silicon technology has been used already to improve diodes' turn-on characteristics in [29]. However, although there have been great improvements, one of the main difficulties is still the selection of the appropriate MOSFET with its antiparallel diode just from datasheets information, as stated in [36].

For high frequencies, another important fact considering VFSRI and the semiconductor's selection criteria, are the switching losses. Taking into account that VFSRI at inductive switching has minimum turn-on losses but higher turn-off losses, one of the main parameters affecting the selection of the device are precisely the turn-off losses. In this case, it is also difficult to make a comparison between devices just considering their datasheets and experimental tests need to be realized to have an accurate analysis, as explained in [26].

Matching transformers and VFSRI

In IH, having high current values in the inductance is interesting because more heat is produced in the workpiece. However, in case of VFSRI, the current in the tank i_{tank} is the same than in the inverter. Considering that the value of the equivalent resistance is usually lower than one ohm, the voltages in the inverter are low and the currents high. From the inverter's point of view, the use of low voltages and high currents produce much more losses and voltage drops.

At the beginning, this was the main limiting problem of VFSRI topology for IH converters with semiconductors and one of the reasons of CFPRI proliferation. However, nowadays, the developments in materials science and manufacturing have permitted the appearance of high performance transformers. These matching transformers allow the use of VFSRI topology in many applications, although making the final product more expensive and lowering the efficiency of the system. Nevertheless, it is worth pointing out that transformers efficiency is usually higher than 95 %. In Section 3.4.2, more details are given considering topologies with matching transformers.

3.3 Current-fed parallel-resonant inverters

In case of parallel tanks, the inductor is connected in parallel with the capacitor. Contrarily to a series connection, the tank behaves like a voltage source and the inverters used are current-fed. This implies that the inverter

3.3 Current-fed parallel-resonant inverters

is fed with a high inductance that maintains the current and behaves as a constant current source. A parallel tank and an ideal CFPRI are shown in Figure 3.17. For the same reasons than for VFSRI, explained in Section 3.2, the inverter used all-along this section is the H-bridge.

In case of current-fed inverters, the current path cannot be opened and switches from the same inverter leg have to overlap. Switches have to be unidirectional in current but bidirectional in voltage. If diodes are not added, the capacitor would discharge, so Figure 3.17 shows a diode in series with a switch.

Similarly to VFSRI, CFPRI has different ways of controlling the power. During this section, it is assumed that the power is controlled by varying the current of the source (I_e in Figure 3.17) and, thus, that switches $SW1$ & $SW4$ and $SW2$ & $SW3$ commutate alternatively with a duty-cycle of 50 %. The inductor-workpiece is also modeled by a constant resistance and inductance in series.
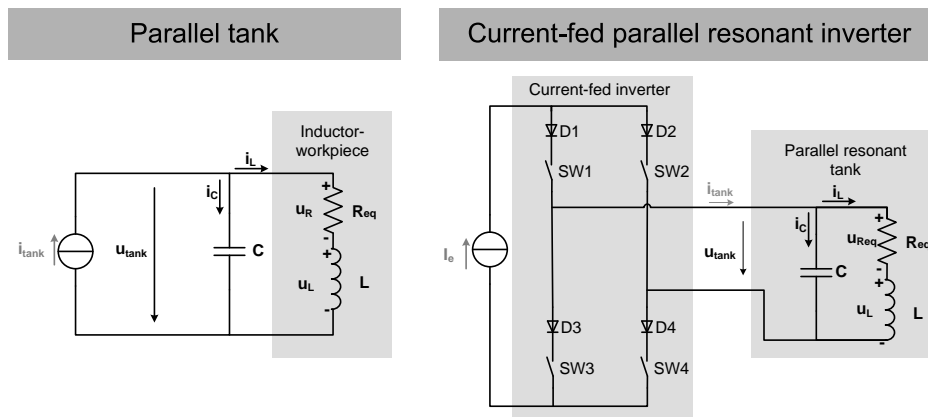
Figure 3.17: Parallel tank and a CFPRI.

In the following sections, some concepts regarding CFPRI performance are introduced. In order to facilitate the comprehension, the distribution of sections and symbols are similar to the ones used during VFSRI explanations. First, in Section 3.3.1, the resonant frequency is found for the case of para-llel tanks, expressing the resemblances with series tanks for high quality factors. Next, in Section 3.3.2, the quality factor and its influence in voltage waveforms is presented. The relation between currents in the tank and in their components, determined by the quality factor, is also explained. Afterwards, in Section 3.3.3, the basic equations for calculating the

power transmitted to the workpiece are shown. After, in Section 3.3.4, the implications of commutating at zero phase-shift, above and below are explained. Finally, in Section 3.3.5, some considerations regarding the optimal commutation procedure and overvoltage protections are presented.

3.3.1 Resonant frequency

Proceeding like in VFSRI but for CFPRI, the RLC circuit in Figure 3.17 accomplishes the following equations

$$i_{tank} = i_C + i_L \tag{3.23}$$

$$i_C = C\frac{du_{tank}}{dt} \tag{3.24}$$

$$i_L = \frac{1}{L}\int u_L dt \tag{3.25}$$

$$u_{tank} = u_L + u_{R_{eq}} \tag{3.26}$$

Using Laplace transformation with initial conditions equal to zero, the follwing equation is obtained

$$I_{tank}(s) = I_C(s) + I_L(s) = sCU_{tank} + \frac{U_{tank}}{sL + R_{eq}} \tag{3.27}$$

obtaining the next second order system with a zero

$$
\begin{aligned}
H_p(s) = \frac{U_{tank}(s)}{I_{tank}(s)} &= \frac{sL + R_{eq}}{s^2 LC + sCR_{eq} + 1} \\
&= (sL + R_{eq})\frac{w_n^2}{s^2 + 2\zeta\omega_n s + \omega_n^2}
\end{aligned}
\tag{3.28}
$$

The roots of this second order system are the same than those found for VFSRI in Equation 3.4. In this case, the same definitions of undamped natural frequency ω_n and damping ratio ζ shown in Equations 3.5 and 3.6 are used. It has to be noted that in CFPRI the transfer function $H_p(s)$ is equivalent to the impedance, whereas in VFSRI the transfer function $H_s(s)$ is equivalent to the conductance.

Transforming Equation 3.28 into the frequency domain, the following equation is obtained

$$H_p(s)|_{s=\omega j} = \frac{R_{eq}}{(1 - \omega^2 LC)^2 + (\omega C R_{eq})^2}$$
$$+ j \frac{\omega \left(L - C R_{eq}^2 - \omega^2 L^2 C \right)}{(1 - \omega^2 LC)^2 + (\omega C R_{eq})^2} \tag{3.29}$$

Assuming the definition of resonant frequency as the maximum of a transfer function, shown in Section 3.2.1, the mathematical expression is more complex for CFPRI than for VFSRI. Proceeding similarly and calculating the maximum with the help of mathematical softwares, the maximum of $H_p(s)$ is

$$\omega_r = \frac{\sqrt{C\sqrt{2LCR_{eq}^2 + L^2} - C^2 R_{eq}^2}}{LC} \tag{3.30}$$

considering the definition of quality factor for the series model of the inductance-workpiece system (Section 1.3.1), Equation 3.30 turns into

$$\omega_r = \omega_n \sqrt{\sqrt{\frac{2}{Q^2} + 1} - \frac{1}{Q^2}} \tag{3.31}$$

which is simplified to ω_n for high Q values, like in the case of VFSRI.

Considering ω_{phase0} as the frequency at which the phase-shift between current and voltage is zero, the imaginary part of Equation 3.29 has to be zero at this frequency. Therefore, ω_{phase0} is equal to

$$\omega_{phase0} = \sqrt{\frac{L - C R_{eq}^2}{L^2 C}} = \omega_n \sqrt{1 - \frac{1}{Q^2}} \tag{3.32}$$

Although Equations 3.31 and 3.32 are different, this difference can be neglected for high Q values, because their values are approximately equal to the undamped natural frequency ω_n.

In Figure 3.18, a Bode analysis of $H_p(\omega)$ (Equation 3.28) for different RLC circuits is shown. The three different circuits have the same inductances (9.78 μH) and capacitances (0.26 μF), having therefore the same undamped natural frequency ω_n . The only difference is the R_{eq} value, that takes the following values: 5.58 Ω, 3.58 Ω and 1.58 Ω. The corresponding values of Q for these three cases are 1.10, 1.71 and 3.88.

It can be observed in this figure that the three frequencies ω_r, ω_{phase0} and ω_n (represented in kHz by f_r, f_{phase0} and f_n) are different. But, the higher the Q value, the more similar they are. In fact, in case of Q equal to 3.88, their values are practically the same with a difference lower than 4 %.
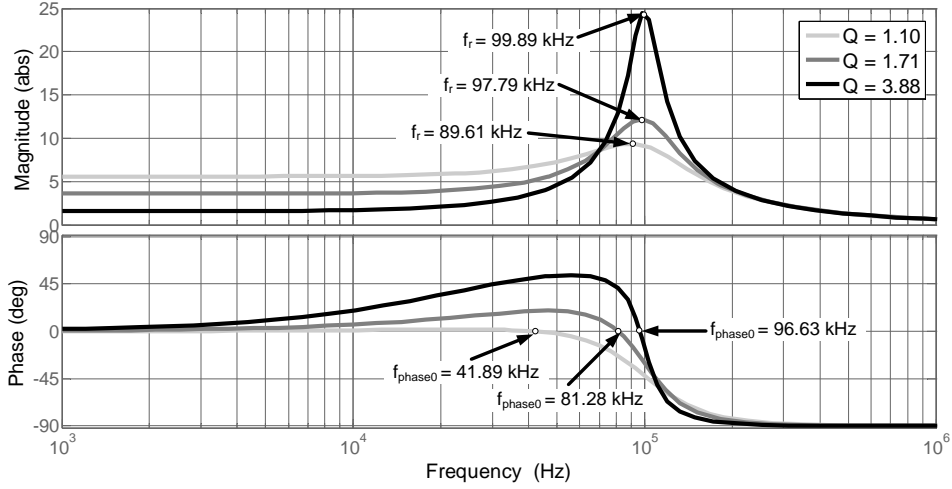
Figure 3.18: Bode analysis of the transfer function $H_p(\omega)$ for three systems with different Q values and $f_n = 100 \ kHz$.

Assuming that the Q factor is high enough so that these three frequencies are equal, the impedance $Z_p(\omega)$ at the resonant frequency ω_r is obtained by substituting ω_n in the module of Equation 3.29. In this case, the following equation is obtained

$$Z_p(\omega_r) \approx |H_p(\omega_n)| = \sqrt{L\frac{L + CR_{eq}^2}{C^2 R_{eq}^2}} = R_{eq}Q\sqrt{Q^2 + 1} \qquad (3.33)$$

Therefore, the complexity of the equations for CFPRI can be solved by assuming high Q values and simplifying these formulas.

Another simplification, assuming also high Q values, can be done by using the parallel model of the inductor-workpiece system explained in Section 1.3.1. In this case, the equivalent resistance of the system is supposed to be in parallel with the inductor, as shown in Figure 3.19.

Considering this, the transfer function of the impedance becomes

$$H_p(s)' = \frac{U_{tank}(s)}{I_{tank}(s)} = \frac{sLR_{eq}'}{s^2LCR_{eq}' + sL + R_{eq}'} \qquad (3.34)$$
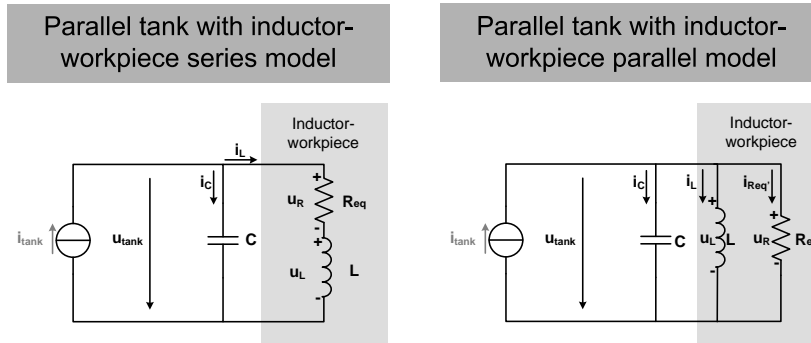
Figure 3.19: Parallel tank with series and parallel models of inductor-workpiece.

Assuming that the equivalent resistance represents the losses originated by the eddy currents in the workpiece, the equivalent resistance in the parallel model R'_{eq} has to accomplish Equation 1.7.

In Figures 3.20 and 3.21, the Bode analysis for $H_p(s)$ (series model) and $H_p(s)'$ (parallel model) are shown for two different RLC circuits. The inductance ($L = 9.78 \ \mu H$) and the capacitance ($C = 0.26 \ \mu F$) are the same in both cases, but the resistance varies . The Q value is 1.71 in Figure 3.20 ($R_{eq} = 3.58 \ \Omega$ and $R'_{eq} = 10.46 \ \Omega$) and 3,88 in Figure 3.21($R_{eq} = 1.58 \ \Omega$ and $R'_{eq} = 23.79 \ \Omega$).

Observing these figures, it is noticed that the behavior of both models is similar when approaching to the undamped natural frequency f_n at 100 kHz. It can also be observed how, the higher Q is, the more resemble both models at f_n. Therefore, this model can be used as far as the Q value is high enough and the analysis is realized in frequencies close to f_n.

The benefit of using this parallel model of inductor-workpiece system is that the resonant frequency ω_r, the frequency at which the phase-shift is zero ω_{phase0} and the undamped natural frequency ω_n are equal (Equation 3.35).

$$\omega_r = \omega_{phase0} = \omega_n = \frac{1}{\sqrt{LC}} \tag{3.35}$$

Taking this into consideration, the impedance at resonant frequency is equal to

$$Z_p(\omega_r)' = \left| H_p(\omega_r)' \right| = R'_{eq} \tag{3.36}$$
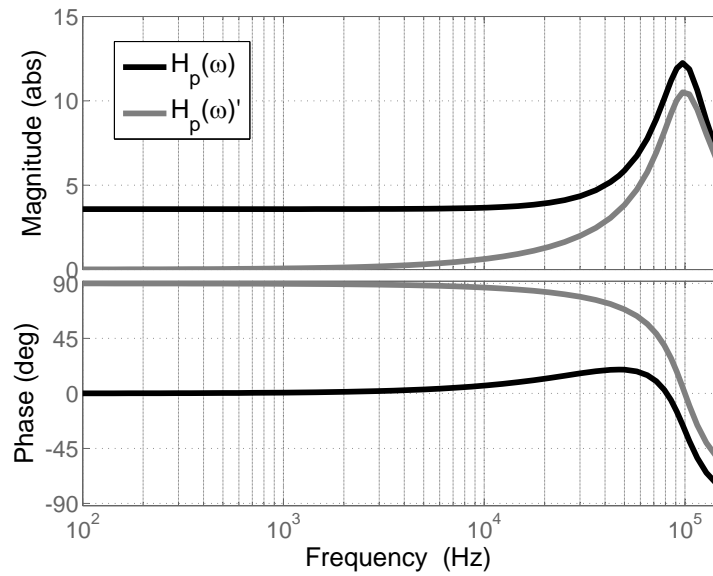
Figure 3.20: Bode analysis of the transfer function for the series $H_p(\omega)$ and parallel $H_p(\omega)'$ models for a system with a Q of 1.71.
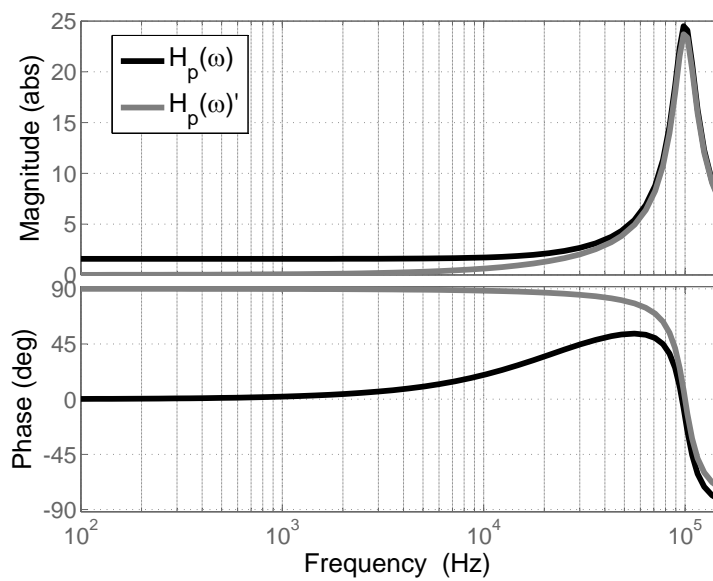
Figure 3.21: Bode analysis of the transfer function for the series $H_p(\omega)$ and parallel $H_p(\omega)'$ models for a system with a Q of 3.88.

with $R'_{eq} = R_{eq}Q^2$ (Equation 1.7). It has to be noted that this equation is similar to Equation 3.33 for high Q values.

3.3.2 Quality factor

As in the case of the series resonant tank, the quality factor allows to define and understand the behavior of the parallel tank. In this section, the relation between the quality factor and voltage is presented and, afterwards, its relation within the gain between currents is explained.

Quality factor and voltage

In case of CFPRI, the parallel tank also acts as a tuned filter at resonant frequency. This can be observed in the Bode diagram of Figure 3.18 in Section 3.3.1. Thus, the only component of the tank voltage u_{tank} is due to the first harmonic of the current square wave i_{tank}. In this case, the current i_{tank} is a square waveform and the voltage u_{tank} is sinusoidal.

Similarly to VFSRI, the Q factor gives an idea of how good is the filtering. In case of having low Q values, the voltage is not sinusoidal because there are more harmonic components than the first one and commutating with soft-switching is not possible. Moreover, in CFPRI, the lower Q is, the more different are ω_{phase0} and ω_r, as shown in Equations 3.31 and 3.32 in the previous section.

Using the same RLC circuits than in Figure 3.18, the voltage u_{tank} and current i_{tank} are plotted for Q equal to 1.71 and Q equal to 3.88 in Figures 3.22 and 3.23 respectively. In both figures, the switching frequency f_{sw} is equal to f_{phase0}.

In Figure 3.22, the voltage is not sinusoidal and there is a phase-shift between current and voltage. Considering the Bode analysis in Figure 3.18, the peak of the impedance transfer function H_p is low. Moreover, the resonant frequency f_r and the frequency at which the phase-shift is zero f_{phase0} are different. Thus, the filtering of the harmonic content is not very good itself and, as the switching frequency is not the resonant frequency, it becomes even worse. That is why the phase-shift is not zero and the voltage u_{tank} is not sinusoidal.

Considering the case with a higher Q value, in Figure 3.23, f_{phase0} and f_r are similar and the peak of H_p is higher. Therefore, the filtering is good enough at the resonant frequency, which is almost the same than f_{phase0},
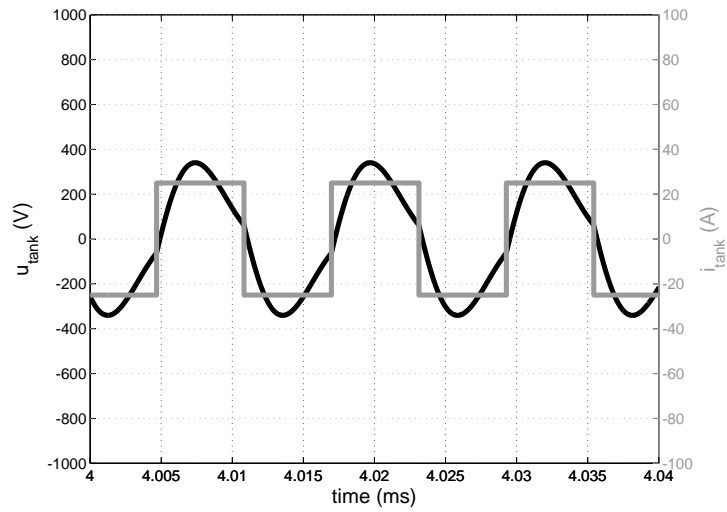
Figure 3.22: Voltage and current in the tank with a Q of 1.71 ($I_e = 25\ A$, $R_{eq} = 3.58\ \Omega$, $L = 9.78\ \mu H$, $C = 0.26\ \mu F$, $f_{sw} = f_{phase0} = 81.28\ kHz\ f_r = 97.79\ kHz$ and $f_n = 100\ kHz$).
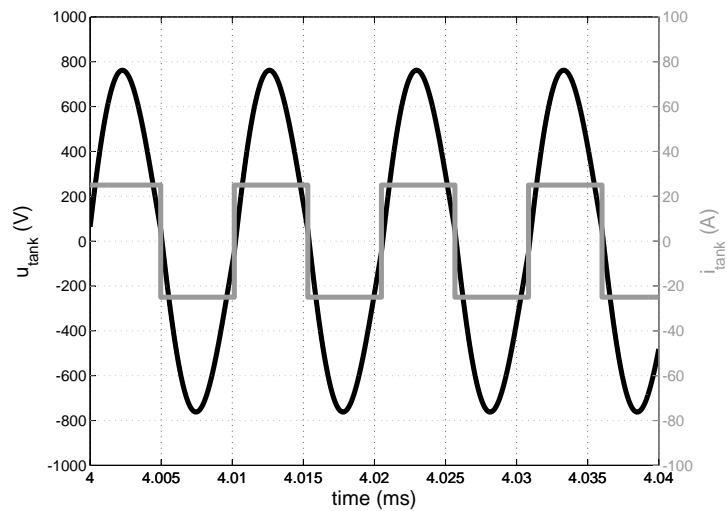
Figure 3.23: Voltage and current in the tank with a Q of 3.88 ($I_e = 25\ A$, $R_{eq} = 1.58\ \Omega$, $L = 9.78\ \mu H$, $C = 0.26\ \mu F$, $f_{sw} = f_{phase0} = 96.63\ kHz\ f_r = 99.89\ kHz$ and $f_n = 100\ kHz$).

the voltage is sinusoidal and the phase-shift is zero. In this case, the first harmonic of the square wave current almost generates all the voltage.

Therefore, low Q values decrease the peak of H_p and the resonant frequency and the frequency of zero phase-shift differ. Under these circumstances, the harmonic content of u_{tank} is high and soft-switching is not possible. Thus, it can be concluded that having high Q values is interesting for an optimum performance of CFPRI.

Quality factor and current gain

Considering the current in the tank and combing Equations 3.23, 3.24 and 3.26, the following equation is obtained

$$i_{tank} = i_C + i_L = C\frac{d\left(u_C\right)}{dt} + i_L = C\frac{d(u_L + u_{R_{eq}})}{dt} + i_L$$
$$= CL\frac{d^2 i_L}{dt^2} + CR_{eq}\frac{di_L}{dt} + i_L \qquad (3.37)$$

Using Laplace transformation, Equation 3.37 is transformed into

$$H_{i_L}(s) = \frac{I_L(s)}{I_{tank}(s)} = \frac{1}{LCs^2 + R_{eq}Cs + 1} \qquad (3.38)$$

which represents the relation between the current in the inductance and at the output of the inverter.

Transferring this equation to the frequency domain, the transfer function $H_{i_L}(s)$ becomes

$$H_{i_L}(s)|_{s=j\omega} = \frac{1}{1 - \omega^2 LC + j\omega CR_{eq}} \qquad (3.39)$$

with the following module

$$|H_{i_L}(\omega)| = \frac{1}{\sqrt{(1 - LC\omega^2)^2 + (CR_{eq}\omega)^2}} \qquad (3.40)$$

Calculating the derivative Equation 3.40 and equaling to zero, the following resonant frequency is obtained

$$\omega_{ri} = \sqrt{\frac{2LC - C^2 R_{eq}^2}{2L^2 C^2}} = \frac{\omega_n}{Q}\sqrt{Q^2 - \frac{1}{2}} \qquad (3.41)$$

being ω_{ri} the frequency at which $H_{i_L}(\omega)$ is maximum. Thus, ω_{ri} is the frequency that maximizes the current in the inductor for a given i_{tank}. It has to be noted that ω_{ri} is approximately equal to the undamped natural frequency ω_n for high Q values, like ω_r and ω_{phase0}.

Assuming a high Q value, substituting ω_n into Equation 3.39 and assuming that $I_{tank}(\omega_n)$ represents the fundamental component of the inverter output current, the gain in current at ω_{ri} is approximately

$$I_L(\omega_{ri}) \approx I_L(\omega_n) = -jQI_{tank}(\omega_n) \tag{3.42}$$

Therefore, the current at resonant frequency is Q times the current at the output of the inverter and 90 degrees delayed.

Proceeding similarly for the current in the capacitor and combining Equations 3.24 and 3.26 with the transfer function H_{i_L} in Equation 3.38, the transfer function for the current in the capacitor and the current in the tank is

$$H_{i_C}(s) = \frac{I_C(s)}{I_{tank}(s)} = \frac{LCs^2 + CR_{eq}s}{LCs^2 + CR_{eq}s + 1} \tag{3.43}$$

Transferring this equation to the frequency domain and assuming a high Q value, then

$$I_C(\omega_{ri}) \approx I_C(\omega_n) = (1 + jQ)I_{tank}(\omega_n) \tag{3.44}$$

Therefore, the current in the capacitor is approximately Q times the current at the output and 90 degrees advanced.

It can be observed from Equation 3.42 that high Q values are interesting because the current in the inductor (and so in the workpiece) is high, while the current in the converter is low.

However, the the tank voltage and the capacitors voltage should be studied carefully. In Figure 3.17, it can be observed that the voltage u_{tank} is the same than at the capacitors and switches. Considering Equation 3.33, the impedance is dependent on the square of Q. For a given i_{tank}, if the Q is high, the current in the inductance and in the resistance is high too. Thus, the impedance is also high and the voltage u_{tank} increases. Therefore, the value of Q has to be high but limited to avoid the destruction of the semiconductors or an oversized system design.

Taking this fact into consideration, the case of heating steels up to their Curie temperature deserves special attention. Under these circumstances, μ

decreases and the penetration depth increases, decreasing the R_{eq} (Section 1.8) and suddenly increasing the Q value and the voltage.

Similarly to VFSRI, but with current, i_{tank} can be simplified for high Q values to its first harmonic. Thus, i_{tank} can be supposed to be equal to

$$I_{tank} \approx \frac{4I_e}{\sqrt{2}\pi} \tag{3.45}$$

being I_{tank} the RMS value of the first harmonic. This simplification can be used in Equations 3.33, 3.42 and 3.44.

In order to see if these assumptions made are correct, Figure 3.24 shows the voltage and current for the same case shown in Figure 3.18 in Section 3.3.1 with Q equal to 3.88. In this case, the current source I_e is set to 25 A and the system is commutating at f_{phase0} to avoid switching losses.
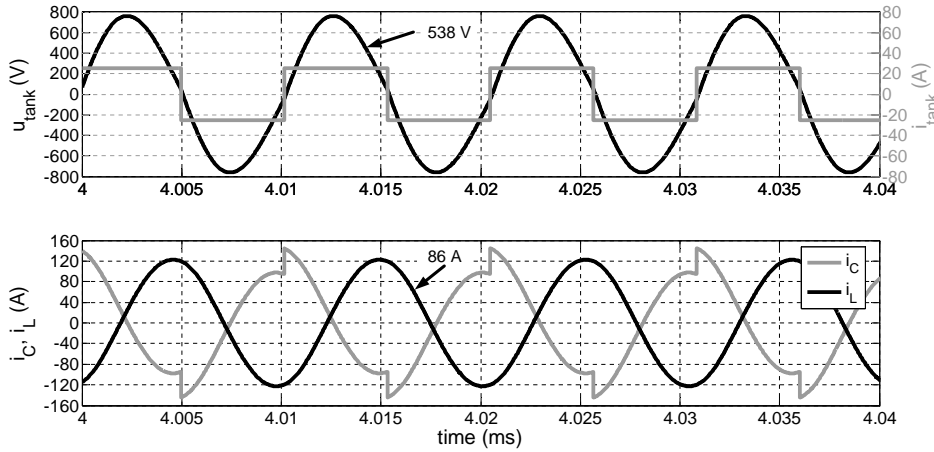
Figure 3.24: Voltage and current in the tank and in the RLC circuit with a Q of 3,88 ($I_e = 25$ A, $R_{eq} = 1.58$ Ω, $L = 9.78$ μH, $C = 0.26$ μF, $f_{sw} = f_{phase0} = 96.63$ kHz).

Observing this figure, the current in the capacitor i_C is advanced approximately 90 degrees and the current in the inductance i_L is delayed 90 degrees, as shown in Equations 3.42 and 3.44. Moreover, using Equation 3.42 and assuming the first harmonic approximation of Equation 3.45, the current in the inductor is 87 A, which is quite similar to the value obtained during the simulations in Figure 3.24. It is analogous when using Equation 3.33 for the voltage, as in this case the voltage obtained is 555 V, whereas in the simulations is 538 V. Thus, the assumptions made by considering high Q values

show good correspondence with the simulations, with an error smaller than 3 % for a Q value of 3.88.

It can be observed that the current in the capacitor i_C is not sinusoidal. This is similar to the inductance voltage for VFSRI. In this case, i_c is the sum of a sinus (approximately Q times the first harmonic of i_{tank}) plus the difference between $i_{R_{eq}}$ (sinusoidal) and i_{tank} (square wave). Nevertheless, Equation 3.44 can be used as a good approximation .

3.3.3 Power in the workpiece

Considering that the current in the inductance is the same as in the equivalent resistance, the power transmitted to the workpiece is equal to

$$P = I_L^2 R_{eq} \tag{3.46}$$

Assuming that for high Q values the resonant frequencies ω_{ri} and ω_r are equal, the current in the equivalent resistance is maximum at the resonant frequency and so it is the power delivered to the workpiece.

Assuming a high Q value and combining Equation 3.47 with 3.45 and 3.42, the power at resonant frequency is

$$P(\omega_r) = I_L(\omega_r)^2 R_{eq} \approx (QI_{tank}(\omega_n))^2 R_{eq}$$
$$\approx (Q\frac{4I_e}{\sqrt{2}\pi})^2 R_{eq} = \frac{8I_e^2 Q^2 R_{eq}}{\pi^2} \tag{3.47}$$

In this case, the power delivered to the wokpiece can be controlled with the current source I_e.

The model of inductor-workpiece used is the model explained in Section 1.3, but the analytical model explained in Section 2.2 can also be applied. In that case, the inductance and resistance are substituted by the sum of inductances and resistances and the power in the workpiece is calculated just with R_w.

3.3.4 Commutation analysis

In previous sections it was explained that, at resonant frequency, the power supplied to the workpiece is maximum and that the commutation is realized with low losses when having high Q values. However, this situation is rarely accomplished due to the inaccuracies of the control and the changes

of the parameters during the heating process. Consequently, all the possible operation manners have to be studied.

In this section, the cases in which the converter is commutating out of resonance are studied more in detail. The objective of this study is to comprehend the sequence of events occurring during the switching process and define the preferable operation for the converter. The explanations realized in this section are based on unreal simplifications that serve as an introduction for the reader. However, the explanation of ZVS and ZCS is only reasonable when considering the parasitic components, as it is done in Section 3.3.5.

In Figure 3.25, a simple scheme of a CFPRI that illustrates the variables used during the explanations is presented. In Figures 3.10, 3.11 and 3.12, the current and the across the tank are shown. The voltage across $SW1$, $D1$ and the switches' gate signals are plotted, with the sequence of events described below the graph. It has to be noted that, in case of CFPRI, two switches of the same inverter leg cannot be opened at the same time as, otherwise, the current circuit is opened and there is an overvoltage. In this case, the overlap is the time at which both switches from the same inverter leg are turned-on. In this section, the overlap-time is neglected and the switching turn-on and off are supposed ideal without any delay.

In the analysis realized in Section 3.2.4 for VFSRI, the resonant frequency f_r is utilized as a reference for that study. In case of CFPRI, the resonant frequency differs from the frequency at which the phase-shift between current and voltage is zero. This is why the frequency chosen as a reference for this section is f_{phase0}. However, both frequencies, f_r and f_{phase0}, are practically equal for high Q values.

Commutating at zero phase-shift ($f_{sw} = f_{phase0}$)

Figure 3.26 shows the corresponding sequence considering that the inverter is commutating at zero phase-shift between current and voltage, that is at f_{phase0}. The commutation, illustrated by the gate signals, occurs when the voltage is crossing zero. Observing the voltage across $SW1$ and $D1$, the voltage is supported by switches half of the cycle while they are turned-off, whereas diodes are always forward-biased.

Under these circumstances, there are just two possible states. The first is when $SW1$ and $SW4$ are conducting and the second when $SW2$ and $SW3$ do. Considering the overlapping of switches in current-fed converters,
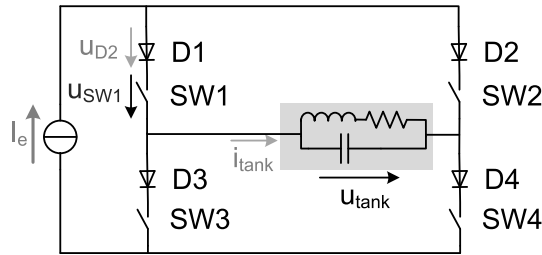
Figure 3.25: CFPRI circuit and variables studied.
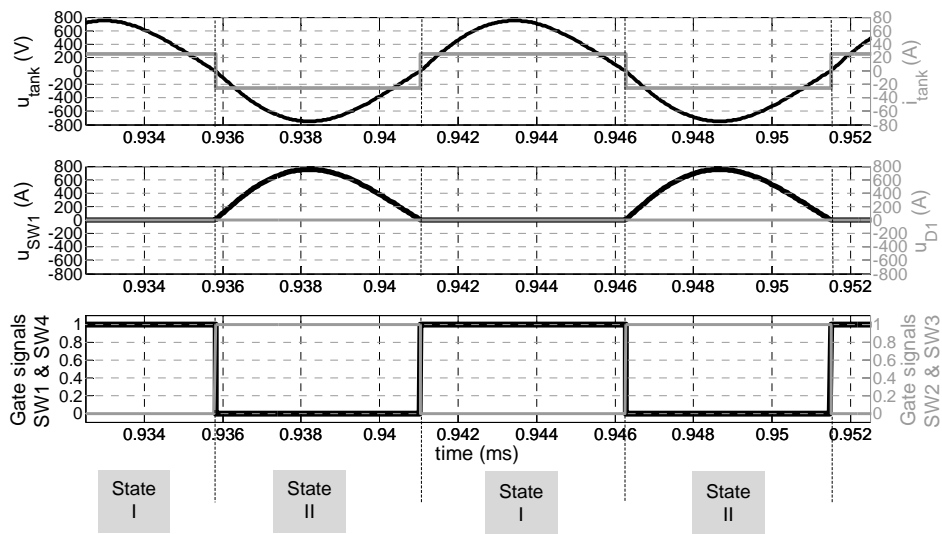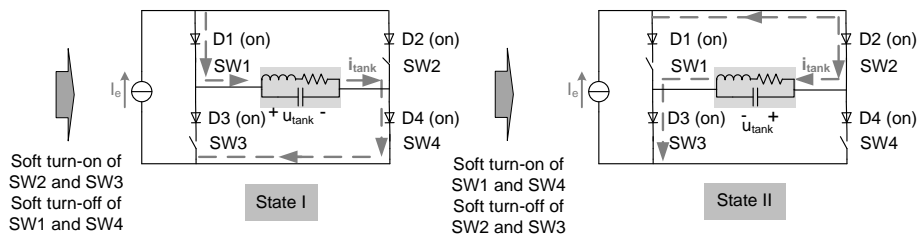
Sequence of events

Figure 3.26: Output waveforms and sequence of events commutating at zero phase-shift switching ($I_e = 25\ A$, $R_{eq} = 1.58\ \Omega$, $L = 9.78\ \mu H$, $C = 0.26\ \mu F$, $f_{sw} = f_{phase0} = 96.63\ kHz$).

$SW1$ and $SW4$ turn-off is preceded by $SW2$ and $SW3$ turn-on, contrarily to VFSRI.

Regarding losses, this case has very few losses because the commutation is realized when the current and voltage are zero. Nevertheless, the probability of being at this frequency during a long period is low and other cases have to be studied.

Capacitive switching ($f_{sw} > f_{phase0}$)

In Figure 3.27, the waveforms and the corresponding sequence of events are shown for the case of switching above f_{phase0}. Observing this figure, the current advances the voltage and so that this type of commutation is also known as capacitive switching. This relation between frequency and current and voltage phase-shift can also be observed in the Bode diagram, shown in Figure 3.18 in Section 3.3.1. It is worth noticing that contrarily to this case, in case of VFSRI, capacitive switching occurs when commutating below resonance.

Under these circumstances, diodes are blocking between the commutation and the change of polarity of u_{tank}. During this period of the time, the voltage is shared between switches and diodes. This can be observed in Figure 3.27, where the sum of voltages in $SW1$ and $D1$ is equal to u_{tank}.

Analyzing the sequence of events of Figure 3.27, in State I the current i_{tank} is first conducting through $SW1$ and $SW4$. Then, $SW2$ and $SW3$ are turned-on while the voltage u_{tank} is still positive. Diodes $D1$ and $D4$ are forced to block (off state), due to u_{tank}, and i_{tank} conducts through $SW2$ and $SW3$ (State II). Afterwards, $SW1$ and $SW4$ are turned-off with ZCS because their series diodes are blocked (State III). Finally, u_{tank} changes polarity and diodes $D1$ and $D4$ are forward biased (on state) with ZVS (State IV). States V and VI are similar to States II and III, but with the opposite switches and diodes.

In this case, diodes' turn-off and switches' turn-on are hard, but the turn-on of diodes and the turn-off of switches are soft. Similarly to the capacitive switching in VFRSI, this situation has to be avoided, otherwise antiparallel diode's recovery currents can create large peak voltage spikes.

Inductive switching ($f_{sw} < f_{phase0}$)

Figure 3.28 shows the waveforms and the corresponding sequence of events for the case of switching below f_{phase0}. In this case, this switching is called
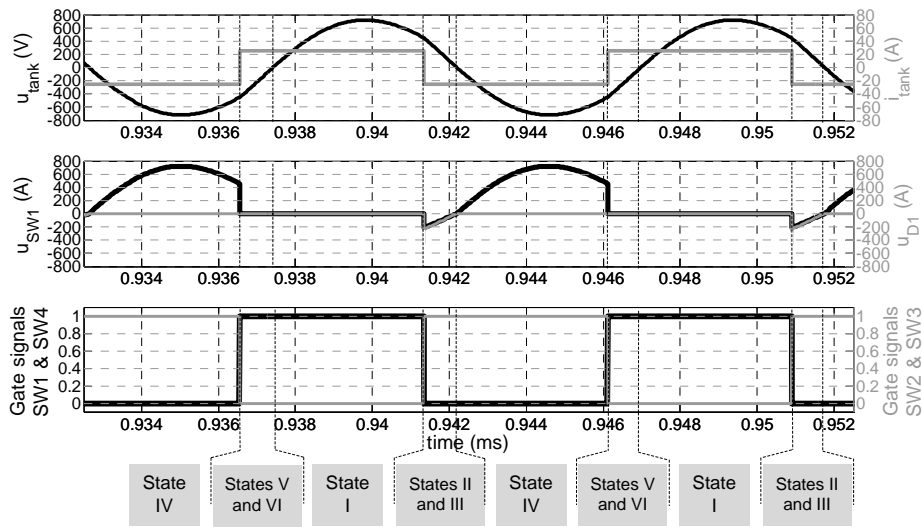
Sequence of events
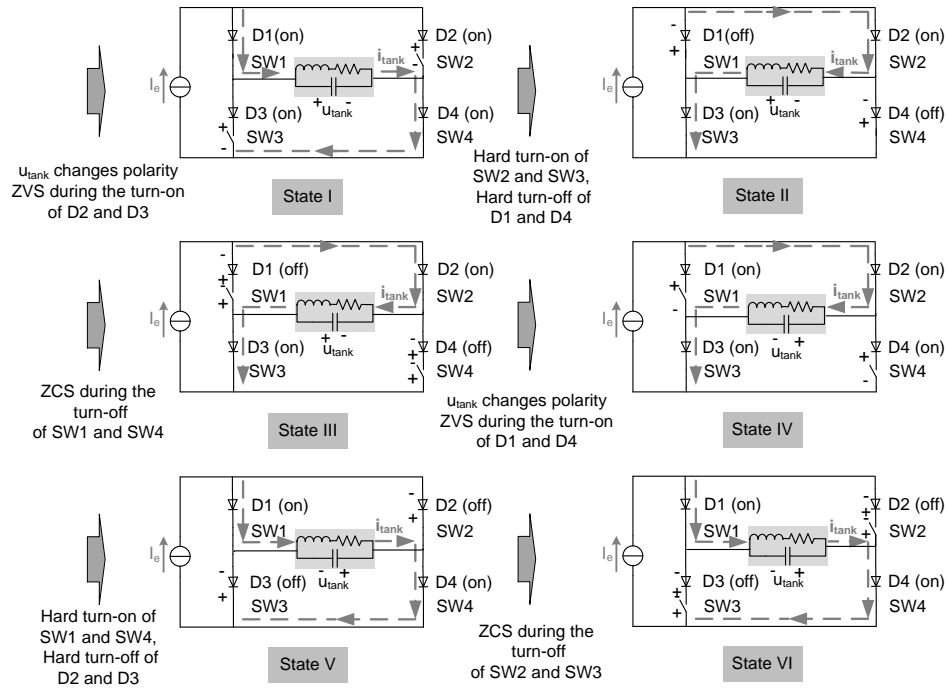
Figure 3.27: Output waveforms and sequence of events commutating above zero phase-shift frequency ($I_e = 25\ A$, $R_{eq} = 1.58\ \Omega$, $L = 9.78\ \mu H$, $C = 0.26\ \mu F$, $f_{sw} = 104.63\ kHz$, $f_{phase0} = 96.63\ kHz$).
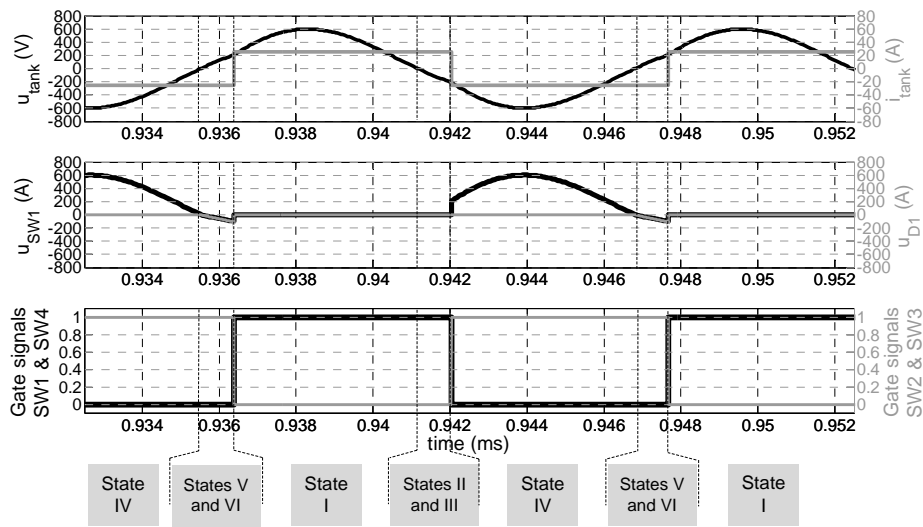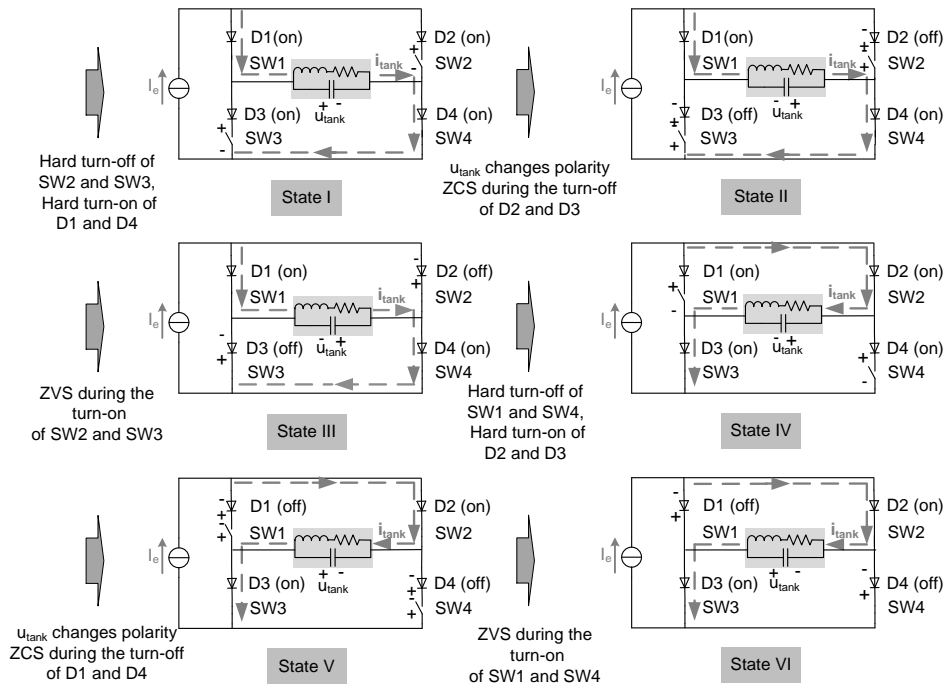
Sequence of events

Figure 3.28: Output waveforms and sequence of events commutating below zero phase-shift switching ($I_e = 25$ A, $R_{eq} = 1.58$ Ω, $L = 9.78$ μH, $C = 0.26$ μF, $f_{sw} = 104.63$ kHz, $f_{phase0} = 96.63$ kHz).

inductive because the voltage advances the current. It has to be noted that, in case of VFSRI, the inductive switching takes place when commutating above resonance.

Similarly to capacitive switching, diodes are blocking during a part of the period although, in this case, the blocking occurs between the change of polarity of u_{tank} and the commutation.

Observing the sequence of events in Figure 3.28, the current i_{tank} is conducting through $SW1$ and $SW4$ in State I. Then, u_{tank} changes polarity, blocking $D2$ and $D3$ with ZCS because their switches in series are not conducting (State II). After this, $SW2$ and $SW3$ are turned-on with ZVS because their series diodes are blocking (State III). Finally, $SW1$ and $SW4$ are turned-off, causing the forward-biasing of $D2$ and $D3$ (State IV). States V and VI are similar to States II and III, but with the opposite switches and diodes.

Contrarily to the previous case, diodes' turn-on and switches' turn-off are hard, but the turn-off of diodes and the turn-on of switches are soft. Thus, in case of not considering the parasitic components, inductive switching is better than capacitive because problems derived from the hard turn-off of antiparallel diodes are avoided.

It has to be noted that the conclusions extracted during this section are valid for the ideal assumptions realized. However, under real circumstances, there are more considerations that have to be taken into account. With regards to this considerations, Section 3.3.5 considers a more realistic situation with parasitic inductances and overlapping-time.

3.3.5 Additional considerations

For the time being, an ideal circuit without any parasitic components and neglecting the overlapping-time has been assumed and it has been proven that inductive switching improves converter's performance. However, in case of considering parasitic inductances and overlapping-time, this conclusion is not correct.

During previous sections, it was assumed that the path for current source I_e was always closed. However, in real installations, some fail in switches can lead to their opening, causing an overvoltage that can damage the converter severely.

Among the many considerations that can be realized regarding CFPRI, in this section just two remarkable considerations are done. The first, regard-

ing the influence of the parasitic inductances and overlapping-times during commutation and, the second, regarding the overvoltage protections of CF-PRI.

Commutation sequence considering parasitic inductances and overlapping-time

In Section 3.3.4, the different sequences of events for an ideal CFPRI were presented. The conclusion was that inductive switching (switching below f_{phase0}) improves the operation of the inverter because avoids the reverse recovery currents of diodes, but this fact changes when the parasitic inductances and the overlapping-time are taken into consideration.

The electrical scheme for a CFPRI considering the parasitic inductance L_p is shown in Figure 3.29. This inductance represents the sum of the parasitic inductances of the switches, diodes and connections.

Bearing in mind the transition between State III and IV for inductive switching, in Figure 3.28, the current changes polarity due to the hard turn-off $SW1$ and $SW4$. In case of having a parasitic inductance L_p, this current variation generates a voltage between its terminals. The problem is that this voltage is added to u_{tank} and increases the voltage at switches, situation that can lead to the destruction of the semiconductors.

In case of capacitive switching, the parasitic inductances also affect the switching process. Observing the transition between States I and II in Figure 3.27, but considering L_p, the voltage at the inductance's terminals opposes to the voltage u_{tank}. Thus, commutating at capacitive switching provides a more reliable operation of the inverter if considering L_p. Although diodes' reverse recovery currents are still a problem, capacitive switching is preferred in CFPRI.

To have soft-switching in diodes' turn on and switches' turn-off in capacitive switching when considering parasitic inductances and overlapping-time, the following sequence is needed (Figure 3.30):

1. Switches $SW1$ and $SW4$ turn-on. This commutation can be realized with ZVS depending on the value of L_p, whose voltage can block the series diodes.

2. The current i_{tank} diminishes and the parasitic inductance L_p changes the voltage polarity to maintain the current.
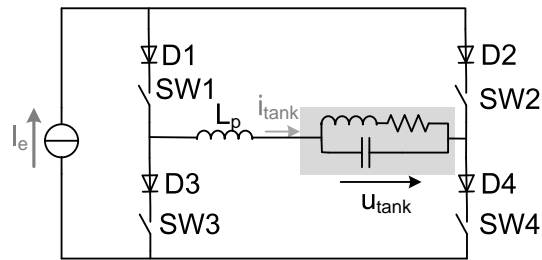
Figure 3.29: CFPRI considering parasitic inductances L_p.
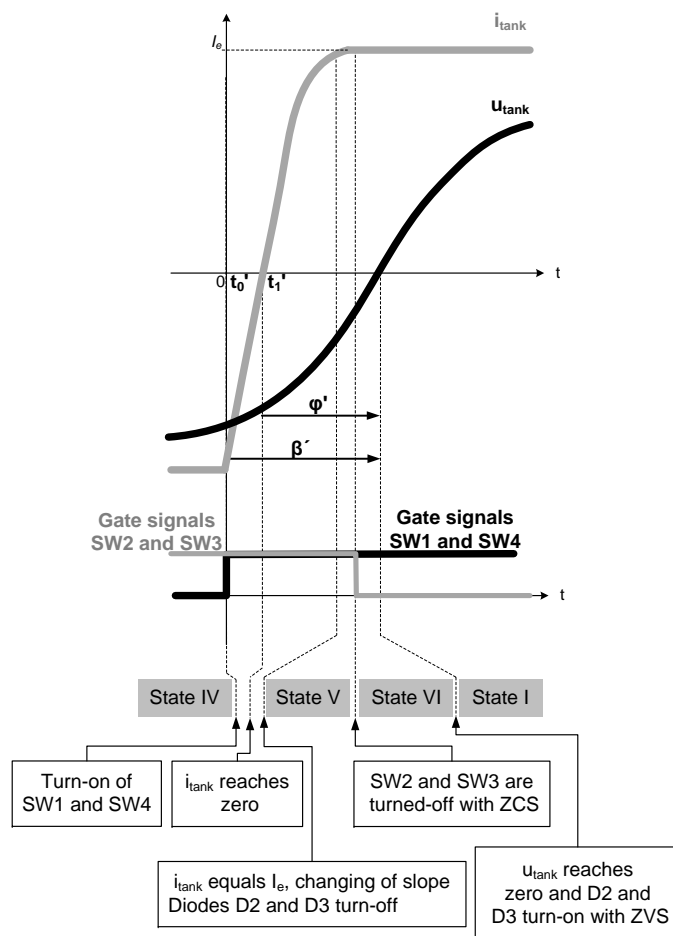
Figure 3.30: Output waveforms and sequence to have ZCS and ZVS commutating at capacitive switching.

3.3 Current-fed parallel-resonant inverters

3. The current i_{tank} equals I_e, the voltage across the inductance L_p is almost zero and diodes $D2$ and $D3$ are blocked due to u_{tank}.

4. Switches $SW2$ and $SW3$ turn-off with ZCS because their series diodes are blocked.

5. The voltage u_{tank} changes polarity, forward-biasing $D2$ and $D3$ with ZVS.

Observing Figure 3.30, it is seen that ZVS and ZCS conditions do not always occur. For example, if the overlapping-time is low, $SW2$ and $SW3$ are turned-off before i_{tank} has reached I_e and there is not ZCS. Another example is the case where the phase-shift between current and voltage is low and the voltage changes polarity before $SW2$ and $SW3$ have turned-off. In this case, there is neither ZVS nor ZCS.

The combination of L_p, voltage, phase-shift and dead-time determine if soft-switching can be reached or not. Different combinations of these parameters and the resulting output waveforms are shown in [37] and more in detail in [8]. A brief resume and the basic equations, including those shown in this section, are found in Appendix C. Considering this, the conditions to obtain the correct sequence described above are:

$$\beta' \geq arccos\left[1 - \frac{2I_eL_p\omega}{\hat{u}_{tank}}\right] \tag{3.48}$$

and

$$\varphi' \geq arccos\left[1 - \frac{I_eL_p\omega}{\hat{u}_{tank}}\right] \tag{3.49}$$

where (see Figure 3.30)

- β' is the phase-shift between the instant at which the gate signal of the switch becomes high and the moment at which u_{tank} changes polarity.

- φ' is the phase-shift between i_{tank} and u_{tank}.

- $\hat{u}_{tank}$ is the amplitude of u_{tank}.

- I_e is the current of the DC source, as shown in Figure 3.29.

- L_p is the sum of the parasitic inductances.

Although diodes' reverse recovery currents are still a problem at capacitive switching, they are minimized when commutating with the optimum process described above, as the current in the diode and the blocking voltage u_{tank} are almost zero when is blocked. In fact, [37] suggests commutating when i_{tank} reaches 90 % of I_e to avoid diodes' reverse recovery currents. Under these circumstances, [38] shows that the series diodes can be avoided because the parasitic inductance blocks the capacitor's voltage. However, the problems derived from any imprecision in the control can destroy the semiconductors.

Similarly to VFSRI, a control based on the optimum switching presented above for CFPRI is limited because of its complexity. Moreover, in case of high β' and φ' values, a more reactive power and frequency are needed, increasing inverter losses [39]. Nevertheless, understanding the commutation procedure allows authors to improve the design and control of IH systems.

Overvoltage protection

In case of CFPRI, overvoltage can occur if the current circuit feeding the inverter is opened, for example if a semiconductor fails and opens. This opening can cause an overvoltage and originate a chain reaction destroying part of the converter. To avoid it, active crowbar systems appear in figures of some articles concerning IH applications, like in [40] and [41].

Due to the speed required for these protection systems, some authors suggest adding capacitors to withstand and retard the first voltage peak, like in [42] and [8, p. 184]. These capacitors permit more time for the activation of a second and more powerful active protection system. This second protection system is usually a switch connected to a resistor that burns the energy stored in the inductance feeding the CFPRI. There are very few authors that have written about this topic, although it is important because of the speed of this failure and the destruction than can cause.

Bearing in mind the importance of reliability in industrial applications, another important fact when considering overvoltage protection in CFPRI, is the need of special drivers for semiconductors. Since most commercial converters in medium power applications are nowadays voltage-fed, most drivers incorporate their protections systems. Thus, most medium power commercial drivers incorporate protection systems in which the driver turns-off the switch in case of short-circuit. Using these drivers in CFPRI can cause the undesired opening of the current path and the destruction of semiconductors.

Therefore, CFPRI tends to use customized drivers, increasing the designing time of the converter.

3.4 Other configurations

Although VFSRI and CFPRI are the basic configurations used in IH applications, there are plenty of variations based on them. This chapter provides a brief and introductory overview of different configurations existing in this area and a primary bibliography on them.

First, in Section 3.4.1, systems based on three element tanks are introduced. Next, in Section 3.4.2, converters using transformers to match the load with the inverter are explained. Afterwards, in Section 3.4.3, converters without a DC/DC intermediate stage to control the power and the different power control techniques are presented. Then, in Section 3.4.4, converters based on parallel and series connections of basic inverters are introduced. Finally, in Section 3.4.5, some special applications like dual frequency inverters or multiload inverters are presented.

3.4.1 Inverters with three element tanks

Series and parallel tanks and their associated inverters have some drawbacks that have led to the investigation of other topologies. In case of VFSRI, the current in semiconductors is the same than in the load, which implies the need of a matching transformer between inverter and load, increasing the cost of the system and decreasing the efficiency. In case of CFPRI, the current in the inverter is Q times lower than in the inductor, but the inverter is current-fed. This makes difficult the use of commercial equipments due to the overvoltage protection systems needed. Moreover, the cable between converter and tank is critical due to the parasitic inductance that limits the distance between them. In order to overcome these limitations, IH systems with three element tanks have been developed.

There are several possibilities concerning tanks with three elements, but the most popular is the LCL (also called LLC), because it has some advantages compared to VFSRI and CFPRI. It is not the aim of this section to provide a deep view on this structure, but some of the main characteristics and advantages are described below. The information exposed during this section is extracted from [39, 43–46] and specially from [9] and [47].

An LCL tank is a parallel tank with an inductance L_s in series, as shown in Figure 3.31. LCL systems are the natural evolution of the parallel and series

tanks. They use voltage-fed inverters, providing the benefits of commercial devices and protection systems, and the current in semiconductors is lower than in the inductor, like in CFPRI. Other topologies with three elements have also been studied, but they do not provide any remarkable advantage compared to classical systems, as explained in [28, pp. 70–77].
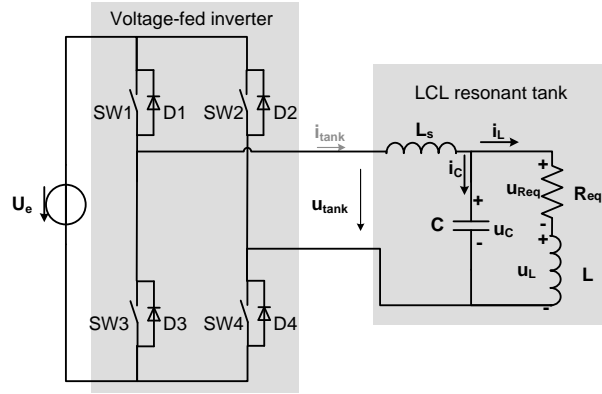
Figure 3.31: Voltage-fed inverter with an LCL tank.

The impedance of an LCL tank can be calculated using Laplace transformation, obtaining the following equation

$$Z_{lcl}(s) = \frac{U_{tank}(s)}{I_{tank}(s)} = \frac{s^3 L_s LC + s^2 L_s R_{eq} C + s(L_s + L) + R_{eq}}{s^2 LC + sCR_{eq} + 1} \qquad (3.50)$$

The Bode analysis of Equation 3.50 is shown in Figure 3.32. It can be observed that there are two resonant frequencies, f_{rp} and f_{rs} . The frequency f_{rp} is equal to the resonant frequency of the parallel circuit and f_{rs} is the resonant frequency of the union with L_s. Usually, converters with an LCL tank commutate slightly above f_{rs}.

Regarding the phase-shift between voltage and current, it has to be noted that, depending on the values of resistance, capacitance and inductance, the system can be capacitive between f_{rp} and f_{rs}. In the case shown in Figure 3.32, it is observed that the impedance is always inductive.

LCL tanks have several advantages, basically that the converter is voltage-fed and the current in the heating inductor i_L is approximately L_s/L times the current i_{tank}. However, these tanks have also some disadvantages.

As can be observed in Figure 3.32, the phase-shift between voltage and current at the resonant frequency f_{rs} is not zero. Thus, there are more
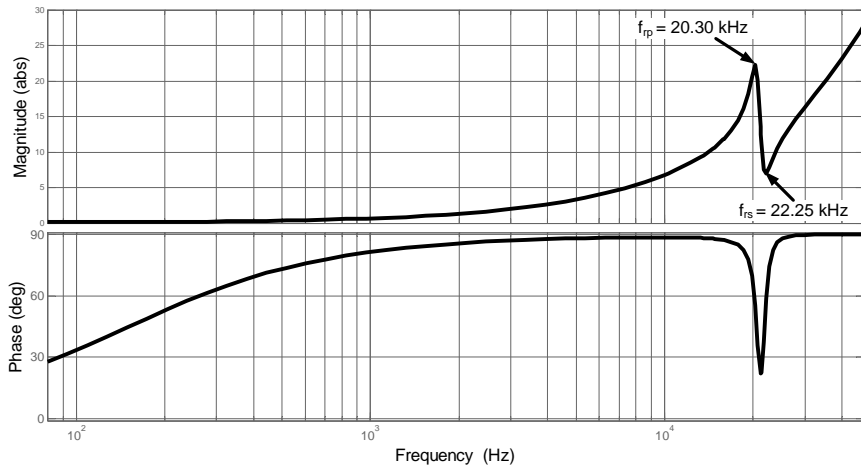
Figure 3.32: Bode analysis of the transfer function $Z_{lcl}(\omega)$ with $R_{eq} = 0.1$ $m\Omega$, $L = 9.78$ μH, $L_s = 95.37$ μH, $C = 6$ μF and $Q = 10.75$.

commutation losses and the converter provides reactive power during normal operation, increasing the current in semiconductors. Another important drawback is that this phase-shift is nor constant neither monotonous and this makes the control of the system more complicated.

To avoid a high reactive power during normal operation, the phase-shift between voltage and current at resonant frequency f_{rs} needs to be minimized. From [47], the phase-shift at resonant frequency is equal to

$$\varphi_{lcl}\left(\omega_{rs}\right) = arctan\left(\frac{L_s/L + 1}{Q}\right) \tag{3.51}$$

To minimize the phase-shift φ_{lcl}, the ratio L_s/L has to be decreased, but the decrease of L_s/L results in a decrease in the current gain between i_L and i_{tank}. To overcome this problem, the quality factor Q needs to be high, in [47] is supposed higher than 6. Under these circumstances, L_s/L can be high and maintain the current gain, while φ_{lcl} is low. Moreover, for high Q values, the system can be controlled by the phase-shift between u_{tank} and u_c, which is monotonous and approximately 90º at f_{rs}.

Another important advantage of LCL tanks is the short-circuit immunity thanks to the inductive behavior of the load [47]. Short-circuits caused by the workpiece and the inductor are common in IH applications. In a short-circuit, the equivalent inductance and resistance diminish and the res-

onant frequency increases suddenly, while the commutation frequency remains constant. Under these circumstances, the first commutations can be capacitive or inductive, depending on the conditions. CFPRI requires overvoltage protection systems to avoid semiconductor's destruction, as explained in [8, pp. 171–186]. For the case of VFSRI, the problem is within the capacitive switching and the reverse recovery currents of diodes. In [28], this problem is deeply investigated for MOSFET inverters, proposing a configuration that annuls the antiparallel diode like in Figure 3.16 in Section 3.2.5. For LCL, a special control that ensures commutations without capacitive switching is used in [47]. This control technique does not allow the switches commutate while current is flowing through their opposite switches' antiparallel diodes. These authors explain that LCL improves VFSRI's performance against short-circuits because, using this control technique, LCL system can continue without disconnecting the converter. In case of a VFSRI and using a similar technique, in [28, pp. 271–276] the converter has to be stopped because, even though the first capacitive commutations can be avoided, at low frequencies the commutations are capacitive.

This advantage has special interest in applications like tube welding, where short-circuits occur often during normal operation for short periods of time. However, it has to be noted that VFSRI have proven to be robust to short-circuits by adding fast diodes to MOSFETs. Moreover, IH companies like EFD Induction$^{\circledR}$ have converters using IGBTs for tube welding with technical specifications explaining their operation under short-circuits.

In [28, p. 76] the main drawbacks of LCL tanks are exposed, explaining that the inclusion of L_s adds more losses to the system due the parasitic resistances and that a transformer is usually required. However, this topology can be useful for certain applications with high Q values. For example, it can be suitable in case of high frequencies, where L_s can be a small air inductor. An interesting discussion about this topology and the design for different applications is found in [47]. During these designs, a minimum and a maximum Q value is considered. This is because the system changes during a heat treatment and all the possible cases have to be considered. Therefore, finding a global solution using LCL tanks can be difficult in case of needing to work with different workpieces.

3.4.2 Converters with matching transformers

In Section 3.2.5, the need of a matching transformer between the VFSRI and the resonant tank was introduced. In case of VFSRIs, the transformer is

generally necessary to avoid high currents in semiconductors. However, these transformers are also used in other topologies to match the load requirements with the converter's specifications.

There are two main groups of matching transformers, the active power transformers and the reactive power transformers. In Figure 3.33 both types of transformers and their combinations are shown. The figures shown refer to a series resonant tank, but both types of transformers are used in parallel, LCL or other resonant tanks.
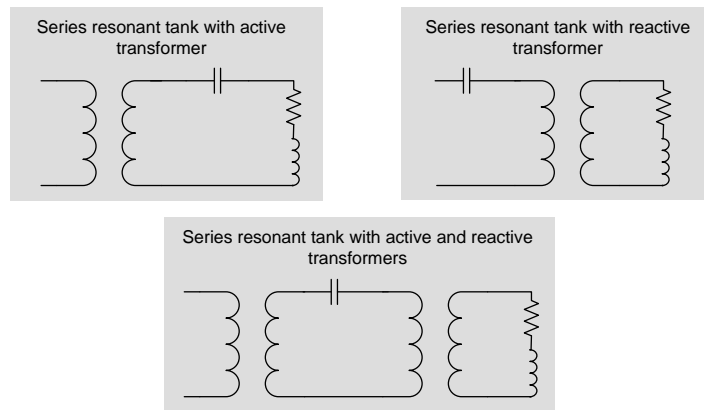
Figure 3.33: Series tank with matching transformers.

In case of active power transformers, the power transferred from the primary to the secondary is just active power. The aim of this transformer is to increase the total impedance seen by the inverter and decrease the current in semiconductors. Supposing an ideal transformer with a transfer ratio equal to i and referring the resonant tank to the primary as shown in Figure 3.34, the impedance is equal to

$$Z'_{tank} = i^2 Z_{tank} \tag{3.52}$$

Thus, the impedance is i^2 higher, decreasing the current and the losses in the primary. For example, in case of VFSRI, the load seen by the converter is equal to $i^2 R_{eq}$ and the power transferred for the transformer at resonant frequency is just active power.

In case of reactive power transformers, the power transferred from the primary to the secondary is reactive. Supposing an ideal transformer with a transfer ratio equal to i and referring the resonant tank to the primary as shown in Figure 3.35, the resonant frequency is equal to

$$f'_r = \frac{1}{2\pi\sqrt{L'C'}} = \frac{1}{2\pi\sqrt{Li^2C}} = \frac{f_r}{i} \tag{3.53}$$

and the quality factor

$$Q' = \frac{2\pi f'_r L'}{R'_{eq}} = \frac{2\pi \frac{f_r}{i} Li^2}{R_{eq}i^2} = \frac{Q}{i} \tag{3.54}$$

In this case, the frequency and the quality factor are i times lower. These type of transformers are used in low impedance inductors, as in the case of coils with few turns, and low frequencies.
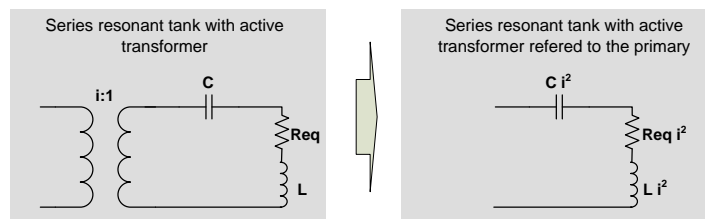
Figure 3.34: Series tank with active transformer referred to the primary.
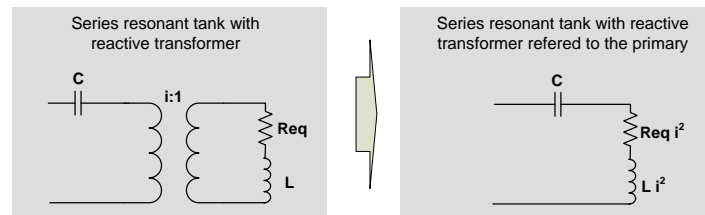
Figure 3.35: Series tank with reactive transformer referred to the primary.

By adding a reactive power transformer, the capacitance and the current conducted by the capacitors is decreased. For example, in case of a VFSRI, the impedance at resonant frequency is also equal to $i^2 R_{eq}$, so that the current in the inverter is also decreased. One of the drawbacks of these transformers is the high reactive power conducted through them, as being Q times the active power of the application. Thus, for a 10 kW application with a quality factor of 5, the transformer has to be at least of 50 kVA.

Another important drawback of using active or reactive power transformers is the decrease in efficiency. It is also very important to take into account

their parasitic inductances, resistances and capacitances depending on the application and the frequency. However, it has to be noted that these transformers have been improving during the last decades and, at the moment, they parasitic inductances and resistances are low and their efficiencies are over 95 %.

In any case, the best proof of transformers' usefulness is that nowadays matching transformers are widely used in IH applications. For example, a series resonant tank and active transformers can be found in [28, 35, 40, 48–56]. Some examples with reactive transformers and series tanks are [57–59] and with parallel tanks and reactive transformers are [60–62]. In [47] an LCL tank with active transformer, reactive transformer and with a combination of them is explained.

There are various specific companies developing matching transformers for IH applications, being two of the most well-known CELEM and Jackson Transformers, and some not so specific, like STS. Most of them provide different taps to vary the transformer ratio. For a better knowledge in the design of these transformers, [2, pp. 656–673] provides a short overview on the materials and core shapes used.

3.4.3 Converters without intermediate power control stage

In previous sections it was assumed that the inverter was commutating near resonant frequency with a 50 % of duty-cycle. Under these circumstances, the power supplied to the workpiece is controlled by means of a variable DC source. Traditionally, a conventional thyristor bridge rectifier has been used to obtain these variable DC source, as shown in Figure 3.36 in Case 1. However, this implies an increase in cost and size of the converter due to the six controlled thyristors and the low frequency inductance needed. At this moment, this topology is only employed for high power converters above hundreds of kVA.

Other solutions with reduced cost and complexity have been developed to have a variable DC source, as for example a diode rectifier with a DC/DC converter, shown in Figure 3.36 in Case 2. In this case, a DC/DC structure with just one switch like a buck converter can be used. However, the inclusion of this DC/DC intermediate stage decreases the efficiency of the overall system until values typically between 70 to 90 %. It has to be noted that, in case of CFPRI with a structure like in Case 1 in Figure 3.36 using thyristors, the choke feeding the inverter has to be high to maintain the current constant, increasing the size and cost of the equipment. In case of

using a DC/DC converter working in current operation mode, it is possible to decrease its value by increasing the commutation frequency.
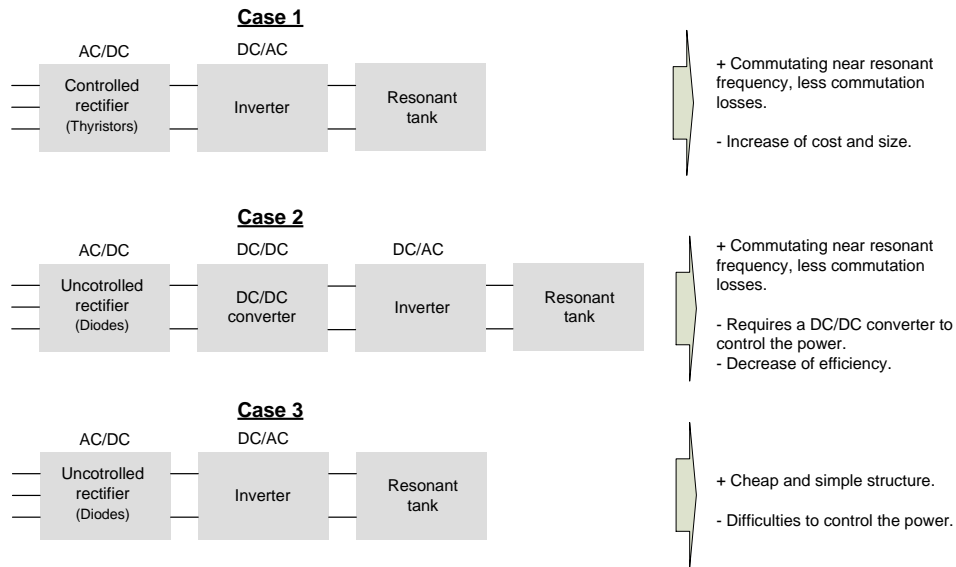
Figure 3.36: Converter topologies depending on the power control technique.

Other solutions for controlling the power, by using simpler and cheaper structures, are those based on an uncontrolled rectifier and an inverter, as shown in Figure 3.36 for Case 3. The problem of this structure is that the voltage and current are constant at the input of the inverter, so another power control technique is needed. The most common power control techniques for this converter, as exposed in [48], are:

- *Frequency regulation*: The inverter is commutating at 50 % of the duty-cycle and the frequency is controlled by varying the commutation frequency. At resonant frequency the power is maximum, so, when moving away from this frequency the power decreases.

  The problem of this control technique is that out of resonant frequency, the phase-shift between current and voltage is not zero. Therefore, the inverter has to supply reactive power, increasing the current in semiconductors and the losses due to the parasitic resistances. Moreover, it is not possible to commutate with soft-switching and the commutation losses increase.

- *Pulse width regulation*: Another technique for controlling the power is by maintaining the frequency near to the resonant frequency, but varying the width of the pulses. Under these circumstances, the maximum power is obtained when the inverter is commutating with 50 % of duty-cycle for an H-bridge inverter.

  In this case, the power factor is higher than in the previous one, but there are still high commutation losses due to hard-switching, as the current and voltage are not zero when the commutation occurs. An example of this type of control is found in [63].

- *Pulse width and frequency regulation*: This power control technique is similar to the previous solution, but varying the frequency to allow a wider range of ZVS during the turn-on. The main drawback of this technique is the reactive power supplied by the converter during normal operation. An example of this strategy can be found in [64].

The main drawbacks derived from these control techniques for the case of an uncontrolled rectifier with an, inverter are the commutation losses and the reactive power. In order to overcome these problems, a series of power control techniques based on pulse density modulation (PDM) have been presented in [48, 56, 65].

PDM is a power control technique that consists in controlling the power by suppressing some of the pulses of the inverter. An example of this commutation strategy for a VFSRI is shown in Figure 3.37. In this figure three power levels are represented, P_1, P_2 and P_3. In P_3, the power supplied to the load is maximum and in the other cases there are some pulses suppressed and, thus, the power supplied is lower. The advantages of this power control technique, as compared with the others, is that the inverter is commutating proximal to the resonant frequency and the reactive power and commutation losses are minimum.

In [48] is demonstrated that the power supplied to the load is approximately equal to

$$\lim_{\tau \to \infty} P = P_{max} \left(\frac{T_{ON}}{T_{PDM}} \right)^2 \tag{3.55}$$

and

$$\lim_{\tau \to 0} P = P_{max} \frac{T_{ON}}{T_{PDM}} \tag{3.56}$$
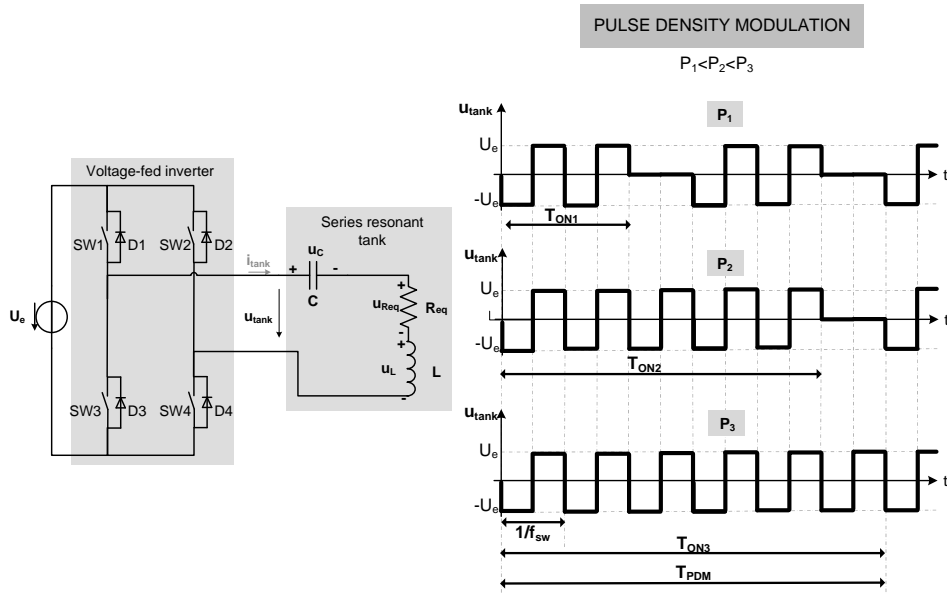
Figure 3.37: VFSRI with PDM power control technique.

with

$$\tau = \frac{2Q}{2\pi f_r} \tag{3.57}$$

being P_{max} the maximum power, obtained when T_{ON} is equal to T_{PDM} (see Figure 3.37). Regarding this control technique, in [66] an asymmetrical pulse width modulation is presented. The difference with PDM is that there are more intermediate power stages because the voltage u_{tank} can be asymmetric with just half of the period suppressed. In this case, it is necessary to pay attention the saturation of the matching transformer.

Although PDM is advantageous compared to classical methods in terms of efficiency, as shown in [65], it has some drawbacks that limit their widespread in industrial equipments, resumed in [28, p. 110] for the same authors. One of these limitations is that the power levels are not continuous, fact that can lead to a non-homogeneous heating of the workpiece. In addition, the definition of the power levels supplied by the converter is not an easy task and, in case of low Q values and low power densities, the power calculation as a function of the pulse density is not obvious. Furthermore, special attention has to be taken in the DC-link design and the input inductors, to avoid

voltage fluctuation and high harmonic content in the mains, as explained in [67].

The power discontinuity in PDM has to be more studied regarding continuous wire heating. For example, in case of using a converter supplying low power to a wire with high velocity, the frequency and the dynamics of the power control have to be high to avoid non-homogeneous heating. In any case, PDM has a great scientific and industrial interest and a proof of that is the recent work developed by [65] for industrial purposes and [68] for cooking applications.

3.4.4 Converters based on series and parallel connection of inverters

In IH, there are some converter structures based on the operation of several basic converters connected in parallel or in series. The aim of this connection is diverse, some authors use converters' parallelization or serialization to increase the power, others to obtain two frequencies at the output and others to reduce the voltage or current stress in semiconductors.

Most of these converters in the bibliography are voltage-fed and have an H-bridge or a half-bridge topology as a fundamental unit. The connection in series or in parallel of two H-bridges leads to the converters shown in Figure 3.38. A revision of the different inverters in IH based on the connection of H-bridges can be found in the next chapter in Section 4.2.2.
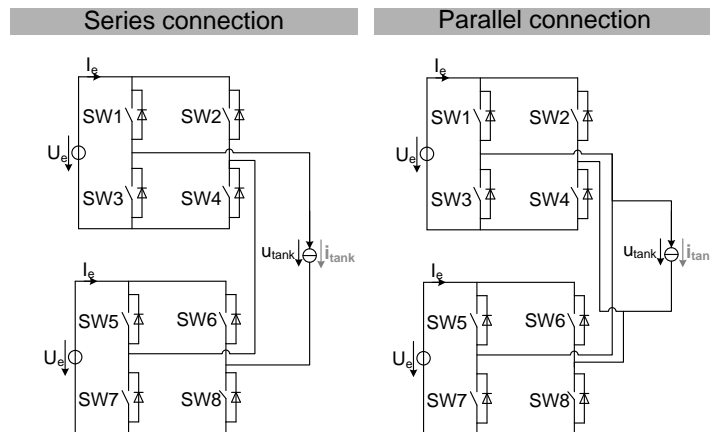
Figure 3.38: Parallel and series connection of H-bridges

3.4.5 Special applications

IH is used in many different fields and a huge variety of solutions have been developed depending on the application. The quantity of converter topologies and tanks found for these different applications, makes difficult to realize a complete review on them. In this study, just the most common structures used in continuous wire heating have been presented. However, there are many different topologies, tanks and control techniques that are used in other applications and that have not been explained. In this section, a selection of some interesting converters are introduced with the aim of providing a wider overview on IH field.

First, a case requiring multiple inverters with multiple inductors and a single workpiece is presented. Afterwards, dual frequency converters used for heating non-uniform shape workpieces are introduced. Then, inverters with multiple inductors used in cooking applications are briefly explained. Finally, a converter that allows the dynamic variation of frequency without decreasing the current is shown.

Multiple inverters with multiple highly coupled inductors

In most IH applications the converter is usually connected to a unique tank heating a workpiece. However, there are some applications where there is a unique workpiece and there are several inductors fed by different converters.

An interesting application regarding these converter-inductor systems heating semiconductors wafers is found in [69] and [70]. In this application, the control of the temperature is critical to maintain an uniform heating and avoid mechanical stress in the wafers. The reason of using different coils is that it allows passing different currents through them, permitting a better control of the temperature in the workpiece. In Figure 3.39, a simple scheme of the connections of these type of systems is shown.

In the case presented, the inductors are concentric and have high mutual coupling. Under these circumstances, there is power recirculation between coils due to the coupling and it becomes difficult to control the current independently. To avoid a circulating power between coils and improve the control of the currents, a control method based on current phase angle is used. This control method consists in synchronizing the currents instead of voltage waveforms, as shown in Figure 3.39. By controlling the phase-shift of currents, their value can be increased or decreased properly, so that the control of temperature is improved compared to a control with voltage synchronization.
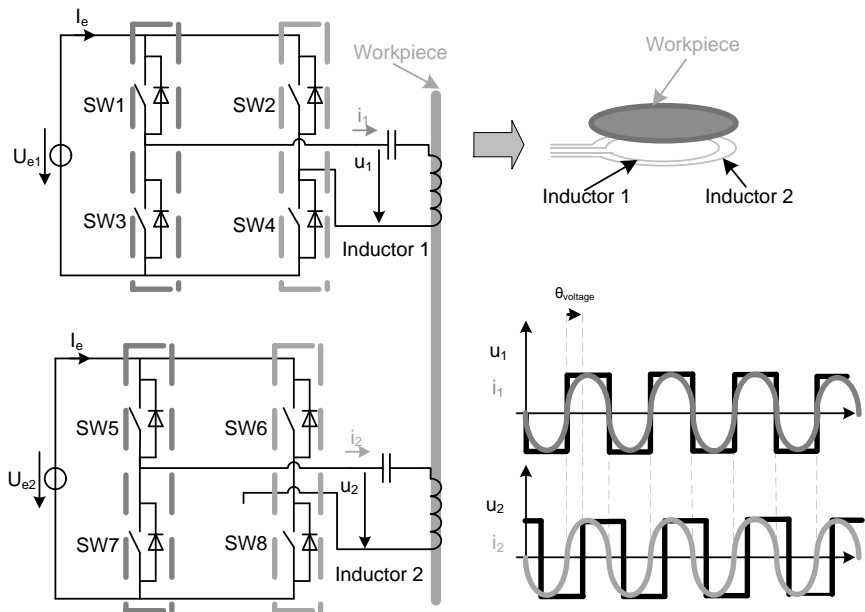
Figure 3.39: Parallel operation of two H-bridges with two highly coupled inductors heating a workpiece.

In case of wire heating, where inductors are not concentric and the temperature homogeneity during the processes is not so critical, this kind of considerations are not usually taken into account.

Dual frequency converters

In case of non uniform shape pieces, as for example gears, the use of two frequencies allows a more uniform and efficient heat treatment. Usually, this heat treatment is done with completely separate systems or with two converters and one coil. Another method presented in [71] is to use one converter and one coil but connecting capacitors and changing the resonant frequency of the tank.

In [72] a unique converter using a unique coil with two resonant frequencies is presented. The tank has 4-elements and two resonant frequencies, which are the heating frequencies. The converter feeding this tank is an H-bridge using a traditional pulse-width modulation technique. In this case, the frequency of the modulating signal is the lower tank's resonant frequency and the frequency of the carrier is the higher resonant frequency. The bene-

87

fits of this system, compared to the traditional ones, is that allows the use of one inductor and one converter, decreasing the cost and allowing both frequencies at the same time.

Inverters with multiple inductors

These converters are considered in this section because they are widely used in IH. Contrarily to the parallel connection of converters for feeding high power loads, these converters are suitable for light loads.

They consist on a unique converter, usually a half-bridge, feeding different inductors. Induction cookers are the most representative application where these converters are used. In these cookers there can be a unique converter supplying power to different burners. Some experiences regarding this kind of converters are explained in [73–76].

In the present study, as the application considered is related to industrial wire heating treatments, where loads usually require much power, these type of structures are not applicable.

Dynamic variable frequency converter

In case of a converter used for different heat treatments requiring different frequencies, it is necessary to vary the resonant frequency of the tank and adapt it to the new frequency. Otherwise, if the resonant frequency of the tank is not changed and the commutating frequency is the new one, the current in the inductor is low and heat would not be generated. Usually, this change of resonant frequency is done manually by means of a change in the capacitance of the resonant tank.

In [77] and [78] a converter that allows a dynamic variation of the frequency while maintaining the current in the inductor is presented. The main advantage of this converter, compared to the traditional ones, is that allows the variation of frequency while the current in the inductor is still high and with no changes in hardware. A scheme of this type of converter is shown in Figure 3.40. It can be observed that it is a current-fed converter, but it has the resonant capacitor connected to the DC-bus. It has to be noted that one of the main drawbacks of this structure is that the current in the load is also conducting in semiconductors. However, this converter is interesting because provides the opportunity of realizing heat treatments with a dynamic variation of the frequency.
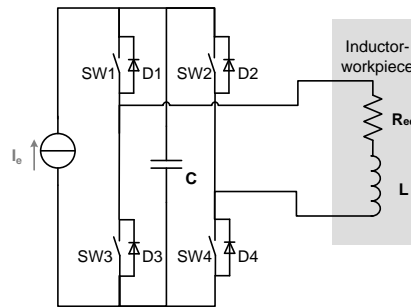
Figure 3.40: Dynamic variable frequency converter.

3.5 Summary

In order to have a high varying current in the inductor and generate heat, most authors tend to use an oscillatory circuit formed by the inductor and a capacitor fed by an converter. In this chapter, the different converter topologies and tanks used in IH applications are revised, focusing on the ones used in applications of continuous wire heating.

The most common converter topologies found in IH applications are the VFSRI and CFPRI. In case of VFSRI, the heating inductor is oscillating with a capacitor in series and the inverter is fed by a constant voltage source. In case of CFPRI, the inductor is connected with the capacitor in parallel and the inverter is fed by a constant current source. In both cases, the power supplied to the workpiece is maximum at the resonant frequency of the oscillatory circuit. Moreover, at this frequency, the phase-shift between current and voltage is zero and, thus, the losses during commutation are lower. Therefore, in an ideal case inverters would usually commutate at resonant frequency, although due to the diode's reverse-recovery or the parasitic components, the inverter commutates above the resonant frequency. This way, the reverse-recovery of diodes is avoided in VFSRI and the overvoltages are avoided in CFPRI. Both topologies have different characteristics, advantages and drawbacks which are summarized in Table 7.1. Due to these differences, these topologies are used for different applications and have led to their actual coexistence.

But the drawbacks found in VFSRI and CFPRI have also caused the development of other topologies based on three element tanks. Between them, the most popular is the LCL because it uses voltage-fed inverters, providing the benefits of commercial devices and protection systems, and because

89

the current in semiconductors is lower than in the inductor. However, this structure also have some drawbacks, like the need of high Q values to avoid high reactive power or the need of an additional inductance. These drawbacks have limited their application to certain cases with high Q values, like high-frequency heating treatments.

Table 3.1: Comparison between VFSRI and CFPRI.

VFSRI	CFPRI
The inverter is fed by a capacitor that maintains the voltage.	The inverter is fed by an inductance that maintains the current.
Dead-time between switches is required to avoid short-circuit.	Ovelap time is required to avoid overvoltage.
Needs short circuit protection.	Has inherent short-circuit capability.
In case of failure all the switches have to be turned-off.	In case of failure all the switches have to be turned-on.
Voltage-fed converters are easily found in medium power applications. Commercial protection circuits can be used in case of short-circuit.	Current-fed converters are usually found for high power applications ($>$ 1 MW). Special protection circuits and drivers are needed in case of overvoltage.
The voltage feeding the tank is a square wave and the current is sinusoidal.	The current feeding the tank is a square wave and the voltage is sinusoidal.
The voltage on the inductor is Q times higher than at the output of the converter, but the current in the tank is the same than in the inductor. Usually a matching transformer is needed between the inverter and the tank.	The current in the inductor is approximately Q times the current at the output of the converter. A matching transformer is not usually required.
High voltage capacitors are sometimes needed for the tank.	High voltage capacitors are not required but more capacitors in parallel are needed.
Switches of the inverter have to be unidirectional in voltage but bidirectional in current. The antiparallel-diode is necessary.	Switches have to be unidirectional in current but bidirectional in voltage. A series diode is needed.
The converter is switching at inductive switching ($f_{sw} > f_r$).	The converter is switching at capacitive switching ($f_{sw} > f_{phase0}$).

Another important element that has solved some of the drawbacks of VFSRI and CFPRI is the matching transformer. These transformers have allowed the widespread of VFSRI by reducing the current in semiconductors,

but they are also used in many applications with different topologies. They can be classified as active power transformers and reactive power transformers.

Regarding the manner of controlling the power supplied to the workpiece, there are different control techniques. One is by commutating the inverter with a 50 % of duty-cycle and controlling the input DC source. In this case, the commutation losses of the inverter are low. However, this DC source is obtained from a thyristor bridge rectifier, increasing the cost and size, or with a DC/DC converter like a buck, which decreases the efficiency of the overall system.

There are other power control techniques that use uncontrolled rectifier, which reduces the cost and complexity of the converter. These techniques are based on controlling the power by varying the inverter's frequency or varying the pulse width. The problems found when using these techniques are the increase of the reactive power supplied by the inverter and the increase of commutation losses. In order to solve these problems but maintain the structure based on an uncontrolled rectifier, PDM techniques have aroused. These techniques are based on the control of the power through the number of pulses supplied to the load, while the inverter is commutating at 50 % of duty-cycle and close to the resonant frequency, thus, decreasing the losses. It has also some drawbacks, like the discontinuity of the power levels or the difficulty to calculate this power at low power levels.

Another important type of converters explained in this chapter are those based on the serialization and parallelization of basic inverters like H-bridges. The aim of serializing basic inverters is to reduce voltage stress in semiconductors and, for example, use MOSFETs in high voltage applications. There are also authors that use this connection for obtaining more frequency at the output. In case of parallelization, the aim is to obtain higher power at the output, but also increasing the frequency at the output which allows, for example, the use of IGBTs in high frequency applications.

In this chapter, the most common topologies, tanks and considerations regarding converters used in wire heating are described. At the end, some special applications are described to provide a wider overview on IH converters. This chapter introduces the concepts used during the work developed in next chapters. Moreover, allows to understand converters' performance, limitations and considerations depending on the structure and the control chosen, that leads to the conclusion that there is not a unique and perfect converter. Every structure has its advantages and limitations, being use-

ful depending on the application or circumstances and requiring a specific analysis for each application.

Chapter 4

Study of a multichannel converter for high-power high-frequency applications

4.1 Introduction

There are many converter topologies and resonant tanks used in IH applications. With regard to this variety, there are converters based on parallel and series connection of basic topologies. The aim of these connections is diverse, being one of them the creation of a basic structure that allows to reach any power at any frequency when implemented repeatedly.

The idea of a converter based on paralleling and serializing basic converter structures is extremely interesting for IH industry. This modularity can produce benefits in terms of maintenance and rapid repairing, which results in increasing the reliability of system. Moreover, in case of failure and with a critical industrial process, these types of structures can allow maintaining the process at half of the power while waiting for a spare part to solve the failure.

In this chapter, this modularity idea is studied for high-power and high-frequency IH converters, in particular for converters in the range of 50 to 500 kVA and 50 to 300 kHz. First, in Section 4.2, the multichannel converter is studied for defining its basic structure. Afterwards, in Section 4.3, a multichannel converter is implemented and finally, in Section 4.4, this chapter is summarized.

4.2 Design of a multichannel converter for induction heating

The underlying idea of the multichannel converter applied to IH field, is the creation of basic hardware structures that are connected in series or parallel to fulfill the converter's specifications. A basic scheme of this concept, which is somehow related to the power electronic building block concept explained in [79], is shown in Figure 4.1. The benefits of this design procedure are the reduction in cost due to a higher volume production, the reduction of engineering effort and time, the reduction of design testing and the reduction of installation and maintenance work.

The principal analysis of the study realized in this chapter is based on the inverter stage and the connection of inverters to form a multichannel converter. First, in Section 4.2.1, some considerations regarding the topology and the semiconductors are given to define the basic structures composing the multichannel converter. Afterwards, in Section 4.2.2, the different inverter topologies based on series and parallel connection of H-bridges are revised. The different connections of H-bridges are studied for the case of the multichannel converter in Section 4.2.3 and, finally, the multichannel converter structure is presented in Section 4.2.4.
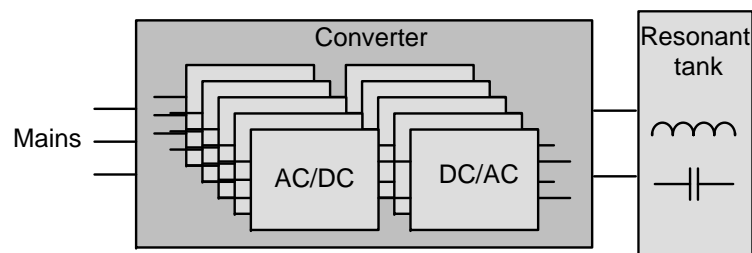
Figure 4.1: Multichannel converter basic scheme.

4.2.1 Preliminary considerations

When considering a converter based on the connection of basic structures, the first step is to define these basic structures. In order to reduce the number of components, it is interesting to eliminate the power control stage between the mains and the inverter, using one of the techniques presented in Section 3.4.3. Taking this into consideration, the AC/DC conversion can be realized with an uncontrolled diode bridge rectifier. With regard to the

4.2 Design of a multichannel converter for induction heating

DC/AC stage, the basic inverter topology used in applications above few kVA is the H-bridge, as shown in Chapter 3.

Concerning the feeding of the H-bridge, there are two possibilities: current and voltage-feeding. In case of a CFPRI, it is possible to increase the power by parallelization. In case of needing an increase of frequency, it is possible to interleave two CFPRI with the output in series. In this case, when one converter is conducting, the other has to be short-circuited. It has to be noted that the use of CFPRI leads to the need of specific drivers and overvoltage protection systems, explained in Section 3.3.5.

In case of VFSRI, commercial devices like drives or power modules with drivers incorporated can be used, benefitting from all the advantages of reliability, flexibility and price reduction. The use of commercial devices is in consonance with the aim of profiting higher volume productions.

With regard to the type of semiconductors used in the H-bridge, IGBTs and MOSFETS are the most commonly used devices in this range of frequency and power. Considering MOSFETs, the main limitation is the maximum power provided by these devices. If a structure without intermediate power control stage is used, the semiconductors have to support at least 800 V because the voltage at the DC bus is 560 V (400 V rectified from the mains).

In case of commercial MOSFETs, as their voltage breakdown increases, the current they can support decreases rapidly. Usually, MOSFETs with breakdown voltages above 600 V cannot conduct more than 60 A at 85 ºC. Moreover, these devices tend to use TO-220, SOT-227 or similar packages, that are more fragile and problematic to manipulate than modules. In addition to these limitations, there are problems derived from using MOSFETs in VFSRIs due to the unwanted turn-on of their parasitic BJTs, as explained in Section 3.2.5. Nevertheless, it has to be noted that new advances in MOS-FETs and the addition of antiparallel FREDFET diodes have substantially reduced this problem.

The problem derived from the use of low power devices can be solved employing high-voltage MOSFETs in parallel or low-voltage MOSFETs in series, but a lot of devices are needed and the cost increases considerably.

The improvement during last years in IGBTs' technology, by reducing the turn-off losses as well as their conduction losses, shown in [80] and [81], make them nowadays a good alternative for IH applications. They allow a higher power density of the converter and, with the appearance of the

Non Punch-Through IGBTs, its parallelization permits increasing the final power up to very high values. This allows a basic structure with fewer components than in case of using MOSFETs. Moreover, power IGBTs are usually encapsulated with modules like D61 or D56, which are better to manipulate, increasing the robustness of the converter.

In any case, it has to be noted that IGBT devices are not exempt of problems and, at the moment, there are some MOSFET manufacturers with commercial 1000 V, 100 A devices with SiC antiparallel diodes and SP6 packages. However, these types of devices are not so common and are more expensive. Therefore, the best choice for the moment is an IGBT-based H-bridge that improves IH converters' performance, volume and cost in this range of power and frequencies.

Considering the comments realized during this section, the converter is formed by two basic structures: a three phases diode rectifier and a voltage-fed H-bridge, as shown in Figure 4.2. With regard to the diode bridge rectifier, this part does not pose much design difficulties, therefore, the following sections are focused mainly in the connection of H-bridge inverters. It has to be noted that in case of high power converters, the diodes can be paralleled and, in case of power values above hundreds of kVA, 12 pulse bridge rectifiers can be used.
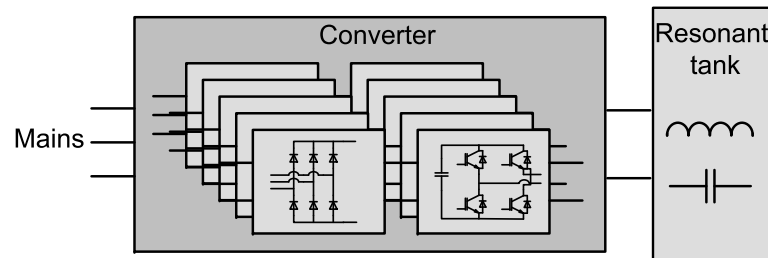
Figure 4.2: Multichannel converter basic configuration.

4.2.2 Revision of inverters based on series and parallel connection of H-bridges

In IH literature, there are several authors using inverter structures based on the parallel or series connection of H-bridges. Some authors use this connection to increase the power, to obtain two frequencies at the output or to reduce the voltage or current stress in semiconductors.

4.2 Design of a multichannel converter for induction heating

In this section, the inverters based on H-bridges series connection are explained first and, afterwards, the inverters based on parallel connection.

Inverters based on series connection of H-bridges

The series connection of H-bridges shown in Figure 4.3 is identical to the topology used in multilevel inverters, specifically known as cascade half-bridge multilevel inverter [82, p. 51]. These types of inverters have been designed to lower the voltage stress in semiconductors for the case of high-voltage applications. The benefits are the use of low-voltage semiconductors with better characteristics and the decrease in the output's harmonic content by using more than two voltage-levels. At this moment, multilevel converters are widely used in high power applications like mining, navy or railways, but they are gaining importance in renewable energies and other fields. In fact, semiconductor manufacturers have packs including these topologies for a wide power range.
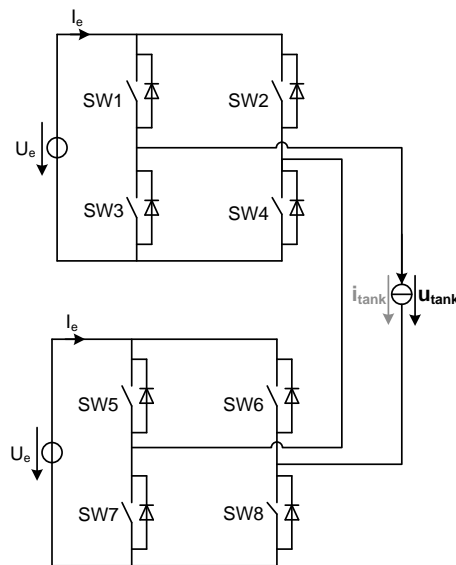
Figure 4.3: Two H-bridge structures connected in series.

In case of IH, some authors like [83] use this topology to reduce the voltage stress in semiconductors. This reduction in voltage stress allows the use of MOSFETs in higher voltage applications and, thus, the construction of high voltage and high frequency converters.

97

The principle of operation of this converter is shown in Case 1 in Figure 4.4. In this figure, the gate signals for switches $SW1$, $SW2$, $SW5$ and $SW6$ are represented. The gate signals of $SW3$, $SW4$, $SW7$ and $SW8$ are not represented, but they are opposite to the previous ones to avoid a short-circuit. The voltages at the output of each H-bridge, u_1 and u_2, are also represented. The underlying idea is to use semiconductors at a voltage U_e, but to obtain a voltage u_{tank} with an amplitude as high as the number of H-bridges forming the converter. In this figure, there are just two H-bridges, thus, the voltage at the output is two times U_e. The voltage u_{tank} is the sum of voltages u_1 and u_2, which are in phase but have different duty-cycles for providing a more sinusoidal shape of u_{tank}. Another author using multilevel structures for the same purpose is [51], in this case with a diode-clamped structure.

Considering Figure 4.4, it can be observed that the shape of the output waveform u_{tank} can be modified by varying the angles θ_1 and θ_2. In [84], this structure is used with the aim of generating an output waveform that contains various frequencies. Observing Figure 4.4 in Case 2, the voltage waveform u_{tank} has a component at the switching frequency f_{sw} and higher harmonic components deliberately created. This waveform is obtained shifting by 180 º the voltage u_2 with respect Case 1, but depending on the angles θ_1 and θ_2 other frequency components can be obtained.

For the case of an equal voltage cascade half-bridge l-level inverter, the Fourier coefficients of the output voltage are [82]

$$U_{s,h} = \frac{4}{h\pi} \left[U_e cos\left(h\theta_1\right) + U_e cos\left(h\theta_2\right) + \ldots + U_e cos\left(h\theta_l\right) \right]$$
$$h = 1, 3, 5, \ldots \qquad (4.1)$$

with h being the order of the harmonic, all of them odd. By displacing the angles θ between $0 < \theta < \pi$, it is possible to increase the value of the harmonic voltage values $U_{s,h}$ deliberately.

It has to be noted that some of the main drawbacks of this structure is the need of isolation between sources, which increases the cost of the converter, and that there is not soft-switching.

Another different converter based on the series connection of H-bridges is found in [85]. In this case, the aim of connecting this structure is to have a converter that doubles the frequency, as shown in Figure 4.5. It can be observed how the frequency of u_1 and u_2 is half of the frequency

4.2 Design of a multichannel converter for induction heating
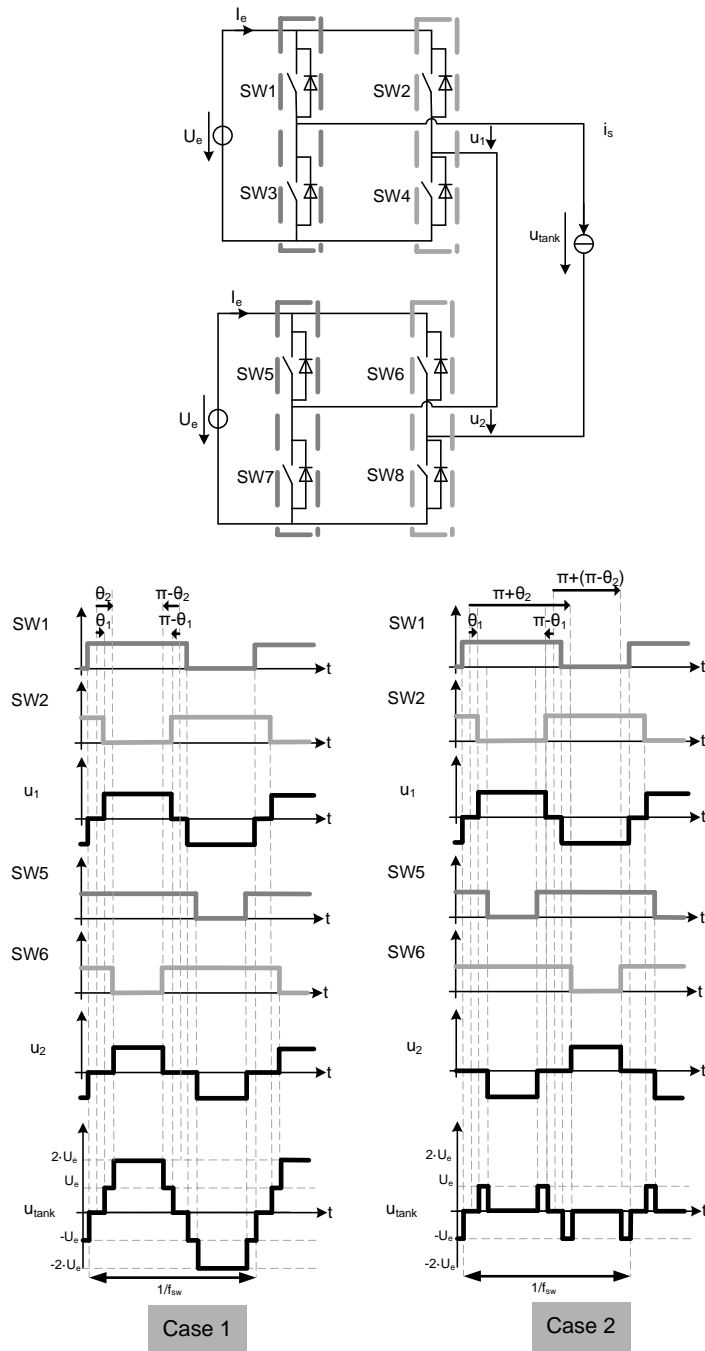
Figure 4.4: Five-level cascade half-bridge multilevel converter.

at the output, u_{tank}. The more H-bridges connected in series, the higher frequencies at the output can be obtained. In the previous case, the aim was to reduce voltage stress in semiconductors and allow the use of MOSFET in high voltage applications. In this case, the aim is to increase the output frequency while maintaining the commutation frequency, thus, allowing the use of IGBTs in high-frequency applications.
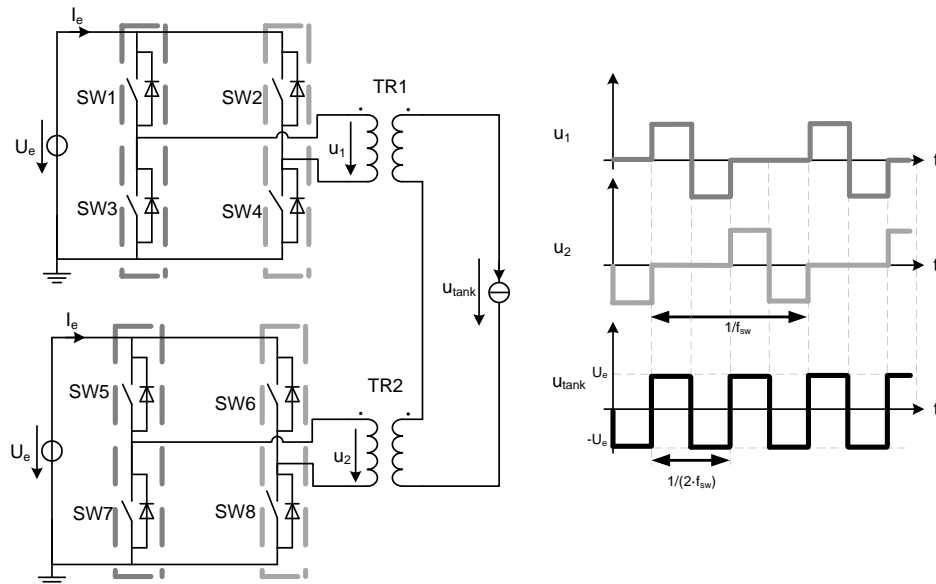
Figure 4.5: Series connection of two H-bridges with transformer doubling the output frequency.

Inverters based on parallel connection of H-bridges

Other inverter topologies found in literature are those obtained from the parallelization of basic inverters shown in Figure 4.6. Usually, the aim of this parallelization is obtaining a higher output power.

In Figure 4.7, a parallel connection of two VFSRI with two different switching sequences is shown. It can be observed that, in case that the voltage U_e is the same in both H-bridges, this structure is similar to the case of paralleling switches.

In Case 1, both H-bridges are commutating synchronized. This can only be done when the connections between H-bridges and the tank have the same impedance and when the DC supply voltage of both bridges have the

4.2 Design of a multichannel converter for induction heating
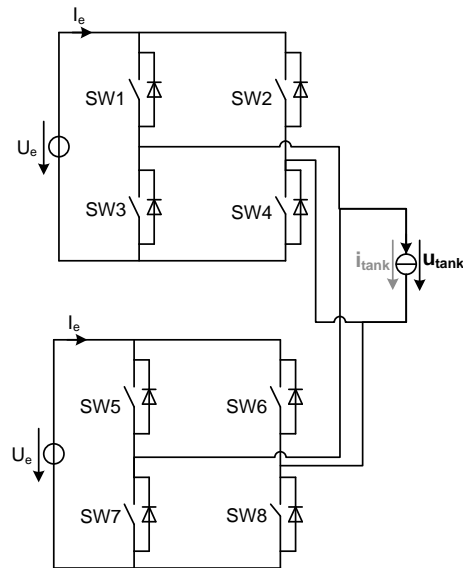
Figure 4.6: Two H-bridge structures connected in parallel.

same value. This operation is similar to paralleling semiconductors, which is a connection used in many applications to increase the power.

Other possibility is to commutate the H-bridges alternatively at half of the frequency, as shown in Figure 4.7 in Case 2. In this case, the frequency of the output waveform u_{tank} is twice the commutation frequency, which allows the use of IGBTs in high frequency applications. This case is similar to the case shown in Figure 4.5 for the series connection. The difference is that all switches of one H-bridge have to be blocked while the other is commutating, whereas in the previous case, two switches need to be conducting while the other H-bridge is commutating.

In [53, 86, 87], this parallelization is used commutating as in Case 2 in Figure 4.7. In [53] and [86], the benefits of this commutation technique are compared to the benefits of commutating as in Case 1 in Figure 4.7 to reach higher frequencies. The underlying idea is the proportional decrease of IGBT losses at high currents. In Case 1, switches' current has an amplitude half of the output current's amplitude. Thus, switches are destressed because the current level is lower and the commutation frequency can be higher. In case 2, the current is also half of the output current because switches conduct half of the period, but the peak current is the same than the output's current. Considering that VFSRI commutate with inductive

101
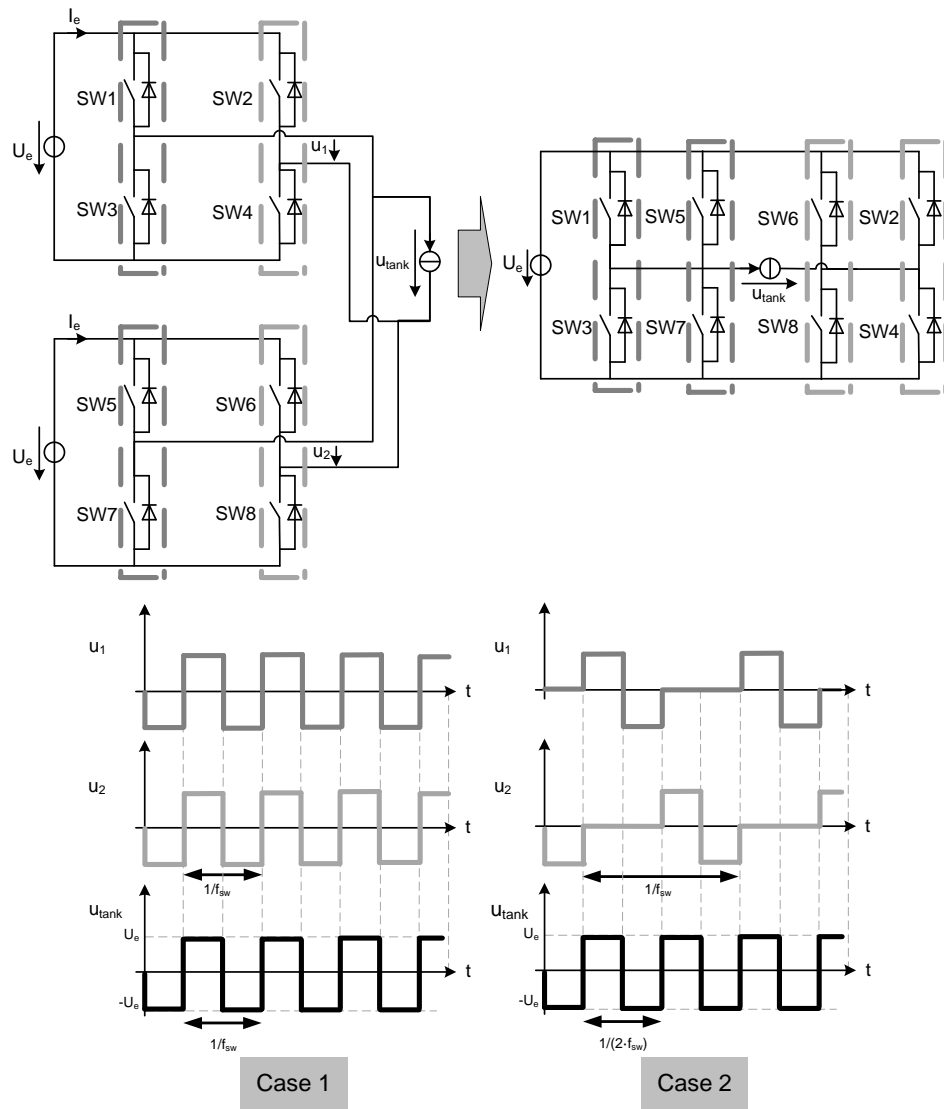
Figure 4.7: Parallel connection of two VFSRI.

4.2 Design of a multichannel converter for induction heating

switching, commutation losses occur during the transistors' turn-off. In case of IGBTs, this energy-loss is proportionally lower in case of high currents than in low currents. Although the conduction losses increase because there are higher currents during less time, the overall losses per semiconductor are lower. Therefore, commutating as in Case 2 improves converter's performance. In any case, it has to be noted that obtaining a realistic value from manufacturers' datasheets for comparing both strategies is difficult and has to be particularized.

Other authors using parallelization of converters with LCL tanks can be found in [45] and [46]. In this case, authors take advantage of the inductance at the output of the inverters, which allows an easy connection between inverters and avoids any recirculation. The aim of this parallelization is to increase the total output power. In Figure 4.8 this connection is shown and it can be observed that the commutation process is equal to Case 1 in Figure 4.7.
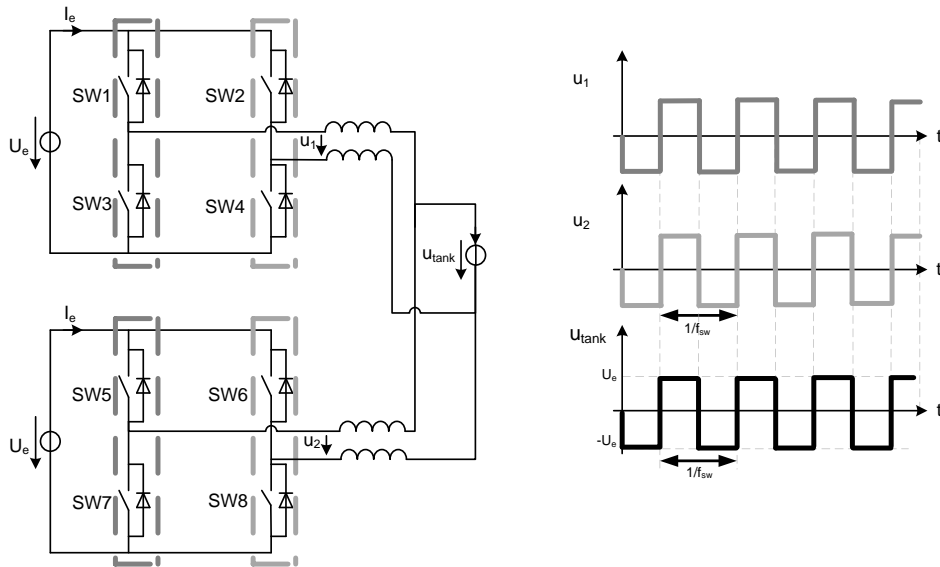
Figure 4.8: Parallel connection of two H-bridges with LCL tank to increase output power.

103

4.2.3 Analysis of H-bridge inverters connection for the multichannel converter

In the previous section, the different topologies of IH converters based on serialization and parallelization of H-bridge inverters are overviewed. In this section, the same structures with different types of commutations are exposed and the advantages and drawbacks of each one for its use in a multichannel converter are explained.

First, the H-bridge converter with its commutation states and commutation techniques is explained with the aim of providing a better understanding of the following analysis. Afterwards, the series and the parallel connection of H-bridges is discussed for the case of a multichannel converter.

H-bridge structure analysis

In Figure 4.9, a voltage-fed H-bridge structure is shown. Considering that two switches of the same inverter leg cannot commutate at the same time, it can be assumed that the state of the switches (ON and OFF) of the same inverter leg are contrary. Thus, there are four possible states in an H-bridge, as shown in Table 4.1.
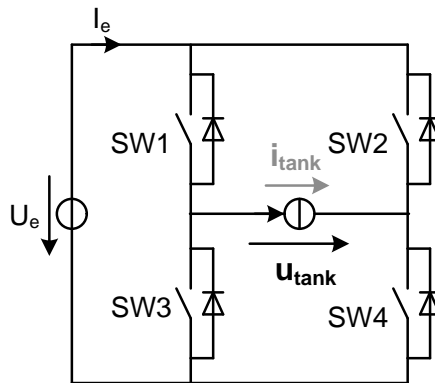
Figure 4.9: H-bridge structure.

In Figure 4.10, three possible commutation methods to obtain an AC voltage at the output of the H-bridge are shown. In Case 1, $SW1$ and $SW2$ have a duty-cycle d of 50 % and commutate shifted 180 °. The resulting waveform is a square wave of $\pm U_e$ and frequency f_{sw}, being f_{sw} the commutation frequency.

4.2 Design of a multichannel converter for induction heating
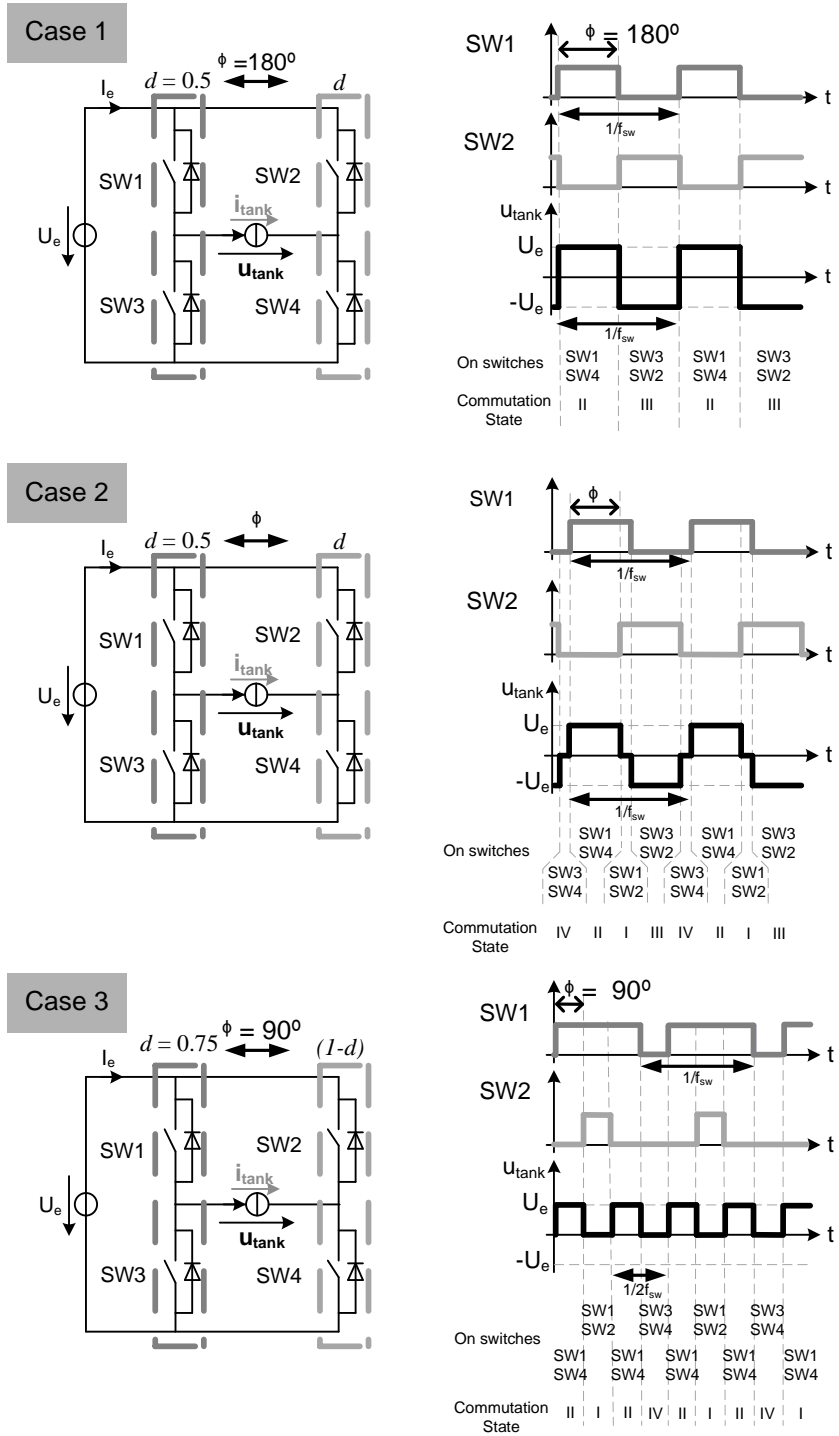
Figure 4.10: Commutation techniques for an H-bridge structure.

Table 4.1: Commutation states for an H-bridge

State	SW1	SW2	u_{tank}
I	ON	ON	0
II	ON	OFF	U_e
III	OFF	ON	$-U_e$
IV	OFF	OFF	0

In Case 2, the duty-cycle is maintained for the two inverter legs, but the phase-shift ϕ is not 180 °. Under these circumstances, the commutation states are States IV-II-I-III and the output waveform is the same than in Case 1, but with zero voltage at States I and IV. In this case, the commutation occurs when the current is not zero and the commutation losses increase.

In the last case, Case 3, the duty-cycles are 75 % and 25 % and their phase-shift is 90º. Under these circumstances, the resulting output waveform doubles the frequency of commutation. However, the voltage is just positive and the first harmonic voltage value in RMS is [88]

$$U_{tank} = \frac{2U_e}{\sqrt{2}\pi} \qquad (4.2)$$

which is half of the value obtained with a $\pm U_e$ waveform, as shown in Equation 7.1 in Section 3.2.2. Thus, the frequency is increased, but the power supplied to the workpiece is a quarter of the power supplied when commutating as in Case 1 (Equation 3.20 in Section 3.2.3). Moreover, this commutation method cannot be used in case of having a matching transformer due to its saturation.

Two H-bridge structures connected in series

In Figure 4.3, the series connection of two H-bridges is shown. In this case, it has to be assumed that both voltage sources are isolated. As in the previous case, it is considered that the switches from the same inverter leg commutate contrarily. The commutation states for this connection are defined in Table 4.2.

In the series connection of H-bridges, there are also several commutation techniques that lead to different output waveforms. In Figure 4.11, 4.12 and 4.13 five different cases are presented.

4.2 Design of a multichannel converter for induction heating

Table 4.2: Commutation states of two H-bridge structures in series.

State	SW1	SW2	SW5	SW6	u_{tank}
I	ON	ON	ON	ON	0
II	ON	ON	ON	OFF	U_e
III	ON	ON	OFF	ON	$-U_e$
IV	ON	ON	OFF	OFF	0
V	ON	OFF	ON	ON	U_e
VI	ON	OFF	ON	OFF	$2U_e$
VII	ON	OFF	OFF	ON	0
VIII	ON	OFF	OFF	OFF	U_e
IX	OFF	ON	ON	ON	$-U_e$
X	OFF	ON	ON	OFF	0
XI	OFF	ON	OFF	ON	$-2U_e$
XII	OFF	ON	OFF	OFF	$-U_e$
XIII	OFF	OFF	ON	ON	0
XIV	OFF	OFF	ON	OFF	U_e
XV	OFF	OFF	OFF	ON	$-U_e$
XVI	OFF	OFF	OFF	OFF	0

In Case 1 in Figure 4.11 , both H-bridges commutate synchronized, the duty-cycle of $SW1$ and $SW5$ is 50 % and the phase-shift ϕ_1 and ϕ_2 are 180º. The resulting waveform has a $\pm 2U_e$ voltage amplitude at a f_{sw} frequency. This case is similar to Case 1 in Figure 4.10 for one H-bridge.

In Case 2, all switches have a 75 % of duty-cycle, $SW5$ is delayed 180º from $SW1$ ($\phi_{12} = 180º$) and $SW2$ and $SW6$ are delayed 90º regarding their opposite switches, SW1 and SW5 respectively. In this case, the resulting output waveform has doubled the frequency of commutation, but has half of the voltage than in the previous case. Case 3 is similar, but the dead-times are different, as shown in Figure 4.12.

Case 4 in Figure 4.13 can be used in case of needing a higher output voltage with higher frequency. In this case, SW1 and SW5 are synchronous and have a duty-cycle of 75 %. $SW2$ and $SW6$ have a 25 % of duty-cycle and they are delayed 90º regarding their opposite switches $SW1$ and $SW5$. Under these circumstances, the resulting waveform has doubled the frequency and has an amplitude of $2U_e$ V. The problem of this commutation technique is that a matching transformer cannot be used. The same happens in Case 5 in Figure 4.13, where the output waveform has quadrupled the frequency,
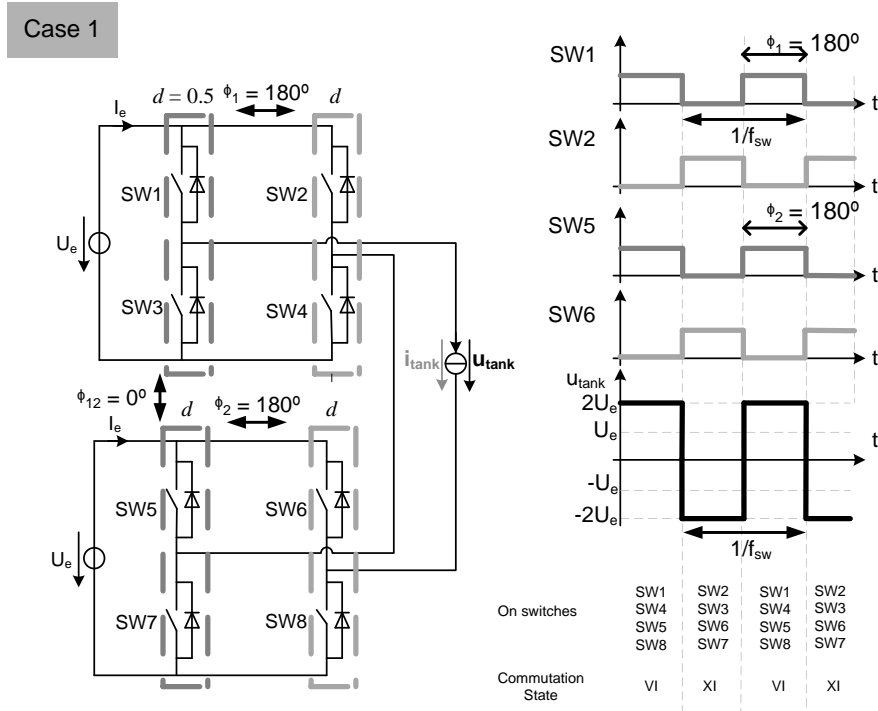
Figure 4.11: Commutation techniques for two H-bridge structures connected in series, Case 1.

but has a positive voltage with amplitude U_e.

Generalizing the results obtained for n H-bridges connected in series, fed at U_e voltage and commutating at f_{sw}, the following output waveforms can be obtained:

- $\pm n U_e$ amplitude and f_{sw} frequency.

- $\pm U_e$ amplitude and $n f_{sw}$ frequency.

- $+U_e$ amplitude and $2n f_{sw}$ frequency.

These different combinations can be obtained by varying the commutation technique by software. The wide output range is interesting because permits to create a multichannel converter by the addition of basic structures, but also adapt a given converter to different load requirements by varying the software. The main drawback of this type of connection is that the sources

4.2 Design of a multichannel converter for induction heating
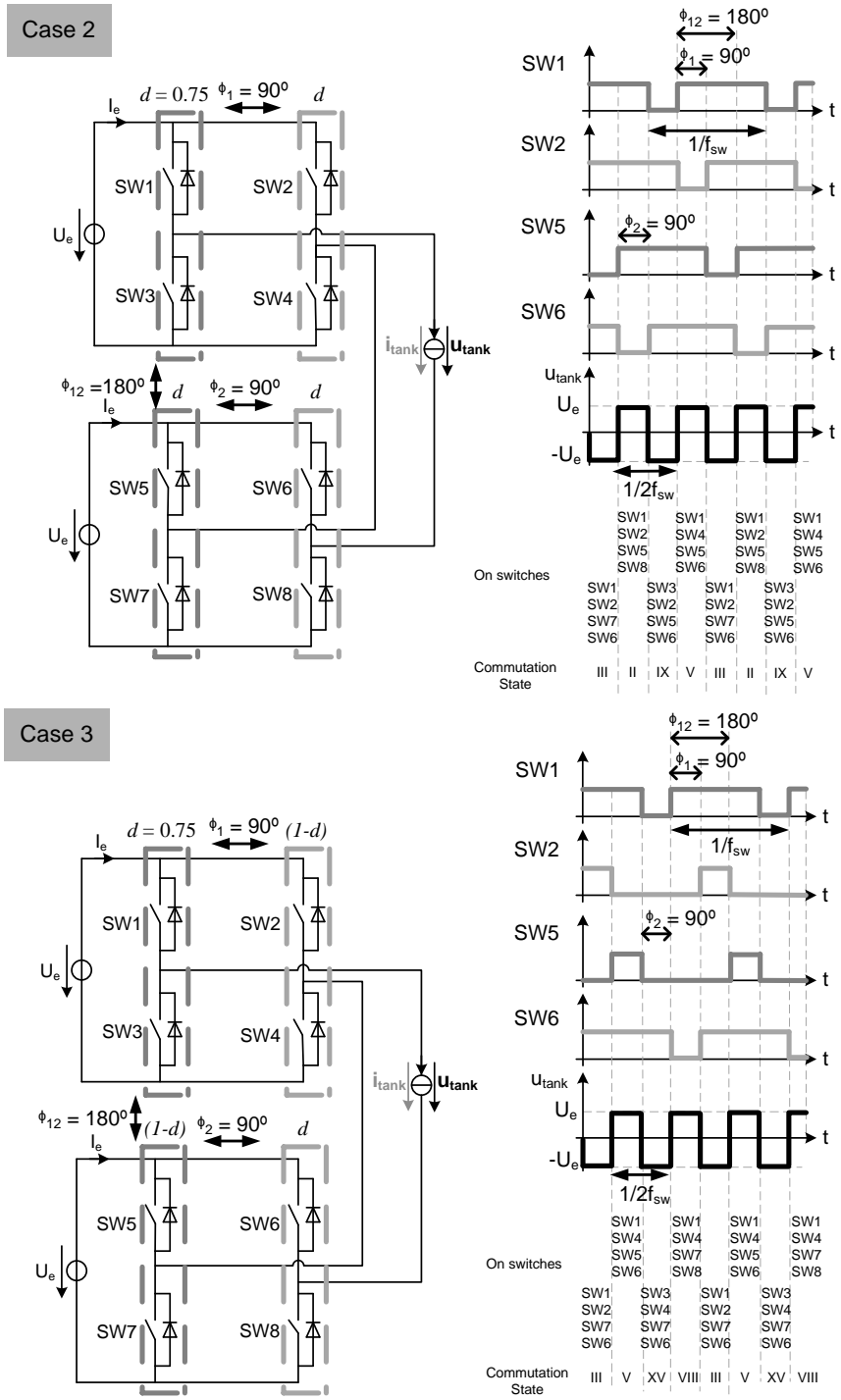
Figure 4.12: Commutation techniques for two H-bridge structures connected in series, Cases 2 and 3.

Figure 4.13: Commutation techniques for two H-bridge structures connected in series, Cases 4 and 5.

4.2 Design of a multichannel converter for induction heating

need to be isolated, otherwise short-circuit occurs in most of the commutation states. For example, if both voltage sources have a common ground and $SW2$ and $SW7$ are ON, then short-circuit occurs.

Considering the structure based on a uncontrolled rectifier plus and H-bridge shown in Figure 4.2, one option to solve this limitation is using a low frequency transformer between the mains and the rectifiers. This would result in a considerable increase of converter's cost and size. Other option is to use a matching transformer at the output of each H-bridge, like [85] and as shown in Figure 4.5 in Section 4.2.2. In this case, the volume is lower, but the cost is still high and it is not possible to use a commutation technique in which the voltage is just positive or negative (Cases 4 and 5 in Figure 4.13).

Therefore, to use this type of connection a matching transformer is required for each inverter, increasing the cost of the system, and the output waveform obtained is $\pm nU_e$ at f_{sw} and $\pm U_e$ at nf_{sw}.

Two Full-bridge structures in parallel

In Figure 4.6, the parallel connection of two H-bridge structures can be observed. The respective commutation states are shown in Table 4.3.

Although both voltage sources are isolated, it can be observed that most of states create a short-circuit. Moreover, in States VI and XI, two voltage sources are connected in parallel, fact that can generate high currents when having a voltage difference between sources. Thus, in order to obtain an output voltage of $\pm U_e$ amplitude and f_{sw} frequency, the voltage sources need to be the same. This case is equal to the case of paralleling switches to increase the power used in many applications.

It has to be noticed that this connection of H-bridges has, a priori, more limitations than the series connection. However, these limitations can be solved by using the state in which all switches are OFF. Considering this, it is possible to use a commutation technique where both H-bridges are commutating alternatively while the other is switched-off, like in Figure 4.14 and in [86]. Under these circumstances, the output voltage has a $\pm U_e$ amplitude at a $2f_{sw}$ frequency.

Generalizing the results obtained for n H-bridges connected in parallel, fed at voltage U_e and commutating at f_{sw}, the following output waveforms can be obtained:

- $\pm U_e$ amplitude and f_{sw} frequency, multiplying by n the current capability.

- $\pm U_e$ amplitude and $n f_{sw}$ frequency.

The great advantage of this connection, compared to the series connection, is that the DC-bus has to be shared and there is no need of isolation. Moreover, the output frequency can be increased by commutating like in Figure 4.14, fact that is interesting in case of using IGBT technology.

Table 4.3: Commutation states of two H-bridge structures in parallel.

State	SW1	SW2	SW5	SW6	u_{tank}
I	ON	ON	ON	ON	0
II	ON	ON	ON	OFF	short-circuit
III	ON	ON	OFF	ON	short-circuit
IV	ON	ON	OFF	OFF	0
V	ON	OFF	ON	ON	short-circuit
VI	ON	OFF	ON	OFF	U_e
VII	ON	OFF	OFF	ON	short-circuit
VIII	ON	OFF	OFF	OFF	short-circuit
IX	OFF	ON	ON	ON	short-circuit
X	OFF	ON	ON	OFF	short-circuit
XI	OFF	ON	OFF	ON	$-U_e$
XII	OFF	ON	OFF	OFF	short-circuit
XIII	OFF	OFF	ON	ON	0
XIV	OFF	OFF	ON	OFF	short-circuit
XV	OFF	OFF	OFF	ON	short-circuit
XVI	OFF	OFF	OFF	OFF	0

4.2.4 Multichannel converter for induction heating

With regard to the previous considerations, the multichannel converter is formed by three-phase diode bridge rectifiers and H-bridge structures. Due to the advantages provided by voltage-fed converters in terms of the possibility to use commercial components, the inverter is a VFSRI. Thus, the resonant tank is a series or an LCL tank. Although high voltage and high power MOSFET devices are available, IGBTs are more common in this range of voltage and power and their use decreases the number of devices needed and the overall cost of the system. In order to increase the output power and frequency, the best option is sharing the DC-bus and the connection

4.2 Design of a multichannel converter for induction heating

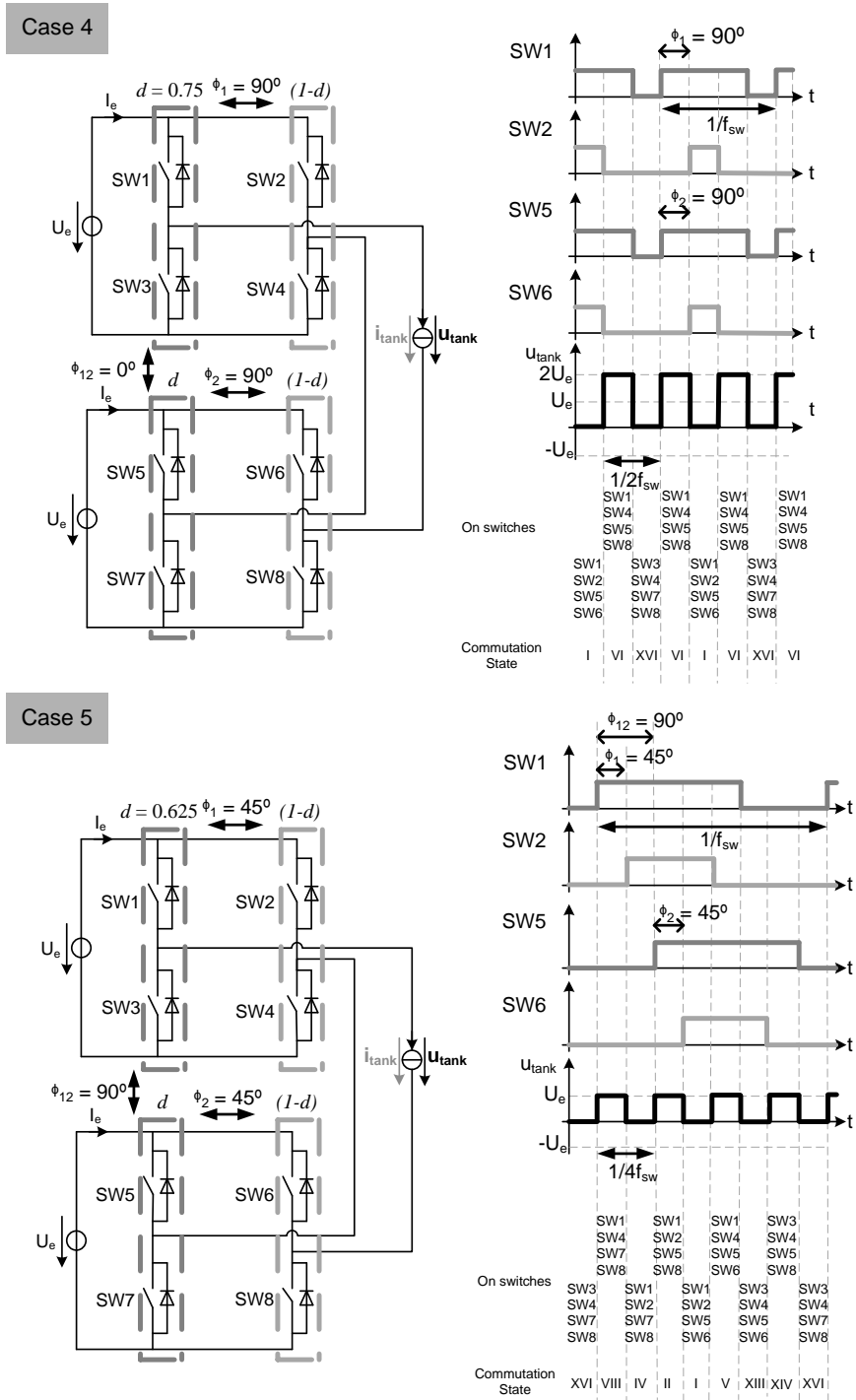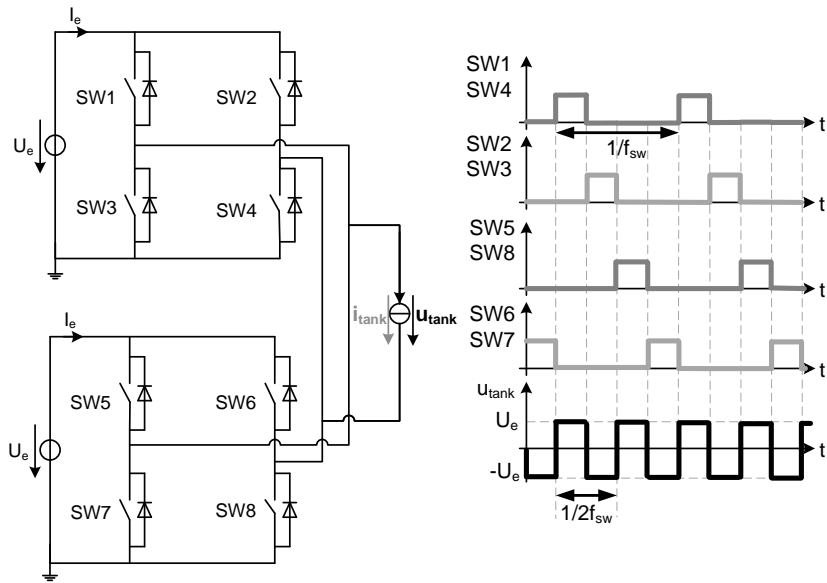Figure 4.14: Commutation technique for two H-bridge structures connected in parallel.
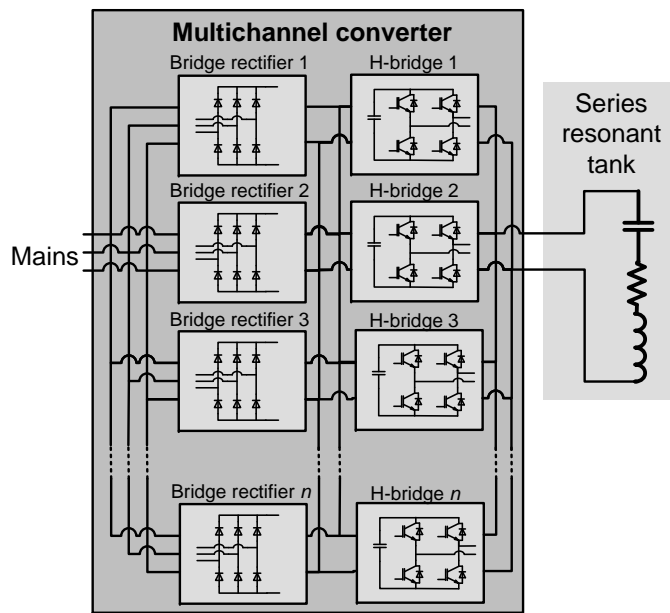
Figure 4.15: Electrical scheme of the multichannel converter.

113

in parallel of the H-bridge structures. Considering this, the multichannel converter scheme can be observed in Figure 4.15.

4.3 Implementation of the multichannel converter

4.3.1 Experimental setup

The control method presented in this chapter has been implemented in a prototype using a microcontroller TMS320F2808 digital signal processor (DSP) from Texas Instruments. During the experimentation, the connection of various rectifiers was not implemented because this type of connection has already been studied broadly and is actually used in many applications. The same happens for the case of commutating two parallel H-bridges synchronized to increase the output power. Therefore, the commutation technique in which both H-bridges commutate alternatively to increase the output frequency as in Figure 4.14 is implemented, because is the most unusual commutation technique.

In the worst case, when using VFSRIs, the DC capacitor has to supply an current equal to i_{tank} rectified. Thus, a low inductance polypropylene capacitor bank of 1200 μF (two 610 μF capacitors from Electronicon in parallel) is connected to supply this high-frequency ripple current. The connection between the polypropylene capacitor bank and the bank of electrolytic capacitors is realized with normal wire and leaving a loop intentionally. The aim of doing this is to profit the parasitic capacitance of the cable and avoid that the electrolytic capacitors supply the high frequency current. With regard to the connections between polypropylene capacitors and IGBTs, it has have been done with copper foils tight together to diminish the parasitic inductance, similarly to a laminated busbar. The same copper foil has been used for connecting the converter with the resonant tank. The aim of using this type of connection is to avoid high power losses due to wire section misuse caused by skin effect.

The resonant tank is composed of a matching transformer with a turns ratio of 10/1 to 18/1, 6 inductors of 16 turns and 8 capacitors of 0.33 μF (CSM150 from Celem). Depending on the test performed, these components are connected in different ways in order to reach the desired load. In this experimental tests, the six coils are connected in parallel and the capacitors are connected or disconnected in order to obtain the desired resonant frequency.

4.3 Implementation of the multichannel converter
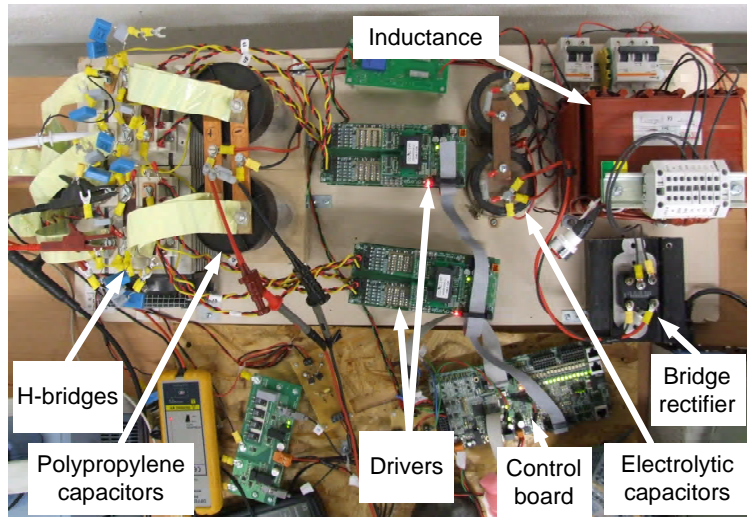
Figure 4.16: Experimental setup used for the multichannel converter.
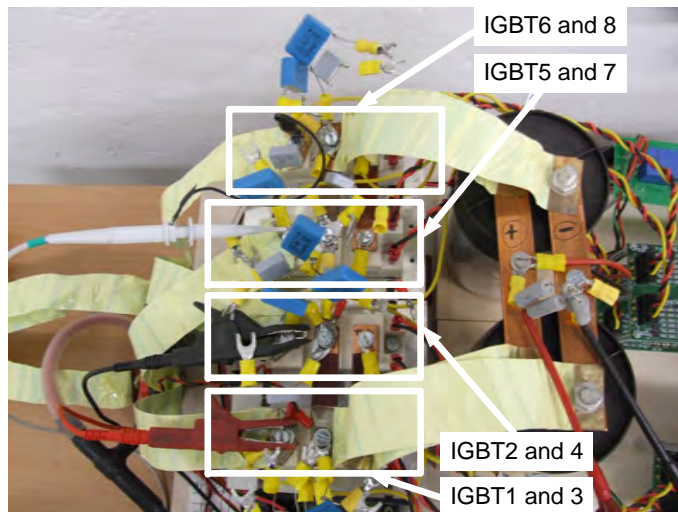
Figure 4.17: Experimental setup used for the multichannel converter, zoom.

.pdf
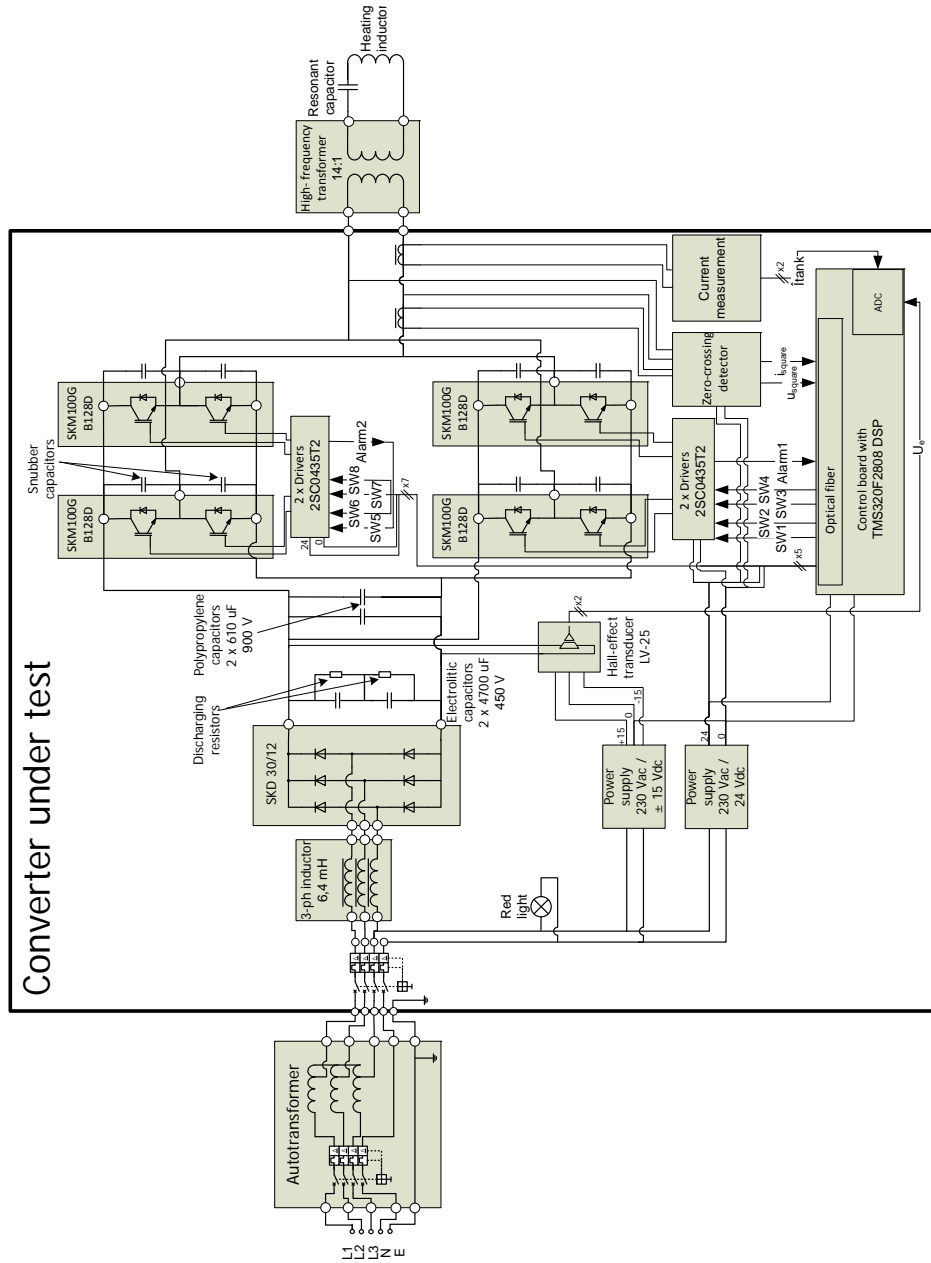
Figure 4.18: Electrical scheme of the experimental setup.

The experimental setup is shown in Figures 4.16 and 4.17 and its electrical scheme in Figure 4.18. A three-phase autotransformer is used to set the voltage U_e to the desired value. In order to ensure a constant voltage value, a three-phase inductor and a 2350 μF capacitor bank (two 4700 μF capacitors in series) act as a low-pass filter.

4.3.2 Experimental results

The variables measured are shown schematically in Figure 4.19. The output current of both H-bridges, i_{HB1} and i_{HB2}, the voltage u_{tank} and the current i_{tank} are shown in Figures 4.20 and 4.21. In the first case the results correspond to a 96 kHz resonant tank and in the second case to a 154 kHz tank.

In Figures 4.20 and 4.21, it can be observed that the current is flowing one full period in H-bridge 1 and another full period in H-bridge 2. It can be also observed that during the dead-times the current conducts in both H-bridges. This is caused by the turning-off of all the IGBT during this interval. Under these circumstances, the current charges the parasitic capacitances of all IGBTs until the antiparallel diodes conduct or the IGBTs' turn-on.

In Figures 4.22 and 4.23, the input current of both H-bridges, i_{e1} and i_{e2}, the voltage u_{tank} and the current i_{tank} are shown for 96 kHz and 154 kHz resonant tanks. It can be observed how the current input of each inverter is half of the total i_{tank} rectified.

It has to be noted that in the figures presented in this section a superimposed high frequency ripple is observed in the waveforms. This ripple is caused by the voltage ringing due to the parasitic components and influences the current measurements (realized with Rogowski coils) when measuring the voltage and the currents at the same time with the same oscilloscope.In this case the voltage was measured with a non isolated voltage probe.

During the hardware implementation, the differences between inverter's connections have been minimized to avoid voltage drops that can lead to the recirculation of currents between inverters. Although the experimental setup is handmade, it has proven to be reliable and allows the increase of the output's frequency without any recirculation. Several tests have been realized with different loads and resonant frequencies obtaining similar results.

The results obtained show that the proper design of the DC-bus and the connections can permit the industrialization of these basic structures, implementing a multichannel converter formed by diode rectifiers and H-bridges. In this case, SKM100GB128D IGBTs from Semikron were used,
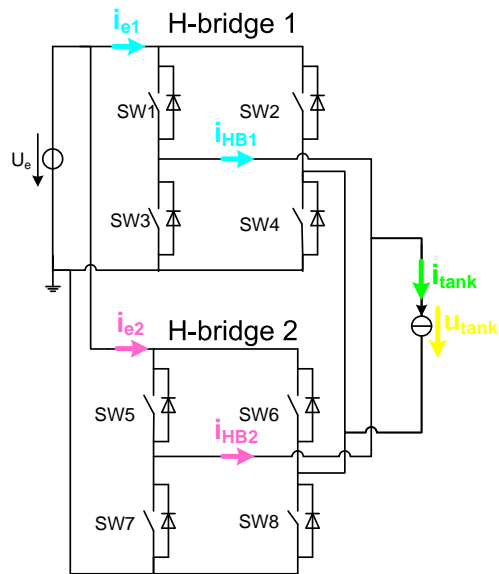
Figure 4.19: Variables measured during the experimentation.
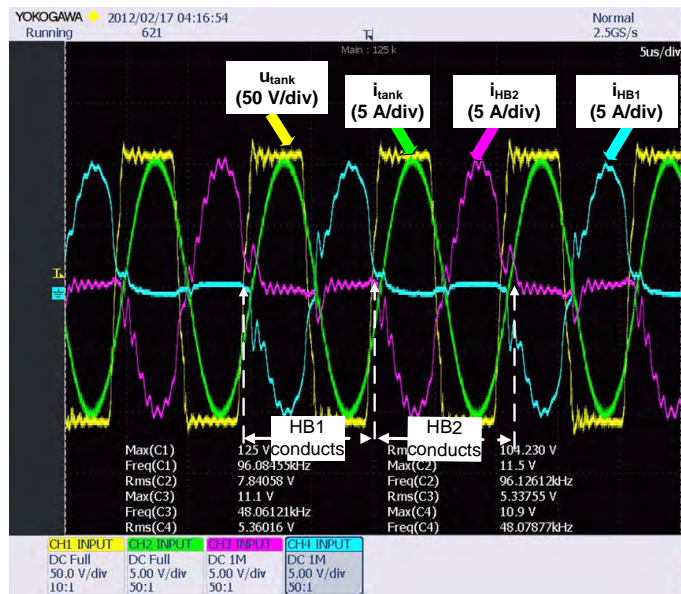
Figure 4.20: Current at the output of the H-bridges, u_{tank} and i_{tank}, for a resonant tank of 96 kHz.
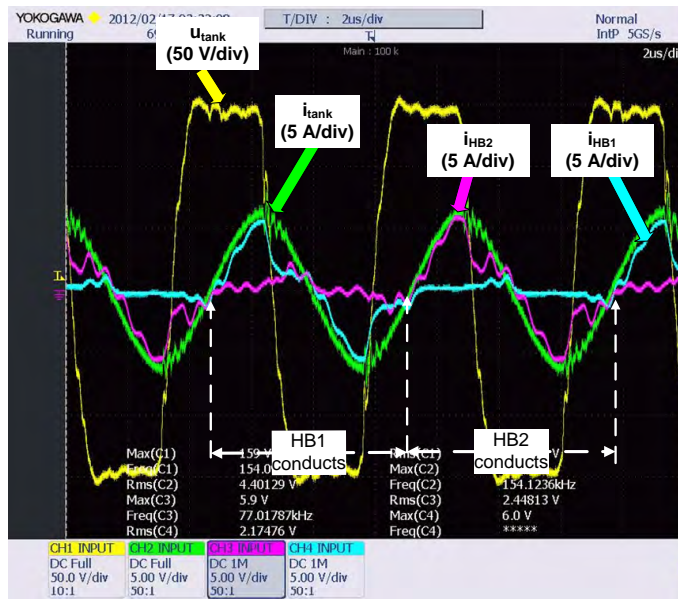
Figure 4.21: Current at the output of the H-bridges, u_{tank} and i_{tank}, for a resonant tank of 154 kHz.
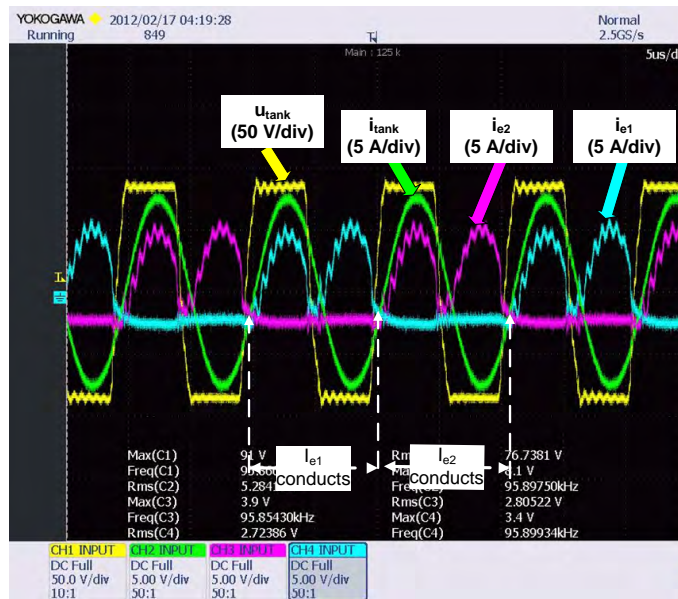
Figure 4.22: Current at the input of the H-bridges, u_{tank} and i_{tank}, for a resonant tank of 96 kHz.
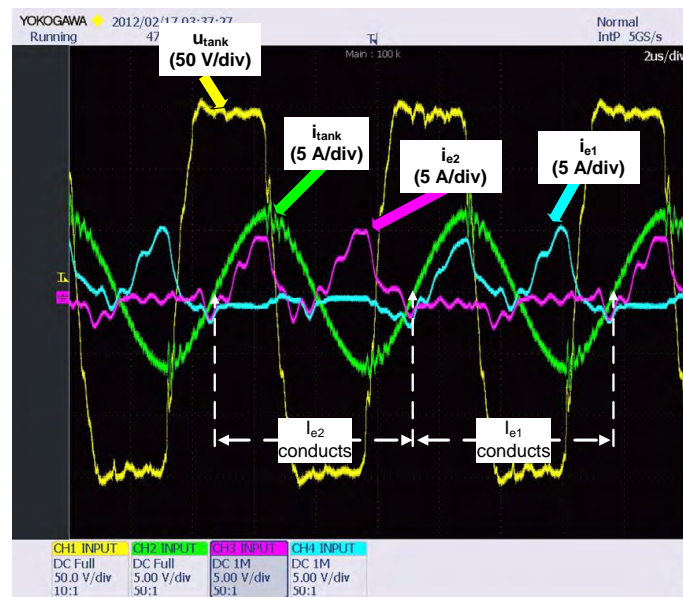
Figure 4.23: Current at the input of the H-bridges, u_{tank} and i_{tank}, for a resonant tank of 154 kHz.

but there are faster devices specially thought for resonant applications that can improve converter's performance. It would be interesting to realize tests with power devices of these characteristics and increment the number of H-bridges. It would be interesting to see the limits of these structure for an specific application and compare it in terms of efficiency and cost with a classical high frequency converter with MOSFETs. Another interesting approach is to test this structure with a change of commutation technique to have high-power at low frequency and high-frequency at low power automatically by software control.

4.4 Summary

A converter structure based on the connection of basic topologies is extremely interesting from an industrial point of view. The benefits of this structure are the reduction of design time and cost, the reduction of cost derived from higher volume production of these basic topologies, the reduction of stock components and the reduction of installation and maintenance work. In this chapter, the structure of a multichannel converter formed

by basic topologies is studied, paying special attention to the connection and commutation techniques of the inverters in order to increase the output power and frequency.

The most simple structure to construct an IH converter for a high-power application is by using an uncontrolled bridge rectifier plus an H-bridge. In this study, the multichannel converter is formed by one or various uncontrolled rectifiers and various H-bridges. With regard to the semiconductors used in the inverters, actually high voltage and high power MOSFET devices are already available. However, IGBTs are more common and their use decreases the number of devices needed and the overall cost of the system. With regard to the type of inverter, the use of VFSRI is advantageous in terms of availability of commercial components.

The H-bridge inverters that compose the multichannel converter can be connected in series or in parallel. The series connection of H-bridges requires a matching transformer at the output of each inverter, increasing the cost of the system. In this case, the output waveform obtained is $\pm nU_e$ at f_{sw} and $\pm U_e$ at nf_{sw}. In case of connecting the inverters in parallel, the inverters can commutate synchronized to increase the power or alternatively to increase the output frequency. The benefits of the parallel connection are that a matching transformer for every inverter is not required and that allows the increase of the output frequency, thus, allowing the use of IGBTs in high frequency applications.

A multichannel converter has been constructed with two H-bridge inverters in parallel and has been tested commutating both inverters alternatively to increase the output's frequency. The system has shown good reliability under different conditions in which has been tested, proving that this commutation technique allows the increase of the output's frequency without any recirculation between inverters. The use of fast IGBTs and the proper design of the inverters' connections can allow the implementation of this type of structure in industrial equipments, allowing the increase of power or frequency depending on the requirements.

Chapter 5

Design of a software phase-locked loop

5.1 Introduction

IH converters commutate close to resonant frequency to supply maximum power to the workpiece. In case of VFSRI and CFPRI, the converter commutates slightly above resonance and, in case of converters with LCL tanks, it commutates above the higher of the two resonant frequencies of the tank. Even those IH systems using power control strategies based on shifting out of resonance need to detect which is the resonant frequency. Therefore, the correct identification of the tanks' resonant frequency is a matter of vital importance in most IH converters.

A manner of detecting the resonant frequency is by calculating the phase-shift between two electric variables. In case of VFSRI and CFPRI, the phase-shift between voltage and current is zero at resonant frequency, so one method of finding the resonant frequency is varying the frequency until the phase-shift is zero. In case of converters with LCL tanks, the base idea is the same, but with a 90 º phase-shift between the voltage at the output of the inverter and the voltage at the capacitor. For controlling this phase-shift between two electric variables, most of IH converters use a phase-locked loop (PLL) system.

In this chapter, a software PLL for IH applications is presented, simulated and implemented in a VFSRI. First, the control principles of PLL systems applied to IH are introduced, presenting the proposed software PLL system and simulating it, in Section 5.2. Then, in Section 5.3, the PLL is implemented in a real industrial application and the chapter is summarized in Section 5.4.

5.2 Software phase-locked loop principles and description

5.2.1 Phase-locked loop description and operation principles

A PLL is a circuit that synchronizes a periodic input signal with a periodic output signal [89, p. 1]. It is composed of three elements: a phase detector, a low-pass filter and a voltage-controlled oscillator (VCO). The scheme of a basic PLL is shown in Figure 5.1. It is not the aim of this study to explain deeply the different parts and techniques of implementing a PLL, but some basic concepts are introduced. Further information can be found in [89].
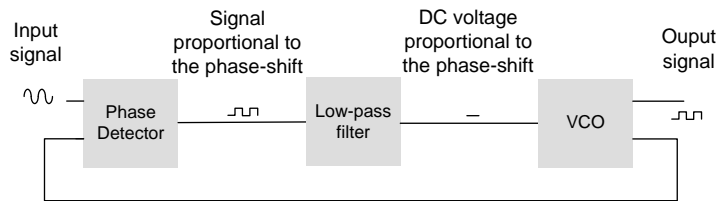
Figure 5.1: Basic scheme of a PLL circuit.

As shown in Figure 5.1, the phase detector produces a signal that is proportional to the phase-shift between the two input signals. Then, this signal is filtered through a low-pass filter, obtaining a DC voltage that is proportional to the phase-shift. Afterwards, a VCO generates an AC signal whose frequency is proportional to its DC input voltage. In case of a feedback loop, the output of the VCO is connected with the input of the phase detector and the VCO adjusts the frequency until the output signal is matched to the input signal.

There are different types of PLLs, depending on the phase detector, the filter and the VCO. A general classification of them is shown in Figure 5.2 [90, p. 8]. Since the first analog PLL integrated circuits appeared in the 60's, PLLs have incorporated more and more digital components. First the digital PLL appeared, which included digital phase detectors with exclusive OR gates or flip-flops, and after the all-digital PLL was made, in which all the components were digital. In the last decades, with the development of high performance microcontrollers and DSPs, PLLs have become all-digital and software implemented. Although digital and all-digital PLLs are still widely used, software-PLLs have advantages regarding the integration, flexibility and control's complexity that with classical PLL systems can be difficult to

124

realize.

Considering PLLs and IH applications, PLL systems are used to control the phase-shift between two electric variables and reach the resonant frequency. Some examples of authors that make use of similar schemes in IH field are [24, 59, 91–98].
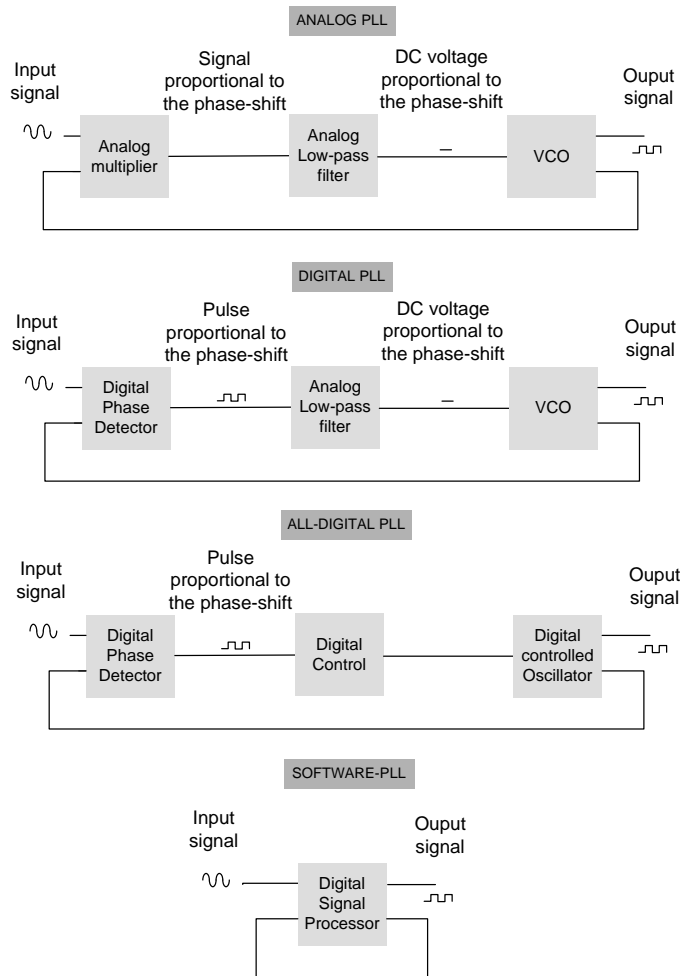
Figure 5.2: Classification of PLL systems.

In case of VFSRI, the voltage and current phase-shift is close to zero at resonant frequency. To control this phase-shift, some authors use PLL systems that just measure i_{tank} and use a feedback loop, as shown in Case

1 in Figure 5.3. Some examples of this type of PLL can be found in [93–96]. In this case, the current i_{tank} is the input signal and the PLL output is a signal that tends to be synchronized with this current. This output signal is connected to the drivers of the H-bridge and, thus, it should be synchronized with the voltage u_{tank}. In this case, the PLL changes the frequency until the phase-shift between these two signals is zero. The trouble of using this control scheme is that it is assumed that there are no delays between the driver signals and the voltage. That is why some authors like [97] and [98] incorporate a compensator that takes into account these delays.

Other authors like [24, 59, 91, 92], tend to use two input signals (u_{tank} and i_{tank}) without any feedback loop, as shown in Case 2 in Figure 5.3. In this case, the inaccuracies caused by the delays are avoided, but there is a cost increase in cost due to the hardware required for measuring and treating these signals.

Regarding the circuits employed, some authors use circuits designed by themselves, like [8, p. 152], but most of them use integrated circuits from the CMOS 4046 circuit family, like [59, 91–95, 98]. Nevertheless, most authors use digital PLL systems, in which just the phase detector is digital, but the low-pass filter and the VCO are analog (Figure 5.2). The phase detector used is a phase-frequency detector similar to the one presented in [89, p. 93].

Although analog control has demonstrated to be effective and accurate, it is less flexible and robust to the degradation of the components than digital control. In digital systems, many of the parameters used during the control, like frequency, dead-time or the filters, can be adjusted without any change in hardware. Additionally, in case of fixing a value like the dead-time, this value remains constant independently of the frequency chosen, as explained in [99].

Due to the advantages of digital control presented above, some authors have started using DSPs or field-programmable gate arrays (FPGAs) to implement the PLLs. To mention some examples, in [100] a DSP is used, but all the components of the PLL (phase detector, low-pass filter and VCO) are external. In [99], a DSP is also used, but with an external phase detector and an analog low-pass filter. In this case, the voltage obtained from the low-pass filter, which is proportional to the phase-shift, is introduced through the analog to digital converter (ADC). However, in both cases the PLL obtained is similar to the digital PLL, which is still a semianalog solution.

Regarding software PLL systems, authors like [96, 101, 102] have started working with FPGA. In these cases, the PLL is customized and incorpo-

5.2 Software phase-locked loop principles and description
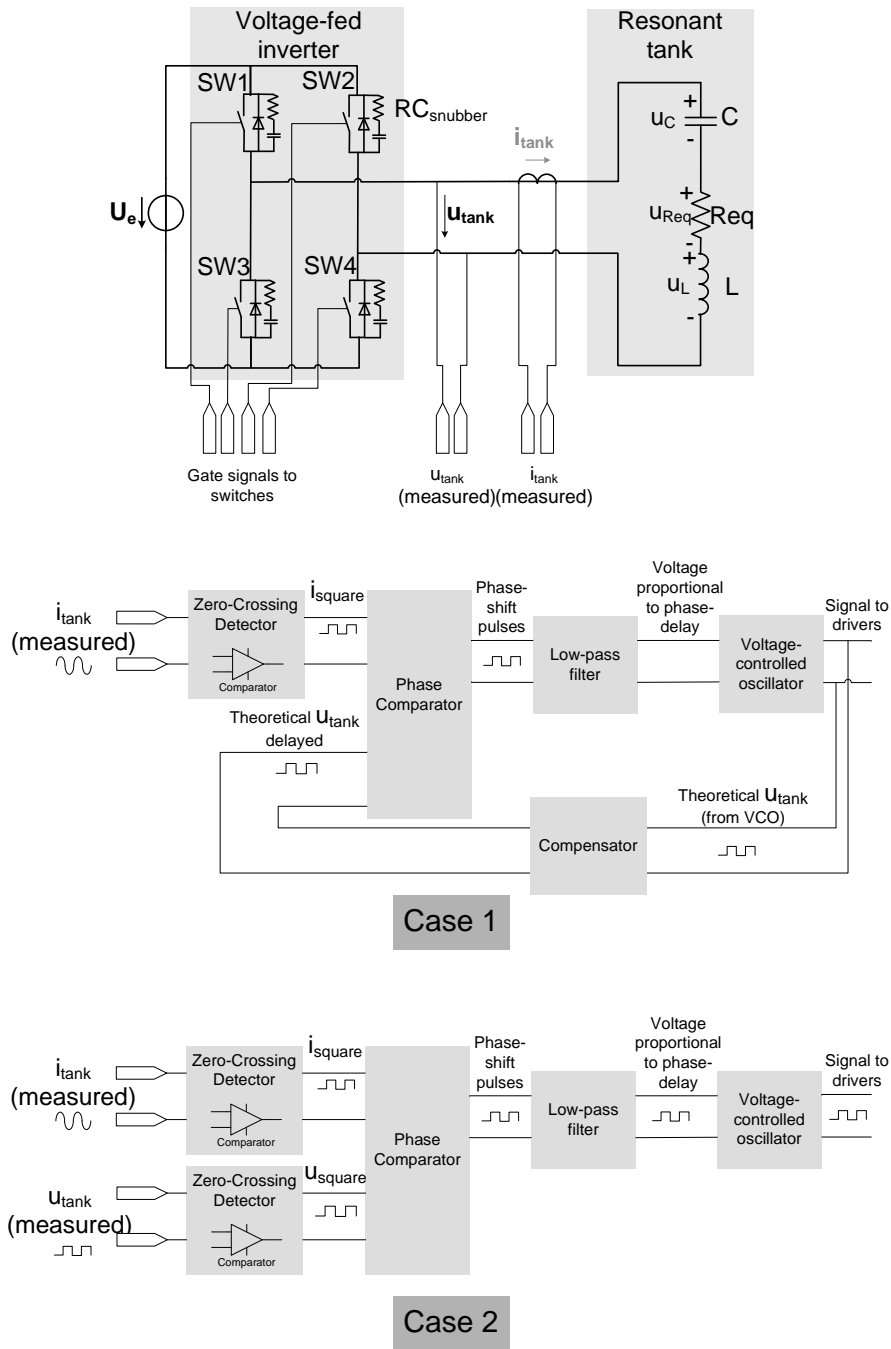
Figure 5.3: Block diagram of the PLL systems used in IH.

rates the filter, as-well as the digital oscillator. Although the incorporation of FPGA allows a fast digital signal processing, the difficulty in the programming is still a barrier and justifies the use of commercial DSP.

5.2.2 Software phase-locked loop for induction heating

Nowadays, there are many microcontroller manufacturers like Microchip, Infineon, Freescale and Texas Instruments, that provide their microcontrollers with the capacity to detect falling and rising edges. This detection is realized thanks to the capture or edge detector module that is incorporated in the microcontrollers and assigned to some of their pins. The control scheme proposed in this section takes advantage of this module, integrating the phase comparator, the low pass filter, the VCO, the compensator and a PI regulator in the same microcontroller. In Figure 5.4, the basic scheme of this software-PLL is shown.

To have a more precise control, both signals u_{tank} and i_{tank} are acquired. These signals are measured and conditioned to obtain a synchronized square-waveform in the voltage range of the microcontroller (u_{square} and i_{square}). Then, the rising edges of these signals are acquired by the microcontroller's edge detector (CAP1A register for the voltage and CAP2A register for the current). In this case, the time delay t_φ is used instead of the phase-shift φ and it is obtained by subtracting the values obtained from the edge detector and multiplying it by the time clock of the counter (t_{clock}). Afterwards, this value is introduced in a PI controller and compared to a reference delay time t_φ^*. The commutation frequency is obtained at the output of the PI, changing the register corresponding to this parameter in the microcontroller. In this case, the control method takes advantage of the built-in PWM generators provided by the microcontroller, allowing an easy change of the commutation frequency as well as the dead-time.
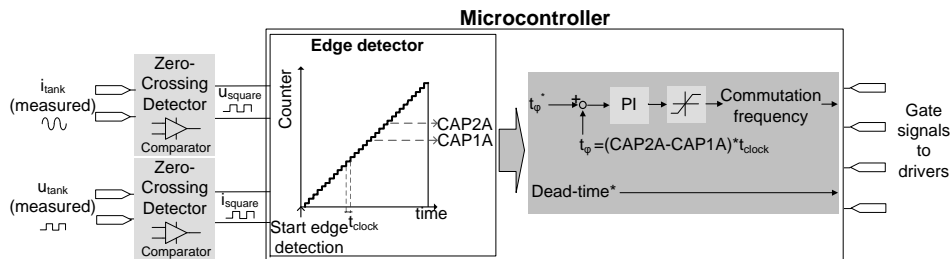
Figure 5.4: Software-PLL based on a DSP microcontroller.

5.2 Software phase-locked loop principles and description

This software PLL permits controlling the converter with less analog components and thus, with less variations due to part spread or temperature drift. However, the major benefit of this system is the easy programming and the flexibility provided to the equipment, since all the parameters (phase-shift reference, PI constants, frequency limits, starting frequency, dead-time, etcetera) can be changed and adapted to different conditions just by modifying the software.

It has to be noted that that the precision of this system relies on the time clock of the microcontroller, which marks the minimum phase-shift that can be detected.

5.2.3 Simulations

Simulation model

The model simulated is a VFSRI with an H-bridge composed of 4 MOSFETs with the parameters shown in Table 7.1.

Table 5.1: Parameters of the simulated system.

	Parameter	Value
	Capacitance	5.62 nF
Resonant tank	Inductance	154 μH
	Resistance	5.75 Ω
	Resonant frequency	170.82 kHz
Mosfet	Parasitic capacitance	4.2 nF
Snubber	Capacitance	30 nF
	Resistance	26.6 Ω

The system is modeled with MATLAB-SIMULINK$^{©}$ using the scheme shown in Figure 5.5. In this case, when u_{tank} crosses zero, there is a rising edge and the edge detector memorizes the counter value in the CAP1A register. The same occurs with the current i_{tank} in the CAP2A register. This value is hold by a sample and hold register and the counter is reseated every cycle. This reseat is realized at $0.5/f_{sw}$ seconds after the start of every cycle to avoid its coincidence with a commutation. The frequency of the time base counter is set to 100 MHz and, thus, the minimum time delay that can be computed is 10 ns (t_{clock}).

In Section 3.2.5, it was explained that the inverters usually commutate at a higher frequency than the resonant frequency to avoid the reverse recovery

129

of diodes (inductive switching). Therefore, during these simulations, the initial switching frequency is set to 175 kHz and the time delay reference is positive.

Two cases have been simulated to illustrate the influence of the time delay and dead-time in the control's performance:

- Case 1: The system is simulated with a low dead-time and time delay, 0.290 μs and 0.117 μs respectively.

- Case 2: The system is simulated with a high dead-time and time delay, 0.550 μs and 0.294 μs respectively.
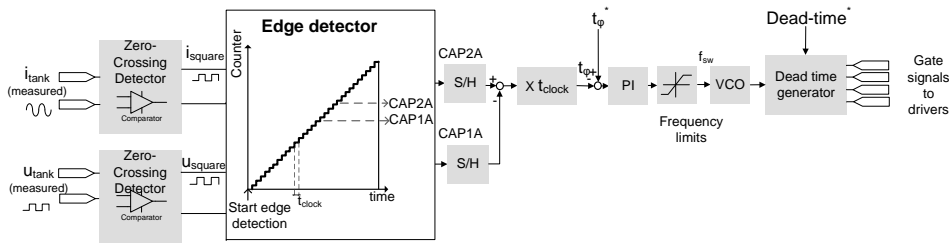
Figure 5.5: Scheme of the modeled system.

Simulation results

In Figure 5.6, the capture module output for the rising edges (CAP1A for the voltage and CAP2A for the current), the measured time delay between voltage and current and the switching frequency are shown for Case 1 (low dead-time and time delay reference). Figure 5.8 shows the zoom of the same parameters when the steady-state is reached and Figure 5.10 shows u_{tank} and i_{tank}, their synchronous square-waveforms and the counter and the capture modules for the rising edges. Figures 5.7, 5.9 and 5.11 show the same variables for Case 2 (high dead-time and time delay reference).

Observing the commutation frequency in Figures 5.6 (Case 1) and 5.7 (Case 2), the frequency starts at 175 kHz in both cases and the behavior is similar. However, in Case 2, the register corresponding to the voltage rising edge (CAP1A) and the time delay have abrupt variations. In case of the register corresponding to the current rising edge (CAP2A), the value is quite stable and with a similar behavior in both cases.

5.2 Software phase-locked loop principles and description
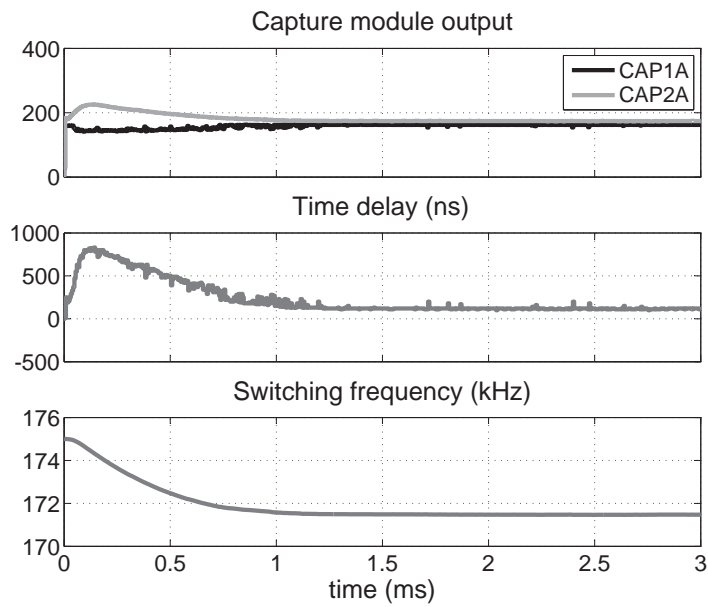
Figure 5.6: Simulation results for Case 1 (dead-time of 0.290 μs and time delay of 0.117 μs), 3 ms.
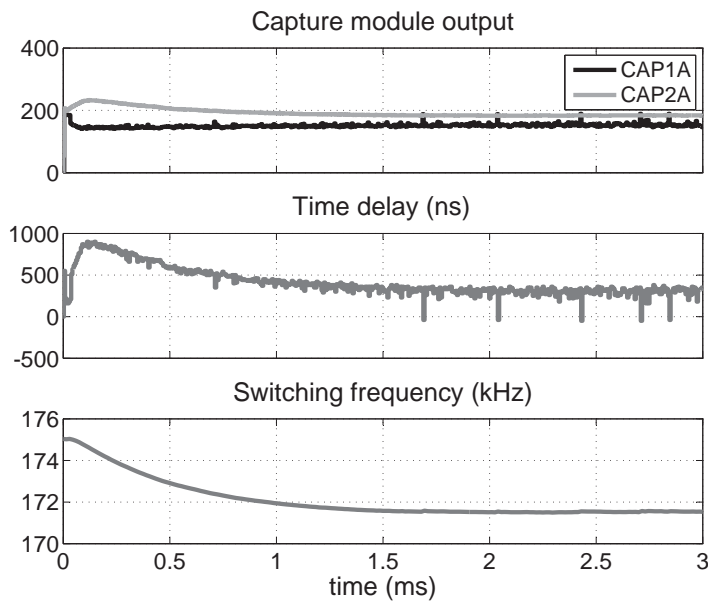
Figure 5.7: Simulation results for Case 2 (dead-time of 0.550 μs and time delay of 0.294 μs), 3 ms.

131
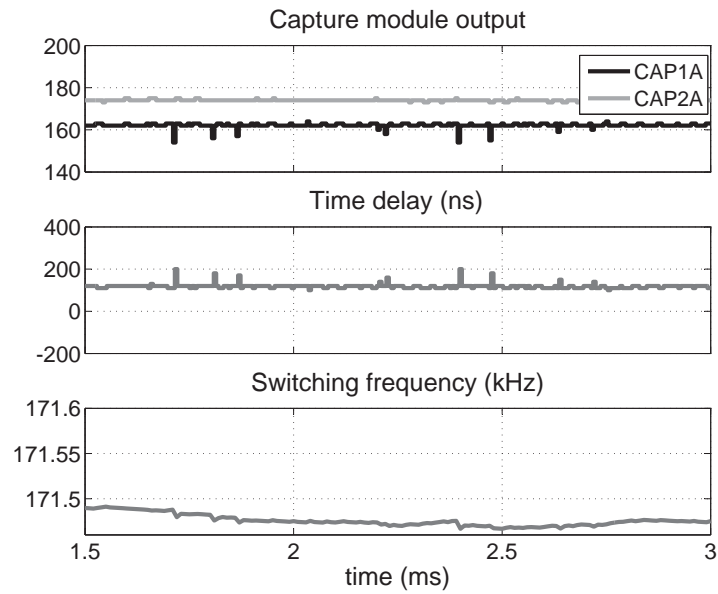
Figure 5.8: Simulation results for Case 1 (dead-time of 0.290 μs and time delay of 0.117 μs), steady-state from 1.5 to 3 ms.
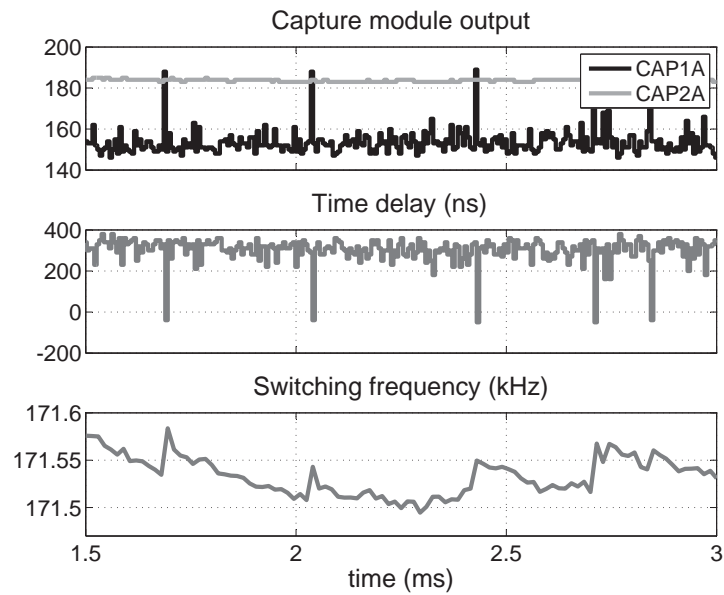
Figure 5.9: Simulation results for Case 2 (dead-time of 0.550 μs and time delay of 0.294 μs), steady-state from 1.5 to 3 ms.

5.2 Software phase-locked loop principles and description
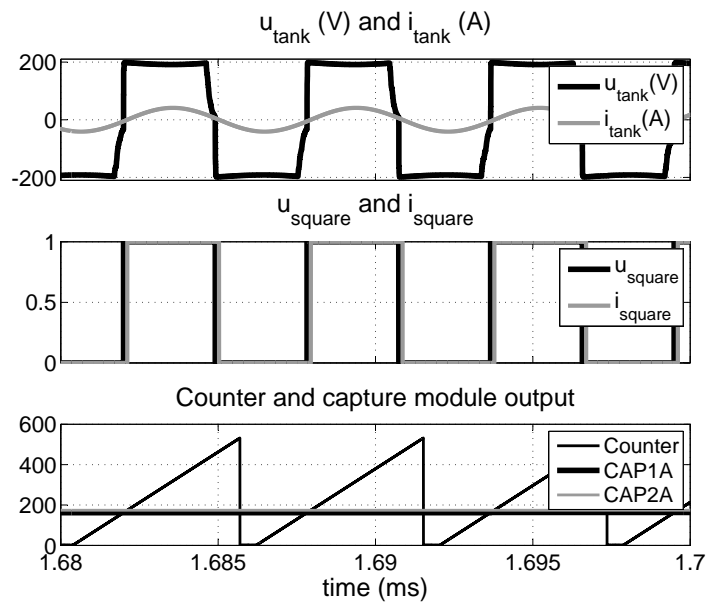
Figure 5.10: Simulation results for Case 1 (dead-time of 0.290 μs and time delay of 0.117 μs), zoom.
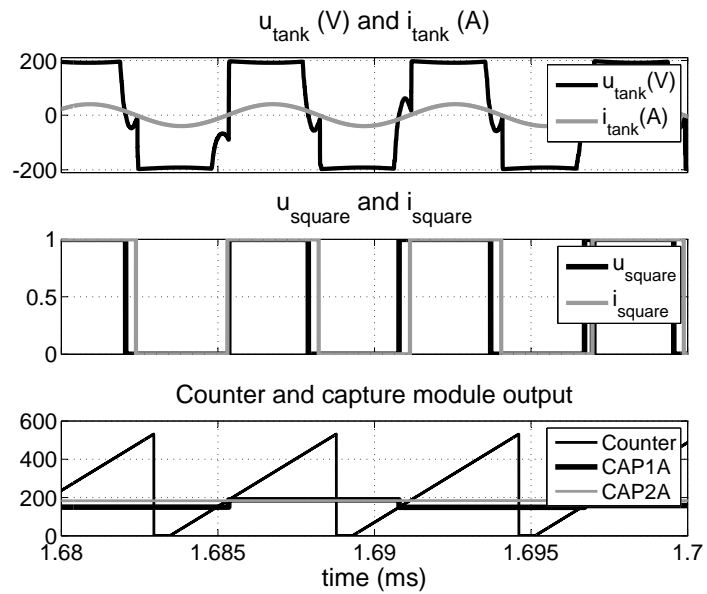
Figure 5.11: Simulation results for Case 2 (dead-time of 0.550 μs and time delay of 0.294 μs), zoom.

133

These sudden changes in CAP2A and in the time delay can be better observed in Figures 5.8 and 5.9, which are a zoom of the same variables between 1,5 and 3 ms. Observing these figures, there is a sudden change in CAP1A value for Case 2. This sudden change causes variations in the time delay value and in the commutation frequency, fact that is reasonable considering the control presented in Figure 5.5.

The abrupt change of CAP1A value in Case 2 is due to the shape of the voltage waveform u_{tank}, which is not monotonous during the commutation. Observing Figure 5.10, in the Case 1, u_{tank} has a monotonous rising slope during the commutation. That occurs because the dead-time is low and the turn-on of switches $SW1$ and $SW4$ occur before the current i_{tank} changes polarity. Consequently, CAP1A value is quite constant. Observing Figure 5.11 for Case 2, the voltage u_{tank} has a non monotonous rising slope during the commutation. That is because the dead-time is too high and the current changes polarity,discharging the parasitic capacitances before the turn-on of SW1 and SW4. This change in the slope cause unwanted, though not critical, variations in the phase-shift and, thus, in the commutation frequency.

Case 2 represents a limit situation because this change of slope takes place close to zero. Thus, depending if it occurs before or after u_{tank} changes polarity, it creates a great variation on CAP1A register, as shown in Figure 5.11.During normal operation, this situation is not common because dead-time references are low. Moreover, the larger the phase-shift (time delay), the larger the switched current and, thus, the chances that the voltage polarity is reversed are reduced. Nevertheless, it has to be taken into consideration to avoid potential uncontrolled situations. Thanks to the flexibility of the software PLL, this situation can be prevented with the configuration of an alarm that warns that two zero-crossings are too close to each other. This alarm would warn the user that the dead-time and phase-shift values should be changed.

5.3 Implementation and experimental results

The microcontroller chosen to implement the software PLL is a TMS320-F2808 DSP from Texas Instruments [103]. This microcontroller integrates all the peripherals needed (PWM, ADC, digital to analog converters and communications) and is flexible for reprogramming, fast in treating digital signals and sturdy against perturbations. It also incorporates an enhanced capture module (eCAP module) with a 32-bit time base and 100 MHz system clock, 4 event time-stamp registers (each of 32 bits) and edge polarity

selection that can be used for implementing the software PLL. Even though
this control can be realized easily with this DSP, it has to be noted that its
implementation can be also realized with other DSPs or with FPGAs with
higher computing performance.

The control has been tested in a real industrial application of continuous
wire heating with a converter designed by CITCEA-UPC, shown in Figure
5.12. The system is a 25 kVA and 250 kHz converter with a series resonant
tank with similar characteristics to the simulated in the previous section in
Table 5.1.

Figure 5.12: Equipment tested in an industrial application of continuous
wire heating.

A simplified diagram of the implemented control is shown in Figure 5.13.
This control scheme is based on the proposed control in Figure 5.4. The
voltage and current square-waveforms u_{square} and i_{square}, obtained from
u_{tank} and i_{tank}, are connected to the capture unit of the microcontroller
and the instant at which their rising/falling edges occur are memorized in
registers (CAP1A and CAP1B registers for the voltage and CAP2A and
CAP2B for the current). In this case, there is an interruption activated
by the time base of the PWM at $0.75/f_{sw}$ that calculates the time delay
(t_φ), calculates the switching frequency, updates the registers and reseats
the counter. The time delay between voltage and current is calculated with
the average value of the substraction of registers CAP2A minus CAP1A and
CAP2B minus CAP1B. Then this value is multiplied by t_{clock} (10 ns). It

135
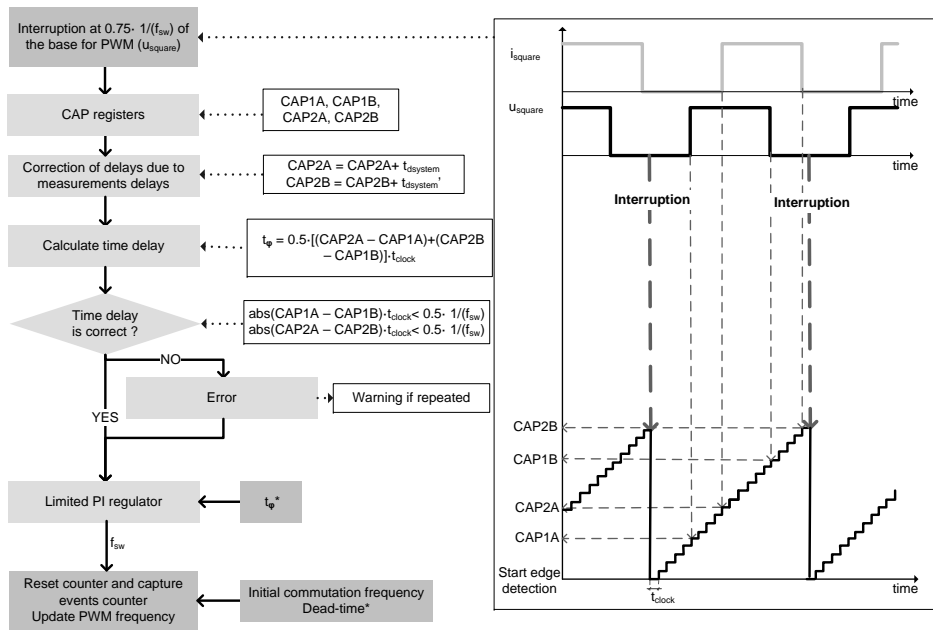
Figure 5.13: Control scheme implemented in the microcontroller.

can be observed in this figures how there is a small correction of the time delays due to the delays of the measurements (amplifiers, fiber optic) which is computed by adding a delay to CAP2 registers.

To validate that the time delay acquired is correct it has to be verified that the difference between two rising/falling edges is higher than half of the commutation period $(1/f_{sw})$. If the difference is minor it means that both rising/falling edges are too close to each other, the frequency is not varied and an error counter increases. In case that this error counter arrives to a limit defined by the user, the control stops the converter's operation and warns the user.

This error can occur when the initial commutation frequency is far away from the resonant frequency and the current is so small that generates false zero-crossings. In this case, the user just has to change the initial commutation frequency register until the system is able to track the resonant frequency. Another situation that can lead to this error, is the case described in Case 2 during the simulations, in which the voltage rising slope crosses zero twice.

One of the advantages of this software PLL is that allows the user to

distinguish both situations. For example, in case that the current zero-crossings are too close to each other, a warning text explaining that the initial commutation frequency is away from resonance warns the user. In case that the voltage zero-crossings are too close to each other, a warning text explaining that the time delay and dead-time references are too high can be programmed. Any warning can be sent by the DSP through the serial communication or another industrial communication like CAN to a programmable logic controller (PLC) that can show the warning through a display.

The proposed control system has been tested for different dead-times and time delays. The voltage u_{tank} and the current i_{tank} are shown for some of these tests in Figures 5.14, 5.15 and 5.16.

In Figure 5.14, the dead-time and time delay references are set to 0.45 μs and 0.2 μs respectively. Under these circumstances, the dead-time is small and the voltage is forced by the opposite switches' turn-on to cross zero before the current. The converter is able to maintain the time delay, even when the load changes due to the variation in material's properties. This situation is similar to the simulations in Case 1, in which the dead-time and time delay are low.
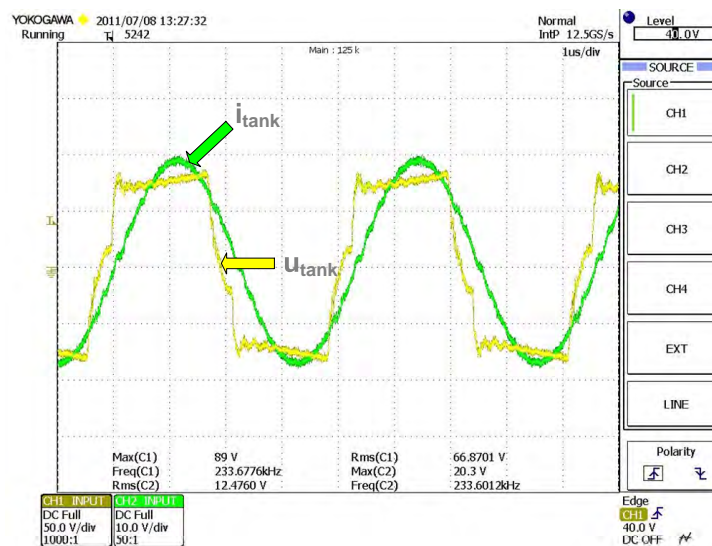
Figure 5.14: i_{tank} and u_{tank} for a dead-time of 0.45 μs and the time delay of 0.2 μs.
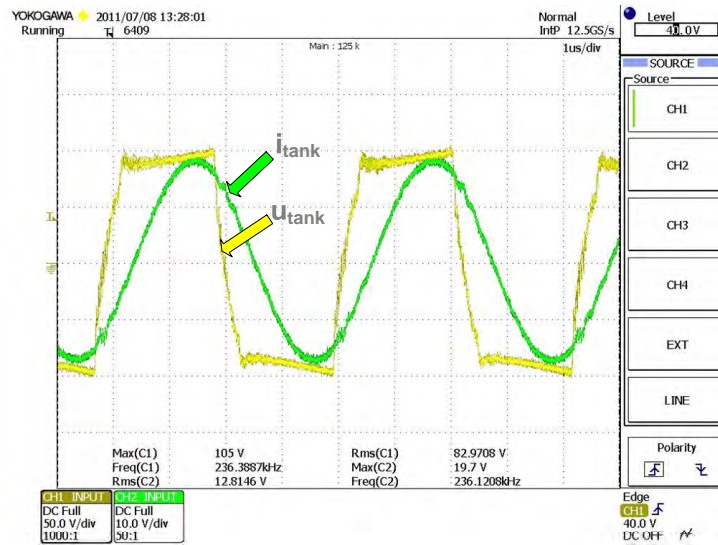
Figure 5.15: i_{tank} and u_{tank} for a dead-time of 0.51 μs and the time delay of 0.2 μs.
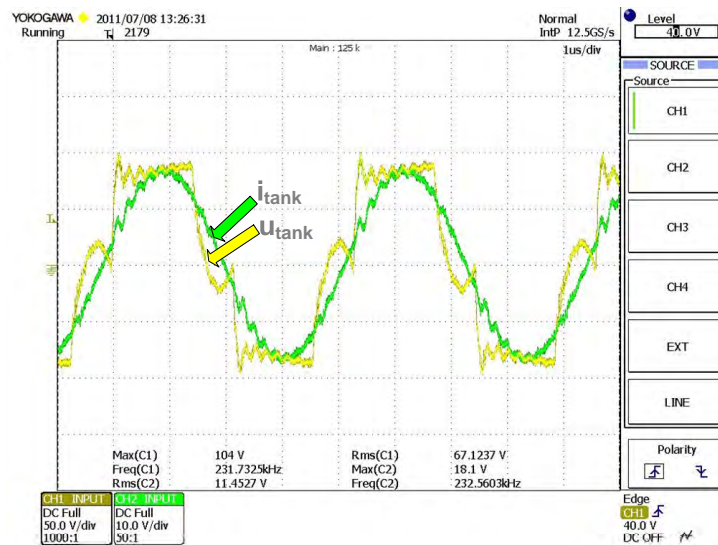
Figure 5.16: i_{tank} and u_{tank} for a dead-time of 0.75 μs and the time delay of 0.3 μs.

5.3 Implementation and experimental results

In Figure 5.15, the dead-time is increased to 0.51 μs. In this case, u_{tank} reaches U_e, the diodes are forward-biased and the transistors are turned-on with ZVS. Then the current changes polarity and the diodes are blocked with ZCS. This is the optimal commutation sequence for a VFSRI, as explained in Section 3.2.5.

In Figure 5.16, the dead-time is increased to 0.75 μs. Under these circumstances, the voltage slope is not monotonous and the change of slope is close to zero, similar to Case 2 during the simulations. In this case, the control detects voltage rising edges too close to each other, the commutation frequency is not varied and the PLL warns the user. Many tests have been performed with different references and uncontrolled situations have not occurred.

During the experimentation, the software PLL has been tested with different tanks, voltages, currents and references, showing a good performance under different situations. It has been observed that the results obtained are similar to those obtained during the simulations, solving the case at which the voltage slope is not monotonous. It has also been observed that the system is able to reach a time delay reference, even when the initial commutation frequency is a 25 % higher than the resonant frequency. Moreover, in case the initial frequency is too far from the resonant frequency and there are false current's zero-crossings, the converter warns the user and the initial frequency can changed by software through a preprogrammed human machine interface. The control system has been tested with tanks in the range of 50 kHz to 250 kHz without any change in converter's hardware and obtaining good performance results.

The major benefit of this control system is to allow a great flexibility, as all the parameters can be changed dynamically by software (dead-time, time delay, starting frequency, etcetera). Therefore, this system provides more flexibility and adaptability to different situations compared to the classical control methods introduced in Section 5.2. Moreover, the possibility of changing dynamically the variables blazes the way to the programming of more complex control algorithms, as for example an optimal commutation sequence similar to the explained in Section 3.2.5.

It has to be noted that the control system presented is verified for a VFSRI, but can be also used for CFPRI. The only change that must be realized is the measuring and adaptation of signals.

5.4 Summary

In IH, the converter measures and imposes the phase-shift between two signals for commutating at resonant frequency. In case of VFSRI, the converter measures the phase-shift between u_{tank} and i_{tank} and varies the frequency until the phase-shift is approximately zero. This control is realized by the converter thanks to a PLL system.

Most authors in IH field use semianalog PLL systems to control the converter, the majority based on the CMOS 4046 integrated circuit family. These systems are affected by the spread of component parameters, component degradation or variation with temperature. Moreover, in case of load changes, the systems have to be tuned. Considering all-digital or software PLL systems, there are very few experiences in IH field, most of them using FPGA.

In this chapter, a DSP-based software PLL is proposed. This control system measures the phase-shift by acquiring the rising edges of voltage and current with the edge detector provided by the microcontroller. This software PLL allows a control with less analog components, avoiding their drawbacks and offering more flexibility to the system.

The proposed software PLL has been simulated, noticing that in case of large time delays and dead-times, u_{tank} has a non-monotonous slope during the commutation which can cause sudden changes in the control variables.

The software PLL has been tested in a real industrial application of continuous wire heating and the control instability detected in the simulations has been solved by software. The converter detects when the difference between two rising edges is lower than half of the commutation's period and the user is warned.

The system has been tested with different tanks and references, providing a good response for different conditions and evidencing its flexibility in a real industrial application. The converter allows the final user to change the parameters by software, in this case through a PLC connected to the DSP. The system also permits a better adaptation of the converter to diverse requirements, an easy implementation and the use of debugging systems that allow faster designing. Moreover, it opens the way to more complex control algorithms, since the time delay, dead-time, frequency and other parameters can be changed dynamically during the heating process.

Chapter 6

Design of a load-adaptive phase-locked loop

6.1 Introduction

IH converters commutate close to resonant frequency to obtain the maximum power and reduce switching losses. In case of VFSRI, the commutation process is determined by the transistor's parasitic capacitors, snubbers and layout capacitance. These capacitances have to be charged before the turn-on of the transistors and the change of polarity of the load's current to ensure soft-switching. To ensure this sequence, the phase-shift and the dead-time have to vary depending on the load.

In this chapter, a load-adaptive PLL based on the software PLL explained in Chapter 5 is presented. This control system allows the variation of the phase-shift and the dead-time to ensure soft-switching. First, in Section 6.2, the commutation process is explained, presenting the proposed control system and simulating it. Afterwards, in Section 6.3, the implementation of this system is exposed and the experimental results are presented. Finally, the chapter is summarized in Section 6.4.

6.2 Commutation process and load-adaptive phase-locked loop description

6.2.1 Commutation process

In Section 3.2.5, the influence of the parasitic capacitances (including transistor's parasitic capacitors, snubbers and layout capacitances) during the commutation process is exposed. It is shown that, to have transistor's ZVS and antiparallel diodes' ZCS, Equations 3.21 and 3.22 have to be accomplished for β and φ. Taking this into consideration, in Figure 6.1, the com-

mutation process considering the parasitic capacitances, the dead-time (t_d) and phase-shift (t_φ) is shown.
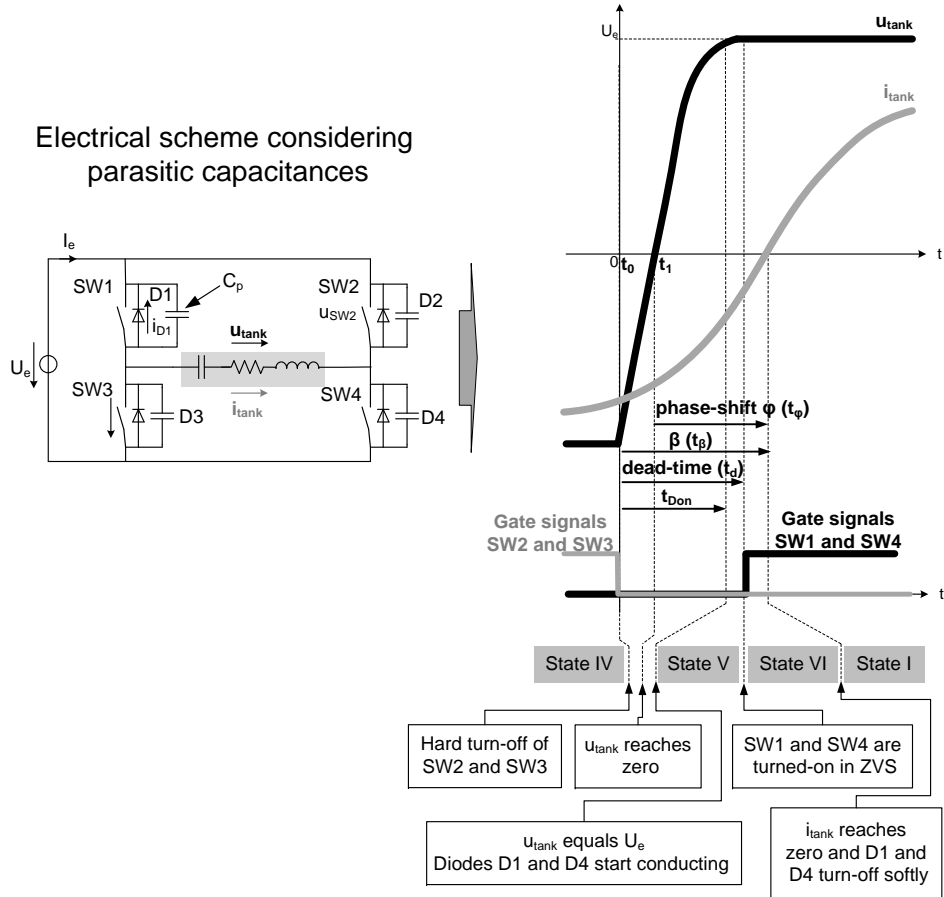
Figure 6.1: Output waveforms and sequence to have ZVS and ZCS commutating above resonance considering dead-time and phase-shift.

The sequence of events to have soft-switching is the following:

- Switches SW2 and SW3 turn-off hardly.

- The parasitic capacitance, C_p, of SW2 and SW3 charge, while C_p of switches SW1 and SW4 discharge. The voltage u_{tank} reaches U_e.

- Diodes D1 and D4 are forward-biased at t_{Don}.

6.2 Commutation process and load-adaptive phase-locked loop description

- Switches SW1 and SW4 are turned-on at t_d with ZVS because their antiparallel-diodes are conducting.

- The current i_{tanc} changes polarity at t_φ, blocking the antiparallel-diodes D1 and D4 with ZCS.

Equations 3.21 and 3.22 are obtained supposing the limit situation at which the diodes are forward-biased, the switches' turned-on and the change of polarity of i_{tank} are immediately consecutive (Appendix B). That is

$$t_{Don} \approx t_d \approx t_\beta \tag{6.1}$$

Therefore, considering t_d and t_φ instead of β and φ, Equations 3.21 and 3.22 turn into

$$t_d \geq \frac{1}{\omega} arccos \left(1 - \frac{2\omega U_e C_p}{\hat{i}_{tank}} \right) \tag{6.2}$$

and

$$t_\varphi \geq \frac{1}{\omega} arccos \left(1 - \frac{\omega U_e C_p}{\hat{i}_{tank}} \right) \tag{6.3}$$

Observing these equations, it is noticed that the control has to adapt the dead-time and phase-shift to the load conditions to ensure soft-switching. Nevertheless, most authors do not incorporate the effect of this capacitance during their control, e.g. [99].

Some authors describe and analyze the influence of this capacitance for different operating conditions, like in [104–106]. In case of [59], this influence is considered in the control by introducing a constant phase-shift delay for a nominal condition. In [65], the minimum dead-time is calculated considering the capacitor's influence, but it is still constant and calculated for a nominal condition. Finally, some authors suggest a load-adaptive control, in which the phase-shift varies linearly depending on the current in [64] or depending on the charge of an equivalent capacitor in [35, p. 96]. However, in all of them, the control is based on analog circuits and the implementation is complex, nonflexible and subjected to the degradation and part spread, typical of analog components.

6.2.2 Load-adaptive phase-locked loop

In order to overcome the drawbacks derived from an analog load-adaptive control, the software PLL presented in Chapter 5 has been used. This PLL

143

is all-digital and is implemented by software, allowing an easier and more flexible implementation.

The basic scheme of the control system proposed is shown in Figure 6.2. In this case, the control variables are the current i_{tank}, the voltage u_{tank} and the power supply voltage U_e. The equivalent capacitance of the switches (C_p) is supposed to be constant and the phase-shift (t_φ) and dead-time (t_d) references are set according to the load conditions imposed by Equations 6.2 and 6.3. The phase-shift is measured using the edge detector provided by the microcontroller. Then, it is compared with the reference and a PI controller is used for calculating the commutation frequency. Finally, the gate signals to drivers incorporating the dead-time reference are obtained.
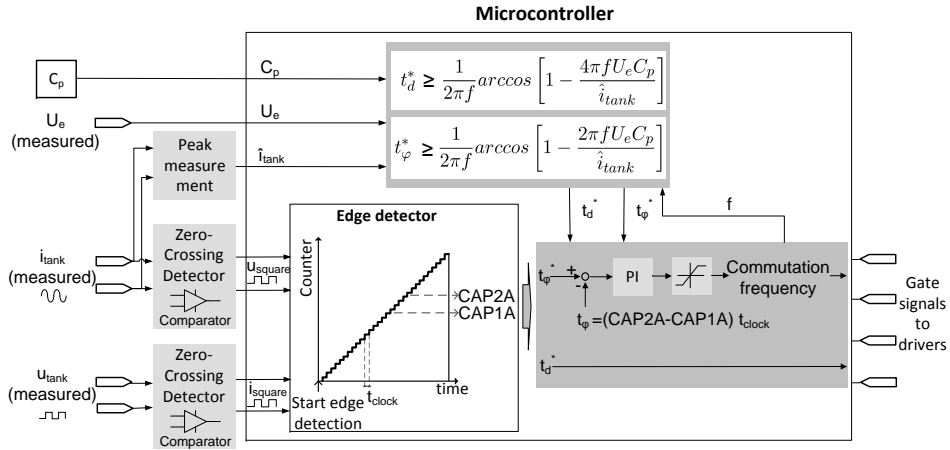
Figure 6.2: Proposed load-adaptive PLL.

6.2.3 Simulations

Simulation model

In Figure 6.3, the scheme used for simulating the load-adaptive PLL is shown. Bearing in mind that the minimum t_d and t_φ to have soft-switching are obtained from the equalities contained in Equations 6.2 and 6.3, the values of t_d and t_φ have to be higher. Thus, during the simulation, the dead-time and phase-shift are calculated according to these equalities, but the result is increased by a gain, k_d for the dead-time and k_φ for the phase-shift.

6.2 Commutation process and load-adaptive phase-locked loop description

It can also be observed in this figure that $\hat{i}_{tank}$ is limited. The aim of this limitation is to avoid low currents that can compute high dead-times and phase-shift values. As regards to the dead-time reference, it is also limited, but in this case with the aim to avoid a lower value than the minimum dead-time that can cause short-circuit. The phase-shift is also limited to avoid negative phase-shifts that can cause capacitive switching and the frequency is limited to the inverters' frequency range.
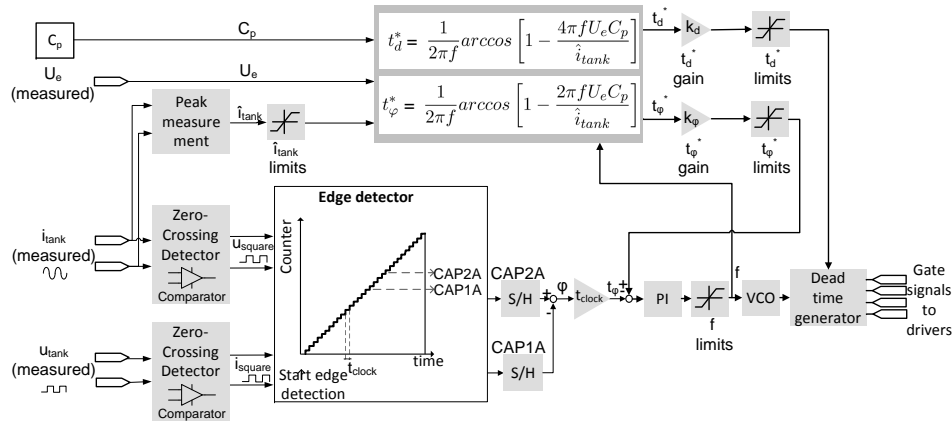
Figure 6.3: Simulation of the load-adaptive PLL.

Table 6.1: Parameters of the simulated system.

	Parameter	Value
	Capacitance	10.38 nF
Resonant tank	Inductance	34.97 μH
	Resistance	9.82 Ω
	Resonant frequency	83.53 kHz
$\hat{i}_{tank}$	Upper limit	42 A
	Lower limit	3 A
t_φ	Upper limit	10 μs
	Lower limit	0.2 μs
t_d	Upper limit	2.5 μs
	Lower limit	0.1 μs
	Upper limit	100 kHz
f	Lower limit	70 kHz
	Initial	84.5 kHz

The control has been simulated with MATLAB-SIMULINK$^{©}$ and the parameters of this simulation are shown in Table 6.1. It has to be noted

that the initial frequency is set higher than the resonant frequency to avoid capacitive switching.

Simulation results

The system has been simulated for different voltages and parasitic capacitances (C_p) to evaluate the control's performance. Figure 6.4 shows the current I_{tank} in RMS, the phase-shift reference t_φ^* and the dead-time reference t_d^* for the case with the voltage U_e equal to 100 V and C_p 15 nF. For the same case, u_{tank}, i_{tank}, the current in the antiparallel-diode of SW1, the gate signals of SW1 and the zero-crossing of i_{tank} are plotted in Figure 6.5. In Figures 6.6 and 6.7, the same variables as in Figure 6.4 are shown, but varying the voltage U_e to 30 V and 200 V respectively. Finally, Figures 6.8 and 6.9 show the same variables, but at 100 V and with different C_p values, 25 nF and 35 nF respectively.

During the simulations, it was observed that, for the case in which k_φ and k_d are equal to 1, the current i_{tank} changes polarity before the switches' turn-on. This change of polarity happens almost at the same time as the turn-on, so, to allow the optimum sequence of events (seen in Section 6.2.1), the phase-shift gain (k_φ) is increased to 1.05.

In Figure 6.4, the current value increases arriving to a steady-state. The phase-shift and dead-time values do not vary much during this process and neither does the frequency. Observing Figure 6.5, the antiparallel-diode D1 is forward-biased, afterwards the transistor SW1 turns-on and, then, the current i_{tank} changes polarity, thus, having soft-switching.

In case of decreasing the voltage U_e to 30 V, shown in Figure 6.6, or increasing it to 200 V, shown in Figure 6.7, the phase-shift and dead-times are almost equal at the steady-state. The current value is different for the three cases (Figures 6.4, 6.6 and 6.7), but the voltage-current ratio is almost the same. That is because the load at the resonant frequency is equal to the resistance of the tank (Section 3.2.1). Thus, the ratio is constant in the three cases and so it is the phase-shift and the dead-time if the other parameters are maintained constant, as shown in Equations 6.2 and 6.3.

In case of increasing the parasitic capacitance C_p to 25 nF and 35 nF, Figures 6.8 and 6.9 respectively, the phase-shift and dead-time increase. The higher the value of the capacitance, the higher the values of phase-shift and dead-time. Thus, there is a slight increase of 750 Hz on the commutation frequency in Figure 6.9 compared to Figure 6.8.

6.2 Commutation process and load-adaptive phase-locked loop description
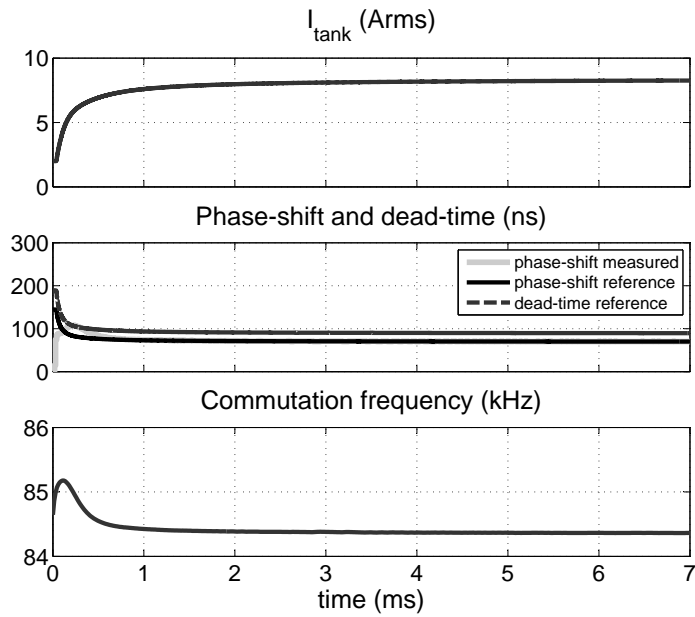
Figure 6.4: Simulation results for U_e 100 V and C_p 15 nF, 7 ms.
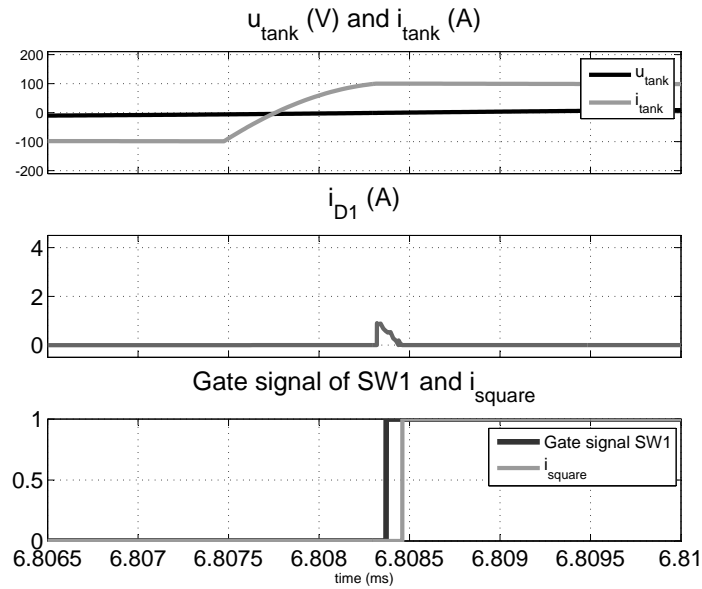
Figure 6.5: Simulation results for U_e 100 V and C_p 15 nF, steady-state from 6.8065 to 6.81 ms.
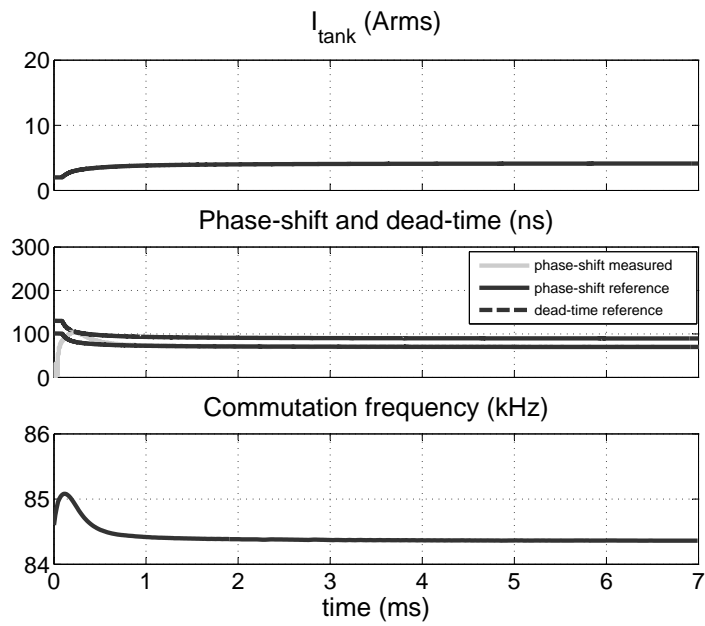
Figure 6.6: Simulation results for U_e 30 V and C_p 15 nF, 7 ms.
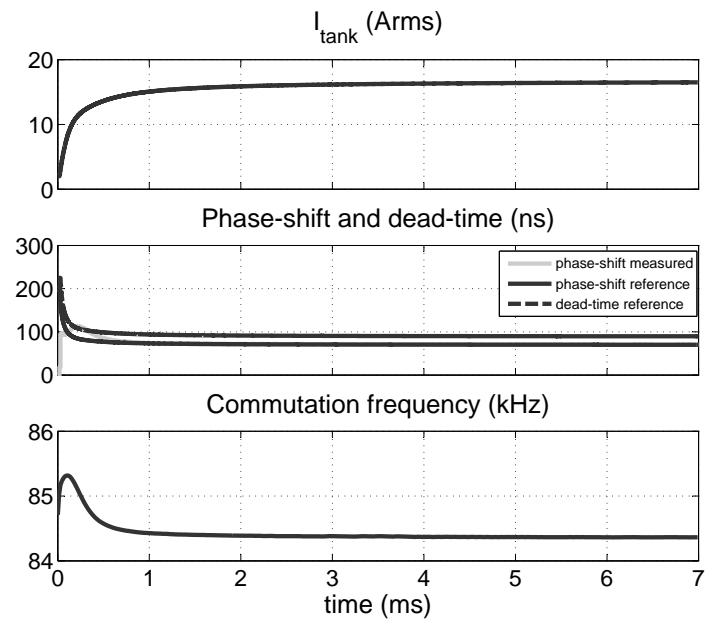
Figure 6.7: Simulation results for U_e 200 V and C_p 15 nF, 7 ms.

6.2 Commutation process and load-adaptive phase-locked loop description
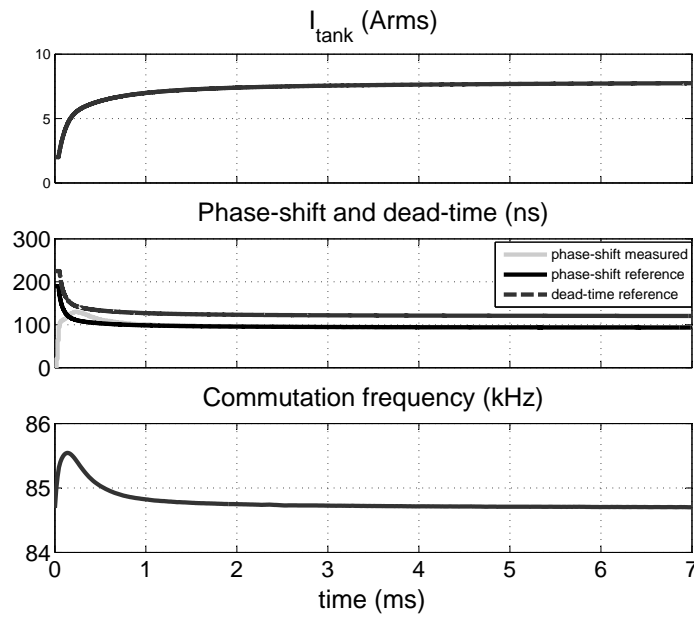
Figure 6.8: Simulation results for U_e 100 V and C_p 25 nF, 7 ms.
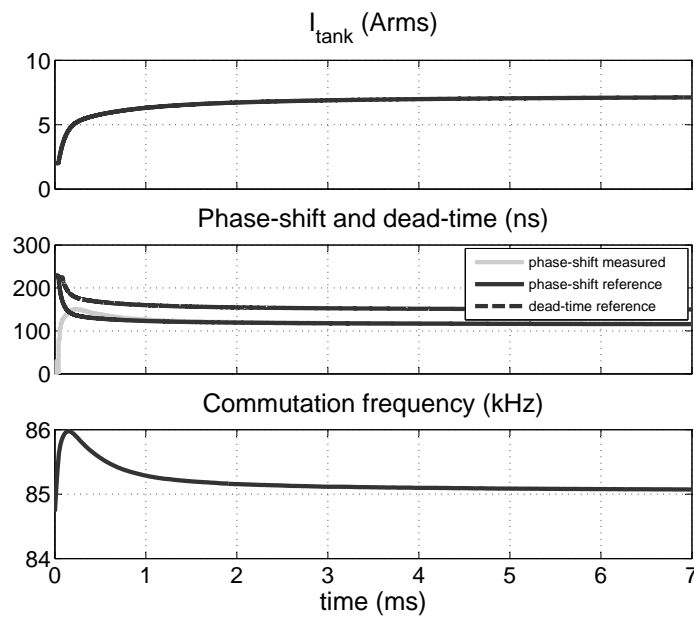
Figure 6.9: Simulation results for U_e 100 V and C_p 35 nF, 7 ms.

149

6.3 Implementation and experimental results

6.3.1 Experimental setup and control implementation

Hardware implementation

To test the load-adaptive PLL, the experimental setup used in Section 4.3.1 for the multichannel converter and shown in Figure 6.10 has been used.
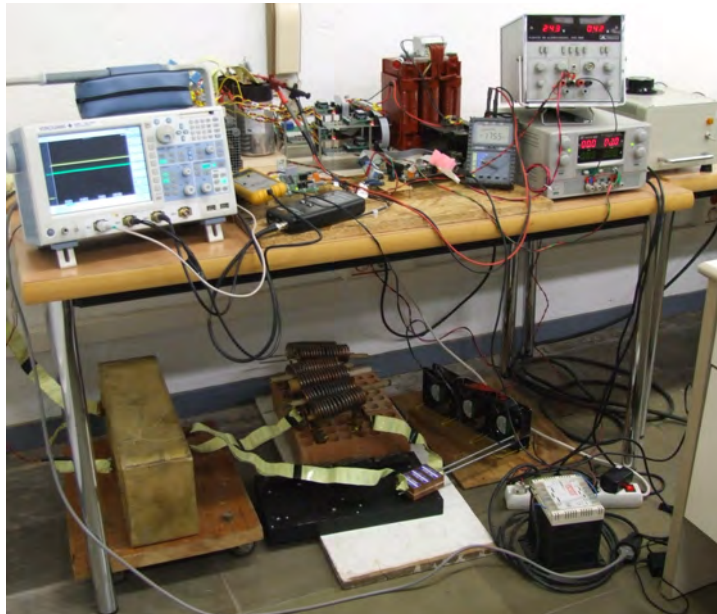
Figure 6.10: Experimental setup used for the load-adaptive control.

Regarding the variables needed for the control, the voltage U_e is measured through a Hall-effect transducer and acquired by the microcontroller's ADC. The current peak $\hat{i}_{tank}$ is obtained using a current transformer that generates a voltage on a resistor, which is rectified as shown in Figure 6.11. The voltage obtained is proportional to the current peak and is measured with the microcontroller's ADC.

With regards to the phase-shift measurements, u_{square} and i_{square} signals are obtained using a resistor and a comparator, as shown in Figure 6.11, and acquired by the microcontroller using the edge detector module, as explained in Chapter 5.
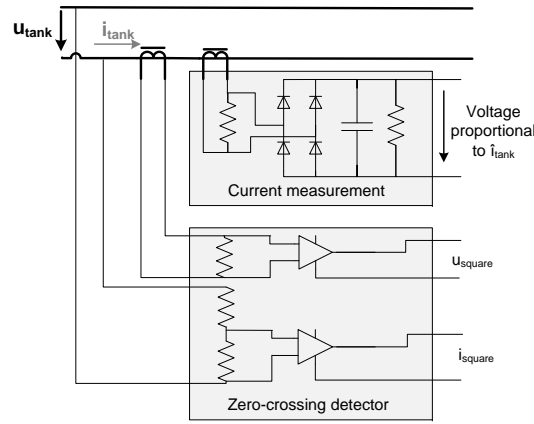
Figure 6.11: Peak current measurement and zero-crossing detectors.

Software implementation

Considering the control program, the *arcos* function in Equations 6.2 and 6.3 have been implemented using its 3rd degree Taylor series expansions. This series expansion is defined for an interval between -1 and +1 and, the closer to the limits, the worst the approximation is. Considering low angles in which the cosine is close to 1, the approximation of the Taylor expansions is not very accurate. Thus, the equations have been implemented using the series expansion of *arcsin*

$$arcsin\left(x\right) \approx x + \frac{1}{6}x^3 + O(x^5) \quad |x| \le 1 \tag{6.4}$$

and assuming the trigonometric identity

$$sin(x)^2 + cos(x)^2 = 1 \tag{6.5}$$

Therefore, Equation 6.2 turns into

$$t_d = \frac{1}{2\pi f} arcsin\left[\sqrt{1 - \left(1 - \frac{2\omega U_e C_p}{\hat{i}_{tank}}\right)^2}\right] \approx \frac{1}{2\pi f}\sqrt{1 - \left(1 - \frac{2\omega U_e C_p}{\hat{i}_{tank}}\right)^2}$$
$$+ \frac{1}{12\pi f}\left[\sqrt{1 - \left(1 - \frac{2\omega U_e C_p}{\hat{i}_{tank}}\right)^2}\right]^3 \tag{6.6}$$

and Equation 6.3 into

$$t_\varphi = \frac{1}{2\pi f} arcsin \left[\sqrt{1 - \left(1 - \frac{\omega U_e C_p}{\hat{i}_{tank}} \right)^2} \right] \approx \frac{1}{2\pi f} \sqrt{1 - \left(1 - \frac{\omega U_e C_p}{\hat{i}_{tank}} \right)^2}$$

$$+ \frac{1}{12\pi f} \left[\sqrt{1 - \left(1 - \frac{\omega U_e C_p}{\hat{i}_{tank}} \right)^2} \right]^3 \quad (6.7)$$

One of the main difficulties on this type of control is to obtain C_p value. In this case, the IGBT used are the SKM100GB128D from Semikron and the value of the parasitic capacitance C_{CE} is obtained from

$$C_{CE} = C_{oes} - C_{res} \quad (6.8)$$

being C_{oes} the output capacitance and C_{res} the Miller capacitance [107, p. 79], both of them with a complex voltage dependency.

Observing the datasheet of the SKM100GB128D IGBT [108], there is not much information about these capacitances. There is just a value for a nominal condition giving a maximum value of C_{CE} of 0.4 nF (for V_{CE} 25 V, V_{GE} 0 V and at 1 MHz), but, this value has a voltage dependency that can lead to an increase of even five times the given value when working at low voltage values. This is shown in [109] and in the application note of Semikron [110]. It can also be observed that this capacitance value tends to stabilize when the voltage increases. In this case, in order to avoid and minimize the effects of this varying capacitance, during the experimentation some snubbers with capacitances above 15 nF have been connected, therefore assuming C_{CE} is negligible.

6.3.2 Experimental results

The system has been tested for different voltages, frequencies and snubber capacitors to evaluate the control system's performance. First, the system is tested with a 80 kHz tank and a 15 nF snubber capacitor at a voltage U_e of 100 V and 200 V. The voltage u_{tank}, the current i_{tank} and the voltage of SW1 gate during turn-on are shown for these cases in Figures 6.12 and 6.13. After this, with the voltage U_e at 100 V, the snubber capacitance has been changed to 25 nF and 32 nF, shown in Figures 6.14 and 6.15. Finally, the system is tested with a 150 kHz tank at 100 V and with a 25 nF and 32 nF snubber capacitance and the results are shown in Figures 6.16 and 6.17. In all of these tests k_d is set to 1 and k_φ is set to 1.3 to ensure soft-switching.

6.3 Implementation and experimental results

In Figure 6.12, it is observed that the correct sequence of events to have switches' ZVS and diodes' ZCS is accomplished. In case of increasing the voltage to 200 V, as is shown in Figure 6.13, the values of phase-shift and dead time are similar and the soft-switching condition is still accomplished. The little influence of the voltage U_e on t_d and t_φ values was observed during the simulations in Section 6.2.3. However, in real cases, there is a slight variation because the load and the equivalent resistance vary with temperature.

In Figures 6.12, 6.14 and 6.15, the system is tested at 100 V with different snubber capacitances. In all the cases, the system is able to maintain ZVS and ZCS and the phase-shifts and dead-times increase with the capacitance.

In case of Figures 6.16 and 6.17, the same variables are shown, but increasing the resonant frequency of the tank to 150 kHz and using a C_p of 25 nF and 32 nF. In Figure 6.16, the soft-switching situation is accomplished, but in case of Figure 6.17 it is not. In this second figure, the dead-time is too low and the turn-on of SW1 occurs before its antiparallel diode is forward-biased, thus, commutating without ZVS. This situation is caused by the simplification realized with the Taylor series expansions. In this case, the value of frequency and capacitance is high and the angle of *arcsin* becomes close to 1 (Equation 6.4). Thus, the approximation realized by using the Taylor expansion is imprecise. For the case in Figure 6.17, the value in dead-time's *arcsin* is 0,99 (Equation 6.6) and the error produced is higher than 20 %.

It has to be noted that the system has shown a good performance during the experimentation for different cases. Moreover, it has proven the flexibility and the potential of the software PLL presented in Chapter 5 for the design of complex controls. It has to be noted that the last tests, with a high frequency and high C_p value, have been realized to evaluate the performance of the control system. However, the situation of Figure 6.17 is not usually found in a real IH application. The lower value of capacitance the better, because allows a lower phase-shift and, therefore, less consumption of reactive power. Additionally, the results of this test show that there is not ZVS, but the losses are still low because the voltage is close to U_e and there is ZCS of the antiparallel diodes. Nevertheless, in case of needing a better accuracy for this case, the angle is close to zero and the imprecision can be avoided by using the *arccos* Taylor expansion.

Figure 6.12: Simulation results for a 80 kHz tank, U_e 100 V and C_p 15 nF.
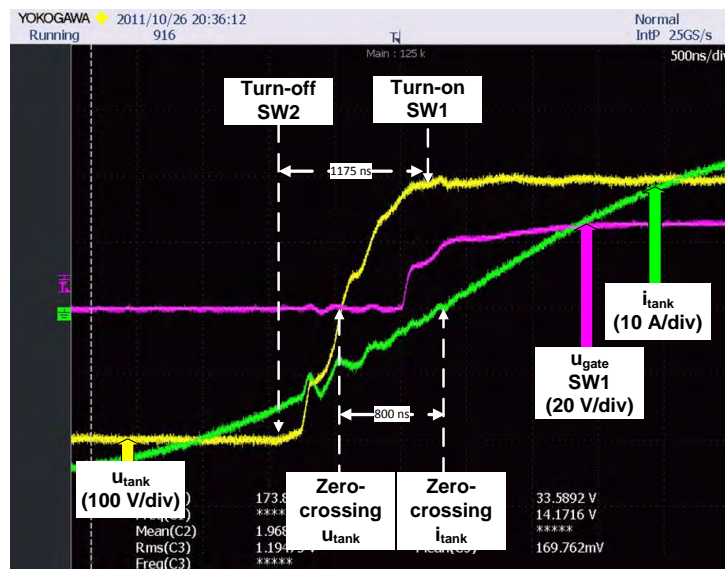
Figure 6.13: Simulation results for a 80 kHz tank, U_e 200 V and C_p 15 nF.

6.3 Implementation and experimental results
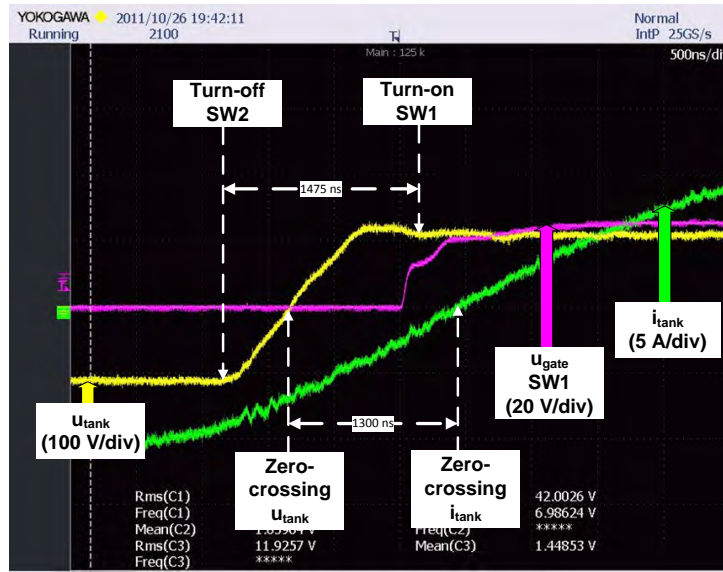
Figure 6.14: Simulation results for a 80 kHz tank, U_e 100 V and C_p 25 nF.
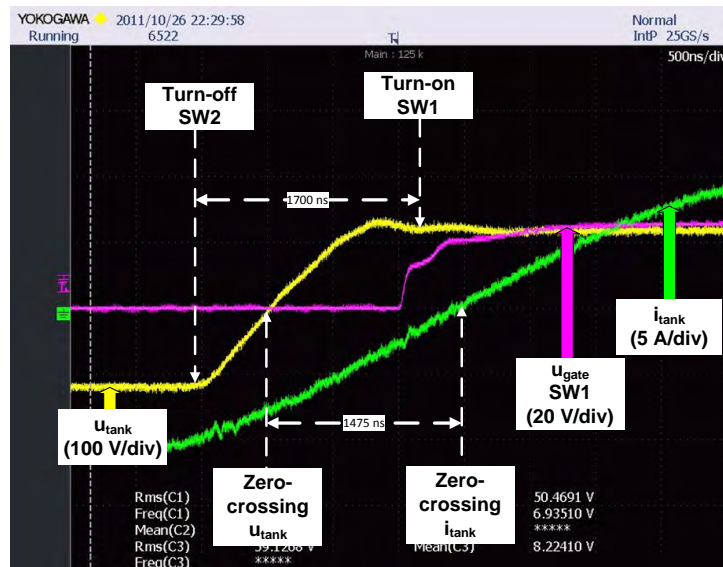
Figure 6.15: Simulation results for a 80 kHz tank, U_e 100 V and C_p 32 nF.
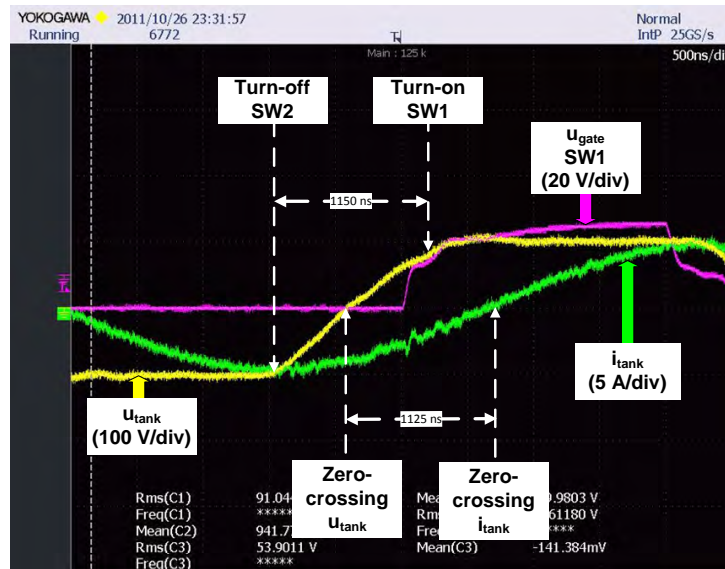
Figure 6.16: Simulation results for a 150 kHz tank, U_e 100 V and C_p 25 nF.
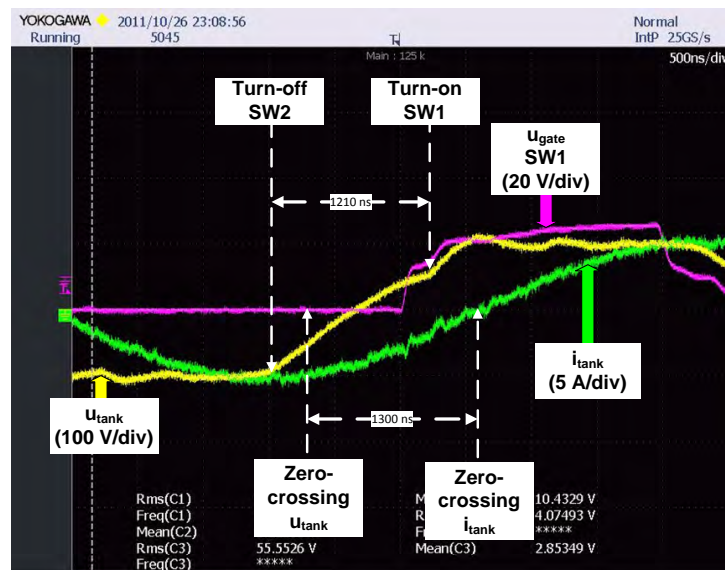
Figure 6.17: Simulation results for a 150 kHz tank, U_e 100 V and C_p 32 nF.

6.4 Summary

In VFSRI, the commutation process and the soft-switching are determined by the transistor's parasitic capacitors, snubbers and layout capacitance. To have soft-switching, these capacitances have to be charged before the turn-on of the transistors and the change of polarity of i_{tank}. In order to accomplish this sequence, the control has to adapt the dead-time and phase-shift to the load conditions during the heating process.

There are some authors analyzing the effect of these capacitances on the commutation process. Some authors propose some control methods based on analog solutions which are complex to implement and nonflexible.

In this chapter, a load-adaptive control for IH converters is presented. This system uses a software PLL, which provides the benefits of an all-digital and a programmable control system. The dead-time and the phase-shift between voltage and current imposed by the control are dependent on i_{tank}, U_e voltage, the commutation frequency and the parasitic capacitance C_p.

The control method has been simulated with different voltages and capacitances. It is observed that there is no influence on the phase-shift and the dead-time values in case of varying the voltage U_e, if the other variables are maintained constant. But, in case of varying the capacitance, the phase-shift and dead-time values increase and so does the final frequency.

The system has been implemented in an experimental setup designed by the author. One of the principal difficulties found during the control implementation has been the determination of the parasitic capacitance. In case of IGBTs, as well as in other semiconductors, their parasitic capacitances have a complex dependency on voltage. To solve this problem, snubber capacitors of higher value have been connected in parallel with the semiconductors.

The control has been tested under different conditions and loads, warranting ZVS and ZCS in most of the cases. In case of a high C_p value and high frequency, just ZCS is reached due to the simplifications done by the microprocessor during the calculations. However, these situations can be solved by software and, in any case, they are not usual in IH applications because imply a high consumption of reactive power.

The load-adaptive control system proposed in this chapter has shown a correspondence with the simulations, ensuring ZVS and ZCS for different loads and conditions and showing its reliability and flexibilty. Moreover, it

has proven the flexibility and the potential of the software PLL presented in Chapter 5 in the design of complex controls for IH applications.

Chapter 7

Modeling of a continuous induction wire hardening system considering the converter's performance

7.1 Introduction

The modeling of IH systems is a complex matter due to the number of fields involved and their interdependence. The properties of the workpiece are dependent on the temperature and the temperature is as well dependent on the magnetic fields. These magnetic fields, at the same time, depend on the current provided by the converter, which, finally, depend on the material properties and the converter control. This mutual influence between the thermal, electromagnetic and electric parameters leads to a difficulty in the modeling of these systems.

This complexity is sometimes solved by simplifying the converter to a constant source or reducing the inductor-workpiece to a constant load. These simplifications are a useful and practical method to solve the problem, but sometimes do not provide an accurate analysis of the overall system behavior.

In Chapter 2, the difficulty of modeling IH systems was discussed, explaining different methods of solving the electromagnetic-thermal problem. However, the converter-load interdependence during an IH process was not presented. In this chapter, this interdependence is studied and incorporated into this modeling. This modeling takes profit of classical approaches and commercial softwares, but including special considerations regarding the converter's performance.

First, in Section 7.2, a real industrial case is presented. This case is chosen for the modeling because presents a great change in workpiece properties that allow a better understanding of the converter-load coupling. Afterwards, in Section 7.3, the problem and the different solving methodologies are re-

viewed. In Section 7.4, another methodology that gives special attention to the converter's performance is explained. The model and the simulation results are presented in Section 7.5 and the experimental results are shown in Section 7.6. Finally, in Section 7.7, the whole chapter is summarized.

7.2 Continuous hardening and tempering of steel wires

One application of IH systems is the continuous hardening and tempering of steel wires, which involves the austenitizing, quenching and tempering of the wire. At the austenitizing stage, the wire is heated above the Curie temperature [1, p. 109] and its relative permeability decreases to one, becoming a non-magnetic material. Moreover, there is a maximum of specific heat at this temperature [2, p. 146].

As a result of this change in properties and, above all, due to the change in the permeability, the penetration depth increases and the efficiency of the process decreases (see Section 1.4.1). To avoid this situation, it is recommended to use two converters during the austenitizing process, especially in case of a continuous heating [2, p. 531]. The first of these converters has a lower frequency and is used for heating the wire below the Curie point, whereas the second, with a higher frequency, is used for heating the wire above the Curie point. A typical schematic configuration of this industrial process can be observed in Figure 7.1.
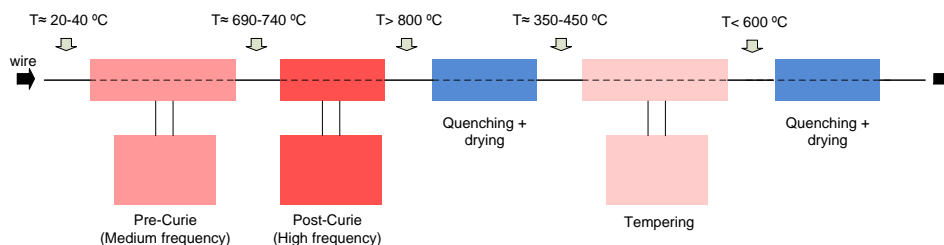
Figure 7.1: Schematic of a typical installation for continuous induction hardening of steel wire.

The above mentioned changes in material's properties affect the control and limits of the Post-Curie converter. In case of steel wires, crossing the Curie temperature causes a sudden decrease in the inductance value that can reach a 20%. But the parameter that affects the converter the most is the drop in the equivalent resistance, arriving up to 70% [111, 112]. This decrease in the equivalent resistance generates an increase in current that

must be considered during the design of the converter. This phenomenon takes place during the startup of the process and is stabilized afterwards. Nevertheless, in order to enter the Post-Curie zone and start working, the converter has to be able to give enough power with high resistance values when the temperature of the whole wire is below the Curie point.

The system modeled in this study is a Post-Curie system, that has to be able to pass from Pre-Curie to Post-Curie temperature and has to deal with the steel's properties change at the start-up. Studying and modeling this situation is interesting because there is a great change in the wire's properties and the interaction between the electrical and electromagnetic-thermal variables is strong.

7.3 The electrical and the electromagnetic-thermal approach

The complexity of IH systems modeling was introduced in Chapter 2. Its simulation involves electric, magnetic and thermal analysis in which the parameters and properties depend upon each other during the whole process. For instance, the magnetic permeability and the electric resistivity are dependent on the temperature of the heated material. Since the energy transferred to the workpiece is dependent on its electric and magnetic properties, the material's final temperature is as well dependent on them. The many fields involved and the difficulty in the analysis have led authors to two main differentiated approaches: electrical and electromagnetic-thermal analysis.

In case of the electrical approach, the equivalent circuit of the load is modeled by a resistor and an inductance whose values depend on many factors such as the frequency, temperature, material or geometry of the inductor and workpiece. However, this equivalent circuit is calculated for certain conditions, normally for the worst conditions for the converter, and are maintained constant during the modeling. This simplification is usually used by converter designers, whose aim is to understand the converter and its control behavior (e.g. [22, 46, 67]). In this case, the load is constant but the voltage and the switching frequency are varied depending on the converter's control performance.

The calculation of the equivalent circuit is usually done with analytical methods, similar to those presented in Section 2.2, or with 1D or 2D

commercial softwares using numerical methods. Once the values of the circuit parameters are obtained, they are used in simulations with specialized converter designing softwares like $Powersym^{©}$, $Pspice^{©}$ or $Matlab - Simulink^{©}$.

This simplification is a useful approximation for converter designers, because it allows fast simulations and rapid prototyping, centering the effort on converter's performance. Moreover, it is a good approximation thanks to the different time constants of the electric and the electromagnetic-thermal problem. However, it does not allow a correct analysis of a transient stage of an induction heating process.

Alternatively, authors whose objective is understanding the efficiency of the heat transfer between inductor-workpiece, tend to use an electromagnetic-thermal analysis. Contrarily to the previous case, the load value changes during the simulation, but the source feeding the circuit is simplified to a constant voltage or current source at a constant frequency (e.g. [113–115]). In these cases, little attention is paid to the converter's performance, as this approach is focused in the heating process itself. This condition is satisfactory in cases with little load parameters variation, but it is not accurate in cases where great changes occur.

In order to overcome this problem, some authors have done some effort trying to link numerical analysis of the electromagnetic-thermal problem with the electrical problem. Example of this is [116], that introduces the converter-load interdependence and solves the problem using an author's program that considers the variation of voltage and frequency. Another example is found in [117], where just the first harmonic of the current source is considered and the frequency and current is varied during the process. Finally, another author like [118] and [119], use a commercial software linked with an authors' program where converter's operation is considered. In this case, the first harmonic approximation, the limits of the converter and the dead-time between opposite transistors are taken into account during the simulations.

It has to be noted that although these articles provide a good starting point, there are still some aspects that are not considered accurately. For example, the converter's performance, control and operation is not completely described and, the most important, none of them provide experimental results that validate the model used.

7.4 Numerical analysis considering the converter's performance

For solving the limitations of electrical and electromagnetic-thermal approaches, the converter and load behavior and their interaction need to be incorporated in the modeling. In this section, this problem is confronted by including some aspects of converter's behavior into the modeling of an IH system.

First, in Section 7.4.1, converter's performance is described to extract some considerations to be used during the simulations. Afterwards, the resolution method and basic equations of the electromagnetic-thermal problem are presented in Section 7.4.2. And finally, the solving procedure combining the converter and the load's behavior is exposed in Section 7.4.3.

7.4.1 Converter description and operation

In IH systems the inductor-workpiece is connected with a capacitor in order to resonate. Regarding the different converter structures and tanks described in Chapter 3, a VFSRI is considered during this chapter. Although other topologies can be used to obtain an alternating voltage, in most applications using high power (that is the case of continuous wire heating) the full-bridge topology is the most commonly used [22].

Considering the different power control strategies explained in Section 3.4.3, in this case, the power is controlled through the DC voltage level. Therefore, the inverter is considered to be commutating with a 50% of duty-cycle. Although VFSRI commutate slightly above resonance (Section 3.2.5), during the simulations the frequency is considered to be equal with the resonant frequency. The dead-time is also neglected during this study.

In this chapter, the system to be modeled is a Post-Curie equipment and in this type of systems the quality-factor is above 20 [112]. Thus, it is supposed that the converter's output voltage is sinusoidal and just the first harmonic of the square-wave is considered, as explained in 3.2.2 and simplified in Equation 7.1.

In VFSRI, all the load's current is supported by the converter. That is the reason why in most applications it is necessary to connect a matching transformer between the tank and the inverter (see Section 3.2.5). In case of Post-Curie systems, where the equivalent resistance and inductance are usually smaller, a transformer with a big transformation ratio (i) is necessary. Moreover, the resonant frequency as well as many other parameters

are strongly affected by any parasitic component such as the transformer's leakage inductances or the connections in the secondary. In this model these parasitic components are incorporated to simulate a more realistic situation, Figure 7.2.

Taking this into account, the electrical and simulated model is shown in Figure 7.2. The AC voltage used during the simulations is

$$U_{tank2_{RMS}} \approx \frac{4U_e}{\sqrt{2}\pi}\frac{1}{i} \approx \frac{0.9U_e}{i} \tag{7.1}$$

being U_e the voltage of the DC source.
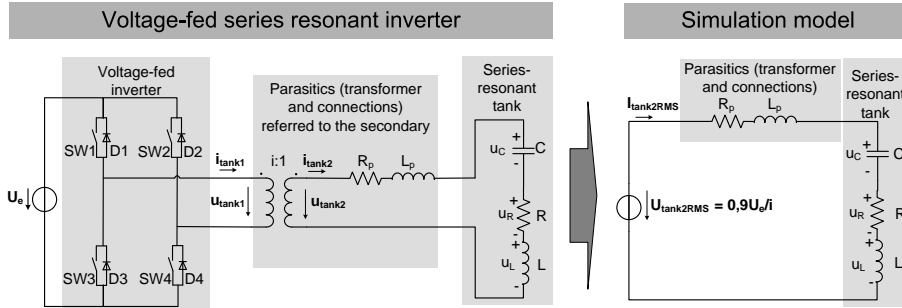
Figure 7.2: Equivalent electrical and simulated model.

IH converters usually have a PLL scheme to control the switching frequency, as seen in Chapter 5. Apart from this control loop, there is another control-loop for controlling the power. An examples of that can be found in [96, 100, 120]). The first control-loop measures the phase-shift between voltage and current, so that the frequency is varied to obtain the desired phase-shift. In this case, the converter is commutating at resonant frequency, which means that the phase-shift is zero. Regarding the power control loop, it usually fixes the voltage of the DC source to obtain the power reference through proportional integral or more sophisticated controllers.

According to this, both control loops are considered during the simulations as shown in Figure 7.3. In order to simulate the PLL and the zero phase-shift, the frequency is varied to maintain zero reactive power, condition that is accomplished at resonant frequency (Section 3.2.1). For the case of the power control loop, the voltage is varied to obtain the desired power reference according to a voltage ramp.

7.4 Numerical analysis considering the converter's performance
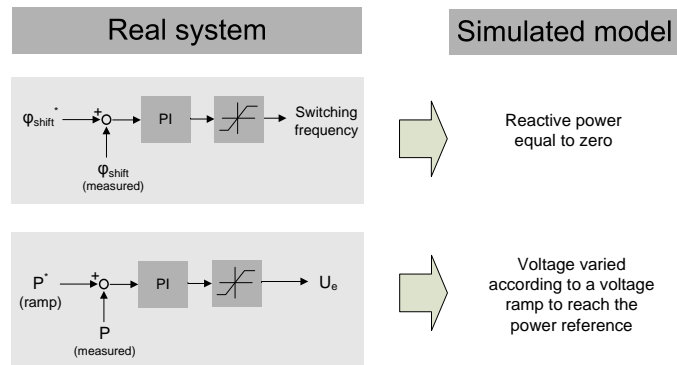
Figure 7.3: Converter control loops and simulated model.

7.4.2 Load modeling

Due to its length and complexity, the electromagnetic and thermal problem is out of the scope of this study. In this Section, just a brief summary of the equations involved is presented. However, a short overview of numerical methods applied to IH and a first bibliography of the equations and assumptions done can be found in Section 2.3.

During this study, there was a research of the different methods and softwares that could perform this simulation. After analyzing and using different commercial softwares, $Flux2D^{©}$ was chosen because allows the coupling of the electromagnetic-thermal and kinematic problems and permits varying the voltage and frequency during the process. It has to be noted, that there are other softwares that could have also been used.

Numerical simulation of IH systems requires a coupled magnetic and thermal model due to the temperature dependence of the material's properties. In case of $Flux2D^{©}$, the equations are solved using FEM (see Section 2.3.2) with an indirect coupling (see Section 2.3.3).

Considering the definitions of magnetic vector potential

$$\mathbf{B} = \nabla \times \mathbf{A} \tag{7.2}$$

and electric scalar potential

$$J_s = -\sigma \nabla \phi \tag{7.3}$$

165

with J_s being the source (excitation) current density and σ the electrical conductivity. Integrating in space the Faraday-Lenz law (Equation 2.10), the electric field strength $\mathbf{E}$ is equal to

$$\mathbf{E} = -\frac{\partial \mathbf{A}}{\partial t} - \nabla \phi \qquad (7.4)$$

Considering that the current desity $\mathbf{J}$ is related to the electrical field strength $\mathbf{E}$ by the conductivity and using Equation 7.4

$$\mathbf{J} = \sigma \mathbf{E} = -\sigma \frac{\partial \mathbf{A}}{\partial t} - \sigma \nabla \phi = J_e + J_s \qquad (7.5)$$

where the first of the terms, $-\sigma \frac{\partial \mathbf{A}}{\partial t}$, represents the eddy currents (J_e) and the second the source currents, (J_s).

Joining Equation 2.14 with 7.5

$$\nabla \times \mathbf{H} = \mathbf{J} = -\sigma \frac{\partial \mathbf{A}}{\partial t} - \sigma \nabla \phi \qquad (7.6)$$

that combined with

$$\mathbf{B} = \mu \mathbf{H} \qquad (7.7)$$

and with the definitions of magnetic vector potential and electric scalar potential (Equations 7.2 and 7.3), becomes

$$\nabla \times \left(\frac{1}{\mu} \nabla \times \mathbf{A} \right) + \sigma \frac{\partial \mathbf{A}}{\partial t} = \mathbf{J}_s \qquad (7.8)$$

where $\mathbf{A}$ is the magnetic vector potential, $\mathbf{J}_s$ is the excitation current density source, μ is the magnetic permeability of the material and σ its electrical conductivity.

Assuming that

$$\nabla \times (\nabla \times A) = \nabla (\nabla \cdot A) - \nabla^2 A \qquad (7.9)$$

and the mathematical definition of vector potential (from Equations 2.13 and 7.2)

$$\nabla \cdot \mathbf{B} = \nabla \cdot (\nabla \times \mathbf{A}) = 0 \qquad (7.10)$$

Therefore, considering μ linear, Equation 7.8 becomes

$$\frac{1}{\mu}\nabla^2\mathbf{A} - \sigma\frac{\partial\mathbf{A}}{\partial t} = -\mathbf{J}_s \tag{7.11}$$

Due to the symmetries in the geometry of the system, this equation can be expressed in cylindrical coordinates with the complex vector $\mathbf{A}$ being independent of the azimuth angle (A(r,z)). In this case, the problem is axisymmetric and $\mathbf{H}$ has two components in the space, whereas $\mathbf{E}$ just one [7, p. 468]. Considering that the variables are sinusoidal time-varying, they are expressed using their complex images (Section 2.3.1). Thus, Equation 7.11 is expressed as

$$\frac{\partial}{\partial r}\left(\frac{1}{\mu r}\frac{\partial}{\partial r}\left(Ar\right)\right) + \frac{\partial}{\partial z}\left(\frac{1}{\mu}\frac{\partial A}{\partial z}\right) - j\omega\sigma A = -J_s \tag{7.12}$$

where ω is the angular frequency of $\mathbf{A}$. This equation is solved by the program and the heat produced by the eddy currents is computed with

$$p_v = \frac{|j\varpi\sigma A|^2}{2\sigma} \tag{7.13}$$

where p_v is the induced power density.

Then, this heat increases the temperature following the Fourier equation

$$\rho_m c_p \frac{\partial T(r,z,t)}{\partial t} - \nabla\left(k\nabla T(r,z,t)\right) = p_v(r,z,t) \tag{7.14}$$

where T is the temperature value, k is the thermal conductivity, c_p is the specific heat and ρ_m is the mass density.

With regards to the movement of the wire, the displacement is considered during the thermal field computation. The method utilized by $Flux2D^{©}$ during the simulations is the translating air-gap technique, using the step by step method explained in [121]. The currents induced by the displacement of the wire are not considered because the velocities are low.

7.4.3 Solving procedure combining converter and load modelling

With reference to the problem of the interdependence between converter and load, the frequency and the voltage of the source are modified in the electromagnetic and thermal problem. The source's frequency is set equal to the resonant frequency of the load and the voltage is varied manually according to the power control-loop presented in Figure 7.3.
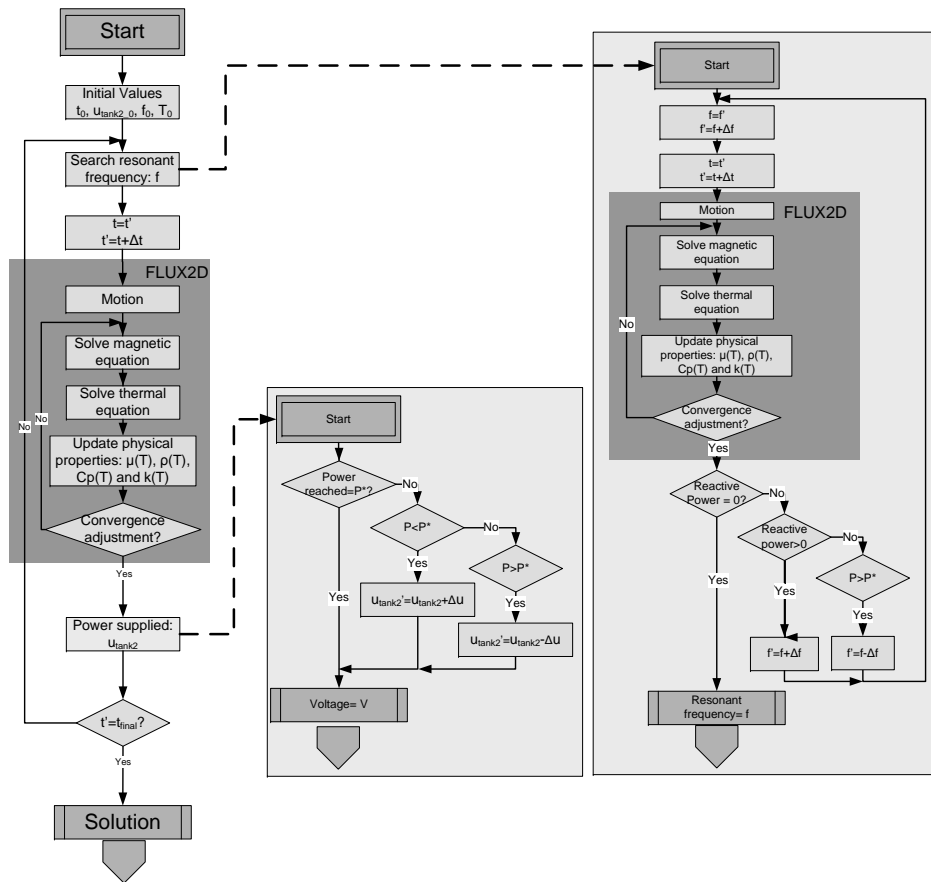
Figure 7.4: Block diagram of the solving procedure combining converter and load modelling.

Concerning the electromagnetic and thermal problem, it is solved using $FLUX2D^{©}$. This program defines an *Steady State AC Magnetic coupled with Transient Thermal application* that solves the equations explained in the previous section with an indirect electromagnetic-thermal coupling and using FEM.

The solving procedure is shown in Figure 7.4 and follows the next iterative process:

1. At t_0, the initial temperature chart and the associated properties of the materials are set and the voltage is kept to the minimum value.

2. Afterwards, the resonant frequency is searched for the initial temperature by maintaining the reactive power equal to zero. The next time step t_1 is computed.

3. Then, the magnetic and electrical properties are evaluated for the initial temperature and the magnetic problem is solved, obtaining the transferred power.

4. The temperature chart is calculated for t_1 and the new properties of the material are found.

5. At this moment, the magnetic and electric properties are evaluated again for the new temperature chart with the new material properties. Then, the thermal problem is solved again, obtaining a second temperature chart. If the difference between both temperature distributions is smaller than a certain error, the solution is validated and the next time step computed. Otherwise the iterations continue until the error diminishes and the solution can be validated for t_1.

6. Once the convergence is reached for t_1, the voltage is modified according to the desired power by increasing the voltage with a 100 V/s ramp and limited to 245 V.

7. The resonant frequency is searched again and the next time step t_2 is computed.

8. The process continues until the end of the heating process at t_{final}.

7.5 Simulations

Following the considerations of Section 7.4, a Post-Curie equipment in the transition between 720 °C and 800 °C is simulated. First, the model is described in Section 7.5.1, explaining the geometrical and physical characteristics. And afterwards, three cases are simulated to compare the results of the solving procedure with classical approaches. This is explained in Section 7.5.2.

7.5.1 Simulated model

The system modeled is a 177 kHz and 4 kW system for continuous steel wire hardening. It is composed of 6 inductors of 10 square-shape turns that are heating a 3 mm diameter wire of AISI 1080 steel, with the characteristics

seen in Tables 7.1 and 7.2. The coils are connected in pairs and series forming three tanks connected in parallel, and the capacitors, as well as the parasitic components, are connected in series. In Figure 7.5, the connections of the electrical circuit are shown, with each turn being modeled by a two terminal solid conductor. In Figure 7.6 a coil and the wire model are shown.

Table 7.1: Parameters of the tank.

	Parameter	Value
	Number of coils	6
	Number of turns	10
	Inner diameter	20 mm
Coil	Outer diameter	32 mm
	turn's width	1 mm
	Space between turns	1 mm
	Space between coils	36 mm
Capacitor	Capacitance	1.6 μF
Parasitic	Resistance	10 $m\Omega$
Components	Inductance	150 nH
Wire	Diameter	3 mm

Table 7.2: AISI 1080 characteristics.

Temperature $^\circ$C	Resistivity $m\Omega mm$	Relative permeability	Specific heat $kJ/(m^{3\circ}\text{C})$	Thermal conductivity $W/(m^\circ\text{C})$
0	0.180	100	3790	47.8
20	0.180	100	3790	47.8
100	0.232	100	3850	48.1
200	0.308	100	4140	45.2
300	0.410	100	4400	41.3
400	0.505	40	4700	38.1
600	0.772	40	5470	32.7
700	0,932	30	5890	30.1
750	1.032	5	15900	30.1
800	1.129	1	4690	24.4
900	1.164	1	4690	24.4
951	1.164	1	4690	24.4
1100	1.164	1	4690	24.4

In this case, the wire length is chosen 2350 mm because it allows a simulation of more than 15 s ensuring that the wire is crossing all the coils during the whole simulation. Thus, the model requires a huge dimension compared to the area of interest, which is just the wire and the area near the coils. For providing an accurate mesh and avoid long computation times, the penetration depth has been calculated to increase the mesh in this area (see Figure 7.7). During the construction of the mesh, a first set of simulations have

been done to ensure the convergence of the results.
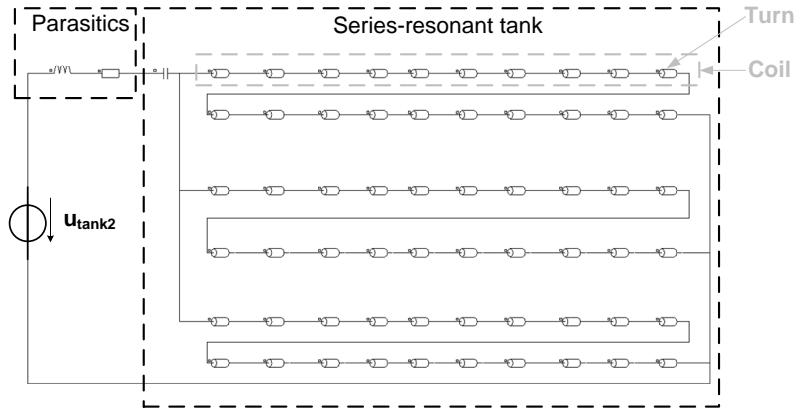
Figure 7.5: Electrical circuit simulated.
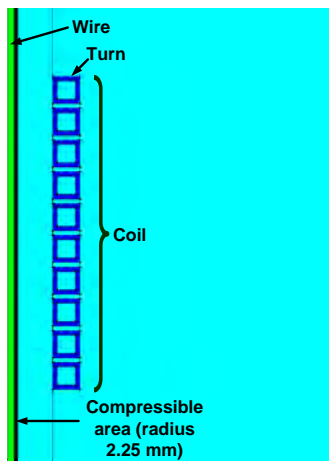
Figure 7.6: A coil and the wire modeled.
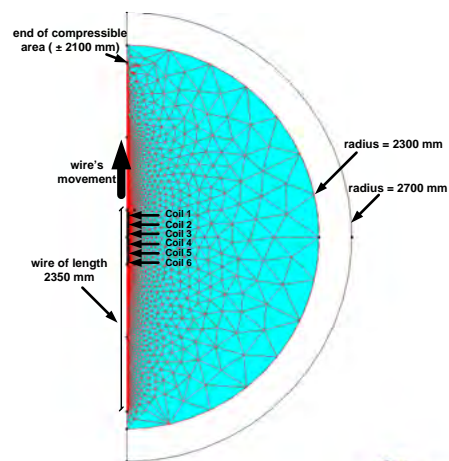
Figure 7.7: Meshing of the system.

$Flux2D^{©}$ requires of the definition of a compressible area where the translation takes place. In this case, the compressible area is formed by a square of 4200 mm per 2.25 mm, as shown in Figures 7.6 and 7.7. The infinite box used by $Flux2D^{©}$ to model an infinite domain is defined by half semicircle of 2300 mm inner radius and 2700 mm external radius.

In the external radius of the wire, a convection boundary condition with an

emissivity of 0.8 and a heat transfer coefficient of 20 $W/(m^2°C)$ is imposed. The velocity of the wire is set to 5 m/min, the temperature of the air at 40 °C and the initial temperature of the wire at 720 °C.

7.5.2 Simulation results

In order to illustrate the importance of considering the converter's behavior during the simulations, three cases have been simulated:

- Case 1: The voltage and the frequency are constant during the whole process, and the frequency is set to the initial resonant frequency of the process.

- Case 2: Equal to Case 1 but the frequency is set to the final resonant frequency of the process.

- Case 3: The voltage and frequency is varied according to the control shown in Figure 7.4 with a power reference set to 3.5 kW and a 100 V/s voltage ramp with a limit of 245 V.

The first and the second case represent the modeling following the e-lectromagnetic-thermal approach explained in Section 7.3. In these cases, the voltage and frequency of the source is constant, whereas in the third case, which is the method presented in Section 7.4, both parameters vary considering the converter's performance.

Taking this into consideration, the active power, reactive power, voltage, current and frequency of the converter for Cases 1, 2 and 3 are plotted in Figures 7.8 and 7.9. The voltage value U_e, in Figure 7.9, is calculated with $U_{tank2_{RMS}}$ obtained from $Flux2D^{©}$ and according to Equation 7.1. The value of current $I_{tank1_{RMS}}$ represents the current in the primary of the transformer, as seen in Figure 7.2. This value is the RMS value calculated with $I_{tank2_{RMS}}$ and using the transformer's transformation ratio (i). The equivalent impedance (inductance plus resistance) of the inductor-work piece and the resonant frequency is plotted in Figure 7.10. Afterwards, the temperature profile for different central points of the wire for the three cases is shown in Figure 7.11.

In Case 1, the reactive power at the beginning is zero because the converter is switching at the resonant frequency. When the temperature of the wire increases, the inductance value decreases due to the variation in the wire's properties and, as a result, the resonant frequency increases, as shown in Figure 7.10. In this case, the switching frequency is constant, thus, when
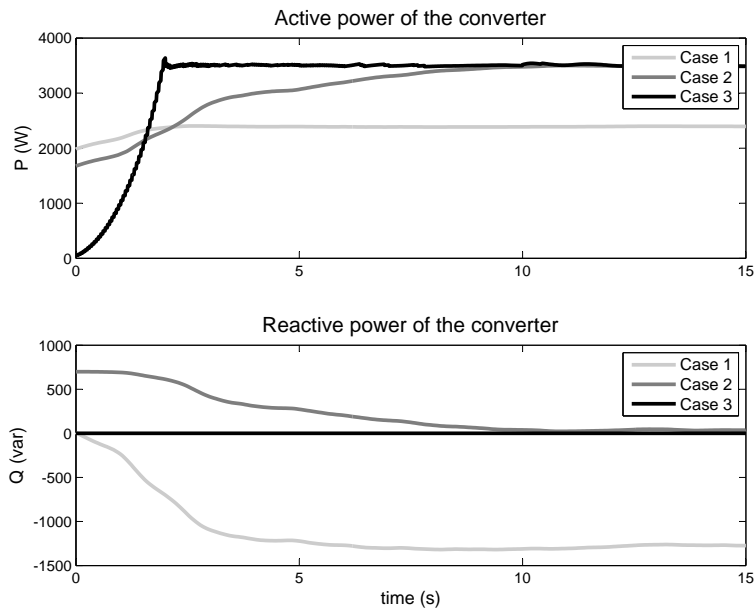
Figure 7.8: Active and reactive power of the converter in Cases 1, 2 and 3.
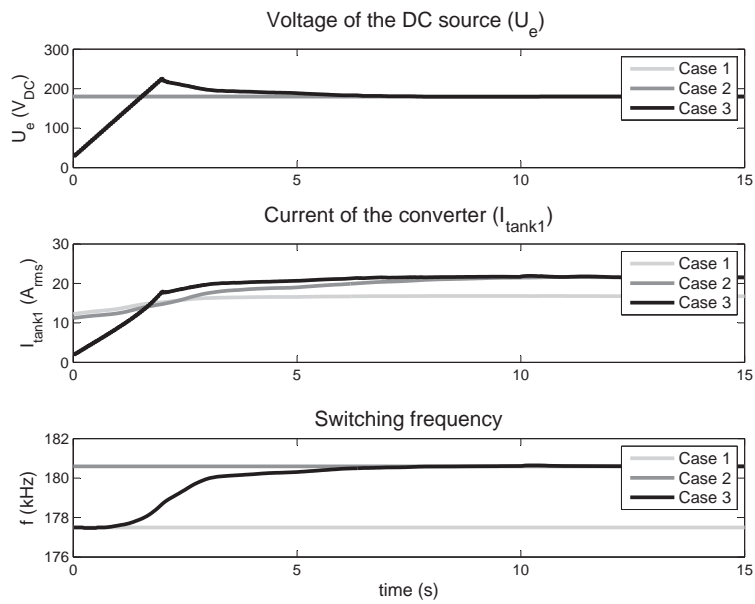
Figure 7.9: DC voltage, RMS current and switching frequency of the converter in Cases 1, 2 and 3.
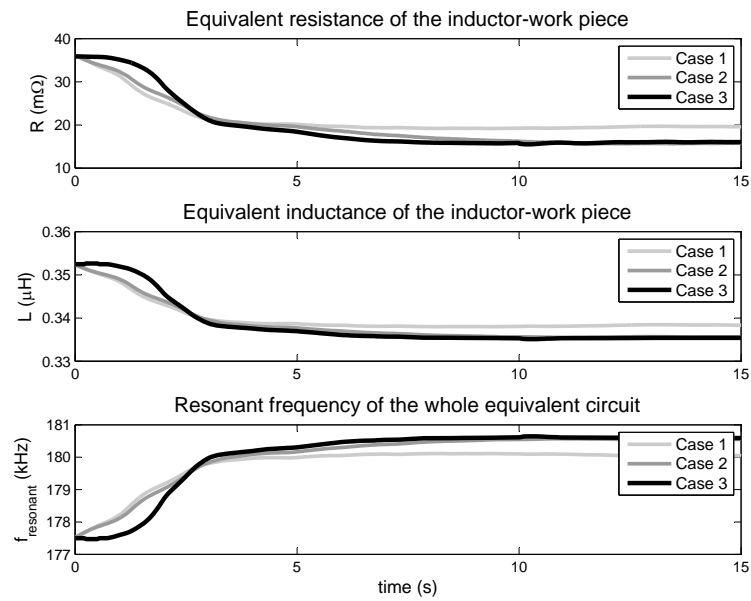
Figure 7.10: Equivalent impedance of inductor-workpiece and resonant frequency for Cases 1, 2 and 3.
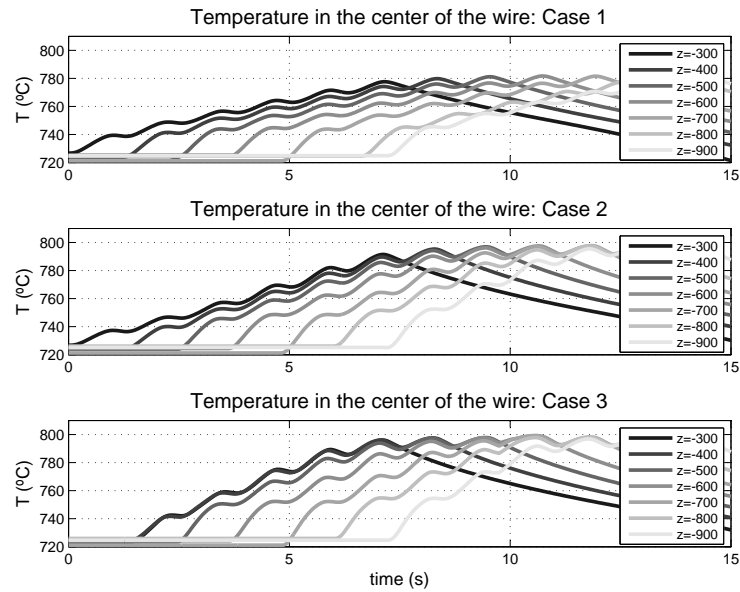
Figure 7.11: Temperature profile for wire's central points in Cases 1, 2 and 3.

the resonant frequency varies, the converter provides reactive power that does not generate heat (Figure 7.8). This is specially noticed at the end of the process, when switching and resonant frequency are most different.

In Case 2, the reactive power at the beginning is not zero, because the switching frequency of the converter is set to the final resonant frequency of the process. However, the reactive power becomes zero as the wire temperature increases and the resonant frequency is reached, as shown in Figures 7.8 and 7.10. Contrary to the previous case, at the beginning there is a part of reactive power that does not produce heat.

In Case 3, the voltage is varied according to a voltage ramp of 100 V/s following a power control-loop set to 3,5 kW and the converter is switching at the resonant frequency (Figures 7.8 and 7.9). In this case, the reactive power is zero during the whole process and all the available power of the converter is used to heat (Figure 7.8). At the beginning, the voltage is zero and increases until the power reference is reached. In this situation, the wire is colder and its equivalent resistance and inductance are higher. As the temperature of the wire increases, its equivalent resistance and inductance values decrease, as can be observed in Figure 7.10. Thus, the current value increases and the control decreases the voltage to maintain the power reference.

Regarding the temperature for different moving central points of the wire in Figure 7.11, the decrease of temperature due to the space between the six coils that the wire crosses can be observed. It can also be observed that the temperature reached in Cases 2 and 3 is slightly higher than in Case 1. The reason is that the active power applied to the wire is higher in Cases 2 and 3. It is also shown that in Case 3 the wire starts to increase the temperature about 2 seconds later. This is due to the voltage value, which is lower than in the other cases. However, the steady-state is reached earlier, in 6 - 7 seconds approximately. Observing Case 2, the final temperature is similar to Case 3, but the steady-state is reached 3 seconds afterwards. The reason is that in Case 2, at the beginning, the source is out of the resonant frequency and only a part of the power is used to heat the wire. In this case, the dynamics depend on the time that the wire takes to be heated and this happens when the resonant frequency equals to the switching frequency and provides the 3.5 kW.

Observing more in detail Figure 7.9 for Case 3, the steady-state is reached at 6 - 7 seconds. Considering that the sum of the 6 coils length is approximately 0.6 m and the wire is moving at 5 m/min, the steady-state is reached when the wire has crossed the six coils, at approximately 7 seconds. In case

3, the converter dynamics is faster and reaches the power reference before the wire has crossed the coils, as seen in Figure 7.8. But, in case of loads that moved faster, the process could arrive to be determined by the converter's performance. Moreover, in case 3 the voltage does not reach the maximum value, set to 245 V, it just arrives to a smaller peak and diminishes afterwards. In case of having a greater impedance, for example with a colder wire, these peak could increase, arriving to the maximum value of 245 V. Under these circumstances, the dynamics of the process would be also conditioned by the converter's performance.

7.6 Experimental results

Experimental tests have been performed with an industrial equipment designed and constructed by the authors of this thesis and shown in Figure 7.12. The inductors and workpieces have the same geometric and physical characteristics than the simulated model. The wire arrives to the first of the 6 coils from a previous heating stage at 720 °C and the converter heats it up to the Curie temperature. The three cases simulated in the previous section have been implemented, focusing on the case where the voltage and frequency vary (Case 3).
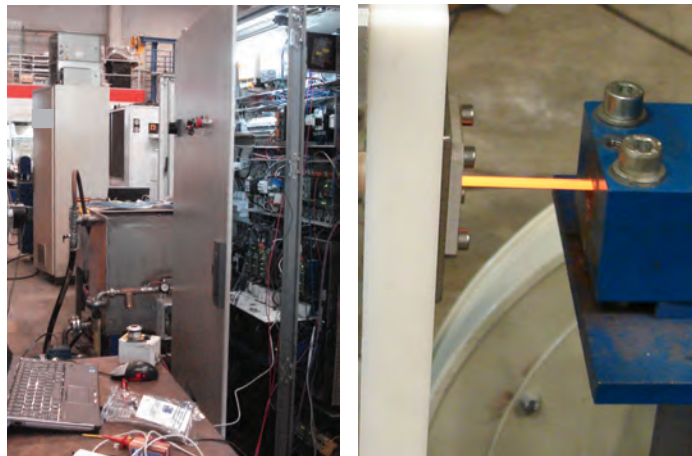
Figure 7.12: Experimental setup used to test the proposed control method.

During the first experimentation, the voltage and frequency were fixed as in Case 1 (constant voltage and frequency set at the initial resonant

frequency). In this case, the converter spent from 5 to 10 seconds more than in the simulations to reach the steady-state. Moreover, it was observed that in case of decreasing the temperature at which the wire enters the inductors, the converter could not heat the wire. The reason was that the impedance of the load was too high and, thus, the current and the power were limited. To give power to the wire, the voltage had to be higher and the converter could not reach it.

In the second experimentation, the voltage and frequency was set like in Case 2 (constant voltage and frequency set at the final resonant frequency). Under these circumstances, the converter always reached the steady-state spending less time to heat the wire than in Case 1. In this case, the final temperature was approximately 10 to 20 °C higher than in the previous case. However, the converter took more than twice longer than within the converter in normal operation, that is when the voltage and frequency vary during the whole process.

In the third experimentation, the converter was working in normal operation. The voltage varied according to a power control-loop and following the resonant frequency, similar to Case 3 in the simulations. For this situation, the voltage and the current in the primary and secondary are shown in Figures 7.13, 7.14, 7.15 and 7.16.

To compare these figures with Figure 7.9, some considerations have to be taken. First, the voltage and currents are plotted as a function of time, whereas in Figure 7.9 the RMS value of the current in the complex form and the value of the voltage DC source are represented. Although they are graphically different, the comparison of both figures is possible as the tendency of the system can be observed. Secondly, in these figures the high part of the square-wave corresponds to the DC value of the source. In case of the current, the maximum is proportional to the RMS value and gives an idea of the value as well as its behavior.

Considering this, in Figure 7.13, the voltage increased reaching the maximum value in approximately 3.5 seconds and afterwards decreased slowly. Comparing with the simulations in Figure 7.9, at the beginning the voltage has more than one slope. In this case, there is a first and fast increase during approximately 0.5 seconds and afterwards a softer increase. The reason for this difference between simulation and experimental results is that real IH converters need an initial voltage to start working. This initial voltage helps the converter to measure the current's zero-crossing and detect the resonant frequency of the tank. Thus, the voltage at the output has to be high enough to have an appropriate current waveform. Otherwise, the current is
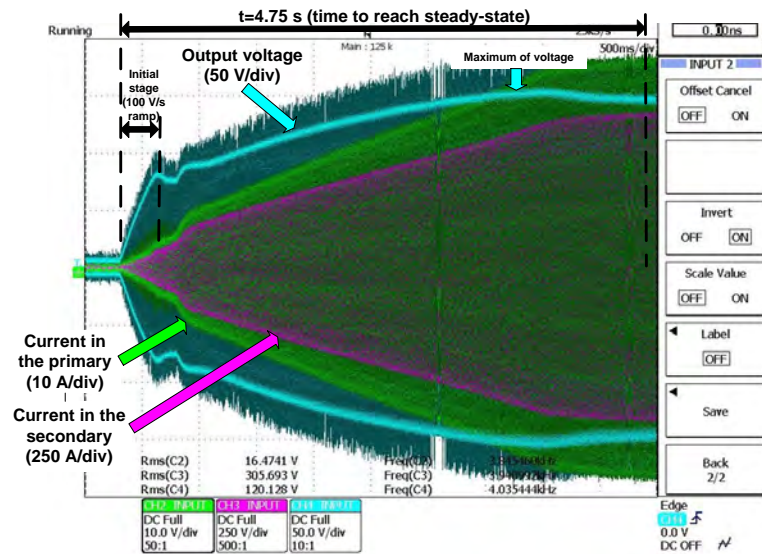
Figure 7.13: Voltage at the output of the converter and current in the primary and secondary when passing from below Curie to Curie temperature.
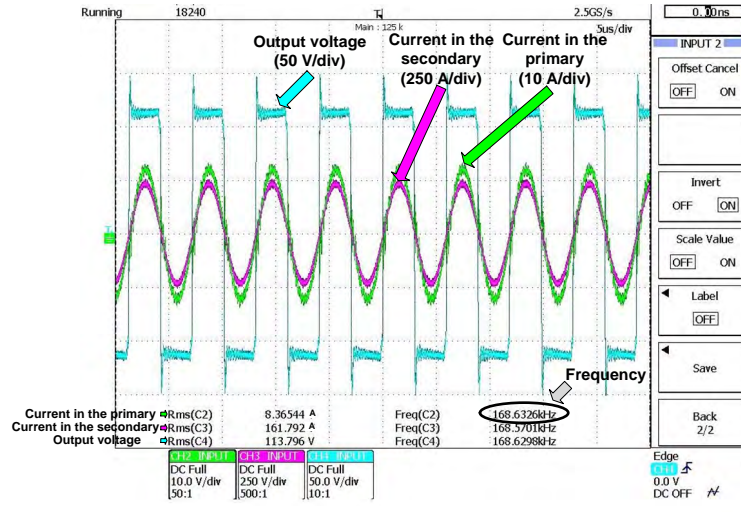
Figure 7.14: Voltage at the output of the converter and current in the primary and secondary below Curie temperature.
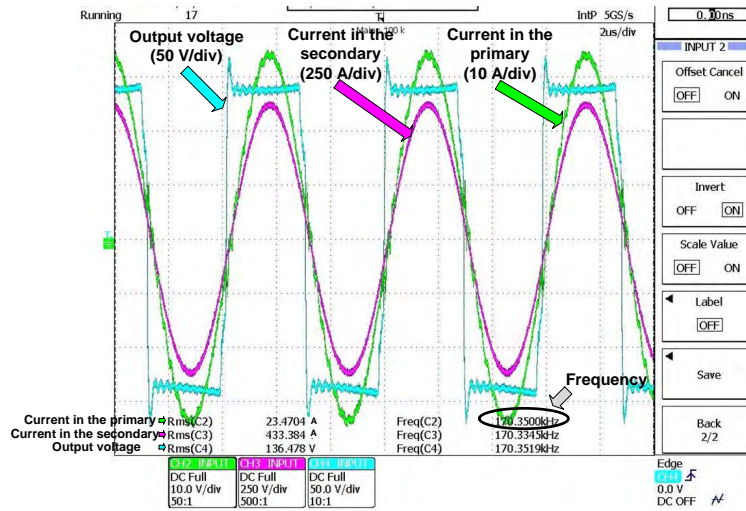
Figure 7.15: Voltage at the output of the converter and current in the primary and secondary at Curie temperature.
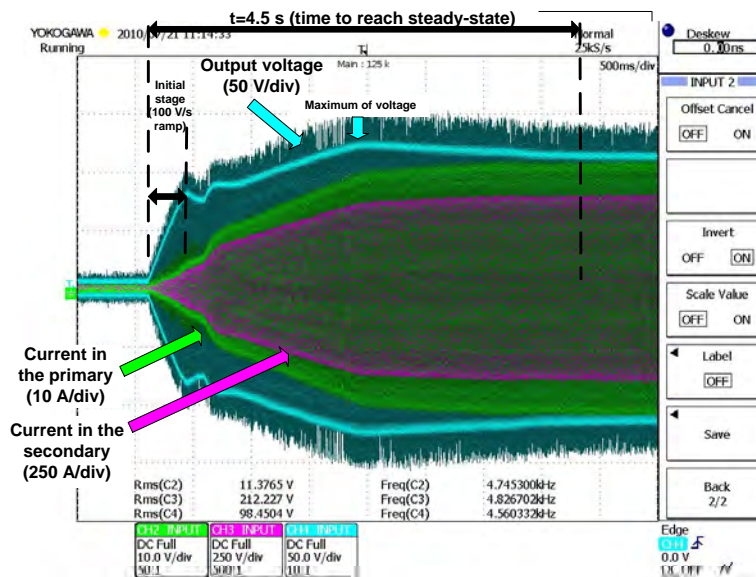
Figure 7.16: Voltage at the output of the converter and current in the primary and secondary when passing from below Curie to Curie temperature for a lower power.

too small and leads to false zero-crossings, disabling the proper control of the converter. Therefore, at the beginning the control increases the voltage automatically with a 100 V/s ramp until the voltage reaches 80 V and the current is high enough. Once the system detects that is switching at the resonant frequency because the phase-shift is zero, the power control-loop starts working. In this case, the power control-loop was a PI controller with a lower dynamic response than the 100 V/s voltage ramp supposed during the simulations. This is the reason why this second slope is lower than the one in the simulations.

Regarding the thermal behavior, the temperature of the wire was 720 °C when reaching the inductors and oscillated between 790 °C and 810 °C at the end.

Figures 7.14 and 7.15 are a zoom of the voltage and the currents during the transition stage. It is observed that the first harmonic approximation done in Section 7.4.1 is correct because the current is perfectly sinusoidal. It can also be observed that the frequency varied from 168 kHz to 170 kHz, which are similar values to the ones obtained during the simulations. It is a small variation because the parasitic components do not vary much during the heating process, since the transformer and connections are water cooled. In further investigations, the parasitic components should be reduced by shortening and paralleling these transformer secondary connections. Nevertheless, in this type of systems the parasitic components should be considered. In Figures 7.14 and 7.15, it is also observed that the assumption of neglecting the dead-time during the simulations is accurate.

Figure 7.16 shows the same parameter than Figure 7.13 but with a lower power reference. The aim of this test was to show that the dynamics of the process was dependant on the wire's velocity. In both cases the voltage increased until the power was reached. Afterwards, the current increased and the voltage decreased to maintain the power reference. In Figure 7.13 the steady-state was reached in approximately 4.75 seconds and in Figure 7.16 at 4.5 seconds, which corresponds to the time spent in crossing the coils. In the real case, the distance between coils was lower than in the simulations and, thus, the time spent in crossing them was also lower (approximately 5 seconds). Therefore, in both cases the dynamics of the process was affected by the velocity of the wire. Moreover, in the first case the maximum voltage was reached at 3.5 seconds and in the second case at only 2 seconds. In both cases the voltage reference was low enough and the converter dynamics fast enough for following it. However, in case of the converters with lower

dynamics or processes with higher velocities, the time to reach the steady state could be conditioned by the converter.

Some of the differences between the simulated and the experimental results are obviously conditioned by the intrinsic differences between the geometries of the pieces, the properties of the heated material and the assumptions made during the modeling. Nevertheless, most of the differences are due to the difficulty of determining the parasitic components and the complexity of simulating the control system of a real converter. Taking these differences into account, the results provided for Case 3 show a correspondence with the real system behavior. The results illustrate the importance of considering the operation and dynamics of the converter during IH simulations, especially in cases where there is a great change in load properties.

7.7 Summary

In this Chapter, an industrial process of continuous hardening and tempering of steel wires has been explained. During this process, the wire needs to be heated above its Curie temperature. At this temperature the steel becomes non-magnetic and there is a great change in the wire's properties that affect the design and the control of the converter. Studying and modeling this situation is interesting because of this change and the high interaction between the electrical and electromagnetic-thermal problems.

The difficulty of modeling IH systems and the interdependence between converter and load is introduced, explaining two different approaches: the electrical and the electromagnetic-thermal approach. The first one is mainly used by converter designers and is based on the supposition that the inductor-workpiece equivalent impedance does not vary, but the source parameters does. Contrarily to this approach, the electromagnetic-thermal approach supposes that the source parameters remain constant, whereas the load varies during the process. Some attempts have been done to combine both approaches, but in none of them the control of the converter and its basic operation are described and experimental results provided.

In order to overcome the mutual influence between the converter and the load, a simple method of simulating IH systems using FEM is presented. The topology of the converter and its operation is explained, assuming some simplifications like neglecting the dead-time or considering just the first harmonic. The parasitic components of the transformer and inductance are taken into consideration and the control-loops of the converter are explained.

Afterwards, the basic equations of the electromagnetic-thermal problem are presented and the solving procedure, considering the converter's operation, is exposed.

The system is simulated with a commercial FEM software ($Flux2D^{©}$), modifying the voltage according to a manual power control-loop and setting the switching frequency to the resonant frequency. In order to compare the method presented with the classical electromagnetic-thermal approaches, two additional simulations have been done maintaining constant the voltage and the frequency. The three simulated cases are:

- Case 1: The voltage and the frequency are constant during the whole process, and the frequency is set to the initial resonant frequency of the process.

- Case 2: Equal to Case 1 but the frequency is set to the final resonant frequency of the process.

- Case 3: The frequency is varied manually according to a frequency control loops similar to the PLL presented in Chapter 5, in which the converter commutates at resonant frequency. The power control loop is controlled by varying the voltage of the DC source, similar to the VFSRI converter explained in Chapter 3. The resonant frequency is set during the simulations by maintaining the reactive power to zero and the power control loop is modeled with a 100 V/s voltage ramp limited to 245 V.

The simulation of these three cases has confirmed the importance of considering the changes in source's voltage and frequency when simulating IH systems. In case of varying these parameters, all the power is used to produce heat during the whole process. The final temperature in Cases 2 and 3 was higher compared to Case 1 and in Case 3 the steady-state was reached earlier. During the simulations, the influence of the converter in the dynamics of the heating process and the interdependence between the load and the converter's behavior was also observed.

Finally, experimental results using an equipment designed and constructed by the authors were presented. Although there are differences between the experimental and simulation results, these are mainly due to the complexity of the converter control system and the difficulty of determining the parasitic components. However, the results obtained have proven to be accurate enough and show a correspondence between experimentation and simulation.

Compared to other simulation methods in literature, the solving procedure presented considers the converter's performance and provides a flexible method of modeling the overall system behavior. Moreover, the simulation procedure presented takes advantage of the flexibility provided by commercial softwares and allows an easy and flexible implementation compared to other simulation procedures. Finally, the experimental setup showed a correspondence with the results obtained, validating the simplifications assumed during the process.

183

Chapter 8

Conclusions

8.1 Contributions

The present thesis has investigated the different converter topologies and structures used in IH field, focusing on the application of wire heating and providing an extensive revision on IH converters in Chapter 3.

Considering the different converter topologies used in IH, a multichannel converter structure is studied for high-power and high-frequency applications. The basic converter topologies and connections are studied with the aim of constructing a converter based on these topologies that can profit this modularity to reduce the designing time, the production cost and the maintenance. As a result of this work, a multichannel converter has been studied, implemented and tested in a prototype in Chapter 4.

The present thesis has also investigated the design of a flexible control for IH applications. As a result of this study, a software PLL has been designed, implemented and tested in a real industrial application in Chapter 5. The main benefit of this software PLL system is that provides a digital control that minimizes the analog components and avoids variations due to part spread or temperature drift. Moreover, it is very flexible and can be used in many different applications because the variations required for each particular case can be implemented by software. Additionally, clears the way to the programming of more complex control algorithms, thanks to the possibility of changing the variables dynamically.

A load-adaptive PLL has also been studied. This control system provides an optimum commutation sequence that allows soft-switching even when the load varies. As a result of this study, a load-adaptive PLL based on the software PLL presented in Chapter 5 has been designed, implemented and tested in a prototype in Chapter 6.

Finally, the present thesis has investigated the different methods of modeling IH systems. In Chapters 1 and 2, the basic concepts regarding analytical

and numerical methods applied to IH field are explained and, in Chapter 7, these methods are used to model a continuous induction wire hardening system considering converter's operation. Compared to other simulation methods, the solving procedure considers the converter's performance and provides a method of modeling the overall system behavior, taking advantage of the flexibility provided by commercial softwares. The system modeled is a real industrial application that has been tested to prove the accuracy of the modeling.

The main contributions of this thesis are summarized below:

- Extensive revision of the main converter topologies and their associated tanks used in IH field (Chapter 3).

- Study of a multichannel converter structure for high-power and high-frequency applications. The study of a multichannel structure based on the combination and connection of basic structures is realized. The final structure is composed of diodes bridge rectifiers and H-bridge inverters connected in parallel commutating synchronized to increase the power or alternatively to increase the frequency. This type of structure allows to reduce the designing time, the production costs and the maintenance of industrial equipments. A prototype based on two H-bridges in parallel for doubling the frequency has been tested showing good results.

- Design of a software PLL for IH applications. This software PLL is all-digital and software programmed, so that minimizes the need of analog components, provides more adaptability to variations and clears the way for the programming of more complex control algorithms. The system has been tested in a real industrial application proving its reliability and flexibility. The contributions are collected in

  - [122] G. Martín-Segura, J. López-Mestre, H. Rivas-Guerrero, M. and Teixidó-Casas and D. Montesinos-Miracle, "A low cost DSP-based control method for high frequency parallel resonant current-fed inverters",in *Proc. 13th European Conf. Power Electronics and Applications*, 2009.
  - [123] G. Martín-Segura, P. Sala-Pérez, C. Ferrater-Simón, J. López-Mestre, D. Montesinos-Miracle and J. Bergas-Jané, "All-digital DSP-based phase-locked loop for induction heating applications", Accepted in *European Transactions on Electrical Power*, 2012.

- Design of a load-adaptive PLL for IH applications. This PLL adapts the phase-shift and dead-time to have soft-switching according to the load requirements. The control system has been tested in a prototype providing good results. The contributions are collected in

  – [124] G. Martín-Segura, C. Ferrater-Simón, J. López-Mestre, G. Gross and D. Montesinos-Miracle, "Load-adaptive phase-shift and dead-time control for induction heating applications", Submitted to *European Transactions on Electrical Power*, 2012.

- Numerical modeling of a continuous induction wire hardening system considering converter's operation. A real industrial process has been modeled with numerical methods incorporating converter's behavior. The results obtained in the simulations and those obtained in a real industrial process are compared, showing its correspondence. The main contributions are collected in

  – [125] G. Martín-Segura, C. Ferrater-Simón, D. Montesinos-Miracle, F. Leach and I. Vadan, "FEM modeling of a continuous induction heating process of steel wire hardening", in *Simpozionului National de Electrotehnica Teoretica*, 2010.

  – [126] G. Martín-Segura, C. Ferrater-Simón, J. López-Mestre, D. Montesinos-Miracle and J. Bergas-Jané, "Simulation of an induction hardening system during Curie temperature transition considering converter's performance", accepted in *COMPEL*, 2012.

  – [127] G. Martín-Segura, P. Sala-Pérez, C. Ferrater-Simón, J. López-Mestre and D. Montesinos-Miracle, "Study of the parasitic inductance and resistance in continuous wire induction heating systems above Curie temperature", to be submitted.

8.2 Future work

There are still many interesting and challenging fields related to the present thesis that can be investigated. Some of the possible studies that can be developed are the following:

- A multichannel converter with two H-bridges has been designed and tested in this thesis. The use of fast IGBTs, specific for IH applications, and the parallelization of more H-bridges can improve the converter's performance. Furthermore, the automatic change of commutation technique or the automatic disconnection of H-bridges can

provide more adaptability and flexibility to the load requirements. Therefore, an interesting research topic is the design of a multichannel converter with IGBTs commutating over 300 kHz and with an automatic change of commutation technique to have high-power at low frequency (inverters commutating synchronized) and high-frequency at low power (inverters commutating alternatively). This system has to be able to disconnect some of the inverters in case that the load requires low-power and low-frequency, allowing the operation in case of an H-bridge's failure.

- During the revision of the different converter topologies used in IH, the benefits in terms of efficiency improvement and cost reduction with the use of PDM techniques has been explained. The multichannel converter is formed by uncontrolled bridge rectifiers and H-bridges, therefore, the study of the application of PDM power control techniques to this converter structure is an interesting matter of research. Even more if considering that the multichannel converter is thought for high-power applications where a 1 % increase in the efficiency can represent considerable savings.

- During the implementation of the load-adaptive PLL, it was observed that the IGBT's parasitic capacitance value had a complex voltage dependence. In order to analyze the affectation of this dependence in the control, the modeling of switches including this dependence and the design of a load-adaptive PLL for VFSRIs incorporating these considerations is interesting.

- In order to ensure soft-switching in VFSRIs, their antiparallel diodes have to conduct before the switches' turning-on and the turning-on has to be realized before the current's change of polarity. In the present thesis, the load-adaptive PLL designed uses the phase-shift and the dead-time as a control variables, incorporating a gain in this variables that ensure the correct sequence of events. However, the dependence of the IGBT's parasitic capacitance on the voltage and the need of simplifications in the calculations, increase the inaccuracies of the system. In this sense, an interesting research topic is the design of a load-adaptive PLL that detects the moment at which the diodes start conducting and imposes that the switches turn-on and the current's change of polarity are done consecutively.

- In CFPRIs, the optimum phase-shift and over-lapping time depend

188

on the parasitic inductance, which value is more constant than the semiconductor's parasitic capacitance. Therefore, the design and implementation of the load-adaptive PLL is an interesting matter of research.

- During the numerical modeling of a continuous induction wire hardening, the variation of frequency and voltage was manually realized utilizing a commercial FEM software. The design of a program linked to a commercial computation program that allows the automatic change of the resonant frequency and the voltage reference according to the converter's control loops is an interesting objective for providing more velocity and flexibility to the analysis. To have this program linked with the simulation programs usually utilized by converter designers would be interesting to speed up and increase the complexity of the simulations.

- In the present thesis, the numerical modeling of the system was realized for a process that heats above Curie temperature, temperature at which there is a great change in the material's properties. This great variation allows a better evaluation of the interdependence between thermal, magnetic and electric variables. However, the modeling of a continuous wire heating below the Curie temperature with numerical methods considering converter's operation is an interesting study. The aim of this study is to evaluate the effect of considering converter's performance during the modeling for this case where the load variation is lower.

- During this thesis, the generation of axial voltage in the wire when it is heated in multi-turn inductor was studied with numerical modeling. However, a deeper study have to be realized to assess the importance of the frequency and coil distribution on this voltage generation.

Bibliography

[1] S. Zinn and S. L. Semiatin, *Elements of Induction Heating - Design, Control, and Applications*. ASM International, Electronic Power Research Institute, Metals Park, Ohio, USA, 1988. v, ix, 1, 5, 6, 9, 10, 11, 160

[2] V. Rudnev, D. Loveless, R. Cook, and M. Black, *Handbook of Induction Heating*. M. Dekker, New York, USA, 2003. v, ix, 1, 3, 5, 9, 10, 11, 12, 13, 23, 25, 29, 81, 160

[3] E. R. Laithwaite, "The influence of michael faraday on power engineering," *Power Engineering Journal*, vol. 5, no. 5, pp. 209–219, 1991. 1

[4] A. Chester and M. Tudbury, *Basics of induction heating (Vol. I)*. John F. Rider Publisher, Inc., New York, USA, 1960. 1, 6, 18

[5] E. J. Davies and P. Simpson, *Induction Heating Handbook*. MCGraw-Hill Book Company, Ltd., London, UK, 1979. 1, 18

[6] E. J. Davies, *Conduction and induction Heating*. P. Peregrinus, Ltd., London, U.K., 1990. 1, 14, 18, 20, 22, 205

[7] C. H. Gür and J. Pan, Eds., *Handbook of thermal process modeling of steels*. CRC Press, 2008. 1, 8, 23, 25, 167

[8] V. Esteve, "Influencia de los componentes parásitos en el análisis y diseño inversores resonantes paralelo para aplicaciones de calentamiento por inducción," Ph.D. dissertation, Universitat de Valencia, Spain, 1999. 5, 73, 74, 78, 126, 221

[9] J. Espí, "Inversor resonante de tres elementos L-LC con característica cortocircuitable para aplicaciones de calentamiento por inducción," Ph.D. dissertation, Universitat de Valencia, Spain, 1998. 5, 7, 9, 75

[10] M. T. Thompson, "Inductance calculation techniques — part ii: Approximations and handbook methods," *Power Control and Intelligent Motion*, Dec. 1999. 6

Bibliography

[11] H. A. Wheeler, "Formulas for the skin effect," in *Proc. of the I.R.E.*, 1942, pp. 412–424. 6

[12] J. Lee, S. Lim, K. Nam, and D. Choi, "An optimal selection of induction-heater capacitance considering dissipation loss caused by esr," *IEEE Trans. Ind. Appl.*, vol. 43, pp. 1117–1125, 2007. 6

[13] T. Spencer and alter, "Induction hardening and tempering," *American Society for Metals, Ohio, USA*, 1964. 14

[14] M. Kennedy, S. Akhtar, J. Bakken, and R. Aune, "Review of classical design methods as applied to aluminum billet heating with induction coils," in *Proc. EPD Congress*, San Diego, USA, 2011, pp. 405–414. 18

[15] V. Nemkov, "Role of computer simulation in induction heating technique," in *International Induction Heating Seminar*, Padua, Italy, 1998. 22

[16] V. S. Nemkov and R.Goldstein, "Computer simulation for fundamental study and practical solutions to induction heating problems," *COMPEL*, vol. 22, pp. 181–191, 2003. 23

[17] R. L. Houghton, "Heat treating technology roadmap update 2006, part i: Process & materials technology," *Heat Treating Progress*, vol. 6, 2006. 23

[18] G. Pfaffmann, "Heat treating technology roadmap update 2006, part iii: Equipment & hardwards materials technology," *Heat Treating Progress*, vol. 6, 2006. 23

[19] J. Lavers, "State of the art of numerical modeling for induction processes," *COMPEL*, vol. 27, pp. 335–349, 2008. 23

[20] G. Benderskaya, "Numerical methods for transient field-circuit coupled simulations based on the finite integration technique and a mixed circuit formulation," Ph.D. dissertation, Technischen Universitat Darmstadt, 2007. 24

[21] N. Mohan, T. M. Underland, and W. P. Robbins, *Power electronics. Converters, Applications and Design*, 2nd ed. John Wiley & Sons, Inc., USA, 1995. 29, 30

192

Bibliography

[22] O. Lucia, L. Barragan, J. Burdio, O. Jimenez, D. Navarro, and I. Urriza, "A versatile power electronics test-bench architecture applied to domestic induction heating," *IEEE Trans. Ind. Electron.*, vol. 58, no. 99, p. 998, 2011. 30, 161, 163

[23] B. C. Kuo, *Sistemas de control automático*, 7th ed. Prentice-Hall Hispanoamericana, S.A., Méjico, 1996. 31, 32, 35

[24] Y.-L. Cui, K. He, Z.-W. Fan, and H.-L. Fan, "Study on DSP-based PLL-controlled superaudio induction heating power supply simulation," in *Proc. of Int. Conf. on Machine Learning and Cybernetics*, vol. 2, 2005, pp. 1082–1087. 39, 125, 126

[25] E. J. Dede, V. Esteve, J. Garcia, A. E. Navarro, and J. A. Carrasco, "On the design of high frequency series resonant converters for induction heating applications," in *Proc. Int. Conf. on Ind. Electronics, Control, and Instrumentation*, vol. 2, 1993, pp. 1303–1307. 45

[26] C. Cases, J. Jordan, J. M. Magraner, V. Esteve, E. Dede, E. Sanchis, E. Maset, A. Ferreres, J. B. Ejea, and E. Gumbau, "Characterization of IGBT devices for use in series resonant inverter for induction heating applications," in *Proc. 13th European Conf. Power Electronics and Applications*, 2009, pp. 1–8. 45, 52

[27] E. J. Dede, J. Jordan, and V. Esteve, "State-of-the art and future trends in transistorised inverters for induction heating applications," in *Proc. 5th IEEE Int. Caracas Conference on Devices, Circuits and Systems*, vol. 1, 2004, pp. 204–211. 49, 50

[28] J. Jordán, "Estudio del comportamiento de generadores serie mosfet de alta potencia y frequencia," Ph.D. dissertation, Universitat de Valencia, Spain, 2003. 49, 50, 51, 76, 78, 81, 84, 215

[29] J. Jordan, J. M. Magraner, C. Cases, V. Esteve, E. Dede, E. Sanchis, E. Maset, A. Ferreres, J. B. Ejea, and E. Gumbau, "Turn on switching losses analysis for Si and SiC diodes in induction heating inverters," in *Proc. 13th European Conf. Power Electronics and Applications*, 2009, pp. 1–9. 50, 51, 52

[30] A. Fiel and T. Wu, "MOSFET failure modes in the zero-voltage-switched full-bridge switching mode power supply applications," in *Proc. 16th Annual IEEE Applied Power Electronics Conf. and Exposition*, vol. 2, 2001, pp. 1247–1252. 50, 51

Bibliography

[31] L. Saro, K. Dierberger, and R. Redl, "High-voltage mosfet behavior in soft-switching converters: analysis and reliability improvements," in *Proc. 20th Int. Telecommunications Energy Conf.*, 1998, pp. 30–40. 50, 51

[32] W. Choi and S. Young, "Improving system reliability using FRFET in LLC resonant converters," in *Proc. IEEE Power Electronics Specialists Conf.*, 2008, pp. 2346–2351. 50, 51

[33] W.-S. Choi, S. mo Young, and D. wook Kim, "Analysis of MOSFET failure modes in LLC resonant converter," in *Proc. 31st Int. Telecommunications Energy Conf.*, 2009, pp. 1–6. 50, 51

[34] H. Aigner, K. Dierberger, and D. Grafham, "Improving the full-bridge phase-shift ZVT converter for failure-free operation under extreme conditions in welding and similar applications," in *33rd IEEE IAS Annual Meeting*, vol. 2, 1998, pp. 1341–1348. 51

[35] L. Grajales, "Analysis and design of a 500 kHz series resonant inverter for induction heating aplications," Ph.D. dissertation, Faculty of the Virginia Polytechnic Institute and State University, Blacksburg, Virginia, USA, November 1995. 51, 81, 143

[36] J. Jordan, V. Esteve, R. Garcia-Gil, E. Sanchis, E. Maset, and E. Dede, "New power MOSFET selection method to avoid failures," in *Proc. 19th Annual IEEE Applied Power Electronics Conf. and Exposition*, vol. 2, 2004, pp. 1257–1261. 52

[37] J. Jordan, V. Esteve, E. Dede, J. M. Magraner, E. Sanchis, E. Maset, and J. E. Ferreres, "Automated calculation method to determine the output power based on the frequency for induction heating IGBT parallel inverter," in *Proc. IEEE Power Electronics Specialists Conf.*, 17–21 June 2007, pp. 713–718. 73, 74

[38] J. M. Magraner, J. Jordan, C. Cases, V. Esteve, E. Dede, E. Sanchis, E. Maset, A. Ferreres, J. B. Ejea, and E. Gumbau, "Firing strategy for bidirectional current switches with unidirectional voltage blocking capability in induction heating parallel resonant inverters," in *Proc. 13th European Conf. Power Electronics and Applications*, 2009, pp. 1–7. 74

194

[39] S. Dieckerhoff, M. J. Ruan, and R. W. De Doncker, "Design of an IGBT-based LCL-resonant inverter for high-frequency induction heating," in *34th IEEE IAS Annual Meeting*, vol. 3, 1999, pp. 2039–2045 vol.3. 74, 75

[40] E. J. Dede, J. Jordan, V. Esteve, J. M. Espi, and S. Casan, "Series and parallel resonant inverters for induction heating under short-circuit conditions considering parasitic components," in *Proc. IEEE Int. Conf. on Power Electronics and Drive Systems*, vol. 2, 1999, pp. 659–662 vol.2. 74, 81

[41] E. J. Dede, J. Jordan, V. Esteve, J. V. Gonzalez, and D. Ramirez, "Design considerations for induction heating current-fed inverters with IGBT's working at 100 kHz," in *Proc. 8th Annual IEEE Applied Power Electronics Conf. and Exposition*, 1993, pp. 679–685. 74

[42] R. Fuentes, P. Lagos, and J. Estrada, "Self-resonant induction furnace with IGBT technology," in *Proc. 4th IEEE Conf. Industrial Electronics and Applications*, 2009, pp. 1371–1374. 74

[43] J. M. Espi, E. J. Dede, A. Ferreres, and R. Garcia, "Steady-state frequency analysis of the LLC resonant inverter for induction heating," in *Proc. 5th IEEE Int. Power Electronics Congress*, 1996, pp. 22–28. 75

[44] J. M. Espi, A. E. Navarro, J. Maicas, J. Ejea, and S. Casans, "Control circuit design of the L-LC resonant inverter for induction heating," in *Proc. 31st IEEE Power Electronics Specialists Conf.*, vol. 3, 2000, pp. 1430–1435 vol.3. 75

[45] A. Schonknecht and R. W. De Doncker, "Novel topology for parallel connection of soft switching, high power, high frequency inverters," in *36th IEEE IAS Annual Meeting*, vol. 3, 2001, pp. 1477–1482 vol.3. 75, 103

[46] A. Schonknecht and R. W. A. A. De Doncker, "Novel topology for parallel connection of soft-switching high-power high-frequency inverters," *IEEE Trans. Ind. Appl.*, vol. 39, no. 2, pp. 550–555, 2003. 75, 103, 161

[47] J. M. Espi Huerta, E. J. Dede Garcia Santamaria, R. Garcia Gil, and J. Castello Moreno, "Design of the L-LC resonant inverter for induction heating based on its equivalent SRI," *IEEE Trans. Ind. Electron.*, vol. 54, no. 6, pp. 3178–3187, 2007. 75, 77, 78, 81

195

Bibliography

[48] H. Fujita and H. Akagi, "Pulse-density-modulated power control of a 4 kW, 450 kHz voltage-source inverter for induction melting applications," *IEEE Trans. Ind. Appl.*, vol. 32, no. 2, pp. 279–286, 1996. 81, 82, 83

[49] A. Okuno, H. Kawano, J. Sun, M. Kurokawa, A. Kojina, and M. Nakaoka, "Feasible development of soft-switched sit inverter with load-adaptive frequency-tracking control scheme for induction heating," *IEEE Trans. Ind. Appl.*, vol. 34, no. 4, pp. 713–718, 1998. 81

[50] E. J. Dede, J. Jordan, V. Esteve, J. M. Espi, and S. Casans, "Behaviour of series and parallel resonant inverters for induction heating in short-circuit conditions," in *Proc. 3rd IEEE Int. Power Electronics and Motion Control Conf.*, vol. 2, 2000, pp. 645–649 vol.2. 81

[51] A. Jangwanitlert, J. Songboonkaew, W. Thammasiriroj, and J. C. Balda, "Analysis of three-level ZVS PWM inverter for induction heating applications," in *Proc. 5th IEEE Int. Power Electronics and Motion Control Conf.*, vol. 2, 2006, pp. 1–5. 81, 98

[52] J. M. Ho and M. T. Lee, "A novel PWM inverter control circuitry for induction heating," in *Proc. 5th IEEE Int. Power Electronics Congress*, 1996, pp. 113–119. 81

[53] A. R. A. M. Makky, H. Abo-Zied, and F. N. Abdelbar, "Parallel operation of IGBTs modular converter system for high power high frequency induction heating applications," in *Proc. 12th International Middle-East Power System Conf.*, 12–15 March 2008, pp. 577–582. 81, 101

[54] N. Yongyuth, P. Viriya, and K. Matsuse, "Analysis of a Full-Bridge inverter for induction heating using asymmetrical phase-shift control under ZVS and NON-ZVS operation," in *Proc. 7th Int. Conf. on Power Electronics and Drive Systems*, 2007, pp. 476–482. 81

[55] C. Chen and J. Zou, "DSP-based high-frequency HVDC source for verifying internal pressure of vacuum chamber," in *Proc. Int. Conf. on Condition Monitoring and Diagnosis*, 2008, pp. 850–853. 81

[56] J. Essadaoui, P. Sicard, E. Ngandui, and A. Cheriti, "Power inverter control for induction heating by pulse density modulation with improved power factor," in *Proc. Canadian Conf. on Electrical and Computer Engineering*, vol. 1, 2003, pp. 515–520 vol.1. 81, 83

[57] E. J. Dede, V. Esteve, E. Maset, J. M. Espi, A. E. Navarro, J. A. Carrasco, and E. Sanchis, "Soft switching series resonant converter for induction heating applications," in *Proc. Int. Conf. on Power Electronics and Drive Systems*, 1995, pp. 689–693 vol.2. 81

[58] S. Zerouali, A. Allag, S. M. Mimoune, A. H. Hamida, S. Khanniche, and M. Feliachi, "An adaptive control applied to series resonant inverter for induction heating," in *Proc. 41st Int. Universities Power Engineering Conf.*, vol. 2, 2006, pp. 633–636. 81

[59] M.-P. Chen, J.-K. Chen, K. Murata, M. Nakahara, and K. Harada, "Surge analysis of induction heating power supply with PLL," *IEEE Trans. Ind. Appl.*, vol. 16, no. 5, pp. 702–709, 2001. 81, 125, 126, 143

[60] E. J. Dede, J. Jordan, V. Esteve, and C. Cases, "New investigations on short-circuit behaviour of current-fed inverters for induction tube welding," in *Proc. 4th IEEE Int. Conf. on Power Electronics and Drive Systems*, vol. 2, 2001, pp. 760–763 vol.2. 81

[61] F. P. Dawson and P. Jain, "A comparison of load commutated inverter systems for induction heating and melting applications," *IEEE Trans. Power Electron.*, vol. 6, no. 3, pp. 430–441, 1991. 81

[62] I. Khan, J. Tapson, and I. de Vries, "An induction furnace employing a 100 kHz MOSFET full-bridge current-source load-resonant inverter," in *Proc. IEEE Int. Symposium on Industrial Electronics*, vol. 2, 1998, pp. 530–534 vol.2. 81

[63] Z. Zhao, Y. Peng, and Y. Li, "Devices dissipation of series-resonant inverter under pulse-width phase-shift operating mode," in *Proc. Asia-Pacific Power and Energy Engineering Conf.*, 2010, pp. 1–4. 83

[64] L. Grajales, J. A. Sabate, K. R. Wang, W. A. Tabisz, and F. C. Lee, "Design of a 10 kW, 500 kHz phase-shift controlled series-resonant inverter for induction heating," in *Proc. IEEE Industry Applications Society*, 1993, pp. 843–849. 83, 143

[65] V. Esteve, E. Sanchis-Kilders, J. Jordan, E. J. Dede, C. Cases, E. Maset, J. B. Ejea, and A. Ferreres, "Improving the efficiency of IGBT series-resonant inverters using pulse density modulation," *IEEE Trans. Ind. Electron.*, vol. 58, no. 3, pp. 979–987, 2011. 83, 84, 85, 143

197

[66] Y. Wenxu, J. Zhicheng, and L. Xianling, "Power control for induction heating by asymmetrical pulse density modulation," in *Proc. 1st IEEE Conf. on Industrial Electronics and Applications*, 2006, pp. 1–5. 84

[67] V. Esteve, E. J. Dede, J. Jordan, C. Cases, R. Herrero, J. M. Magraner, E. Sanchis-Kilders, and E. Maset, "Stabilization of the DC-link for inverters with PDM power control," in *Proc. 13th European Conf. Power Electronics and Applications*, 2009, pp. 1–9. 85, 161

[68] O. Lucia, J. M. Burdio, L. A. Barragan, J. Acero, and C. Carretero, "High frequency pulse density modulation for cost-effective and efficient multiple induction-heater architectures," in *Proc. 26th IEEE Applied Power Electronics Conf. and Exposition*, 2011, pp. 1118–1123. 85

[69] H. Fujita, N. Uchida, and K. Ozaki, "A new zone-control induction heating system using multiple inverter units applicable under mutual magnetic coupling conditions," *IEEE Trans. Power Electron.*, vol. 26, no. 7, pp. 2009–2017, 2011. 86

[70] H. P. Ngoc, H. Fujita, K. Ozaki, and N. Uchida, "Phase angle control of high-frequency resonant currents in a multiple inverter system for zone-control induction heating," *IEEE Trans. Power Electron.*, vol. 26, no. 11, pp. 3357–3366, 2011. 86

[71] S. Okudaira and K. Matsuse, "Power control of an adjustable frequency quasi-resonant inverter for dual frequency induction heating," in *Proc. 3rd Int. Power Electronics and Motion Control Conf.*, vol. 2, 2000, pp. 968–973 vol.2. 87

[72] V. Esteve, J. Jordan, E. J. Dede, E. Sanchis-Kilders, and E. Maset, "Induction heating inverter with simultaneous dual-frequency output," in *Proc. 21st IEEE Applied Power Electronics Conf. and Exposition*, 2006, pp. 5 pp.–. 87

[73] F. Monterde, P. Hernadez, J. M. Burdio, J. R. Garcia, and A. Martinez, "A new ZVS two-output series-resonant inverter for induction cookers obtained by a synthesis method," in *Proc. 31st IEEE Power Electronics Specialists Conf.*, vol. 3, 2000, pp. 1375–1380 vol.3. 88

[74] F. Forest, E. Laboure, F. Costa, and J. Y. Gaspard, "Principle of a multi-load/single converter system for low power induction heating," *IEEE Trans. Power Electron.*, vol. 15, no. 2, pp. 223–230, 2000. 88

198

Bibliography

[75] J. M. Burdio, F. Monterde, J. R. Garcia, L. A. Barragan, and A. Martinez, "A two-output series-resonant inverter for induction-heating cooking appliances," *IEEE Trans. Power Electron.*, vol. 20, no. 4, pp. 815–822, 2005. 88

[76] J. Acero, J. M. Burdio, L. A. Barragan, D. Navarro, R. Alonso, J. Ramon, F. Monterde, P. Hernandez, S. Llorente, and I. Garde, "Domestic induction appliances," *IEEE Ind. Appl. Mag.*, vol. 16, no. 2, pp. 39–47, 2010. 88

[77] T. Isobe, K. Usuki, N. Arai, T. Kitahara, K. Fukutani, and R. Shimada, "Variable frequency induction heating using magnetic energy recovery switch (mers)," in *Proc. IEEE Power Electronics Specialists Conference PESC 2008*, 2008, pp. 2139–2145. 88

[78] T. Isobe, Y. Miyaji, T. Kitahara, K. Fukutani, and R. Shimada, "Soft-switching inverter for variable frequency induction heating using magnetic energy recovery switch (MERS)," in *Proc. 13th European Conf. Power Electronics and Applications*, 2009, pp. 1–10. 88

[79] T. Ericsen, Y. Khersonsky, P. Schugart, and P. Steimer, "PEBB - power electronics building blocks, from concept to reality," in *Proc. 3rd IET Int. Conf. Power Electronics, Machines and Drives*, 2006, pp. 12–16. 94

[80] P. M. Shenoy, S. Shekhawat, and B. Brockway, "Application specific 1200 V planar and trench IGBTs," in *Proc. 21st IEEE Applied Power Electronics Conf. and Exposition*, 2006. 95

[81] R. Francis and M. Soldano, "A new SMPS nonpunch thru IGBT replace MOSFET in SMPS high frequency applications," in *Proc. 18th IEEE Applied Power Electronics Conf. and Exposition*, vol. 2, 2003, pp. 953–957. 95

[82] G. Holmes and T. A. Lipo, *Pulse width modulation for power converters: principles and practice.* Wiley-IEEE Press, 2003. 97, 98

[83] L. QingFeng, W. HuaMin, and L. ZhaoXia, "Discuss on the application of multilevel inverter in high frequency induction heating power supply," in *Proc. IEEE TENCON*, 2006, pp. 1–4. 97

[84] B. Diong, S. Basireddy, K. Corzine, and Y. Familiant, "Multilevel inverters with equal or unequal sources for dual-frequency induction

heating," in *Proc. 19th IEEE Applied Power Electronics Conf. and Exposition*, vol. 2, 2004, pp. 825–831. 98

[85] H. A. Zied, P. Mutschler, and G. Bachmann:, "A modular IGBT converter system for high frequency induction heating applications," in *PCIM Conference*, 2000. 98, 111

[86] F. Kleveland, T. M. Undeland, and J. K. Langelid, "Increase of output power from IGBTs in high power high frequency resonant load inverters," in *Proc. IEEE Industry Applications Conf.*, vol. 5, 2000, pp. 2909–2914 vol.5. 101, 111

[87] F. Kleveland, J. K. Langelid, and L. Markegård, "New HF converter for induction heating," in *Proc. of the Electromagnetic Processing of Materials Int. Conf.*, 2003. 101

[88] D. W. Hart, *Introducción a la electrónica de Poténcia.* Prentice Hall, Inc., Madrid, Spain, 2001. 106

[89] R. E. Best, *Phase-Locked Loops : Design, Simulation, and Applications*, 3rd ed. McGraw-Hill Companies, Inc., 1997. 124, 126

[90] S. Goldman, *Phase-Locked Loops Engineering Handbook for Integrated Circuits.* Artech House, Inc., 2007. 124

[91] A. Okuno, M. Hayashi, H. Kawano, H. Yasutsune, E. Hiraki, and M. Nakaoka, "Phase-lock loop operated load-resonance inverter using static induction power transistors and its practical characteristic evaluations," in *Proc. IEEE-IAS Conf. Emerging Technology*, 1995, pp. 1–7. 125, 126

[92] A. Okuno, M. Hayashi, H. Kawano, H. Yasutsune, and M. Nakaoka, "Series resonant frequency tracking-based high-frequency inverter using static induction power transistors for electromagnetic industrial induction metal surface heating and feasible evaluations," in *Proc. Int. Conf. on Power Electronics and Drive Systems*, vol. 1, 1995, pp. 212–217. 125, 126

[93] I. Khan, J. Tapson, and I. De Vries, "Automatic frequency control of an induction furnace," in *Proc. IEEE AFRICON*, vol. 2, 1999, pp. 913–916. 125, 126

[94] I. Khan, J. Tapson, and I. de Vries, "Frequency control of a current-fed inverter for induction heating," in *Proc. IEEE Int. Symposium on Industrial Electronics*, vol. 1, 2000, pp. 343–346. 125, 126

[95] S. Chudjuarjeen, C. Koompai, and V. Monyakul, "Full-bridge current-fed inverter with automatic frequency control for forging application," in *Proc. IEEE TENCON*, vol. 4, 2004, pp. 128–131. 125, 126

[96] J. Tian, J. Petzoldt, T. Reimann, M. Scherf, and G. Berger, "Control system analysis and design of a resonant inverter with the variable frequency variable duty cycle scheme," in *Proc. 37th IEEE Power Electronics Specialists Conf.*, 2006, pp. 1–5. 125, 126, 164

[97] E. J. Dede, J. V. Gonzalez, J. A. Linares, J. Jordan, D. Ramirez, and P. Rueda, "25-kW/50-kHz generator for induction heating," *IEEE Trans. Ind. Electron.*, vol. 38, no. 3, pp. 203–209, 1991. 125, 126

[98] H. Sheng, Y. Pei, X. Yang, F. Wang, and C. W. Tipton, "Frequency tracking control for a capacitor-charging parallel resonant converter with phase-locked loop," in *Proc. 22nd IEEE Applied Power Electronics Conf.*, 2007, pp. 1287–1292. 125, 126

[99] N. S. Bayindir, O. Kukrer, and M. Yakup, "DSP-based PLL-controlled 50-100 kHz 20 kW high-frequency induction heating system for surface hardening and welding applications," *IEE Proc. Electric Power Applications*, vol. 150, no. 3, pp. 365–371, 2003. 126, 143

[100] J. Calpe, E. Sanchis, M. Martinez, V. Esteve, and A. Rosado, "DSP-based control for a series resonant heating generator," in *Proc. 28th IEEE Conf. Industry Applications Society*, vol. 3, 2002, pp. 1960–1965. 126, 164

[101] C. Zhang, Y. Li, and H. Li, "The implementation and analysis of a new self-sampling P1 control all digital phase-locked loop," in *Proc. IEEE TENCON*, 2006, pp. 1–4. 126

[102] H. Li, Y. Li, and Y. Peng, "FPGA-based all digital phase-locked loop controlled induction heating power supply operating at optimized ZVS mode," in *Proc. IEEE TENCON*, 2006, pp. 1–4. 126

[103] *TMS320F2809, TMS320F2808, TMS320F2806, TMS320F2802, TMS320F2801, TMS320C2802, TMS320C2801, TMS320F28016,*

Bibliography

$TMS320F28015$, *Digital Signal Processors, Data Manual.*, Texas Instruments Incorporated, Texas Instruments, Dallas, Texas, 2003-2009. 134

[104] S. Nagai, H. Nagura, M. Nakaoka, and A. Okuno, "High-frequency inverter with phase-shifted PWM and load-adaptive PFM control strategy for industrial induction-heating," in *Proc. IEEE Conf. Industry Applications Society*, 1993, pp. 2165–2172. 143

[105] P. Viriya, N. Yongyuth, and K. Matsuse, "Analysis of transition mode from phase shift to zero-phase shift under ZVS and NON-ZVS operation for induction heating inverter," in *Proc. Power Conversion Conf.*, 2007, pp. 1512–1519. 143

[106] L. A. Barragan, J. M. Burdio, J. I. Artigas, D. Navarro, J. Acero, and D. Puyal, "Efficiency optimization in ZVS series resonant inverters with asymmetrical voltage-cancellation control," *IEEE Trans. Power Electron.*, vol. 20, no. 5, pp. 1036–1044, 2005. 143

[107] M. H. Rashid, *Power electronics handbook*, 2nd ed. Elsevier, Inc., 2007. 152

[108] *SKM 100GB128D Datahseet*, Semikron, October 2006. 152

[109] S. Tominaga, H. Urushibata, H. Fujita, H. Akagi, T. Horiguchi, S. Kinouchi, and T. Oi, "Modeling of igbts with focus on voltage dependency of terminal capacitances," in *Proc. 14th European Conf. Power Electronics and Applications*, 2011, pp. 1–9. 152

[110] M. Hermwille, "Application note AN-7004 IGBT driver calculation," Semikron, Tech. Rep., Oct. 2007. 152

[111] H. W. E. Koertzen, P. C. Theron, J. A. Ferreira, and J. D. Van Wyk, "A new induction heating circuit with clamped capacitor voltage suitable for heating to above Curie temperature," in *Proc. Int. Conf. on Industrial Electronics, Control, and Instrumentation*, vol. 2, 1993, pp. 1308–1313. 160

[112] H. Sewell, D. Stone, and C. Bingham, "Dynamic load impedance matching for induction heater systems," *COMPEL*, vol. 22 Iss: 1, pp. 30–38, 2003. 160, 163

202

[113] T. Tudorache and V. Fireteanu, "Magneto-thermal-motion coupling in transverse flux heating," *COMPEL*, vol. 27, pp. 399 – 407, 2008. 162

[114] H. Liu and J. Rao, "Coupled modeling of electromagnetic-thermal problem in induction heating process considering material properties," in *Proc. Int. Conf. Information Engineering and Computer Science*, 2009, pp. 1–4. 162

[115] S. Yafei, S. Jing, and N. Dongjie, "Numerical simulation of induction heating of steel bar with nonlinear material properties," in *Proc. IEEE Int. Conf. Automation and Logistics*, 2009, pp. 450–454. 162

[116] Y. Blinov, F. Dughiero, and S. Lupi, "Mutual influence between load and frequency converter in the induction heating of steel," in *Proc. IEEE Industry Applications Society*, vol. 1, 1994, pp. 679–683. 162

[117] X. Yang, Y. Wang, and W. Yan, "Simulation of induction heating device with double inductors for continuously heating up steel bars," in *Proc. World Automation Congress*, 2008, pp. 1–5. 162

[118] J. Zgraja and J. Bereza, "Computer simulation of induction heating system with series inverter," *COMPEL*, vol. 22, pp. 48–57, 2003. 162

[119] J. Zgraja, "Computer simulation of induction hardening of moving flat charge," *IEEE Trans. Magn.*, vol. 39, no. 3, pp. 1523–1526, 2003. 162

[120] P.-C. Lin, Y.-Y. Ku, C.-M. Lai, Y.-H. Liao, and Y.-S. Huang, "Implementation of a PLL-based high frequency resonant ac power supply," in *Proc. SICE Annual Conf.*, 2008, pp. 1329–1334. 164

[121] V. Fireteanu and T. Tudorache, "Numerical simulations of continuous induction heating of magnetic billets and sheets," *COMPEL*, vol. 22, pp. 68 –78, 2003. 167

[122] G. Martin-Segura, J. Lopez-Mestre, H. Rivas-Guerrero, M. Teixido-Casas, and D. Montesinos-Miracle, "A low cost DSP-based control method for high frequency parallel resonant current-fed inverters," in *Proc. 13th European Conf. Power Electronics and Applications*, 2009, pp. 1–7. 186

[123] G. Martín-Segura, P. Sala-Pérez, C. Ferrater-Simón, J. López-Mestre, D. Montesinos-Miracle, and J. Bergas-Jané, "All-digital DSP-based

phase-locked loop for induction heating applications," *Accepted in European Transactions on Electrical Power*, 2012. 186

[124] G. Martín-Segura, C. Ferrater-Simón, J. López-Mestre, G. Gross, and D. Montesinos-Miracle, "Load-adaptive phase-shift and dead-time control for induction heating applications," *Submittedto European Transactions on Electrical Power*, 2012. 187

[125] G. Martín-Segura, C. Ferrater-Simón, D. Montesinos-Miracle, F. Leach, and I. Vadan, "FEM modeling of a continuous induction heating process of steel wire hardening," in *Simpozionului National de Electrotehnica Teoretica*, 2010. 187

[126] G. Martín-Segura, C. Ferrater-Simón, J. López-Mestre, D. Montesinos-Miracle, and J. Bergas-Jané, "Simulation of an induction hardening system during Curie temperature transition considering converter's performance," *Accepted in COMPEL*, 2012. 187

[127] G. Martín-Segura, P. Sala-Pérez, C. Ferrater-Simón, J. López-Mestre, and D. Montesinos-Miracle, "Study of the parasitic inductance and resistance in continuous wire induction heating systems above curie temperature," in *Submitted to the 3rd Int. Symposium on Power Electronics for Distributed Generation Systems*, 2012. 187

Appendix A

Electrical model of a long solenoid heating a solid cylinder

In Section 2.2 an electrical model of the inductor-workpiece for a long solenoid heating a cylinder extracted from [6] is presented. In this section, a brief resume of the equations and mathematics involved are explained deeply. The aim of this appendix is to compile all the equations and explanations found in [6] and show the complexity of the process to obtain them and the assumptions made. The problem is developed and solved for a long solenoid heating a solid cylinder, but it can be found in [6] for another simple workpiece shapes like slabs, cylinders and tubes.

First, in Section A.1, the equivalent magnetic circuit is presented. The formulation assumes that the inductor, workpiece and air-gap share a common magnetic field intensity. Starting from this assumption, the equations of the magnetic fluxes in these areas are encountered. Afterwards, in Section, A.2, the equivalent electrical circuit inductor-workpiece is deduced from these magnetic fluxes, obtaining a circuit composed of three inductances (from air-gap, workpiece and inductor) and two resistances (from workpiece and inductor).

A.1 Equivalent magnetic circuit of the inductor-workpiece

The present model derives from Baker's series circuit [6, p. 233] and is based on the assumption that the inductor, the workpiece and the air-gap between them share a common magnetic field intensity, H_s, as seen in Figure A.1.

In Figure A.1, ϕ_c, ϕ_w and ϕ_a represent the magnetic fluxes in the coil, the workpiece and the air-gap respectively. In next sections the equations of these magnetic fluxes are developed: in Section A.1.1 the inductor flux, in Section A.1.2 the workpiece flux and in Section A.1.3 the air-gap flux.
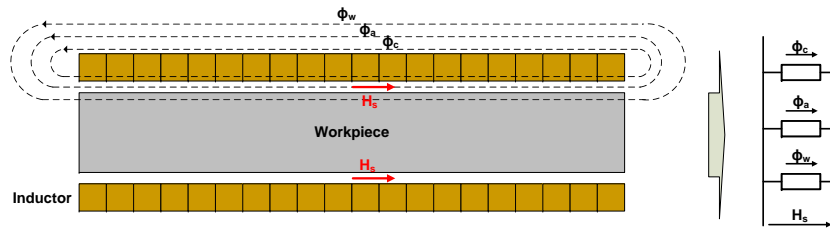
Figure A.1: Magnetic field intensity and flux paths in the inductor-workpiece system and its equivalent magnetic circuit.

A.1.1 Magnetic flux in the inductor

To proceed with the equations involved in the process, it is much easier to think in a coil of infinite radius with a workpiece inside of infinite radius too. In Figure A.2 a coil of infinite length is represented. Assuming the radius is infinite, it is possible to think in the coil as a semi-infinite slab. The inductor and the workpiece are considered to be so near that the magnetic field at the surface is the same and equal to H_s. It is assumed that there is just magnetic field in the x direction and current flowing in the z direction.
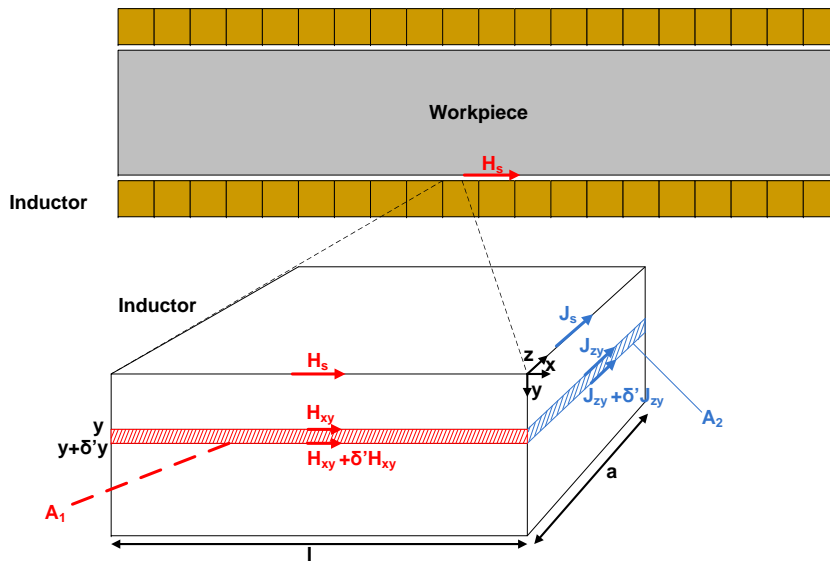
Figure A.2: Qualitative representation of the induced currents through the cross-sectional area of the inductor.

A.1 Equivalent magnetic circuit of the inductor-workpiece

Considering the portion of the coil shown in Figure A.2, δ' represents a very small but finite change of a variable. H_{xy} represents the magnetic field H in the x direction and J_{zy} the current density J in the z axis as a function of y. Taking into account the general formulation of Ampere's law for a curve C

$$\oint_C \mathbf{H}d\mathbf{l} = I \tag{A.1}$$

where

$$I = \int_S \mathbf{J}d\mathbf{S} \tag{A.2}$$

Applying these equations in the surface area A_1 and the curve defined by this area, then is accomplished ignoring the second-order differentials

$$H_{xy}l - \left(H_{xy} + \delta'H_{xy}\right)l = J_{zy}\left(l\delta'y\right) \tag{A.3}$$

that becomes

$$\frac{dH_{xy}}{dy} = -J_{zy} \tag{A.4}$$

Considering the general formulation of Farady's law for a curve C

$$\oint_C \mathbf{E}d\mathbf{l} = -\frac{d\phi}{dt} \tag{A.5}$$

and

$$\mathbf{E} = \rho\mathbf{J} \tag{A.6}$$

$$\phi = \int_S \mathbf{B}d\mathbf{S} \tag{A.7}$$

$$\mathbf{B} = \mu\mathbf{H} \tag{A.8}$$

Observing Figure A.2, the follwing expression is obtained for the surface area A_2 and the curve defined by this area

$$\rho J_{zy}a - \rho\left(J_{zy} + \delta'J_{zy}\right)a = -\frac{d\left[\mu\left(-H_{xy}\right)a\delta'y\right]}{dt} \tag{A.9}$$

Assuming that the magnetic field is sinusoidal with an angular frequency of ω

$$H_{xy} = H_{xy}^{max} cos\left(\omega t\right) \tag{A.10}$$

then, Equation A.9 becomes

$$\rho\delta' J_{zy} = -j\omega\mu H_{xy}\delta' y \tag{A.11}$$

and thus

$$\rho\frac{dJ_{zy}}{dy} = -j\omega\mu H_{xy} \tag{A.12}$$

Combining Equations A.4 and A.12 we obtain the following ordinary differential equation

$$\frac{d^2 H_{xy}}{dy^2} - \frac{j\omega\mu}{\rho}H_{xy} = 0 \tag{A.13}$$

Considering

$$k^2 = \frac{\omega\mu}{\rho} \tag{A.14}$$

The solution of Equation A.13 has the following form

$$H_{xy} = C_1 e^{\sqrt{j}ky} + C_2 e^{-\sqrt{j}ky} \tag{A.15}$$

with C_1 and C_2 being constants. Considering that when $y = \infty$ the magnetic field is 0 and when $y = 0$ it is equal to H_s, then C_1 is equal to 0 and C_2 equal to H_s. Therefore, the solution of Equation A.13 is

$$H_{xy} = H_s e^{-\sqrt{j}ky} = H_s e^{-\sqrt{\frac{j\omega\mu}{\rho}}y} \tag{A.16}$$

Considering the total flux per meter width through the coil, ϕ'_c, and Equations A.7 and A.8, then

$$\phi'_c = \mu \int_0^\infty H_{xy}dy = \mu \int_0^\infty H_s e^{-\sqrt{\frac{j\omega\mu}{\rho}}y}dy = H_s\sqrt{\frac{\mu\rho}{\omega}}e^{-\frac{\pi}{4}j} \tag{A.17}$$

Regarding Equation 1.13, the penetration depth in the coil is

$$\delta_c = \sqrt{\frac{2\rho_c}{\mu_c\omega}} \tag{A.18}$$

and Equation A.17 becomes

A.1 Equivalent magnetic circuit of the inductor-workpiece

$$\phi'_c = H_s\sqrt{\frac{\mu_c\rho_c}{\omega}}e^{-\frac{\pi}{4}j} = \frac{H_s\mu_c}{\sqrt{2}}\sqrt{\frac{2\rho_c}{\mu_c\omega}}\left(\frac{1-j}{\sqrt{2}}\right) = \frac{H_s\mu_c\delta_c}{2}\left(1-j\right) \quad \text{(A.19)}$$

Considering a width equal to the perimeter of the coil, the total flux in the coil is

$$\phi_c = k_r\frac{H_s\mu_c\delta_c}{2}\left(1-j\right)2\pi r_c \quad \text{(A.20)}$$

being r_c the inner radius of the coil and k_r a correction factor lying between 1 and 1.5 (usually 1.15). It has to be noted that in most of applications the inductor is made of copper and the magnetic permeability is equal to the permeability of the air (μ_0).

A.1.2 Magnetic flux in the workpiece

Proceeding like in the previous section but for the workpiece, it is assumed that there is just magnetic field in the x direction and current flowing in the z direction, as seen in Figure A.3. Using Ampere's law (Equation A.1) for the shaded area of the workpiece, A_3, the following equation is obtained

$$\left(H_{zr} + \delta'H_{zr}\right)l - H_{zr}l = J_{\theta r}\left(l\delta'r\right) \quad \text{(A.21)}$$

Therefore,

$$\frac{dH_{zr}}{dy} = J_{\theta r} \quad \text{(A.22)}$$

Considering Faraday's law (Equation A.5) and Equations A.6 to A.8, for the shaded area A_4 the following equation is accomplished

$$\rho\left(J_{\theta r} + \delta'J_{\theta r}\right)\left[2\pi\left(r + \delta'r\right)\right] - \rho\left(J_{\theta r}\right)2\pi r = -\frac{d\left[\mu\left(-H_{zr}\right)A_4\right]}{dt} \quad \text{(A.23)}$$

Assuming that the magnetic field is sinusoidal, as in Equation A.10, and neglecting the square roots of small quantities, A_4 equals to

$$A_4 \approx 2\pi r\delta'r \quad \text{(A.24)}$$

and Equation A.23 turns into

$$\frac{\rho\left(J_{\theta r}\right)}{r} + \frac{dJ_{\theta r}}{dr} = \mu j\omega H_{zr} \quad \text{(A.25)}$$
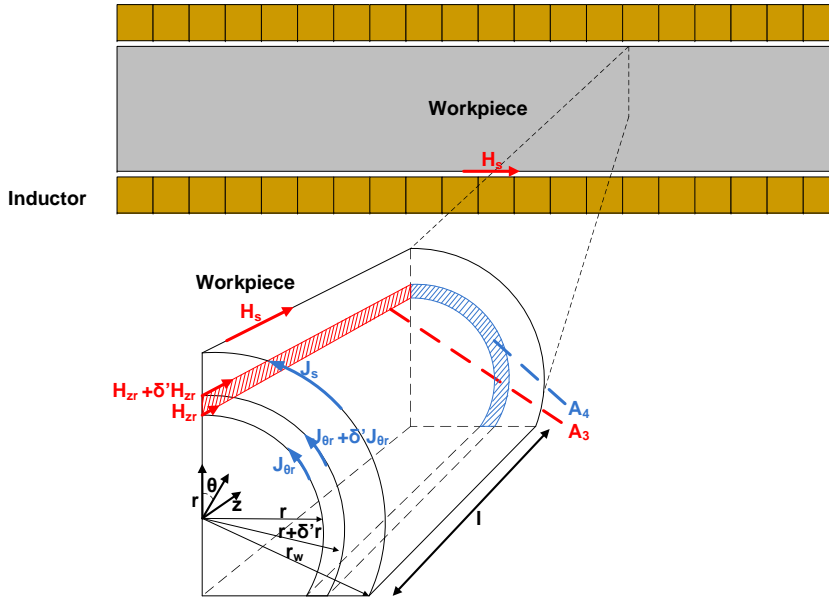
Figure A.3: Qualitative representation of the induced currents through the cross-sectional area of the workpiece.

Combining Equations A.22 and A.25, the following equation is obtained

$$r^2\frac{d^2H_{zr}}{dr^2} + r\frac{H_{zr}}{dr} - j\frac{r^2\mu\omega}{\rho}H_{zr} = 0 \tag{A.26}$$

which is a second-order ordinary differential equation.

Given that the modified Bessel differential equation has the following form

$$x^2\frac{d^2y}{dx^2} + x\frac{dy}{dx} - \left(x^2 + n^2\right)y = 0 \tag{A.27}$$

where y is the function, x the variable and n the order of the Bessel function.

Rearranging A.26 considering Equation A.14, we obtain

$$r^2\frac{d^2H_{zr}}{dr^2} + r\frac{H_{zr}}{dr} - \left(\sqrt{j}kr\right)^2 H_{zr} = 0 \tag{A.28}$$

which is a modified Bessel differential equation of order 0. Therefore, the solution of this equation is

A.1 Equivalent magnetic circuit of the inductor-workpiece

$$H_{zr} = AI_0\left(\sqrt{j}kr\right) + BK_0\left(\sqrt{j}kr\right) \tag{A.29}$$

where A and B are constants, $I_0(x)$ and $K_0(x)$ are the modified Bessel functions of order 0 of the first and second kind.

Considering that $K_0(0) = \infty$ and that at $r = 0$ the magnetic field H_{zr} can not be infinity, B is zero and the solution becomes

$$H_{zr} = AI_0\left(\sqrt{j}kr\right) = A\left[ber_0\left(kr\right) + bei_0\left(kr\right)j\right] \tag{A.30}$$

being $ber_0(x)$ and $bei_0(x)$ the so called Kelvin functions, which are the real and imaginary part of $I_0(\sqrt{j}x)$. and have the following series form

$$ber_0(x) = 1 + \sum_{n=1}^{\infty} \frac{(-1)^n \left(\frac{1}{2}x\right)^{4n}}{[(2n)!]^2} = 1 - \frac{(x/2)^4}{2!^2} + \frac{(x/2)^8}{4!^2} - \cdots \tag{A.31}$$

$$bei_0(x) = \sum_{n=0}^{\infty} \frac{(-1)^n \left(\frac{1}{2}x\right)^{2+4n}}{[(2n+1)!]^2} = \left(\frac{x}{2}\right)^2 - \frac{(x/2)^6}{3!^2} + \frac{(x/2)^{10}}{5!^2} - \cdots \tag{A.32}$$

Being r_w the radius of the workpiece, when $r = r_w$ the magnetic field equals to H_s, thus

$$H_s = A\left[ber_0\left(kr_w\right) + bei_0\left(kr_w\right)j\right] \tag{A.33}$$

Dividing the magnetic field H_{zr} by the magnetic field in the surface H_s, we obtain

$$\frac{H_{zr}}{H_s} = \frac{A\left[ber_0\left(kr\right) + bei_0\left(kr\right)j\right]}{A\left[ber_0\left(kr_w\right) + bei_0\left(kr_w\right)j\right]} \tag{A.34}$$

and

$$H_{zr} = H_s \frac{\left[ber_0\left(kr\right) + bei_0\left(kr\right)j\right]}{\left[ber_0\left(kr_w\right) + bei_0\left(kr_w\right)j\right]} \tag{A.35}$$

Considering the total flux through the workpiece, ϕ_w, and Equations A.7 and A.8, then

$$\phi_w = \mu \int_S H_{zr} dS = \mu \int_0^{r_w} \left(H_s \frac{ber_0\left(kr\right) + bei_0\left(kr\right)j}{ber_0\left(kr_w\right) + bei_0\left(kr_w\right)j}\right)(2\pi r)\, dr \tag{A.36}$$

knowing that

$$\int_0^x x ber_0\left(k'x\right) dx = \frac{x}{k'} bei_0'\left(k'x\right) \tag{A.37}$$

$$\int_0^x x bei_0\left(k'x\right) dx = -\frac{x}{k'} ber_0'\left(k'x\right) \tag{A.38}$$

with $ber_0'(x)$ and $bei_0'(x)$ being the derivative Kelvin functions of the first kind $ber_0(x)$ and $bei_0(x)$. Equation A.36 becomes

$$\phi_w = \frac{2\pi\mu H_s r_w}{k} \frac{bei_0'\left(kr_w\right) - ber_0'\left(kr_w\right)j}{ber_0\left(kr_w\right) + bei_0\left(kr_w\right)j} \tag{A.39}$$

Isolating the real and imaginary part of ϕ_w, we can obtain

$$\phi_w = \mu H_s A_w \left(q - pj\right) \tag{A.40}$$

being A_w the cross-sectional area of the workpiece

$$A_w = \pi r_w^2 \tag{A.41}$$

and p and q two functions defined by

$$p = \frac{2}{r_w k} \frac{ber_0\left(kr_w\right) ber_0'\left(kr_w\right) + bei_0\left(kr_w\right) bei_0'\left(kr_w\right)}{ber_0^2\left(kr_w\right) + bei_0^2\left(kr_w\right)} \tag{A.42}$$

$$q = \frac{2}{r_w k} \frac{ber_0\left(kr_w\right) bei_0'\left(kr_w\right) - bei_0\left(kr_w\right) ber_0'\left(kr_w\right)}{ber_0^2\left(kr_w\right) + bei_0^2\left(kr_w\right)} \tag{A.43}$$

that can be expressed as a function of the penetration depth (δ_w, Equation 1.13), and the radius of the wire

$$p = \frac{\sqrt{2}\delta_w}{r_w} \frac{ber_0\left(\sqrt{2}r_w/\delta_w\right) ber_0'\left(\sqrt{2}r_w/\delta_w\right) + bei_0\left(\sqrt{2}r_w/\delta_w\right) bei_0'\left(\sqrt{2}r_w/\delta_w\right)}{ber_0^2\left(\sqrt{2}r_w/\delta_w\right) + bei_0^2\left(\sqrt{2}r_w/\delta_w\right)}$$
$$\tag{A.44}$$

$$q = \frac{\sqrt{2}\delta_w}{r_w} \frac{ber_0\left(\sqrt{2}r_w/\delta_w\right) bei_0'\left(\sqrt{2}r_w/\delta_w\right) - bei_0\left(\sqrt{2}r_w/\delta_w\right) ber_0'\left(\sqrt{2}r_w/\delta_w\right)}{ber_0^2\left(\sqrt{2}r_w/\delta_w\right) + bei_0^2\left(\sqrt{2}r_w/\delta_w\right)}$$
$$\tag{A.45}$$

A.1.3 Magnetic flux in the air-gap

Assuming that the air-gap is the space between inductor and workpiece and keeping in mind Equations A.7 and A.8, the flux in the air-gap is equal to

$$\phi_a = \mu_0 H_s A_a \tag{A.46}$$

where A_a is the cross-sectional area, equivalent to

$$A_a = \pi r_c^2 - \pi r_w^2 \tag{A.47}$$

A.2 Equivalent electrical circuit of the inductor-workpiece

Taking into consideration Figure A.1 and Equations A.20, A.40 and A.46, the total flux is

$$\phi_t = \phi_c + \phi_w + \phi_a = \mu_0 H_s \left[(k_r \pi r_c \delta_c + \mu_w A_w q + A_a) - j \left(k_r \pi r_c \delta_c + \mu_w A_w p \right) \right] \tag{A.48}$$

Assuming that the coil is long and all the magnetomotive force is used to make the flux ϕ_t and using Ampere's law (Equation A.1), for an inductor with N_c turns is accomplished

$$H_s = \frac{I_c N_c}{l_c} \tag{A.49}$$

where I_c is the current through the coil and l_c its length.

Considering Faraday's law (Equation A.5) in the coil and a sinusoidal flux with an angular frequency of ω, the voltage in the coil is equal to

$$U_c = N_c j \omega \phi_t \tag{A.50}$$

Therefore

$$\phi_t = \frac{U_c}{N_c j \omega} \tag{A.51}$$

Substituting Equations A.49 and A.51 into Equation A.48, the following expression is obtained

$$U_c = \frac{\mu_0 \omega I_c N_c^2}{l_c} \left[(k_r \pi r_c \delta_c + \mu_w A_w p) + j \left(k_r \pi r_c \delta_c + \mu_w A_w q + A_a \right) \right] \tag{A.52}$$

that is analogous to the assume an equivalent circuit similar to the one shown in Figure A.4 where R_w represents the workpiece resistance, R_c is the coil resistance, L_a is the air-gap inductance, L_w is the workpiece inductance and L_c is the coil inductance.
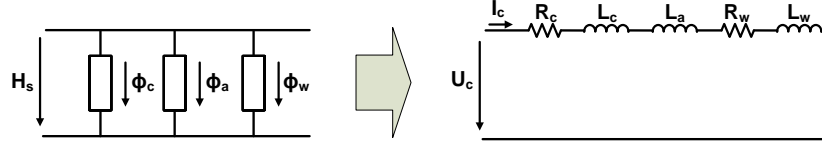
Figure A.4: Inductor-workpiece equivalent magnetic and electical circuit.

The values of the circuit's components are

$$R_w = \frac{\mu_0 \omega N_c^2}{l_c} \mu_w A_w p \tag{A.53}$$

$$L_w = \frac{\mu_0 \omega N_c^2}{l_c} \mu_w A_w q \frac{1}{\omega} = \frac{\mu_0 N_c^2}{l_c} \mu_w A_w q \tag{A.54}$$

$$R_c = \frac{\mu_0 \omega N_c^2}{l_c} k_r \pi r_c \delta_c \tag{A.55}$$

$$L_c = \frac{R_c}{\omega} = \frac{\mu_0 N_c^2}{l_c} k_r \pi r_c \delta_c \tag{A.56}$$

$$L_a = \frac{\mu_0 \omega N_c^2}{l_c} A_a \frac{1}{\omega} = \frac{\mu_0 N_c^2}{l_c} A_a \tag{A.57}$$

Appendix B

Zero voltage and zero current switching conditions for VFSRI at inductive switching

The sequence of states and events for an ideal VFSRI commutating at resonance, below and above is described in Section 3.2.4. Assuming the inverter is rarely at resonance, it is verified that commutating above resonance (inductive switching) improves the performance of the converter. The reason is that reverse recovery currents of the antiparallel diodes are avoided. Taking this into account, in Section 3.2.5, the conditions for having ZVS and ZCS considering parasitic components are introduced, but not completely described.

In this appendix, the conditions to have soft-switching at inductive switching are described and developed. The explanations in this appendix are extracted from the work realized by [28, pp. 157–170]. The main idea and its basic equations are briefly presented to enhance the comprehension of this study.

B.1 Sequence of events considering dead-time and parasitic components

In Section 3.2.4, Figure 3.12 shows the different states and events considering an ideal inverter. In case of real converters, the dead-time between switches and the parasitic capacitances have to be considered. These two parameters affect the sequence of events and determine having ZVS during switches' turn-on and ZCS during diodes' turn-off.

In Figure B.1, the circuit incorporating the parasitic capacitance of switches C_p is shown. The output waveforms and the sequence of events considering these capacitances and the dead-time is also presented. The states in this

figure are related to those seen in Figure 3.12 in Section 3.2.4. It has to be noted that the switches are supposed to commutate instantaneously without any delay.
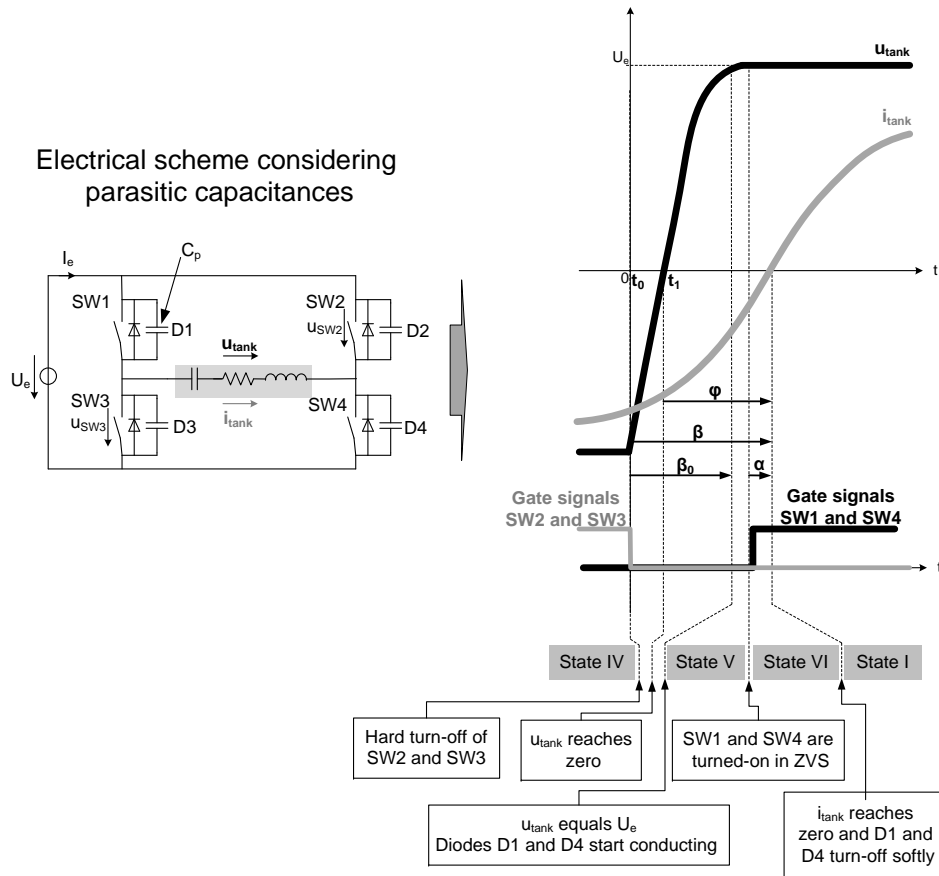

Figure B.1: Output waveforms and sequence to obtain ZVS and ZCS at inductive switching.

In order to have ZVS during switches' turn-on and ZCS in antiparallel diodes' turn-off, the following sequence have to be accomplished:

1. Switches $SW2$ and $SW3$ are turned-off hardly.

2. The parasitic capacitance, C_p, of SW2 and SW3 charge, while C_p of switches $SW1$ and $SW4$ discharge.

3. The voltage of the charging capacitors exceeds U_e and the antiparallel diodes $D1$ and $D4$ start conducting hardly.

4. Switches $SW1$ and $SW4$ are turned-on. The turning-on have no losses (ZVS) because their antiparallel diodes are conducting.

5. The current i_{tanc} changes polarity and conducts through $SW1$ and $SW4$, turning-off with ZCS the antiparallel diodes $D1$ and $D4$.

Considering this, the following parameters are defined (see Figure B.1):

- β is the phase-shift between the instant at which the gate signal of the switch becomes low and i_{tank} reaches zero.

- β_0 is the phase-shift between the instant at which the gate signal of the switch becomes low and the moment at which the voltage u_{tank} reaches U_e.

- φ is the phase-shift between u_{tank} and i_{tank}.

- α is the phase-shift between the instant at which the gate signal of the opposite switch becomes high and the moment at which i_{tank} crosses zero.

B.2 Zero voltage and zero current switching conditions

In order to have the correct sequence described in the previous section for having ZVS and ZCS, the following condition needs to be accomplished

$$(\beta - \beta_0) \geq \alpha \geq 0 \tag{B.1}$$

Considering this, two conditions for β and φ can be derived from this inequality.

B.2.1 β condition

Taking the moment at which $SW2$ and $SW3$ turn-off as a zero reference, the current is expressed as

$$i_{tank}(t) = \hat{i}_{tank} sin(\omega t - \beta) \tag{B.2}$$

Before diodes $D1$ and $D4$ starts conducting, the parasitic capacitances C_p of $SW2$ and $SW3$ have to be charged and those from $SW1$ and $SW4$ discharged. Considering that the voltage across $SW2$ at t_0 is 0 because in the previous moments was conducting, then

$$u_{SW2}(t) = \frac{\hat{i}_{tank}}{2\omega C_p} [cos(\omega t - \beta)]_0^t \tag{B.3}$$

thus

$$u_{SW2}(t) = \frac{\hat{i}_{tank}}{2\omega C_p} [cos(\beta - \omega t) - cos(\beta)] \tag{B.4}$$

The voltage u_{tank} at t_0 is equal to

$$u_{tank}(t) = -U_e + u_{SW2}(t) + u_{SW3}(t) \tag{B.5}$$

Assuming that $u_{SW2}(t)$ and $u_{SW3}(t)$ are equal and combining Equation B.6 with B.4, the tank voltage is

$$u_{tank}(t) = -U_e + \frac{\hat{i}_{tank}}{\omega C_p} [cos(\beta - \omega t) - cos(\beta)] \tag{B.6}$$

Regarding that the voltage u_{tank} is equal to U_e at β_0 (Figure B.1), the following equation is accomplished

$$u_{tank}\left(\frac{\beta_0}{\omega}\right) = U_e \tag{B.7}$$

so

$$u_{tank}\left(\frac{\beta_0}{\omega}\right) = -U_e + \frac{\hat{i}_{tank}}{\omega C_p} [cos(\beta - \beta_0) - cos(\beta)] = U_e \tag{B.8}$$

and

$$cos(\beta - \beta_0) = \frac{2U_e C_p \omega}{\hat{i}_{tank}} + cos(\beta) \tag{B.9}$$

Bearing in mind the condition expressed in Equation B.1 for having ZVS and ZCS, it can be transformed into

$$cos(\beta - \beta_0) \leq cos(\alpha) \tag{B.10}$$

that combined with Equation B.9 becomes

B.2 Zero voltage and zero current switching conditions

$$\frac{2U_e C_p \omega}{\hat{i}_{tank}} + cos\left(\beta\right) \leq cos\left(\alpha\right) \tag{B.11}$$

that leads to the following condition

$$\beta \geq arccos\left[cos\left(\alpha\right) - \frac{2U_e C_p \omega}{\hat{i}_{tank}}\right] \tag{B.12}$$

Considering the limit situation where the turning-on of $SW1$ and $SW4$ occur just before the crossing of zero, $\alpha = 0$ and Equation B.12 becomes

$$\beta \geq arccos\left[1 - \frac{2U_e C_p \omega}{\hat{i}_{tank}}\right] \tag{B.13}$$

B.2.2 φ condition

Regarding that t_1 is the moment at which u_{tank} changes polarity (Figure B.1), from Equation B.6

$$u_{tank}\left(t_1\right) = -U_e + \frac{\hat{i}_{tank}}{\omega C_p}\left[cos\left(\beta - \omega t_1\right) - cos\left(\beta\right)\right] = 0 \tag{B.14}$$

Observing Figure B.1, the phase-shift between voltage and current is equal to

$$\varphi = \beta - \omega t_1 \tag{B.15}$$

Therefore, Equation B.14 turns into

$$u_{tank}\left(t_1\right) = -U_e + \frac{\hat{i}_{tank}}{\omega C_p}\left[cos\left(\varphi\right) - cos\left(\beta\right)\right] = 0 \tag{B.16}$$

and

$$cos\left(\beta\right) = cos\left(\varphi\right) - \frac{U_e C_p \omega}{\hat{i}_{tank}} \tag{B.17}$$

Combining Equation B.13 with B.17, the following inequality emerges

$$cos\left(\varphi\right) - \frac{U_e C_p \omega}{\hat{i}_{tank}} \leq 1 - \frac{2U_e C_p \omega}{\hat{i}_{tank}} \tag{B.18}$$

that simplified is equal to

$$\varphi \geq arccos\left[1 - \frac{U_e C_p \omega}{\hat{i}_{tank}}\right] \tag{B.19}$$

Appendix C

Zero current and zero voltage switching conditions for CFPRI at capacitive switching

In Section 3.3.4, the sequence of states and events is described for an ideal CFPRI commutating at zero phase-shift between voltage and current, above and below this frequency. Although inductive switching is presumed to avoid reverse recovery currents of series diodes, capacitive switching improves the operation when considering the parasitic inductance L_p, as explained in Section 3.3.5. The conditions to have ZCS and ZVS considering parasitic components are introduced in that section, but not completely described.

In this appendix, the conditions to have soft-switching in case of capacitive switching are described and developed. The explanations in this appendix are extracted from the work realized by [8, pp. 88–150], presenting just the main ideas and equations in this appendix. For facilitating the understanding, the explanation procedure and the notation are similar than in Appendix B.

C.1 Sequence of events considering overlap-time and parasitic components

In Section 3.3.4, Figure 3.27 shows the different states and events considering an ideal inverter. In case of real converters, the overlap-time between switches and the parasitic inductances have to be considered. These two parameters affect the sequence of events and determine having ZCS during switches' turn-off and ZVS during diodes' turn-on.

The circuit incorporating the parasitic inductance of connections and switches L_p is shown in Figure C.1. The output waveforms and the sequence of events regarding these considerations are also presented. It has

to be noted that in CFPRI, contrary to VFSRI, during overlap-time all switches are conducting. In this case, switches are supposed to commutate instantaneously without any delay. The states presented in this figure are related to those seen in Figure 3.27 in Section 3.3.4.

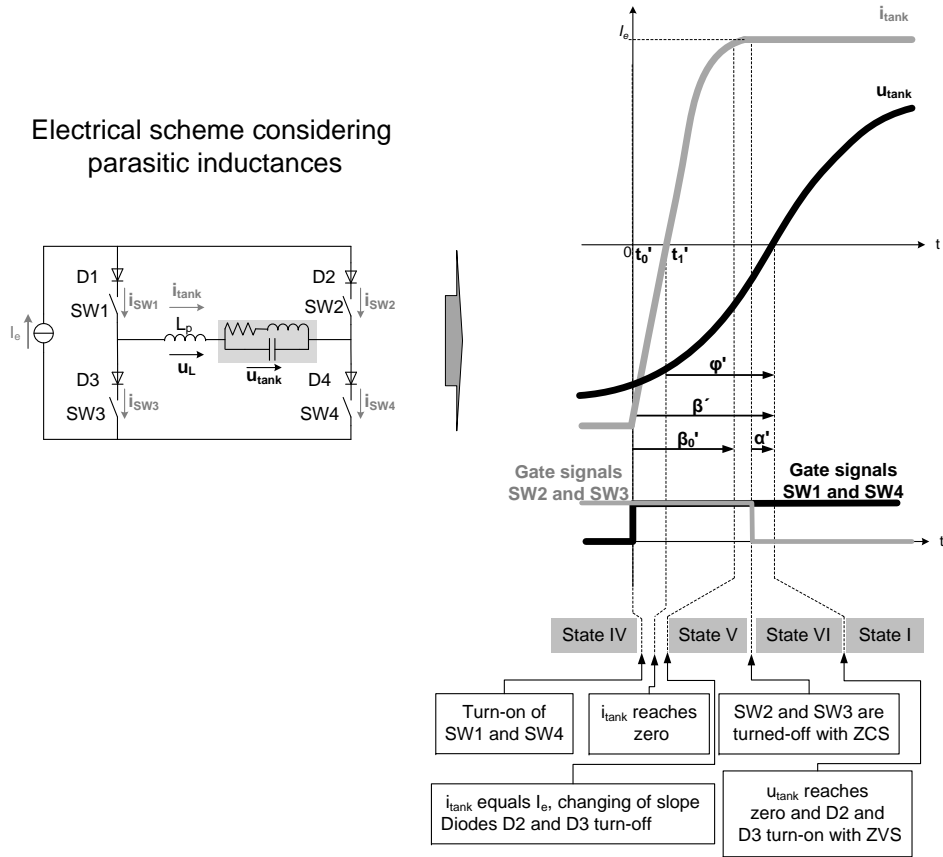Figure C.1: Output waveforms and sequence to obtain ZCS and ZVS at capacitive switching.

In order to have ZCS during switches' turn-off and ZVS in diodes' turn-on, the following sequence have to be accomplished:

1. Switches $SW1$ and $SW4$ are turned-on. This commutation can be realized with ZVS depending on the value of L_p, whose voltage can block the series diodes.

2. The current in the tank i_{tank} starts to decrease.

3. The voltage across the parasitic inductance u_L increase, opposing to the change in current. Its value is equal to u_{tank}, annulling voltage across switches.

4. The current in the tank i_{tank} reaches I_e, changing of slope.

5. The voltage across the inductance terminals is almost zero and diodes $D2$ and $D3$ are blocked due to voltage u_{tank}.

6. Switches $SW2$ and $SW3$ are turned-off with ZCS.

7. The voltage across the tank u_{tanc} changes polarity and diodes $D2$ and $D3$ are forward-biased with ZVS.

Considering this, the following parameters are defined (see Figure C.1):

- β' is the phase-shift between the instant at which the gate signal of the switch becomes high and u_{tank} reaches zero.

- β_0' is the phase-shift between the instant at which the gate signal of the switch becomes high and the moment at which the current i_{tank} reaches I_e.

- φ' is the phase-shift between i_{tank} and u_{tank}.

- α' is the phase-shift between the instant at which the switches' gate signal becomes low and the moment at which u_{tank} crosses zero.

C.2 Zero current and zero voltage switching conditions

In order to have the correct sequence described in the previous section and commutate with ZCS and ZVS, the following condition needs to be accomplished

$$\left(\beta' - \beta_0'\right) \geq \alpha' \geq 0 \tag{C.1}$$

Considering this, two conditions for β' and φ' can be derived from this inequality.

C.2.1 β' condition

Taking the moment at which $SW1$ and $SW4$ turn-on as a zero reference, the tank voltage is expressed as

$$u_{tank}\left(t\right) = \hat{u}_{tank}sin\left(\omega t - \beta'\right) \tag{C.2}$$

Before diodes $D2$ and $D3$ are blocked, all switches are conducting and the parasitic inductance L_p is connected to the tank. Under these circumstances, the inductance voltage is equal to the tank voltage. Thus, the current in the inductance, which is equal to i_{tank}, is as follows

$$i_L\left(t\right) = -\frac{1}{L_p}\int u_{tank}dt = \frac{\hat{u}_{tank}}{\omega L_p}cos\left(\omega t - \beta'\right) + C \tag{C.3}$$

Considering the current in the inductance at $t'_0 = 0$ is $-I_e$ (Figure C.1), Equation C.3 becomes

$$i_L\left(t\right) = \frac{\hat{u}_{tank}}{\omega L_p}cos\left(\omega t - \beta'\right) - \frac{\hat{u}_{tank}}{\omega L_p}cos\left(\beta'\right) - I_e \tag{C.4}$$

Assuming the current at β'_0 is equal to I_e, the following equation is accomplished

$$i_{tank}\left(\frac{\beta'_0}{\omega}\right) = I_e \tag{C.5}$$

combining with Equation C.4

$$i_L\left(\frac{\beta'_0}{\omega}\right) = \frac{\hat{u}_{tank}}{\omega L_p}cos\left(\beta'_0 - \beta'\right) - \frac{\hat{u}_{tank}}{\omega L_p}cos\left(\beta'\right) - I_e = I_e \tag{C.6}$$

and, thus

$$cos\left(\beta' - \beta'_0\right) = \frac{2I_e L_p \omega}{\hat{u}_{tank}} + cos\left(\beta'\right) \tag{C.7}$$

Considering the condition expressed in Equation C.1 for ZCS and ZVS at capacitive switching and combining with Equation C.7, then

$$\frac{2I_e L_p \omega}{\hat{u}_{tank}} + cos\left(\beta'\right) \leq cos\left(\alpha'\right) \tag{C.8}$$

that leads to the following condition

$$\beta' \geq arccos\left[cos\left(\alpha'\right) - \frac{2I_e L_p \omega}{\hat{u}_{tank}}\right] \tag{C.9}$$

C.2 Zero current and zero voltage switching conditions

Taking into consideration the limit situation where switches' turn-off occur immediately before u_{tank} reaches zero, then, $\alpha' = 0$ and Equation C.9 becomes

$$\beta' \geq arccos\left[1 - \frac{2I_e L_p \omega}{\hat{u}_{tank}}\right] \tag{C.10}$$

that represents the limit situation for having switches' ZCS and diodes' ZVS.

C.2.2 φ' condition

Considering that t'_1 is the moment at which i_{tank} changes polarity, the following equation is obtained from Equation C.4

$$i_{tank}\left(t'_1\right) = \frac{\hat{u}_{tank}}{\omega L_p}cos\left(\omega t'_1 - \beta'\right) - \frac{\hat{u}_{tank}}{\omega L_p}cos\left(\beta'\right) - I_e = 0 \tag{C.11}$$

Observing Figure C.1, the phase-shift between current and voltage is equal to

$$\varphi' = \beta' - \omega t'_1 \tag{C.12}$$

Therefore, Equation C.11 turns into

$$i_{tank}\left(t'_1\right) = \frac{\hat{u}_{tank}}{\omega L_p}cos\left(\varphi'\right) - \frac{\hat{u}_{tank}}{\omega L_p}cos\left(\beta'\right) - I_e = 0 \tag{C.13}$$

and

$$cos\left(\beta'\right) = cos\left(\varphi'\right) - \frac{I_e L_p \omega}{\hat{u}_{tank}} \tag{C.14}$$

Combining Equation C.10 with C.14, the following inequality emerges

$$cos\left(\varphi'\right) - \frac{I_e L_p \omega}{\hat{u}_{tank}} \leq 1 - \frac{2I_e L_p \omega}{\hat{u}_{tank}} \tag{C.15}$$

that simplified equals to

$$\varphi' \geq arccos\left[1 - \frac{I_e L_p \omega}{\hat{u}_{tank}}\right] \tag{C.16}$$